

Inert gas ion irradiation effects on microstructural and optical properties of monoclinic zirconia

by

P. Balasaritha

Enrolment No.: PHYS 02 2014 04 004

**Indira Gandhi Centre for Atomic Research, Kalpakkam,
Tamil Nadu, India 603102**

*A thesis submitted to the
Board of Studies in Physical Sciences
In partial fulfillment of requirements
for the Degree of*

DOCTOR OF PHILOSOPHY

of

Homi Bhabha National Institute

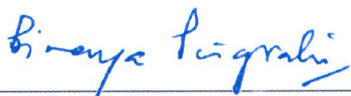


June 2020

Homi Bhabha National Institute

Recommendations of the Viva Voce Committee

As members of the Viva Voce Committee, we certify that we have read the dissertation prepared by P. Balasaritha entitled "Inert gas ion irradiation effects on microstructural and optical properties of monoclinic zirconia" and recommend that it may be accepted as fulfilling the thesis requirement for the award of Degree of Doctor of Philosophy.



Chairman: **Dr. B. K. Panigrahi**

Date: 15-04-2021



Guide/ Convener: **Dr. S. Amirthapandian**

Date: 15.04.2021



External Examiner: **Prof. S.V.S Nageswara Rao**

Date: 15/04/2021



Member 1: **Dr. N. V. Chandra Shekar**

Date: 15.04.2021



Member 2: **Dr. Arup Dasgupta**


15.04.2021
Date:

Final approval and acceptance of this thesis is contingent upon the candidate's submission of the final copies of the thesis to HBNI.

I hereby certify that, I have read this thesis prepared under my direction and recommend that it may be accepted as fulfilling the thesis requirement.

Date: 15.04.2021

Place: Kalpakkam


Dr. S. Amirthapandian
(Guide)

Homi Bhabha National Institute

Recommendations of the Viva Voce Committee

As members of the Viva Voce Committee, we certify that we have read the dissertation prepared by P. Balasaritha entitled "Inert gas ion irradiation effects on microstructural and optical properties of monoclinic zirconia" and recommend that it may be accepted as fulfilling the thesis requirement for the award of Degree of Doctor of Philosophy.



Chairman: **Dr. B. K. Panigrahi**

Date: 15-04-2021



Guide/ Convener: **Dr. S. Amirthapandian**

Date: 15.04.2021



External Examiner: **Prof. S.V.S Nageswara Rao**

Date: 15/04/2021



Member 1: **Dr. N. V. Chandra Shekar**

Date: 15.04.2021



Member 2: **Dr. Arup Dasgupta**

15.04.2021
Date:

Final approval and acceptance of this thesis is contingent upon the candidate's submission of the final copies of the thesis to HBNI.

I hereby certify that, I have read this thesis prepared under my direction and recommend that it may be accepted as fulfilling the thesis requirement.

Date: 15.04.2021

Place: Kalpakkam



Dr. S. Amirthapandian

(Guide)

Statement by Author

This dissertation has been submitted in partial fulfillment of requirements for an advanced degree at Homi Bhabha National Institute (HBNI) and is deposited in the Library to be made available to borrowers under rules of the HBNI.

Brief quotations from this dissertation are allowable without special permission, provided that accurate acknowledgement of source is made. Requests for permission for extended quotation from or reproduction of this manuscript in whole or in part may be granted by the Competent Authority of HBNI when in his or her judgment the proposed use of the material is in the interests of scholarship. In all other instances, however, permission must be obtained from the author.

Date: 15/4/2021

Place: Kalpaklam



(P. Balasaritha)

Declaration

I, hereby declare that the investigation presented in the thesis has been carried out by me. The work is original and has not been submitted earlier as a whole or in part for a degree / diploma at this or any other Institution / University



(P. Balasaritha)

List of Publications arising from the thesis

Journals

1. Ion beam induced phase transformation and krypton bubble formation in monoclinic zirconium oxide
P. Balasaritha, S. Amirthapandian, P. Magudapathy, R. M. Sarguna, S. K. Srivastava, B. K. Panigrahi
Journal of Nuclear Materials., (2018), **508**, 385–394
2. Low energy Ar⁺ ion irradiation effects in monoclinic zirconia
P. Balasaritha, S. Amirthapandian, P. Magudapathy, R. M. Sarguna, S. K. Srivastava, R. Krishnan
Nuclear Instruments and Methods in Physics Research B., (2019), **441**, 23–32.

Manuscripts under preparation

1. Photoluminescence studies on low energy krypton ion and laser irradiated monoclinic zirconia
P. Balasaritha, S. Amirthapandian, S. K. Srivastava, P. Magudapathy, R. Krishnan
2. Helium ion induced phase transformation and bubble formation in monoclinic zirconia
P. Balasaritha, S. Amirthapandian, P. Magudapathy, R. M. Sarguna, S. K. Srivastava

Conference Proceedings

1. Krypton ion induced structural phase transition in zirconia thin film
P. Balasaritha, S. Amirthapandian, P. Magudapathy, R. Krishnan, B. K. Panigrahi
AIP conference proceedings., (2017), **1832**, 030015 -030017.

Conference Presentations

1. Low energy krypton ion irradiation effects in ZrO₂
P. Balasaritha, S. Amirthapandian, P. Magudapathy, B.K. Panigrahi
International conference on Ion Beams in Materials Engineering and Characterizations (IBMEC-2016), Inter-University Accelerator Centre, New Delhi, September 28-October 1, 2016.
2. Low energy Argon ion irradiation induced phase transformation in zirconia-TEM analysis
P. Balasaritha, S. Amirthapandian, P. Magudapathy, B.K. Panigrahi
International Conference on Electron Microscopy and Allied Techniques (EMSI-2017), Mahabalipuram, Tamilnadu, India, July 17-19, 2017.
3. Phase transformation in low energy Ar⁺ ion irradiated monoclinic zirconia
P. Balasaritha, S. Amirthapandian, P. Magudapathy, R. M. Sarguna, S. K. Srivastava
5th international conference on Nanostructuring by ion beams (ICNIB-2019), IGCAR, Tamilnadu, India, November 6-8, 2019.



(P. Balasaritha)

Dedicated to my parents

During the 1960s

Acknowledgements

I take this opportunity to thank my guide Dr. S. Amirthapandian. He has sensibly designed my research program with due care, and amidst his busy schedule, he did have a constant vigil on my research progress. His technical interpretations on the experimental data and the corrections in manuscripts were the closing remark and the final word on the issue.

I am very much grateful to the dedication and enthusiasm shown by Mr P. Magudapathy to finish my Ph.D. He literally assumed the role of guide throughout my research career. I thank him, for carrying out number of irradiation and XRD measurements. I am grateful for the assistance he provided in handling the equipment and the enthusiasm he showed in correcting the thesis and journals

I am very much grateful to the dedication and enthusiasm shown by Dr. P Jegadeesan to finish my Ph.D. I sincerely thank Dr. K. Sarvanan for assisting me in carrying out the experiments. He has shared many technical details of the equipment and the knacks of the experiments. I thank Dr. Sachin Kumar Srivastava for helping me in luminescence experiments and their analysis. I gratefully acknowledge the technical guidance and scientific discussions provided by him in spite of his busy schedule. I thank Mrs. Sruthi Mohan for helping me in analyzing TEM data and for other scientific discussions.

I express special thanks to Dr. R. M. Sarguna for carrying out the GIXRD measurements. I also thank Dr. R. Krishnan for allowing me to carry out the pulsed laser deposition technique for depositing thin films and the excimer laser for the laser irradiation experiments. I thank Mrs. M. S. Sinduja for helping me in SEM measurements and I would like to thank Ms. Jagnaseni Pradhan for her assistance in luminescence measurements.

My special and sincere thanks to lab members for providing support and motivation. I like to thank them for the help they provided me throughout my research.

I sincerely thank all my section colleagues for their cooperation. I sincerely thank Dr. B. K. Panigrahi chairman of the doctoral committee. I thank Dr. N. V. Chandra Shekar and Dr. Arup Dasgupta for their encouragement and support.

I also thank Dr. R. Rajaraman, Dean Physical Science for helping me during the final years of the programme.


P. Balasaritha

Table of contents

List of Publications arising from the thesis.....	v
Acknowledgements	ix
Abstract	xi
Table of contents	xiii
List of Figures	xvi
List of tables	xxiii

Chapter 1 Introduction 1

1.1. Background	1
1.2. Phase transformation in zirconia	2
1.2.1. Role of grain size	2
1.2.2. Role of temperature	4
1.2.3. Role of pressure	5
1.2.4. Ion irradiation induced phase transformation	6
1.3. Inert gas bubble formation in oxide	14
1.3.1. Mechanism of bubble formation	15
1.3.2. Bubble induced swelling	16
1.4. Luminescence properties of zirconia	18
1.5. Objective of the thesis	20

Chapter 2 Experimental Techniques 21

2.1. Synthesis-thermal decomposition method	21
2.2. Irradiation facility.....	23
2.3. Grazing incidence X-ray diffraction	24
2.3.1. Crystallite size –Scherrer formula	25
2.3.2. Strain calculation-WH method	25
2.4. Raman scattering	27
2.4.1. Confocal Raman Microscopy	27
2.5. Time resolved photoluminescence spectroscopy	28
2.6. Electron microscopy.....	31
2.6.1. Scanning electron microscopy.....	31
2.6.2. Transmission electron microscopy	33
2.7. Summary	37

Chapter 3 Ion irradiation induced phase transformation in monoclinic zirconia..... 39

3.1. Motivation	39
3.2. Synthesis of monoclinic zirconia	40
3.3. Ion Irradiation and characterization methods.....	40

3.4. Results.....	41
3.4.1. Grazing incidence X-ray diffraction analysis.....	41
3.4.2. Electron diffraction analysis.....	50
3.4.3. Raman scattering analysis	54
3.5. Discussion	61
3.6. Conclusions.....	64
Chapter 4 Bubble induced swelling in monoclinic zirconia.....	67
4.1. Introduction.....	67
4.2. Experiments	67
4.3. Morphological analysis using scanning electron microscopy	68
4.3.1. SEM analysis of the as-sintered zirconia	68
4.3.2. SEM analysis of the He ⁺ ion irradiated zirconia samples	68
4.3.3. SEM analysis of the Ar ⁺ ion irradiated zirconia samples.....	74
4.3.4. SEM analysis of the Kr ⁺ ion irradiated zirconia samples.....	78
4.4. Microstructural analysis using transmission electron microscopy	81
4.4.1. TEM analysis of the He ⁺ ion irradiated zirconia samples	81
4.4.2. TEM analysis of the Ar ⁺ ion irradiated zirconia samples	85
4.4.3. TEM analysis of the Kr ⁺ ion irradiated zirconia samples	88
4.5. Bubble induced swelling in ion irradiated zirconia	91
4.6. Discussion	92
4.7. Conclusions.....	96
Chapter 5 Optical properties of ion irradiated monoclinic zirconia	99
5.1. Introduction.....	99
5.2. Experiment.....	99
5.3. SEM analysis of laser irradiation effects on ion irradiated surfaces.....	100
5.3.1. SEM analysis of laser irradiated zirconia.....	100
5.3.2. SEM analysis on laser irradiated on He ⁺ ion irradiated zirconia samples	101
5.3.3. SEM analysis on laser irradiated on Ar ⁺ ion irradiated zirconia samples	104
5.3.4. SEM analysis on laser irradiated on Kr ⁺ ion irradiated zirconia samples	108
5.4. Photoluminescence analysis of laser and ion irradiated ZrO ₂	111
5.4.1. PL analysis of as-sintered and laser irradiated zirconia samples	111
5.4.2. PL analysis of He ⁺ ion irradiated and laser irradiated zirconia samples	113
5.4.3. PL analysis of Ar ⁺ ion irradiated and laser irradiated zirconia samples	117
5.4.4. PL analysis of Kr ⁺ ion irradiated and laser irradiated zirconia samples	119
5.5. Time resolved photoluminescence spectroscopy	123

5.6. Discussion	126
5.7. Conclusions	130
Chapter 6 Summary and scope for future work.....	131
6.1. Summary	131
6.2. Phase transformation upon ion irradiation	131
6.3. Bubbles formation and bubble induced swelling.....	132
6.4. Luminescence properties of ion and laser irradiated monoclinic zirconia.....	133
6.5. Scope for future work.....	133
Appendix A	135
A.1 X-Ray Fluorescence spectroscopy	135
References	137

List of Figures

Figure 1.1	Phase stability crossover of nanocrystalline zirconia[19].	3
Figure 1.2	Phase diagram of ZrO_2 as a function of temperature and pressure[23]	4
Figure 1.3	The nuclear and electronic energy loss of krypton ions in ZrO_2 as a function of ion energy. The data is calculated from SRIM software[37].	6
Figure 1.4	Selected area electron diffraction (SAED) patterns of the bilayer nanocrystalline zirconia film subjected to 1 MeV Kr^{2+} irradiation at room temperature for various ion fluences: (a) original (b) 3.13×10^{14} ions/ cm^2 (c) 6.25×10^{14} ions/ cm^2 and (d) 3.13×10^{15} ions/ cm^2 . The appearance of the diffraction ring d_{102} in the SAED patterns ((c) and (d)) demonstrates that the tetragonal phase was formed upon ion irradiation[41].	11
Figure 1.5	Raman spectra at ambient conditions of different ZrO_2 samples: (a) pressurized to 10.5 GPa but not irradiated, (b) irradiated with 2×10^{12} U-ions/ cm^2 but without pressure and the fraction of transformed phase was $(6.3 \pm 0.8)\%$, (c) irradiated with 2×10^{12} U-ions/ cm^2 under pressure of (10.3 ± 0.3) GPa and the fraction of the transformed phase was $(91.2 \pm 3.4)\%$ [42].	12
Figure 1.6	X-ray diffraction patterns of the un-irradiated amorphous-dominant ZrO_2 and ZrO_2 thin films irradiated with 350 keV O^+ ion for the ion fluence $5 \times 10^{16}/\text{cm}^2$ [21].	13
Figure 1.7	HRTEM images of the cross-section of T'-YSZ samples irradiated (300 K) with 60 keV He^+ ions with the ion fluences of 1×10^{18} ions/ cm^2 [89]	17
Figure 1.8	Krypton bubbles observed in ZrO_2 thin films irradiated with 60 keV Kr^+ ion for the ion fluence of 1×10^{17} ions/ cm^2 [76]	17
Figure 1.9	Photoluminescence of various types of zirconia (1) Y stabilized zirconia single crystal ZrO_2 (2) commercial powder (3) Y stabilized nanocrystals (4) undoped nanocrystals prepared by hydrothermal method and (5) undoped nanocrystals synthesized by plasma synthesis[93]	18
Figure 1.10	Schematic representation of the photoluminescence process in zirconia	18
Figure 2.1	(a) Schematic diagram of a tubular furnace used for the decomposition of zirconium acetyl acetate (b) Schematic representation of the chemical reaction during the thermal decomposition.	22
Figure 2.2	(a) Photograph of 150 kV ion accelerator used for the ion irradiation experiments (b) Schematic diagram of the 150 kV ion accelerator.	23
Figure 2.3	Schematic diagram of the GIXRD and X-ray penetration depth in the specimen.	24
Figure 2.4	Williamson Hall plot for the measurement of crystallite size and strain in the samples. The intercept ($K\lambda/L$) gives the crystallite size and the slope ϵ gives the strain.	26

Figure 2.5	(a) Photograph of the WITec RA 300 confocal Raman imaging system (b) Schematic diagram of confocal Raman imaging system with optical components.	28
Figure 2.6	Photograph of FLS 980 UV-Vis absorption spectrometer.	29
Figure 2.7	Schematic diagram of TRPL measurement system.	29
Figure 2.8	Schematic diagram of TCSPC technique used for TRPL measurement.	30
Figure 2.9	(Left) Schematic representation of electron interaction with specimen and (Right) Interaction volume (blue) of the electron beam inside the specimen.	31
Figure 2.10	(Left) Photograph of Zeiss Crossbeam 360 SEM equipment (Right) Schematic diagram of the components of scanning electron microscopy.	32
Figure 2.11	(Left) Photograph of LIBRA 200FE high resolution electron microscope (Right) the illustration of the electron path in the TEM	33
Figure 2.12	Schematic diagram showing the two basic types of operating modes of TEM (a) diffraction mode and (b) imaging mode[121].	34
Figure 2.13	Schematic representation of various types of beam focusing conditions in TEM[121].	35
Figure 2.14	TEM images of 120 keV He^+ ion irradiated ZrO_2 (ion fluence 2×10^{17} ions/cm ² , 300 K) taken in different focusing conditions.	36
Figure 3.1	(a) GIXRD pattern of the precursor zirconium acetyl acetate. (b) Stick pattern of the ICCD Card No 00-018-1515 corresponding to monoclinic phase of zirconium acetyl acetate. GIXRD pattern of the samples obtained as a result of thermal decomposition (c) 600 °C for 5 hour and (d) 900 °C for 18hrs. (e) Stick pattern tetragonal phase (ICCD Card No 00-050-1089) and (f) monoclinic phase (ICCD Card No 01-070-2491) of zirconia.	42
Figure 3.2	GIXRD pattern of the as-sintered and 120 keV He^+ ion irradiated (at 300 K) zirconia samples.	43
Figure 3.3	GIXRD pattern of the as-sintered and 120keV He^+ ion irradiated (at 143 K) zirconia samples.	44
Figure 3.4	(a) Variation of peak position (plane 111) as a function of He^+ ion fluence for ion irradiation temperatures 300 K and 143 K (b) Variation of macrostrain as a function of the He^+ ion fluence for He^+ ion irradiated zirconia samples (300 K and 143 K).	45
Figure 3.5	GIXRD pattern of the as-sintered and 120 keV Ar^+ ion irradiated zirconia samples for the ion irradiation temperatures 300 K and 143 K. The tetragonal peak corresponding to the plane (101) is marked.	46
Figure 3.6	(a) Variation of peak position (plane 111) as a function of Ar^+ ion fluence for ion irradiation temperatures of 300 K and 143 K (b) Variation of macrostrain induced in the zirconia samples upon ion irradiation (300 K and 143 K) as a function of Ar^+ ion fluence.	47

- Figure 3.7 (a-e) GIXRD pattern of the as-sintered and 60 keV Kr^+ ion irradiated (at 300 K and 143 K) zirconia samples. The tetragonal peak corresponding to the plane (101) is marked with an arrow 48
- Figure 3.8 (a) Variation of peak position (plane 111) as a function of Kr^+ ion fluence for both the ion irradiation temperatures 300 K and 143 K (b) Variation of macrostrain induced in the zirconia samples as a function of the Kr^+ ion fluence. 49
- Figure 3.9 (a) Low magnification bright field TEM image, (b) dark field TEM image,, (c) particle size distribution of the as-sintered zirconia sample and (d) HRTEM image of the as-sintered zirconia. In the HRTEM image, the planes (200) and (100) corresponds to the monoclinic structure of zirconia and the angle between them 53.4° are clearly marked. 50
- Figure 3.10 Selected area electron diffraction pattern and corresponding radial intensity profile of the (a),(b) as-sintered, (c),(d)120 keV He^+ ion irradiated (ion fluence 1×10^{17} ion/cm², 300 K) and (e),(f) 120 keV He^+ ion irradiated (ion fluence 2×10^{17} ion/cm², 143 K) zirconia samples respectively. The new peaks (marked with “*”) are corresponding to the tetragonal phase and other peaks are from the monoclinic phase. 51
- Figure 3.11 Selected area electron diffraction pattern and corresponding radial intensity profile of the (a),(b) 120 keV Ar^+ ion irradiated (ion fluence 1×10^{17} ion/cm², 300 K) and (c),(d) 120 keV Ar^+ ion irradiated (ion fluence 2×10^{17} ion/cm², 143 K) zirconia samples respectively. The new peaks (marked with “*”) are corresponding to the tetragonal phase and other peaks are from the monoclinic phase. 52
- Figure 3.12 Selected area electron diffraction pattern and corresponding radial intensity profile of the (a),(b) 60 keV Kr^+ ion irradiated (ion fluence 1×10^{17} ion/cm², 300 K) and (c),(d) 60 keV Kr^+ ion irradiated (ion fluence 1×10^{17} ion/cm², 143 K) zirconia samples respectively. The new peaks (marked with “*”) are corresponding to the tetragonal phase and other peaks are from the monoclinic phase. 53
- Figure 3.13 Raman spectra of the as-sintered and the 120 keV He^+ ion irradiated zirconia at (a) 300 K and (c) 143 K. (b), (d) shows the expanded view of (a) and (c) respectively. 55
- Figure 3.14 Variation of the peak positions of the Raman modes as a function of He^+ ion fluences for the ion irradiation temperature at (a) 300 K and (b) 143 K. 56
- Figure 3.15 Raman spectra of the as-sintered and the 120 keV Ar^+ ion irradiated zirconia at (a) 300 K and (c) 143 K The appearance of the mode (E_g) at 144 cm^{-1} confirms the formation of tetragonal phase upon ion irradiation. (b), (d) shows the expanded view of (a) and (c) respectively and it clearly shows the shift in the E_g mode (144 cm^{-1}) 57
- Figure 3.16 Variation of peak position of the Raman modes as a function of Ar^+ ion fluence for the irradiation temperature at (a) 300 K and (b) 143 K. 58

Figure 3.17	Raman spectra of the as-sintered and the 60 keV Kr^+ ion irradiated zirconia at (a) 300 K and (c) 143 K. The appearance of the mode (E_g) at 144 cm^{-1} confirms the formation of tetragonal phase upon ion irradiation. (b), (d) shows the expanded view of (a) and (c) respectively and it clearly shows the shift in the E_g mode (144 cm^{-1}).	59
Figure 3.18	Variation of peak position of the Raman modes as a function of Kr^+ ion fluence for the irradiation temperature at (a) 300 K and (b) 143 K.	60
Figure 4.1	(a) SEM image and (b) the grain size distribution of the as-sintered zirconia sample. The shape of the grains is spherical in nature.	68
Figure 4.2	SEM images of the 120 keV He^+ ion irradiated zirconia samples for the ion fluences of (a) 5×10^{15} ions/ cm^2 , (b) 1×10^{16} ions/ cm^2 , (c) 5×10^{16} ions/ cm^2 and (d) 1×10^{17} ions/ cm^2 at 300 K.	69
Figure 4.3	Plots showing the grain size distribution in 120 keV He^+ ion irradiated zirconia samples for the ion fluences of (a) 5×10^{15} ions/ cm^2 , (b) 1×10^{16} ions/ cm^2 , (c) 5×10^{16} ions/ cm^2 and (d) 1×10^{17} ions/ cm^2 at 300 K.	70
Figure 4.4	SEM images of the He^+ ion irradiated zirconia samples for the ion fluences of (a) 1×10^{16} ions/ cm^2 , (b) 5×10^{16} ions/ cm^2 , (c) 1×10^{17} ions/ cm^2 and (d) 2×10^{17} ions/ cm^2 at 143 K.	71
Figure 4.5	Grain size distribution of the He^+ ion irradiated zirconia samples for the ion fluences of (a) 1×10^{16} ions/ cm^2 , (b) 5×10^{16} ions/ cm^2 , (c) 1×10^{17} ions/ cm^2 and (d) 2×10^{17} ions/ cm^2 at 143 K.	72
Figure 4.6	Fractional area of free space “a/A” as a function of ion fluence, for the He^+ ion irradiated zirconia samples at (a) 300 K and (b) 143 K	73
Figure 4.7	SEM images of the 120 keV Ar^+ ion irradiated zirconia samples for the ion fluences of (a) 1×10^{15} ions/ cm^2 , (b) 5×10^{15} ions/ cm^2 , (c) 1×10^{16} ions/ cm^2 and (d) 5×10^{16} ions/ cm^2 at 300 K.	74
Figure 4.8	Grain size distribution of the the zirconia sample upon Ar^+ ion irradiation at 300 K for the ion fluences of (a) 1×10^{15} ions/ cm^2 , (b) 5×10^{15} ions/ cm^2 , (c) 1×10^{16} ions/ cm^2 , (d) 5×10^{16} ions/ cm^2 .	75
Figure 4.9	SEM images of the 120 keV Ar^+ ion irradiated zirconia samples for the ion fluences of (a) 5×10^{16} ions/ cm^2 and (b) 2×10^{17} ions/ cm^2 at 143 K.	76
Figure 4.10	Grain size distribution of the Ar^+ ion irradiated zirconia samples for the ion fluences of (a) 5×10^{16} ions/ cm^2 and (b) 2×10^{17} ions/ cm^2 at 143 K.	77
Figure 4.11	Fractional area of free space “a/A” as a function of ion fluence, for the Ar^+ ion irradiated zirconia samples at (a) 300 K and (b) 143 K.	77
Figure 4.12	SEM images of the 60 keV Kr^+ ion irradiated zirconia samples for the ion fluences of (a) 1×10^{16} ions/ cm^2 , (b) 1×10^{17} ions/ cm^2 and (c) 5×10^{17} ions/ cm^2 at 300 K.	78
Figure 4.13	SEM images of the 60 keV Kr^+ ion irradiated zirconia samples for the ion fluences of (a) 1×10^{16} ions/ cm^2 , (b) 5×10^{16} ions/ cm^2 , (c) 1×10^{17} ions/ cm^2 and (d) 5×10^{17} ions/ cm^2 at 143 K.	79

- Figure 4.14 Grain size distribution of the 60 keV Kr^+ ion irradiated zirconia samples for the ion fluences of (a) 1×10^{16} ions/cm² and (b) 5×10^{16} ions/cm² at 143 K 80
- Figure 4.15 Fractional area of free space “a/A” as a function of ion fluence, for the Kr^+ ion irradiated zirconia samples at (a) 300 K and (b) 143 K. 81
- Figure 4.16 TEM image of zirconia samples irradiated with 120 keV He^+ ions at 300 K. (a), (c) and (e) show the low magnification bright filed TEM images of the samples irradiated for the ion fluences 1×10^{16} ions/cm², 1×10^{17} ions/cm² and 2×10^{17} ions/cm², respectively. (b), (d) and (f) show the corresponding HRTEM images of the samples. All the images are recorded at under-focus condition in TEM, where the bubbles are identified with their Fresnel fringes. 82
- Figure 4.17 The bubble size distribution in the He^+ ion irradiated (at 300 K) zirconia samples for the ion fluence of (a) 1×10^{16} ions/cm², (b) 1×10^{17} ions/cm² and (c) 2×10^{17} ions/cm². 83
- Figure 4.18 (a) Low magnification bright field TEM image of zirconia samples irradiated with 120 keV He^+ ions at 143 K for the ion fluences of (a) 1×10^{17} ions/cm² and (c) 2×10^{17} ions/cm². (b) and (d) show the corresponding HRTEM images of the samples. All the TEM micrographs are recorded in underfocus condition. 84
- Figure 4.19 The size distribution of the helium bubbles in the zirconia samples irradiated with 120 keV He^+ ions at 143 K, upto the ion fluence of (a) 1×10^{16} ions/cm² and (b) 2×10^{17} ions/cm². 85
- Figure 4.20 (a) Low magnification bright filed TEM image of zirconia samples irradiated with 120 keV Ar^+ ions at 300 K for the ion fluence of (a) 5×10^{16} ions/cm² and (c) 1×10^{17} ions/cm². (b) and (d) show the corresponding the HRTEM images of the samples. All the TEM micrographs are recorded in underfocus condition. 86
- Figure 4.21 The bubble size distribution of the Ar^+ ion irradiated (at 300 K) ZrO_2 samples for the ion fluence of (a) 5×10^{16} ions/cm²) and (b) 1×10^{17} ions/cm² 86
- Figure 4.22 (a) Bright field TEM image of 120 keV Ar^+ ion irradiated ZrO_2 (2×10^{17} ions/cm², 143 K) recorded in underfocus condition, and (b) the corresponding HRTEM image. The plane 111 corresponding to the monoclinic phase is clearly seen. Some of the argon bubbles are marked with arrows. 87
- Figure 4.23 The size distribution of the bubbles in zirconia sample irradiated with Ar^+ ion irradiated at 143 K for the ion fluence of 2×10^{17} ions/cm². 87
- Figure 4.24 (a) Low magnification bright field TEM image of the zirconia samples irradiated with 60 keV Kr^+ ions at 300 K for the ion fluence of (a) 1×10^{16} ions/cm², (c) 5×10^{16} ions/cm² and (e) 1×10^{17} ions/cm². (b), (d) and (e) show the corresponding HRTEM images of the samples. All the TEM micrographs are recorded in underfocus condition. 89

Figure 4.25	(a) Low magnification bright field TEM image and (b) HRTEM image of zirconia sample irradiated with 60 keV Kr^+ ions at 143 K for the ion fluence 1×10^{17} ions/cm ² . Both the images are recorded in underfocus condition. The 502 plane of the monoclinic phase is marked in (b).	90
Figure 4.26	The bubble size distribution of the Kr^+ ion irradiated ZrO_2 samples for the ion fluence of (a) 1×10^{16} ions/cm ² (300 K), (b) 1×10^{17} ions/cm ² (300 K) (c) 2×10^{17} ions/cm ² (300 K) and (d) 1×10^{17} ions/cm ² (143 K)	91
Figure 5.1	SEM images of the laser irradiated zirconia samples for the laser shots of (a) 200 shots and (b) 2000 shots.	101
Figure 5.2	SEM images of the laser (200 shots) irradiated on He^+ ion (at 300 K) irradiated zirconia samples for the ion fluences of (a) 1×10^{16} ions/cm ² and (b) 2×10^{17} ions/cm ² .	101
Figure 5.3	SEM images of the laser (2000 shots) irradiated on He^+ ion (at 300 K) irradiated zirconia samples for the ion fluences of (a) 1×10^{16} ions/cm ² and (b) 2×10^{17} ions/cm ² .	103
Figure 5.4	SEM images of the laser (200 shots) irradiated on He^+ ion (at 143 K) irradiated zirconia samples for the ion fluences of (a) 1×10^{16} ions/cm ² and (b) 2×10^{17} ions/cm ² .	103
Figure 5.5	SEM images of the laser (2000 shots) irradiated on He^+ ion (at 143 K) irradiated zirconia samples for the ion fluences of (a) 1×10^{16} ions/cm ² and (b) 2×10^{17} ions/cm ² .	104
Figure 5.6	SEM images of the laser (200 shots) irradiated on Ar^+ ion irradiated (at 300 K) zirconia samples for the ion fluences of (a) 1×10^{16} ions/cm ² and (b) 5×10^{16} ions/cm ²	105
Figure 5.7	SEM images of the laser (2000 shots) irradiated on Ar^+ ion irradiated (at 300 K) zirconia samples for the ion fluences of (a) 1×10^{15} ions/cm ² and (b) 5×10^{16} ions/cm ² .	106
Figure 5.8	SEM images of the laser (200 shots) irradiated on Ar^+ ion irradiated (at 143 K) zirconia samples for the ion fluences of (a) 5×10^{16} ions/cm ² and (b) 2×10^{17} ions/cm ² .	107
Figure 5.9	SEM images of the laser (2000 shots) irradiated on Ar^+ ion irradiated (at 143 K) zirconia samples for the ion fluences of (a) 5×10^{16} ions/cm ² and (b) 2×10^{17} ions/cm ² .	107
Figure 5.10	SEM images of the laser (200 shots) irradiated on Kr^+ ion irradiated (at 300 K) zirconia samples for the ion fluences of (a) 1×10^{16} ions/cm ² and (b) 5×10^{17} ions/cm ² .	108
Figure 5.11	SEM images of the laser (2000 shots) irradiated on Kr^+ ion irradiated (at 300 K) zirconia samples for the ion fluences of (a) 1×10^{16} ions/cm ² and (b) 5×10^{17} ions/cm ² .	109
Figure 5.12	(a) SEM images of the laser (200 shots) irradiated on Kr^+ ion irradiated (at 143 K) zirconia samples for the ion fluences of (a) 1×10^{16} ions/cm ² and (b) 5×10^{17} ions/cm ² .	110

- Figure 5.13 SEM images of the laser (2000 shots) irradiated on Kr^+ ion irradiated (at 143 K) zirconia samples for the ion fluences of (a) 1×10^{16} ions/cm² and (b) 5×10^{17} ions/cm². 110
- Figure 5.14 Photoluminescence spectra of the as-sintered and laser (200 shots and 2000 shots) irradiated zirconia samples 112
- Figure 5.15 (a) Decay of the photoluminescence intensity with respect to time of exposure obtained from the as-sintered and laser (200 and 2000 shots) irradiated zirconia samples and (b) Time constants of the PL intensity decay extracted by bi exponential curve fitting. 112
- Figure 5.16 PL spectra of zirconia samples with different conditions. (a) He^+ ion irradiated (at 300 K), and further irradiated with laser for (b) 200 shots, and (c) 2000 shots, (d) He^+ ion irradiated (at 143 K) and further irradiated with laser for (e) 200 shots, and (f) 2000 shots. 113
- Figure 5.17 Decay of the photoluminescence intensity with respect to time of exposure obtained from the zirconia samples (a) He^+ ion irradiated (at 300 K), (b) He^+ ion irradiated (at 300 K) and further irradiated with laser for 2000 shots, (c) He^+ ion irradiated (143 K) and (d) He^+ ion irradiated (143 K) further irradiated with laser for 2000 shots. 115
- Figure 5.18 PL spectra of zirconia samples with different conditions. (a) Ar^+ ion irradiated (at 300 K), and further irradiated with laser for (b) 200 shots, and (c) 2000 shots, (d) Ar^+ ion irradiated (at 143 K), further irradiated with laser for (e) 200 shots, and (f) 2000 shots. 117
- Figure 5.19 PL spectra of zirconia samples with different conditions. (a) Kr^+ ion irradiated (at 300 K), and further irradiated with laser for (b) 200 shots, and (c) 2000 shots, (d) Kr^+ ion irradiated (at 143 K), further irradiated with laser for (e) 200 shots, and (f) 2000 shots. 120
- Figure 5.20 (a) Excitation and emission spectra and (b) time resolved photoluminescence (TRPL) spectrum for the as-sintered zirconia sample 123
- Figure 5.21 Time resolved photoluminescence spectra for the zirconia samples irradiated with He^+ ions for the ion fluences of (a) 1×10^{16} ions/cm² (at 300 K) (b) 2×10^{17} ions/cm² (at 300 K) (c) 1×10^{16} ions/cm² (at 143 K) and (d) 2×10^{16} ions/cm² (at 143 K). 124
- Figure 5.22 Plot of PL intensity ratio ($I_{\text{Ion irradiated}} / I_{\text{As-sintered}}$) as a function ion fluence for (a) He^+ (b) Ar^+ and (c) Kr^+ ion irradiated zirconia samples. The samples are irradiated at 300 K and 143 K. 128

List of tables

Table 1.1	Different crystal structures and its unit cell parameters of zirconia[22, 30, 33–36]	5
Table 1.2	Time scale for the production of defects in the irradiated material[39].	9
Table 3.1	Details of ion irradiation parameters.	41
Table 3.2	Details of ions, ion energy, ion irradiation temperature, ion fluence, damage (in dpa) and the fraction of tetragonal phase formed as a result of ion irradiation (in %)	61
Table 4.1	The table lists the average bubble size and the areal density of bubbles for all the ion irradiated zirconia sample.	92
Table 5.1	The table explains the convention followed while giving codes for different zirconia samples which were initially irradiated with an inert gas ion for different ion fluences, at 300 K or 143 K, followed by laser irradiation upto 200 shots or 2000 shots. The sample code does not include information about the inert gas ion used for irradiation.	100
Table 5.2	Average grain size values of the He^+ ion irradiated at 300 K and 143 K, and laser (200 and 2000 shots) irradiation on He^+ ion irradiated zirconia samples	102
Table 5.3	Average grain size values of the Ar^+ ion irradiated (at 300 K and 143 K) and laser (200 and 2000 shots) irradiation on Ar^+ ion irradiated zirconia samples	105
Table 5.4	Average grain size values of the Kr^+ ion irradiated (at 300 K and 143 K) and laser (200 and 2000 shots) irradiation on Kr^+ ion irradiated zirconia samples	108
Table 5.5	Decay time constants (τ_1 and τ_2) of the PL intensity with respect to time of exposure obtained from the He^+ ion irradiated (at 300 K and 143 K) and further laser (200 and 2000 shots) irradiated zirconia samples.	116
Table 5.6	Decay time constants (τ_1 and τ_2) of the PL intensity with respect to time of exposure obtained from the Ar^+ ion irradiated (at 300 K and 143 K) and further laser (200 and 2000 shots) irradiated zirconia samples	118
Table 5.7	Decay time constants (τ_1 and τ_2) of the PL intensity with respect to time of exposure obtained from the Kr^+ ion irradiated (at 300 K and 143 K) and further laser (200 and 2000 shots) irradiated zirconia samples.	122
Table 5.8	PL lifetime of the as-sintered and ion (He^+ , Ar^+ and Kr^+) irradiated (at 300 K and 143 K)) zirconia samples. It is to be noted that the lifetime is in nano seconds	125
Table 6.1	The table lists the fraction of tetragonal phase, swelling and macrostrain in the zirconia samples upon inert gas ion irradiation.	132

Chapter 6

Summary and scope for future work

6.1. Summary

This thesis deals with the low energy inert gas ion irradiation in monoclinic zirconia. Ion irradiation was carried out for creating damage and the effects were studied using GIXRD, Raman scattering, electron diffraction, photoluminescence and time resolved photoluminescence spectroscopy. Further, laser irradiation was carried on the ion irradiated zirconia sample to study the effects created by 1MeV/nucleon and to understand the nature of the defects produced during ion irradiation.

In the present thesis, low energy inert gas ion irradiation effects in monoclinic zirconia is studied to understand the correlation between phase transformations (monoclinic to tetragonal), bubble induced swelling and luminescence properties. For this purpose, monoclinic zirconia (synthesized by thermal decomposition method) was irradiated using low energy inert gas ions (120 keV He⁺, 120 keV Ar⁺ and 60 keV Kr⁺) at 300 K and 143 K.

6.2. Phase transformation upon ion irradiation

Radiation stability of irradiated monoclinic zirconia was studied using GIXRD, Raman scattering and transmission electron microscopy. GIXRD patterns showed the presence of a tetragonal phase and the diffraction peaks are shifted for all irradiated samples irrespective of the ions and irradiation temperatures. Raman scattering showed the presence of tetragonal peak (144 cm⁻¹, E_g mode) and shift in the Raman modes associated with monoclinic phase in all the ion irradiated zirconia samples. Selected area electron diffraction pattern also revealed the presence of tetragonal phase.

Phase transformation is attributed to pure radiation damage process and the amount of oxygen vacancies produced during the ion irradiation plays an important role in the phase transformation. Oxygen vacancies are known to induce strain and when their concentration reaches a threshold value, the strain lowers the phase transformation temperature. The amount of transformed phase was found to be more for the samples ion irradiated at 143 K compared with the samples irradiated at 300 K for the same ion fluence. In addition, strain was also found be higher when the irradiation was carried out at 143 K. The faster rate of phase transformation is attributed to the immobility of the defects and continuous production of oxygen vacancies. It was observed that the amount of

transformed tetragonal phase was low in the Kr^+ ion irradiated zirconia samples, compared to the Ar^+ ion irradiated zirconia samples (*refer* Table 6.1). This is attributed to the shallow range (23 nm) of the Kr^+ ions and the high sputtering yield (8.8 atoms/ion) compared to Ar^+ ions (sputtering yield: 4.6 atoms/ion).

Table 6.1 The table lists the fraction of tetragonal phase, swelling and macrostrain in the zirconia samples upon inert gas ion irradiation.

Energy Ions	Temp.	Ion Fluence (ions/cm ²)	Dpa	Macro Strain (%)	Fraction of tetragonal phase (%)	Swelling (%)
120 keV He^+	300 K	1×10^{16}	0.048	0.04	-	1.4
		2×10^{17}	9.6	0.06	-	2.7
	143 K	1×10^{16}	0.048	0.09	-	
		2×10^{17}	9.6	0.33	-	0.009
120 keV Ar^+	300 K	1×10^{16}	20		9	
		1×10^{17}	200	0.10	9	1.6
	143 K	1×10^{16}	20		10	
		2×10^{17}	400	0.18	20	0.009
60 keV Kr^+	300 K	1×10^{16}	34.8	0.08	2.5	0.03
		5×10^{16}	174	0.02	3	
		1×10^{17}	348		4.5	0.04
	143 K	1×10^{16}	34.8	0.04	4.5	0.1
		5×10^{16}	174	0.03	5.5	
		1×10^{17}	348		8.5	0.03

6.3. Bubbles formation and bubble induced swelling

Morphological and microstructural changes in the ion irradiated zirconia samples were characterized by scanning electron microscopy and transmission electron microscopy. SEM images revealed that upon ion irradiation, the porosity of the samples decreases. In addition to the reduction in the porosity, joining of the grains was also observed. In case of Kr^+ ion irradiation, the joining of the grains is so high that they formed a network due to local melting during ion irradiation. These structures resembled more like the high burn up structure. TEM results revealed the formation of inert gas bubbles upon ion irradiation for all the ions irrespective of the irradiation temperatures (300 K and 143 K).

Average bubble size, bubble density and swelling was calculated (*refer* Table 4.1) and it was found that bubble number density is very low in the samples irradiated at 143 K. The bubble formation was explained in terms of heterogenous nucleation process. Bubble areal density and bubble induced material swelling was found to be low when the irradiation was carried out at 143 K. This is because of the immobility of the defects at

such low temperatures. Bubble areal density was high (for the same ion fluence) in case of the Ar^+ ion irradiation compared to the He^+ and Kr^+ ion irradiation. However, it is expected to be high for the Kr^+ ion irradiation, but the sputtering of the Kr^+ ion irradiated layer (due to its high sputtering yield and shallow projected range) makes the bubble formation less favorable compared to the Ar^+ ion irradiation.

6.4. Luminescence properties of ion and laser irradiated monoclinic zirconia

To study the effects produced by the fission fragment damage which is similar to SHI irradiation, laser irradiation (200 and 2000 shots) were employed. In order to study the evolution of the defects produced during the ion irradiation, photoluminescence and time resolved photoluminescence spectroscopy were employed.

PL measurements show the presence of a broad band around 2.53 eV. This broad band is attributed to the oxygen vacancies. The slow lifetime (4-5 ns) obtained from the TRPL measurements also confirmed the production of defects (oxygen related vacancies) upon ion (He^+ , Ar^+ and Kr^+) irradiation presence of defects. The PL intensity ratio ($I_{\text{ion irradiated}}/I_{\text{as-sintered}}$) as a function of ion fluence was also plotted (*refer* Figure 5.22). From the PL intensity ratio it was observed that, in case of He^+ ion irradiation, the ion irradiation induced annealing was observed. However, in case of Ar^+ ion irradiation, the PL intensity ratio was found to increase with the ion fluence as defect production varies in proportion with the ion fluence. In case of Kr^+ ion irradiation, whether the vacancy assists the bubble formation or gets accommodated in the lattice determines the PL intensity ratio.

When the vacancies are mobile and form bubbles, the stress due vacancies are less in the sample which gives rise to the reduction in monoclinic to tetragonal phase transformation as evident from Raman scattering and electron diffraction experiments. From the observations of GIXRD, SAED, Raman scattering, electron microscopy, PL and TRPL measurements, it is concluded that the oxygen vacancy concentration dictates the phase transformation (stress induced by oxygen related vacancies) and swelling (stress relieved by bubble formation).

6.5. Scope for future work

In addition to the irradiation conditions used in the thesis work, inclusion of other conditions like high temperature and pressure would also lead to more structural phase transformation. This could make possible the transformation that is not possible at ambient conditions. In addition, fission fragment damage in inert gas ion implanted monoclinic

zirconia and its interaction, bubble induced swelling and damage by the swift heavy ions can be studied. As yttria stabilised zirconia is found to be radiation resistant, its radiation response to low energy inert gas ions could be studied to explore the structural transformation and morphological changes.

Abstract

Growing concern on proliferation, radiotoxicity and disposal of plutonium has increased the interest in the inert matrix fuels (IMF). The term IMF refers to any nuclear fuel containing a low activation matrix as the carrier for the fissile material. An IMF should have neutron transparency, good thermal conductivity, high melting point, good mechanical properties and stability against radiation. Several materials (oxides and carbides) have been proposed for the use of IMF. Zirconia is one of the proposed candidate materials for IMF because of its radiation resistance. The swelling behaviour and radiation response of zirconia is being studied using accelerators and research reactors. Fission gases like Xe and Kr, released from the fuel, accumulate inside the fuel matrix and induce gas bubble formation, which gives rise to swelling. It leads to degradation in the performance of the material. In the present thesis, low energy inert gas ion irradiation effects in monoclinic zirconia is studied to understand the correlation between phase transformations (monoclinic to tetragonal), bubble induced swelling and luminescence properties.

Single phase monoclinic zirconia was synthesized and low energy inert gas ion (He^+ , Ar^+ and Kr^+) irradiations were carried out using 150 kV ion accelerator at 300 K and 143 K. The ion irradiated samples were characterized using GIXRD, electron diffraction and Raman scattering techniques. The results show the phase transformation from monoclinic to tetragonal phase of zirconia. The fraction of the transformed phase was estimated from Raman scattering results and was found to increase with the ion fluence. The amount of the transformed phase (tetragonal) is found to be higher in the case of ion irradiation at 143 K. It was confirmed that the size of the zirconia particles had no role in the transformation as the average crystallite size of the zirconia was > 60 nm which is the greater than the size required for the stabilization of tetragonal phase. The phase transformation is attributed to the oxygen vacancies and also to the strain induced by these oxygen vacancies in the zirconia lattice. The higher amount of transformed phase in the ZrO_2 (ion irradiated at 143 K) is attributed to the immobility and the continuous production of defects during the ion irradiation.

Electron microscopy analysis on ion irradiated zirconia samples revealed that the morphology of the grains are altered which resulted in such that reduction in porosity and joining of particles (due to localized surface melting). Apart from that, inert gas bubbles are clearly observed in TEM analysis. Helium bubbles are faceted while argon and

krypton bubbles are spherical in shape. The swelling (due to these bubbles) is found to be less when the irradiations were carried out at low temperatures compared to irradiation at 300 K. It is attributed to the immobility of the defects. Swelling was also found to be dependent on the damage produced during ion irradiation.

The ability of ultrafast lasers and swift heavy ion (SHI) irradiation to rearrange and disorder the structures through identical damage processes, provides the link between the two processes (ultrafast laser and SHI irradiation) of depositing large amounts of ionizing energy into the material. Therefore, laser irradiation can be employed to study the fission fragment damage (energy of $\cong 1$ MeV/nucleon, typical energy of SHI). Laser irradiation was carried out on the as-sintered and the ion irradiated zirconia samples. The nature of the defects was studied through photoluminescence (PL) spectroscopy and the decay of the PL intensity. PL band was observed around 2.53 eV (490 nm) for all ion irradiated samples and it is attributed to the oxygen vacancies. The slow lifetime obtained from the time resolved photoluminescence spectroscopy measurements also indicated the production of (oxygen vacancies related) defects.

Thus low energy inert gas ion irradiation in zirconia leads to the phase transformation from monoclinic to tetragonal phase. The amount of transformed phase was found to be higher when the ion irradiation was carried out at 143 K. When the vacancies are mobile and form bubbles, the stress due to vacancies are less in the sample which gives rise to the reduction in monoclinic to tetragonal phase transformation. In addition to the phase transformation, irradiation induced strain was also observed and the strain was high when the ion irradiation was carried out at 143 K. Along with the phase transformation, formation of bubbles were also observed and the calculated bubble induced swelling was less when the irradiation was carried out at 143 K. The photoluminescence and TRPL measurements revealed the production of defects (oxygen vacancies related) during ion irradiation.

Chapter 1

Introduction

1.1. Background

Inert matrix fuels (IMF) refers to any nuclear fuel containing a low activation matrix as the carrier for the fissile material. An IMF should have neutron transparency, good thermal conductivity, high melting point, good mechanical properties and stability against radiation. Different types of IMF materials were proposed including elements (Al, C), intermetallic (ZrSi, AlSi), carbides (TiC, SiC), nitrides (TiN, ZrN), oxides (CaO, MgO, MgAl_2O_4 , ZrSiO_4 , YSZ and $\text{Y}_3\text{Al}_5\text{O}_{12}$)[1]. In aqueous media, carbides have low tolerance to radioactivity and the carbide structure weakens at high doses, making it more soluble[2]. Majority of the reactors operate with reactor fuels as metal oxide fuels (MOX), hence the oxides as IMF find great attention. Oxides proposed for the use of IMF includes ZrO_2 , MgO, CeO_2 , CaO, Y_2O_3 and ThO_2 [1]. It was found that, thorium oxide improved the performance of the IMF, however, it has demerits in view of reactivity induced accidents[3]. In literature, ion irradiation experiments on SiC, CeO_2 , ZrO_2 doped SiC suggested that the swelling was independent of irradiation temperatures and also not strongly dependent on the ion dose[4]. However, doped ZrO_2 and SiC, showed the least swelling upon ion irradiation[4].

Even though zirconia (ZrO_2) is known for its high tensile strength, high refractoriness, low brittleness, low thermal conductivity, high melting point, low thermal expansion etc[5–7], the fact that radiation inertness of zirconia plays a vital role. Zirconia is considered as a natural analogue to study the radiation resistance in the context of zirconia based radioactive waste[8, 9]. Radiation response of insulating materials, such as zirconia, ranges from isolated point defects to phase transformation, which in turn lead to modifications in dimensional, mechanical, electrical and thermal properties. IMF materials suffer from two important issues during reactor operation, (1) fission gas induced swelling and (2) fission fragment induced damage. The fission fragments with the energy $\sim 1\text{MeV}/\text{amu}$, produces ionization induced defects.

Fission gases like Xe and Kr, released from the fuel, accumulate inside the fuel matrix and induce gas bubble formation, which gives rise to swelling and it leads to degradation in the performance of the fuel material[10]. Hence it is important to study the fission gas effects in zirconia. In the present thesis, the fission gas induced effects are

studied using inert gas ion irradiation and characterization with different experimental techniques.

1.2. Phase transformation in zirconia

Zirconia was found to undergo phase transformation, when subjected to changes in grain size, temperature, pressure, low energy ion irradiation and swift heavy ion irradiation. The phase transformations under different conditions are discussed in the following sections.

1.2.1. Role of grain size

Zirconia, in its bulk form, exists in monoclinic structure at ambient conditions. When the grain size decreases, zirconia changes its crystal structure from monoclinic to tetragonal structure. In bulk form of zirconia, the phase transition (monoclinic to tetragonal) temperature is 1170 °C, however the transition temperature decreases with the grain size[11, 12]. The lower transition temperature is due to the competition between surface energy and bulk energy. This causes changes in the surface and volumetric enthalpy, entropy as well as the interfacial energy and strain[13].

Garvie has derived a formula for the critical radius for the stability of tetragonal phase. According to Garvie[14, 15], when two phases are at equilibrium, their free energies must be equal. Hence, the difference in the free energy of the two polymorphs can be expressed by the following equation[15, 16]

$$\Delta G = \frac{4}{3}\pi r^3(\Psi - \Psi') + 4\pi r^2(Y - Y') + \frac{4}{3}\pi r^3(\varepsilon - \varepsilon') \quad \text{Eqn.1.1}$$

r = radius of a microcrystal

Ψ = free energy per unit volume of a crystal with infinite size

Y = surface free energy

ε = strain energy per unit volume for a particle,

and the primed symbols represent the low temperature phase. Changes in the volume free energy and surface free energy are included in the first two terms and the changes in mechanical energy, caused by strain is included in the last term. From Eqn.1.1, it is observed that for the critical radius r_c , ΔG become zero for a temperature well below the transition temperature, hence

$$r_c = - \frac{3\Delta\gamma}{\Delta\Psi + \Delta\varepsilon} \quad \text{Eqn.1.2}$$

where $\Delta\gamma$ is the difference between the surface energies of the two phases and its value is 0.36 J/m^2 (for incoherent particles) and $\Delta\varepsilon$ is the change in the internal strain. For tetragonal zirconia embedded in cubic zirconia matrix, the value of strain energy is $0.46 \times 10^8 \text{ J/m}^2$ [15]. The difference in the volume free energy ($\Delta\Psi$) is equal to $q = \left(1 - \frac{T}{T_b}\right)$, where q is the heat of transformation per unit volume ($-2.82 \times 10^8 \text{ J/m}^3$) and T_b is the transformation temperature of the bulk material (1450 K) [17]. Inserting all the values, in the Eqn.1.2, gives the critical radius of 6.1 nm. Bremholm *et al.*, [18] have studied decomposition of zirconium acetate in high temperatures and pressures (200 °C and 250 bar), and the nucleation and growth of zirconia was observed. The authors were able to synthesize monoclinic zirconia with crystallite size of few tens of Angstrom [18]. Hence, in order to induce monoclinic to tetragonal phase transition at room temperature, the crystallite size has to be at least below 20 nm in diameter.

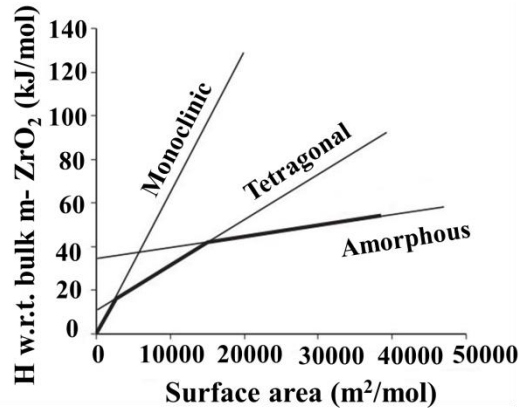


Figure 1.1 Phase stability crossover of nanocrystalline zirconia [19].

Pitcher *et al.*, [19] have studied the phase stability of zirconia. The authors synthesized amorphous, monoclinic and tetragonal zirconia and carried out enthalpy measurements. By using the Gibbs free energy formula ($\Delta G = \Delta H - T\Delta S$), the authors were able to establish the effects of entropy, enthalpy on the crossover between different phases. Further, with increase in the surface area, the monoclinic phase gains enthalpy faster than the tetragonal phase thereby making it the least favorable phase. The authors have also concluded that the amorphous zirconia is the most energetically favorable phase in the high surface area regime due to its low surface energy. The phase stability crossover of zirconia as a function of surface area is shown in Figure 1.1. The darker lines represent

the energetically stable phase (lowest enthalpy). This crossover suggests that the metastable phases become thermodynamically stable at nanoscale.

Namavar *et al.*, [20] have reported a correlation between grain size and phases in ZrO_2 thin films. As a result of grain coalescence, cubic-to-monoclinic phase transformation was observed in thermally annealed nanocrystalline cubic ZrO_2 thin films. Lu *et al.*, [21] have observed, upon annealing at 500 °C, that there is a phase transformation from amorphous to tetragonal phase (grains of ~10 nm-20 nm). When the annealing was carried out at 1000 °C, the authors were able to observe a transition to monoclinic phase (40 nm-50 nm), the most stable phase at high temperatures compared to the tetragonal phase.

1.2.2. Role of temperature

As a function of temperature, zirconia exists in three crystallographic structures namely monoclinic, tetragonal and cubic (*refer* Figure 1.2). At high temperatures (2450 °C to 2675 °C), zirconia exists in cubic fluorite structure that consists of a simple cubic packing arrangement of oxygen anions with the Zr cations in center of every other cube. At lower temperature (<2450 °C), displacive transition occurs in which the alternate pairs of oxygen anions are slightly offset forming a tetragonal phase [22]. At 1173 °C, the tetragonal zirconia undergoes a martensitic transformation to a monoclinic polymorph in which Zr cations are coordinated to only 7 oxygen atoms. At room temperature, the monoclinic phase is the stable one. Even though the tetragonal and cubic form cannot be quenched (at room temperatures), the phases can be stabilized by the addition of 15 mol% of large cations (like lanthanides and yttrium).

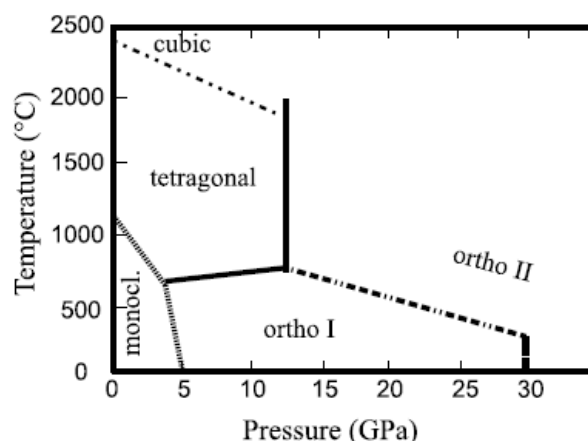


Figure 1.2 Phase diagram of ZrO_2 as a function of temperature and pressure [23]

The cooling of tetragonal to monoclinic zirconia at 950 °C, causes volume expansion of 4% [24] accompanied by shear strain (0.016) [25] and this causes the zirconia to crack. In order to avoid volume expansion, zirconia is often stabilized in its high temperature forms by the addition of soluble oxides such as Y_2O_3 , MgO , CaO , and Ce_2O_3 that suppresses the transformation into its monoclinic structure. Y_2O_3 not only stabilizes in high temperature cubic phase but also creates oxygen vacancies in every mole of the dopant Y_2O_3 . When these oxygen vacancies displace any oxygen ion from the equilibrium position, the monoclinic to tetragonal transformation is suppressed [26]. In general, tetragonal phase is stabilized at 3 mol% (partially stabilized zirconia) and cubic phase becomes dominant above 8 mol% (fully stabilized zirconia). Thus depending upon the dopant concentration, either the tetragonal or the cubic phase is stabilized.

1.2.3. Role of pressure

Depending upon pressure, monoclinic zirconia changes its crystal structures to orthorhombic (I) and orthorhombic (II) as given in Table 1.1. Figure 1.2 shows that the monoclinic to orthorhombic (I) phase transition occurs between the pressures of 4 GPa and

Table 1.1 Different crystal structures and its unit cell parameters of zirconia [22, 30, 33–36]

Crystal Structure	Space Group	Lattice parameter (Å)	Density (g/cm ³)
Monoclinic $a \neq b \neq c$ $\alpha = \gamma = 90$ $\beta > 90$	P_{21}/c	$a = 5.296$ $b = 5.094$ $c = 5.326$ $\beta = 99.3$	5.7
Tetragonal $a = b \neq c$ $\alpha = \beta = \gamma = 90$	$P4_2/nmc$	$a = 3.608$ $c = 5.187$	6.1
Cubic $a = b = c$ $\alpha = \beta = \gamma = 90$	$Fm\bar{3}m$	$a = 5.128$	6.3
Orthorhombic (I) $a \neq b \neq c$ $\alpha = \beta = \gamma = 90$	P_{bca}	$a = 10.1745$ $b = 5.3148$ $c = 5.1357$	6.8
Orthorhombic (II) $a \neq b \neq c$ $\alpha = \beta = \gamma = 90$	P_{nma}	$a = 5.6140$ $b = 3.3474$ $c = 6.5658$	--

7 GPa[23, 27]. The transition from monoclinic to orthorhombic (I) is very sluggish at room temperature and also depends on the crystallite size. A detectable traces of monoclinic phases were seen even at pressures of 10 GPa[23].

Zirconia exists in two phases at high pressure namely orthorhombic-I and orthorhombic-II. Orthorhombic (I) to orthorhombic (II) transformation takes place at a pressure of 12.5 GPa ($> 600\text{ }^{\circ}\text{C}$)[28]. At room temperature, orthorhombic (I) transforms to orthorhombic (II) between 22 GPa[29, 30], 25 GPa[31], 28 GPa[32], and 35 GPa[27]. The transition from orthorhombic (I) to orthorhombic (II) needs the reconstruction of the lattice and for a full transition, a pressure > 15 GPa is needed[23]. Haines *et al.*,[28] have observed only 50% of orthorhombic (II) phase even for pressures above 37 GPa at room temperature. According to the authors, reorganization of the anion and cation sub lattices, (that increases the coordination number of the Zr^{4+} from seven to nine) is needed for the orthorhombic (I) to orthorhombic (II) transformation. Hence the transformation is kinetically slow to the point of being irreversible at room temperature[28].

1.2.4. Ion irradiation induced phase transformation

Ion irradiation is a non-equilibrium process. Upon ion irradiation, materials undergo crystalline – crystalline transition, crystalline to amorphous transition and metastable phase formation in metals, semiconductors and insulators. Before discussing about ion beam induced phase transformation, the ion solid interactions are discussed in the following sections.

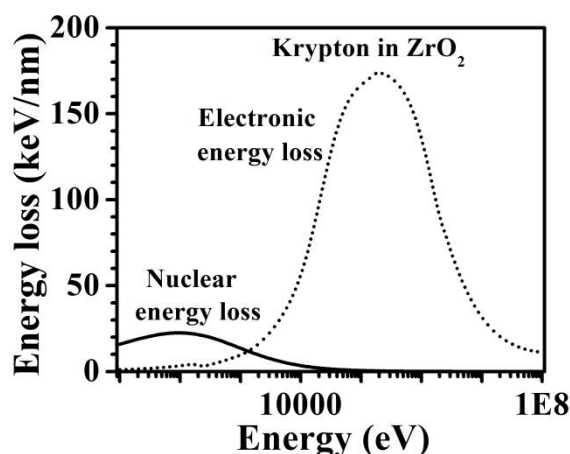


Figure 1.3 The nuclear and electronic energy loss of krypton ions in ZrO_2 as a function of ion energy. The data is calculated from SRIM software[37].

1.2.4.1. Ion Solid Interaction

When an energetic ion traverses through a solid, it interacts with the target atoms and transfers some of its kinetic energy to the target atoms. By imparting kinetic energy,

the energy of the ions slow down and the ion also produces collision cascades. The incident ion loses its energy by nuclear and electronic energy loss processes. Total energy loss (S_{total}) is the sum of nuclear energy loss (S_n) and electronic energy loss (S_e) and is expressed as

$$S_{total} = S_n + S_e \quad \text{Eqn.1.3}$$

1.2.4.2. Nuclear energy loss

When the nuclear energy loss is dominant, the ion interacts with the target atoms and the collision between the ions and target atoms is elastic (knock on process) collisions. This causes displacement of the target atoms from their original lattice sites. Figure 1.3 shows the typical energy loss values of Kr^+ ions in ZrO_2 and the data was obtained from the SRIM (Stopping and Range of Ions in Matter) software [37]. From Figure 1.3, it is observed that the nuclear energy loss is dominant in the low energy regimes.

1.2.4.3. Electronic energy loss

When the projectile ion energy is very high, the ion excites and ionizes the target electrons. Due to the high velocity of the projectile ions, interaction with the target nuclei does not occur. The overall energy loss is well described by Bethe-Bloch equation that considers the momentum transfer to a target electron in a coulomb potential along with the correction terms[38]. Bethe-Bloch equation is given as

$$\left(-\frac{dE}{dX}\right)_e = \frac{4\pi (Z_p^{eff})^2 Z_t N_t}{m_e v_p^2} * \left(\ln \frac{2m_e v_p^2}{I} - \ln(1 - \beta) - \beta^2\right) \quad \text{Eqn.1.4}$$

Z_p^{eff} = effective charge of the projectile

Z_t = atomic number of the target material

N_t = amount of target atoms per unit volume

v_p = projectile ion velocity

m_e = electron mass

I = effective ionization potential of the target material

β = ratio between ion velocity and speed of light

From the energy loss values of Kr^+ ions in ZrO_2 (refer Figure 1.3), it is observed that the electronic energy loss is dominant in the high energy regimes. When the projectile ion passes through the target atoms, the ion loses its energy to bound electrons whose orbital velocity (v_0) is smaller than the projectile velocity (v). Hence, a correction factor is taken into account that considers the nuclear charge shielding of the projectile. Hence, it

is necessary to consider the charge exchange between the projectile ion and the target atoms. The loosely bound electrons are easily stripped off during the scattering process. This is called as Bohr stripping. This leads to an effective charge (Z_p^{eff}) of the projectile that is smaller than the nuclear charge (Z_p). Effective charge Z_p^{eff} is given in the following equation.

$$Z_p^{eff} = Z_p \left(1 - \exp \left(\frac{-\frac{v}{v_0}}{Z^{2/3}} \right) \right) \quad \text{Eqn.1.5}$$

1.2.4.4. Projected range

Ion range is defined as the penetration depth of an ion (with an initial kinetic energy (E_0)) in a material until it is stopped. The integration of the inverse of the stopping power of the medium over the energy, gives the total range. Range (R) describes the mean range, as all the ions do not transfer same amount of energy to the target material. The ion range (R) is expressed as

$$R = \int_0^{E_0} \left(\frac{dE}{dX} \right)^{-1} dE \quad \text{Eqn.1.6}$$

The range distribution at the end of the trajectories is called the straggling. In the present work, the values of the ion range, ion straggling were calculated using the SRIM (Stopping and Range of Ions in Matter) software[37].

1.2.4.5. Radiation damage

Radiation damage[39] deals with the transfer of ion energy (projectile) to the target atom and the distribution of atoms in the target. It comprises of the following process

1. Interaction of the projectile ions with the target atom.
2. Transfer of kinetic energy of the ions to the lattice atoms that leads to primary knock on atom (PKA).
3. Displacement of the target atom from its lattice site position.
4. The displaced atoms traverse through the lattice and creates additional knock on atoms.
5. Production of displacement cascades.
6. Termination of the primary knock on atoms as an interstitial.

The time scales of radiation damage events are given in Table 1.2. The radiation damage event is concluded, when the PKA comes to rest in the lattice as an interstitial. The result of a radiation damage event is the creation of a collection of point defects (vacancies and interstitials) and clusters of these defects in the crystal lattice. The entire process occurs in the time scale of 10^{-11} seconds. Subsequent events involving the migration of the point defects and defect clusters and additional clustering or dissolution of the clusters are classified as radiation damage effects[39].

Table 1.2 Time scale for the production of defects in the irradiated material[39].

Time (s)	Event	Result
10^{-18}	Energy transfer from the incident particle	Creation of a primary knock-on atom (PKA)
10^{-13}	Displacement of the lattice atoms by PKA	Displacement cascade
10^{-11}	Energy dissipation, spontaneous recombination and clustering	Stable Frenkel pairs
$>10^{-8}$	Defect reactions caused by thermal migration	Single interstitial atom (SIA) and vacancy recombination, clustering, trapping and defect emission

In literature, there are many efforts to understand the effects of ion irradiation in zirconia[21, 40–43]. When zirconia is irradiated with ions, large number of defects like vacancies, interstitials and voids are produced. In addition to the production of defects, phase transformation[40, 44, 45], grain growth[46], amorphisation[47, 48], bubble formation[49] were also reported. Several groups have reported phase transformations induced by low energy, high energy and swift heavy ion (SHI) irradiations in zirconia.

1.2.4.6. High energy ion irradiation induced phase transformation

During swift heavy ion irradiation, the electronic energy loss is the dominant energy loss mechanism. SHI losses its energy via ionization and electronic excitation, and it produces cylindrical ion tracks. In a crystalline material, these ion tracks are amorphous in nature. Ion tracks can be easily formed in insulating material, but not in pure metals as the high electronic conductivity of the metal dissipates the electronic heat before the ion track formation. SHI can (i) produce anisotropic deformation in the amorphous solid (Klaumünzer's effect)[50–52], (ii) induce recovery of defects created by nuclear collisions [53] in metal and (iii) create damage in the material (latent tracks), irrespective of its original structure (amorphous[54, 55] or crystalline[56, 57]).

Two models, namely (i) Coulomb explosion model[58, 59] and (ii) thermal spike model[60–63], have been proposed to explain the atomic displacement due to the electronic energy loss and also to explain the formation of ion/latent tracks.

Coulomb explosion model:

Coulomb explosion model was proposed on the observation that the latent tracks are observed in the insulating materials. Coulomb explosion model is based on the electrostatic repulsion of the ions created by the incident ion that can disrupt the crystalline structure. According to Coulomb explosion model, the incoming ions deposit its energy to the electrons of the target, thereby ionizing the atoms. Then, these ions leave cylindrical areas of ionized cores, along the path of their trajectory. The ions inside the cylindrical area experience an intense coulomb repulsion, leading to the explosion of the ions. The ionic repulsion can lead to the displacement of the atom[59] or to the propagation of shock waves[64] that can result in the phase transformation. According to this model, tracks should not be observed in the materials with high thermal conductivities, but tracks are indeed observed in materials with high thermal conductivity. Hence, there is a limitation to this model.

Thermal spike model:

According to thermal spike model, an energetic ion that passes through a target material, transfers its energy to the electrons, that leads to rapid local heating of the electron subsystem to a temperature (T_e). Then, a highly non-equilibrium region with hot electrons and cold lattice arises[65]. The energy of the electron is then transferred to the atomic subsystem through electron phonon coupling that leads to increase in the temperature of the target atoms (T_a). Subsequently local melting along the ion trajectory can occur under certain conditions (strong electron phonon coupling, low melting conditions). Upon rapid quenching, frozen defects are created, further leading to the formation of ion tracks.

Szenes model[62] is used to deduce the threshold value of the electronic energy loss and also to understand the formation of the latent tracks upon ion irradiation. According to Szenes model the threshold electronic energy (S_{eth}) is given by the formula

$$S_{eth} = \pi r^2 \rho c \left(\frac{T_a}{g} \right) \quad \text{Eqn.1.7}$$

where r is the radius of the ion track, ρ is the density and c is the specific heat of the material and g is the electron phonon coupling constant. $T_a = (T_m - T_s)$, T_m is the

melting temperature and T_s is the substrate temperature during ion irradiation. It is also possible to determine the radius of the track (R_e) by extending the model. R_e is given by

$$R_e^2 = \frac{r^2 \ln(g) S_e}{\pi \rho c T_s r^2} \quad \text{Eqn.1.8}$$

In the above methods, as the time scale for track formation is inaccessible by any characterization technique, hence, it is not easy to identify the mechanism. It was found that out of the two models, the thermal spike is the most appropriate model to explain the formation of latent tracks[66].

Swift heavy ions (SHI) not only produce defects but also induces phase transformation (amorphisation[48], crystalline to crystalline transformation[40, 45]). Several groups have reported crystalline to crystalline phase transformation in oxide materials using swift heavy ions[67–74]. Lu *et al.*,[48], have reported swift heavy ion (1.33 GeV U_{238}) beam induced amorphisation in monoclinic zirconia where the extreme electronic energy loss (52 keV/nm), high energy state of the nanostructured materials and high thermal confinement (due to less effective heat transport within the transient hot zone) were responsible for amorphisation. Lian *et al.*,[41] have observed amorphous to tetragonal phase transition upon 1 MeV Kr^{2+} ion irradiation, in bilayer (amorphous and

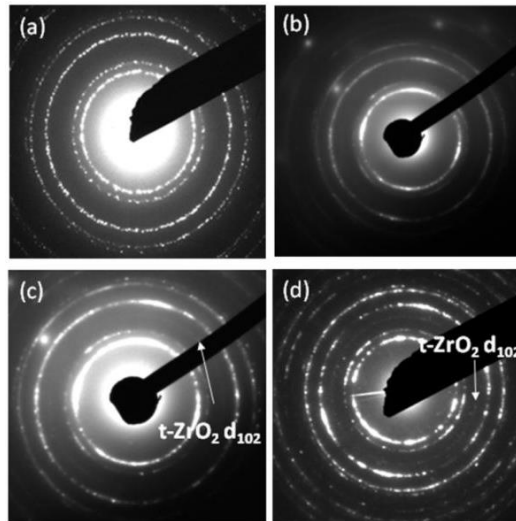


Figure 1.4 Selected area electron diffraction (SAED) patterns of the bilayer nanocrystalline zirconia film subjected to 1 MeV Kr^{2+} irradiation at room temperature for various ion fluences: (a) original (b) 3.13×10^{14} ions/cm² (c) 6.25×10^{14} ions/cm² and (d) 3.13×10^{15} ions/cm². The appearance of the diffraction ring d_{102} in the SAED patterns ((c) and (d)) demonstrates that the tetragonal phase was formed upon ion irradiation[41].

cubic) zirconia film. The authors have suggested that the tetragonal phase is energetically favoured under the non-equilibrium conditions (during ion beam irradiation). Monoclinic

to tetragonal phase transformation was observed in zirconia, when the ZrO_2 samples were irradiated at room temperature (with 92 MeV, Kr^+ ions)[75]. The strain field (produced during the Kr^+ ion irradiation) was found to be responsible for stabilizing the tetragonal phase.

Lian *et al.*[41] reported a transformation to tetragonal phase from amorphous phase in bilayer ZrO_2 (amorphous layer and cubic nanocrystalline ZrO_2 films) upon 1 MeV Kr^{2+} ion irradiation, as a result of radiation induced recrystallization process (*refer* Figure 1.4). The authors have also reported that, the monoclinic-to-tetragonal phase transition observed in nano-sized zirconia (50 nm) is similar to the monoclinic to tetragonal phase transformation of bulk samples induced by ion irradiation[41].

Schuster *et al.*,[42] have observed monoclinic to tetragonal phase transformation under high pressure (10 GPa) upon heavy ion (150-200 MeV/u, U_{238}) irradiation. Monoclinic to tetragonal phase transformation was observed in zirconia, when irradiated with U^+ ions of energy 11.1 MeV/u (1×10^{13} ions/cm²).

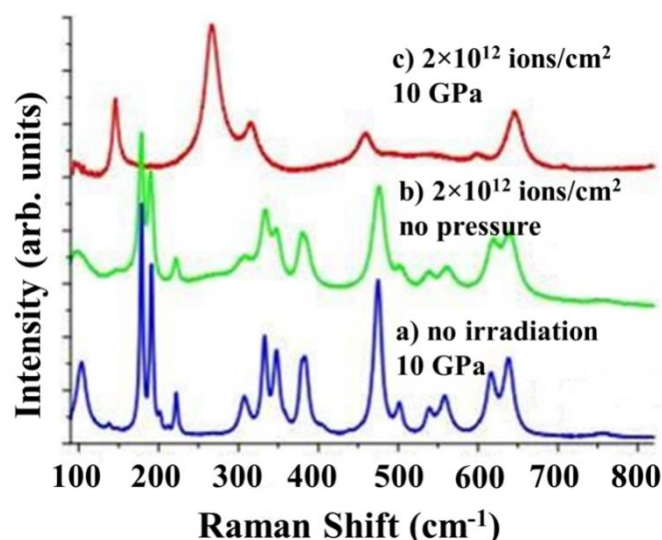


Figure 1.5 Raman spectra at ambient conditions of different ZrO_2 samples: (a) pressurized to 10.5 GPa but not irradiated, (b) irradiated with 2×10^{12} U-ions/cm² but without pressure and the fraction of transformed phase was $(6.3 \pm 0.8)\%$, (c) irradiated with 2×10^{12} U-ions/cm² under pressure of (10.3 ± 0.3) GPa and the fraction of the transformed phase was $(91.2 \pm 3.4)\%$ [42].

The phase transition is accounted to the pre-damage in the structure caused by the overlapping of ion tracks[42]. The authors have also reported ion beam induced transformation from monoclinic to tetragonal structure $(91.2 \pm 3.4)\%$ for the ion fluence of 2×10^{12} ions/cm² in pressurized zirconia, where as it was only $(6.3 \pm 0.8)\%$, when the

ion irradiation was carried at ambient pressure (refer Figure 1.5). The faster phase transformation rate is due to the introduction of stress in pressurized zirconia.

Benyagoub *et al.*, [66], have reported that the overlapping of the ion tracks are necessary to induce phase transformation, as the evolution of tetragonal phase fraction with ion fluence followed a sigmoidal behavior. The authors have irradiated zirconia pellets with 595 MeV Xe⁺ ions leading to the electronic energy loss of 28 keV/nm. Upon irradiation, the authors observed monoclinic to tetragonal phase transformation. The authors attributed the phase transformation to the double ion impact mechanism, in contrast to the amorphisation, where single ion impact is invoked. In case of the double ion impact, the first ion impact is used to create radiation defects most likely the oxygen vacancies that is the prerequisite for the phase transformation and the second ion impact is used to induce the phase transformation. For phase transformation to occur, the threshold electronic energy loss for monoclinic to tetragonal phase transformation was found to be 12 keV/nm [68–70, 74].

1.2.4.7. Low energy ion irradiation

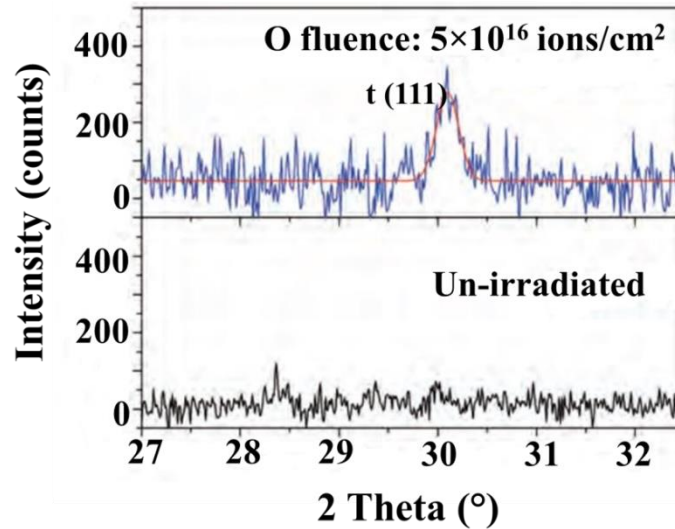


Figure 1.6 X-ray diffraction patterns of the un-irradiated amorphous-dominant ZrO₂ and ZrO₂ thin films irradiated with 350 keV O⁺ ion for the ion fluence $5 \times 10^{16}/\text{cm}^2$ [21].

Several groups have carried on low energy ion irradiation in zirconia to understand the phase transformation [21, 44, 76]. Valdez *et al.*, [44] have observed monoclinic to tetragonal phase transformation upon light ion (150 keV Ne⁺) irradiation at cryogenic temperatures. The transformation was found to be complete at the peak damage region. In the near surface region, both the monoclinic and tetragonal phases were observed, with the absence of amorphous or cubic phase.

Lu *et al.*, [21] have irradiated thermally annealed ZrO_2 thin films with 350 keV O^+ ions and observed the transformation from amorphous phase to tetragonal phase in ZrO_2 (see Figure 1.6). The authors have attributed that ionizing radiation-enhanced recrystallization processes are responsible for the amorphous to tetragonal phase transformation. The authors have also concluded that under non-equilibrium conditions, the energetic beam bombardment provides enough energy to overcome the energy barrier among two phases, thereby making the amorphous to tetragonal phase transformation possible.

Several studies have correlated the relation between the stabilization of tetragonal zirconia and oxygen vacancy [77, 78]. It is also known that oxygen vacancies could stabilize tetragonal zirconia at room temperatures by doping with cations [26]. The phase transformation from monoclinic to tetragonal and tetragonal to cubic could also be carried out by increasing the oxygen vacancy concentration. Thus when the accumulation of oxygen vacancies occurs and if the O-vacancy concentration exceeds the critical value of vacancy concentration (as a result of increase in ion fluence), monoclinic to tetragonal phase transformation becomes possible.

The other possible mechanism for phase transformation is cascade overlap during ion irradiation. When the cascades overlap, the temperature of the cascades core increases beyond the transition temperature for the timescale of picoseconds and it can lead to the monoclinic to tetragonal phase transformation [21]. Apart from the phase transformation, inert gas ion irradiation on zirconia also shows the inert gas bubble formation.

1.3. Inert gas bubble formation in oxide

When materials are irradiated with inert gas ions, the insoluble inert gases form bubbles in the material which affects the physical and the mechanical properties of the materials. In IMF material, the inert gases like Kr and Xe are produced as fission gases and these gas atoms are completely insoluble in the fuel matrix and their normal state is gas rather than solid. These gas atoms could be either completely released from the fuel matrix due to high temperature or just precipitate as gas bubbles in the material. These gas bubbles induce swelling or results in loss of density of the material. Thus swelling becomes inevitable due to the precipitation of these fission gases [10].

1.3.1. Mechanism of bubble formation

In order to know the effects of bubbles in the material, it is necessary to understand the process like gas production, bubble nucleation and growth. Following are the process involved in the formation of bubbles[10].

1. **Production:** The gases are produced by the fission process. Important factors are the rate and amount of production of these fission gases.
2. **Nucleation:** Nucleation happens either homogeneously or heterogeneously. Homogeneous nucleation occurs when the gas atoms happens to meet each other. Heterogeneous nucleation occurs when the gas atoms encounter defects, dislocations, grain boundaries which act as a nucleation site.
3. **Growth of the bubbles:** Growth of bubbles is caused due to atomic migration. The growth process is affected by the availability of vacancies, so that the bubbles could expand as gas, by the effects of surface tension and the stress of the fuel matrix. These factors determine the stability of the bubble. The bubbles tend to grow by gas atoms either attracted towards other existing bubbles or towards a vacancy that already has an existing gas bubble.
4. **Resolution of the gas atoms:** The gas atoms within the bubble also have the property of resolubility.
5. **Migration of bubbles:** Migration occurs either as a random walk, when no direct forces acts on the bubble or they are biased when forces are acting upon them. Temperatures, stress gradient, restraining forces due to dislocations, grain boundaries are the sources of the forces acting on a solid. These forces cause the bubble to move in a particular direction. On the other hand, the forces due to the crystal defects can act either to pin the bubble if they are immobile, or sometimes they drag the bubble, if the bubbles are themselves under motion. The motion of bubble can also occur due to the dislocation line sweeping, grain boundary sweeping.
6. **Interaction of bubbles:** The bubbles also tend to interact with the defects in the crystal like dislocations, grain boundaries.
7. **Release of fission gases:** The fission gases are released either to the external surfaces like cracks in the fuel, void, or to the grain boundaries. These bubbles in the grain boundaries when they become large in number, link themselves and are released to any of the external surfaces.

Sometimes the fission gases are released by the direct flight of the energetic fission fragments out to the external surfaces. This release method is significant at low temperatures.

1.3.2. Bubble induced swelling

Xenon and krypton bubbles were observed in the fissile materials. After annealing the UO_2 (irradiated with krypton ion) material at 1500 °C, krypton bubbles were observed under transmission electron microscopy[10]. Generally, the bubble induced swelling (S) can be calculated by[10, 79].

$$S = \frac{\left(\frac{\pi}{6} \sum d^3\right)}{st} \times 100\% \quad \text{Eqn.1.9}$$

where d is the measured bubble diameter, s is the total area used for calculating bubble number density, t is the thickness. By calculating the amount of swelling induced in the material, the performance of the material could be determined.

Nanostructured materials tends to be resistant to radiation including low swelling, retention of ductility and mechanical properties due to the increase in the number of grain boundaries which acts as sinks for the defects[80–83]. Experiments conducted by various groups have observed bubble formation in oxides like CeO_2 [79], UO_2 [84–86] and yttria stabilized zirconia[87, 88].

Bubbles were observed in UO_2 single crystals, when irradiated with 150 keV Kr^+ ions (25 °C and 600 °C) and 1 MeV Kr^{2+} ions (800 °C). The average bubble size, density and swelling were found to be dependent on the ion fluence of Kr^+ ions. In single crystal UO_2 irradiated at 800 °C, the values of swelling and bubble size was found to be 2.3 and 1.4 times respectively higher than the samples ion irradiated at 600 °C. Due to the vacancy generation and low mobility, bubble aggregation was not observed in the grain boundaries[84].

Krypton bubbles (both in nanograin and micrograin regimes) were reported in the CeO_2 (surrogate material for UO_2), when CeO_2 was irradiated with 150 keV Kr^+ ions. The authors have observed that, the nanograin regions consisted of krypton bubbles of small size and lower density compared to the bubbles in the micrograin regions. According to the authors, the reduction of ion induced swelling in the nanosized regime is due to the grain boundaries which act as efficient sinks.[79]. Pu *et al.*,[89] have irradiated T'-YSZ (tetragonal - yttria stabilized zirconia) with 60 keV He^+ ions to study the mechanical properties of the material. The authors were able to observe phase transformation to partial

tetragonal and partial cubic YSZ structures for the ion fluences $>2 \times 10^{17}$ ions/cm². With further increase in the ion fluence 1×10^{17} ions/cm² (refer Figure 1.7), the authors have observed different shapes of helium bubbles (spherical, disc, ribbon) and dislocation loops that contributed to the reduction in the hardness and elastic modulus.

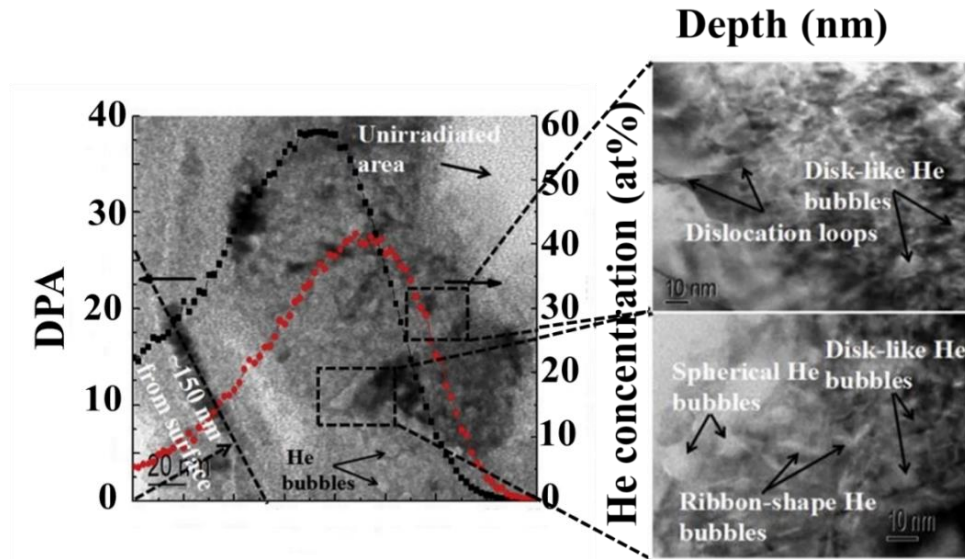


Figure 1.7 HRTEM images of the cross-section of T'-YSZ samples irradiated (300 K) with 60 keV He⁺ ions with the ion fluences of 1×10^{18} ions/cm²[89]

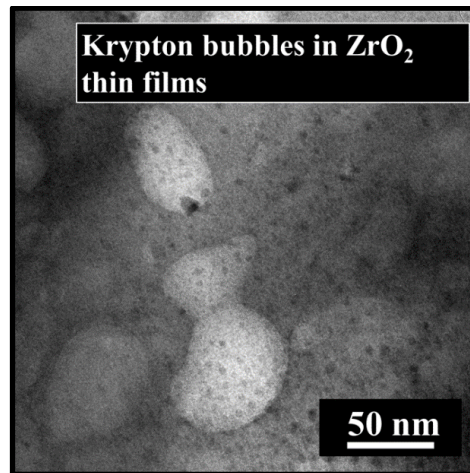


Figure 1.8 Krypton bubbles observed in ZrO₂ thin films irradiated with 60 keV Kr⁺ ion for the ion fluence of 1×10^{17} ions/cm²[76]

Hojou *et al.*, [87] have irradiated (300 K and 923 K) yttria stabilized ZrO₂ single crystals with 35 keV He⁺ and 60 keV Xe²⁺ ions. Upon irradiation, the authors have observed the formation of helium and xenon bubbles in the material. Irrespective of the ion irradiation temperatures, the authors were unable to observe amorphisation in both the cases of ion irradiation (He⁺ (up to 16 dpa)) and Xe²⁺ (up to 40 dpa)). In the case of monoclinic zirconia thin films, monoclinic to tetragonal transformation along with the

formation of krypton bubbles (size ~ 40 nm) was observed in 60 keV Kr^+ ion irradiated zirconia thin films (refer Figure 1.8)[76].

1.4. Luminescence properties of zirconia

Luminescence is a very strong tool for the detection and identification of point defects in insulators and semiconductors. Zirconia has immense applications in the field of optics like oxygen sensors, electro optical devices as they exhibit large optical band gap, high refractive index, high transparency in the visible, near infra-red regions and low optical loss[90–92]. When zirconia is excited with ultraviolet (UV) rays, zirconia exhibits a broad emission spectrum. The broad PL band centered at 2.5 eV (refer Figure 1.9) is mainly due to the overlapping of PL bands[93], charge carriers and lattice interactions.

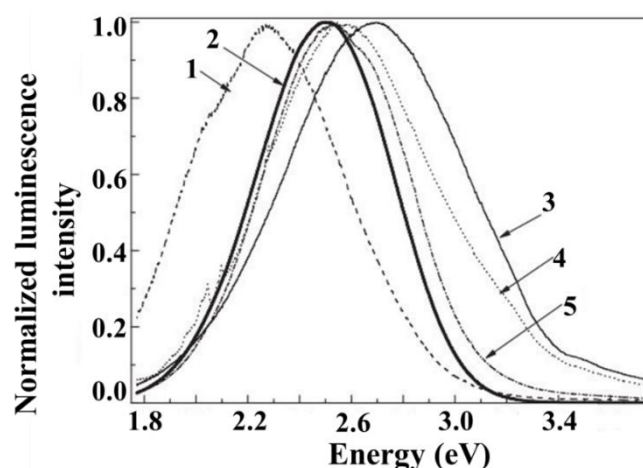


Figure 1.9 Photoluminescence of various types of zirconia (1) Y stabilized zirconia single crystal ZrO_2 (2) commercial powder (3) Y stabilized nanocrystals (4) undoped nanocrystals prepared by hydrothermal method and (5) undoped nanocrystals synthesized by plasma synthesis[93]

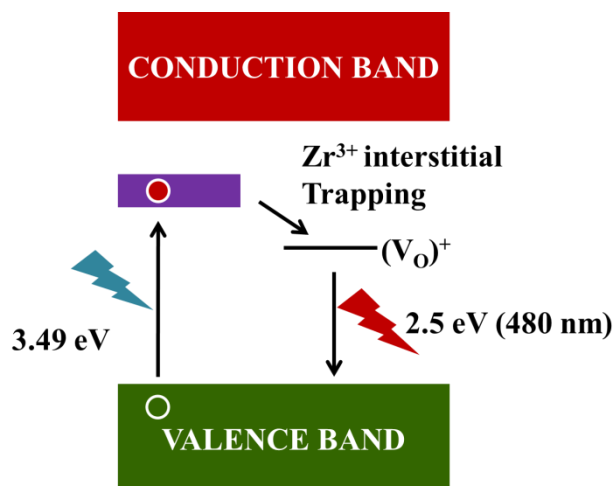
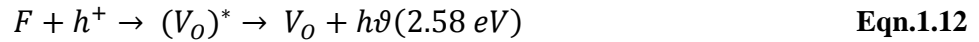


Figure 1.10 Schematic representation of the photoluminescence process in zirconia

Ideally zirconia does not show any luminescence, but in the presence of structural defects, luminescence is observed and it is due to the introduction of electronic energy levels within the band gap. The recombination process includes ionization, migration, recombination and emission. Electron-hole pairs are produced, when the sample is excited with photons of energy greater than the band gap of the zirconia. The oxygen vacancies (V_O) at once, tend to trap the electrons by creating F centres. The recombination of the holes with the F centers creates excited states of the emitter that undergoes a radiative transition to the ground state.

The recombination is explained by the equations[94]



And the schematic representation of the recombination process in zirconia is shown in Figure 1.10

The radiative decay of intrinsic electron-hole pair and self-trapped excitons are attributed to the luminescence observed at 294 nm from the ZrO_2 thin films[95]. The ionized oxygen vacancies (F^+ and F^- centers) from the conduction band is attributed to the PL band centered at 379 nm[96]. The peak at ~ 2.53 eV (490 nm) can be attributed to the effect of impurity titanium ions[97–99] (which are present in trace concentrations) and/or attributed to the transitions of F^+ centers (the oxygen vacancies that trapped one electron) from the excited state into the ground state[94, 100].

In earlier reports[95, 98, 99], the PL band at ~ 2.53 eV (490 nm) is attributed to the presence of impurity titanium in trace levels. When Ti doped ZrO_2 is excited with ultraviolet (UV) irradiation, electron hole pairs are created and excited. These excited electrons are trapped by the shallow level which is due to the oxygen vacancies. The holes are trapped by the Ti^{3+} creating Ti^{4+} centers[95, 98]. The thermal energy in ambient conditions causes the release of electrons from the shallow traps and then the recombination of these electrons with the Ti^{4+} creates the excited state of Ti^{3+} leading to the emission of ~ 2.53 eV (490 nm). The PL band centered at 612 nm in ZrO_2 powder, is attributed to the involvement of mid-gap trap states[101]. Thus luminescence in ZrO_2 can be attributed to (1) impurity/dopants, (2) intrinsic self-trapped excitons[95, 102] and (3) intrinsic defects (F , F^+ and Zr^{3+})[95, 102]. The photonic properties were also found to be influenced by the size/thickness[103, 104].

Smits *et al.*, [105] reported that the luminescence centers are intrinsic defects, possibly the oxygen vacancies distorted ZrO_2 lattice cells. The authors concluded that the luminescence spectrum and the band position strongly depends on the excitation wavelength due to the quasi-continuum of states [105]. Salah *et al.*, [106] have studied the PL excitation and emission spectra of ZrO_2 nanoparticles and reported that the PL emission bands are due to the transitions from the surface trap states in the conduction band to lower energy levels close to the valence band.

A report on the effects of annealing temperature on the PL properties of nanocrystalline zirconia thin films prepared by sol-gel dip [104] coating method, revealed that, upon annealing at elevated temperature, the PL intensity has increased. The authors concluded that, the increase in the PL is related to the reduction in OH groups, increase in crystallinity and reduction in the non-radiative related defects. Further the authors have also shown that, the blue shift of PL spectra had originated from the change in stress of the thin film due to lattice distortion. Xie *et al.*, [107] have investigated the PL properties of Tb-doped ZrO_2 nanofibers prepared by electro spinning technique. The authors demonstrated that the intensity of the green light emission could be controlled by oxygen vacancy concentration.

Rittman *et al.*, [108] have employed ultrafast laser irradiation on ZrO_2 and have observed monoclinic to tetragonal phase transformation and the results are identical to those produced by SHI irradiation. The ability of ultrafast lasers and SHI irradiation to rearrange and disorder the structures through identical damage processes, provides the link between the two processes (ultrafast and SHI irradiation) of depositing large amounts of ionizing energy into the material. Therefore, laser irradiation can be employed to study the fission fragment damage that has energy of about 1 MeV/nucleon (like SHI).

1.5. Objective of the thesis

There are several works on irradiation effects in zirconia using high energy (SHI) and low energy ion irradiation. As described in the present chapter, phase transformation, amorphisation, bubble formation, bubble induced swelling were observed in zirconia. However, systematic investigations and correlation between these effects has not been well established. Hence in the present thesis, an attempt has been made to establish the correlation between phase transformation, bubble induced swelling and the nature of defects produced during ion irradiation.

Chapter 2

Experimental Techniques

This chapter deals with the details about various experimental techniques utilized for characterization of the samples. In the present thesis work, monoclinic zirconia was synthesized using thermal decomposition method and the samples were irradiated with He^+ , Ar^+ and Kr^+ ions using 150 kV ion accelerator. In order to study the nature of defects, phase transformation and swelling, the characterization techniques like grazing incidence X-ray diffraction (GIXRD), Raman scattering, scanning electron microscopy (SEM), transmission electron microscopy (TEM) and photoluminescence spectroscopy (PL) were employed. This chapter provides a brief description of the sample preparation and characterization techniques used in the thesis.

2.1. Synthesis-thermal decomposition method

Zirconia was synthesized by many methods, such as sol/gel method[109], vapor phase method[110], chemical vapor deposition[111], spray pyrolysis[112], hydrolysis[113], hydrothermal[114], and microwave plasma[115] method. However, these methods have many limitation factors such as complicated procedures, high reaction temperature, long reaction time, toxic reagents, by-products use, and high cost of production, hence, it is difficult to prepare zirconia nanoparticles on a large-scale production. The present thesis deals with the synthesis of zirconia by thermal decomposition method.

Thermal decomposition method involves chemical decomposition with the help of heat. Decomposition reaction involves a single substance being separated into multiple compounds. Heat can be used to decompose substances either physically or chemically. Heat is required to break the chemical bonds so that decomposition occurs. The temperature at which the substance chemically decomposes is called as the decomposition temperature. Physical decomposition involves separation of compounds that are attached physically. One such example includes the decomposition of hydrated copper sulfate into copper sulfate and water[116]. The same reaction could be made reversible if water is added to the copper sulfate forming hydrated copper sulfate with the release of heat. Decomposition reaction is generally an endothermic reaction as heat is supplied externally. General example is the formation of calcium with the release of carbon dioxide, when the calcium carbonate is decomposed. When oxides are considered, oxygen

is released as seen in the formation of mercury from mercury oxide upon decomposition. In the present thesis work, zirconium acetyl acetonate was used as a precursor for the thermal decomposition method[117].

Steps involved in the thermal decomposition method are as follows:

1. Zirconium acetyl acetonate (ZrAcAc) (from Sigma Aldrich (98 %)) was used without further purification.
2. ZrAcAc powder weighing about 4 grams was placed in the alumina boat for calcination.
3. Thermal decomposition method consists of three stages starting from 75 °C and ending at 480 °C. The decomposition of moisture and volatile impurities occur during the first stage of decomposition (75 °C to 180 °C). In the second stage of decomposition, decomposition of acetyl acetonate occur in the temperature range 180 °C to 240 °C
4. The third stage (240 °C to 480 °C) leads to the decomposition of oxycarbonate at 400 °C and finally the zirconia powder at 500 °C.

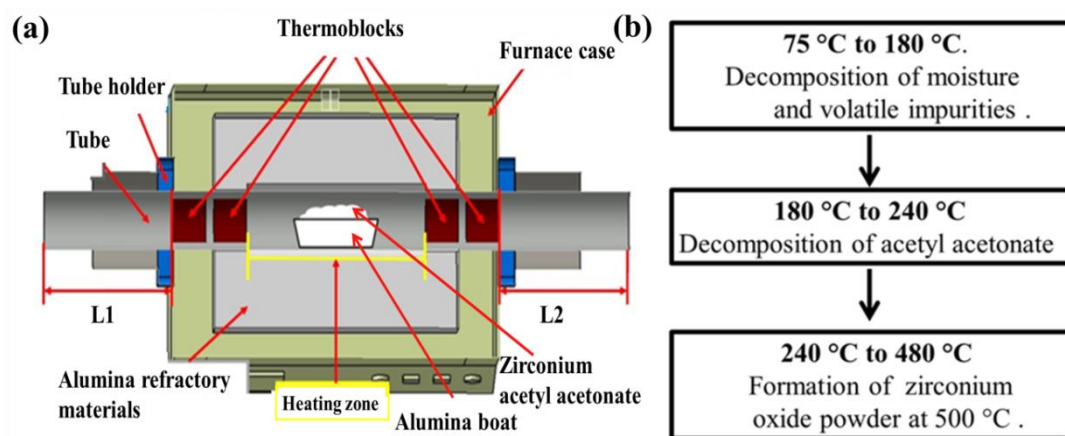


Figure 2.1 (a) Schematic diagram of a tubular furnace used for the decomposition of zirconium acetyl acetonate (b) Schematic representation of the chemical reaction during the thermal decomposition.

5. The powder produced (0.2 grams) were of mixed phase, namely, monoclinic and tetragonal zirconia. In order to obtain single phase monoclinic zirconia, the obtained mixed phase zirconia was optimized under heat treatment at different temperatures and duration.
6. Single phase monoclinic zirconia was obtained by heat treatment at 900 °C for 18 hrs.

7. The zirconia powder was pelletized using a mechanical pelletizer by applying pressure of 10 MPa. The zirconia pellet was then sintered at 930 °C for four hours.

2.2. Irradiation facility

Ion irradiation experiments were carried out using the 150 kV ion accelerator. Figure 2.2 (a)) and Figure 2.2 (b) show the photograph and schematic diagram of 150 kV ion accelerator. A RF ion source produces the gaseous ions. The pressure maintained in the source side is about 10^{-6} bar. The ions are accelerated and mass analyzed by a 45° mass analyzing magnet. The ions are then focused by a quadrupole lens and transport to the irradiation chamber.

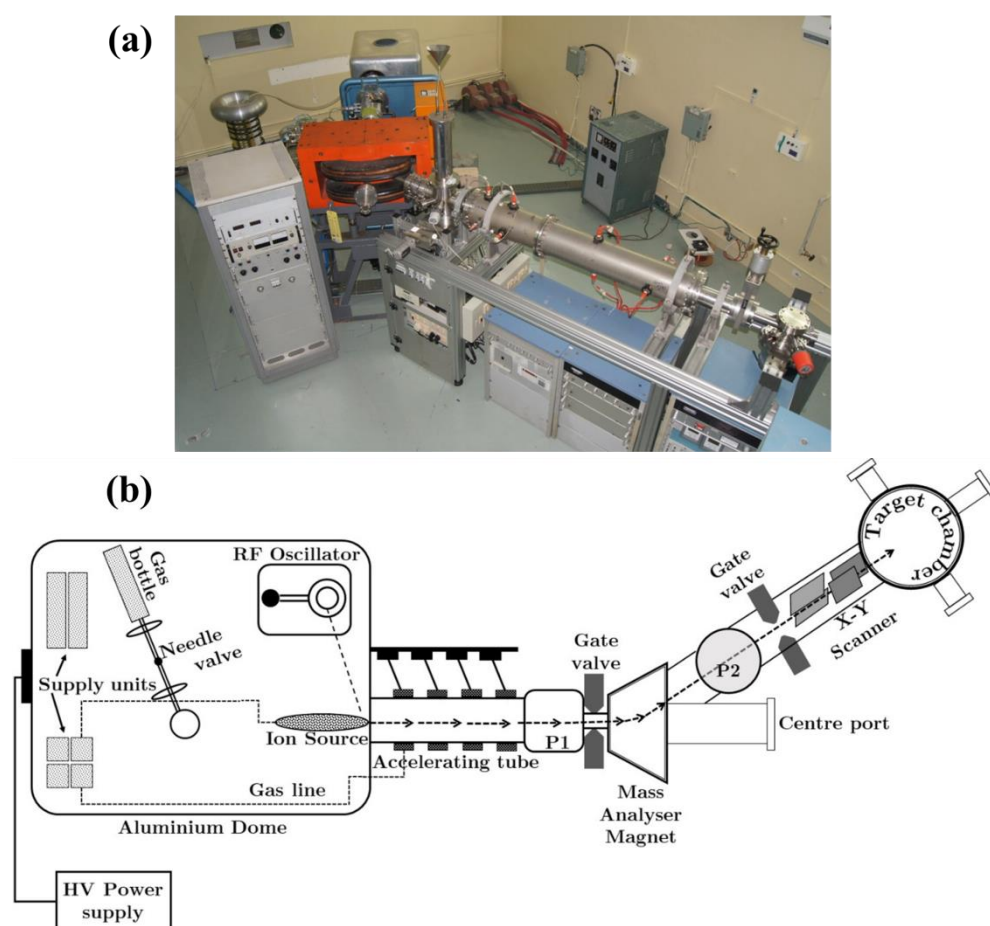


Figure 2.2 (a) Photograph of 150 kV ion accelerator used for the ion irradiation experiments
(b) Schematic diagram of the 150 kV ion accelerator.

The vacuum in the irradiation chamber is about 10^{-6} mbar which is achieved with the help of turbo molecular pump. The samples are kept on the copper block which is mounted on the sample manipulator. This copper block is electrically isolated from the rest of the chamber to facilitate the beam current measurements. A secondary electron

suppressor was used to avoid the error and false current measurements caused by the secondary electron emission. In order to suppress the secondary electrons, voltage of -40 V was applied to the secondary electron trap. The beam current and ion fluence are measured with the help of a current integrator. Even though the accelerator has the capacity to deliver ion beam current of several μA , the beam current was maintained less than $1 \mu\text{A}$ to avoid beam heating of the sample. In order to maintain clean vacuum liquid nitrogen trap is used for trapping oil vapour (from diffusion pump) and hydrocarbon. In order to carry out the irradiation experiments at low temperature, liquid nitrogen cryostat was used. The ion irradiation experiments were carried out at room temperature (300 K) and at 143 K.

2.3. Grazing incidence X-ray diffraction

X-ray diffraction experiment is powerful tool to analyse the crystal structure. The short wavelength of the X-rays makes them to get scattered by adjacent atoms in crystals that interfere and give rise to diffraction effects. Each atom acts as a diffraction center and the entire crystal acts as a diffraction grating. Thus the diffraction pattern produced by the crystals gives details about internal arrangement of the crystal. X-ray diffraction is well explained by Bragg's law and it is given by the equation

$$2d \sin\theta = n\lambda \quad \text{Eqn.2.1}$$

In thin films, the X-ray diffraction is carried out with grazing incidence to avoid signal from the substrate.

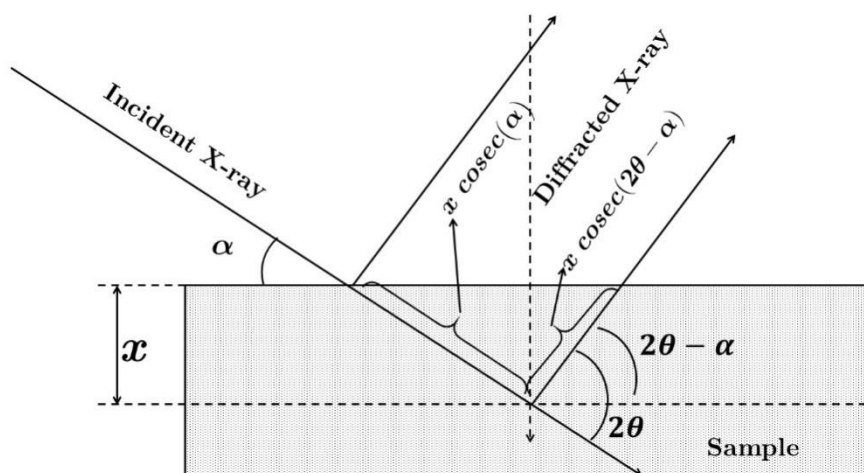


Figure 2.3 Schematic diagram of the GIXRD and X-ray penetration depth in the specimen.

According to Beer Lambert Law, $I = I_0 \exp(-\mu t)$, where I is the intensity of the X-rays after passing through the specimen thickness of t , I_0 is the intensity of the incident

X-rays and μ is the linear mass absorption coefficient of the specimen. From Figure 2.3, it is seen that α is the incident angle of the X-rays, 2θ being the collective angle, x is the probing depth of the X-rays. The total distance travelled by the X-rays in the material is given by

$$x = \text{cosec}(2\theta - \alpha) + x \text{cosec}(\alpha) \quad \text{Eqn.2.2}$$

For the 99% absorption of intensity becomes $\ln(100) = \mu t$

$$x = \frac{\ln(100)}{\mu \text{cosec}(2\theta - \alpha) + \text{cosec}(\alpha)} \quad \text{Eqn.2.3}$$

Using the above equation it is easy to calculate the total distance travelled by the X-rays in the material. Generally the probing depth t of the X-rays is of the order of μm . In low energy ion irradiated samples, the damage is produced in few nanometers from the surface. Hence, in case of GIXRD measurement on ion irradiated sample, the incident angle α is kept as small as possible so that the X-rays probe the ion irradiated region which is of the order of few nanometers.

2.3.1. Crystallite size –Scherrer formula

X-ray diffraction is used as a tool to calculate the crystallite size of the crystal. The crystallite size L depends on the full width at half maximum (FWHM) (β) of the diffraction peak, wavelength (λ) of the X-rays, the Scherrer constant (K), the diffraction angle θ . The $FWHM$ (β) varies inversely with size (L)[118].

$$\beta = \frac{K\lambda}{L \cos \theta} \quad \text{Eqn.2.4}$$

The Scherrer constant is affected by the factors like the crystallite size, crystal shape and size distribution.

2.3.2. Strain calculation-WH method

There are different types of strain namely lattice strain, microstrain and macrostrain in the crystals. Strain is generally indicated by the broadening of the diffraction peaks and shift in the diffraction peak positions. The strain in the crystal leads to change in the d spacing. Compressive strain would make the d spacing smaller and a tensile stress would make the d spacing larger. According to Williamson-Hall (WH) method, peak broadening is represented as

$$\beta \cos \theta = \frac{K\lambda}{L} + 4\epsilon \sin \theta \quad \text{Eqn.2.5}$$

where β is the FWHM of the diffraction peak, K is the Scherrer constant, λ is the wavelength, L is the crystallite size, ϵ is the strain and θ is the diffraction angle.

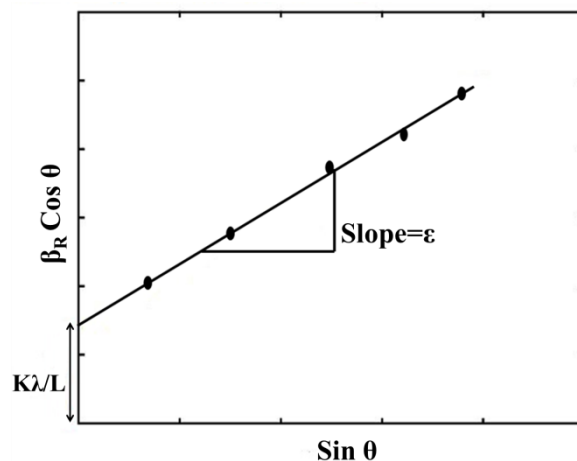


Figure 2.4 Williamson Hall plot for the measurement of crystallite size and strain in the samples. The intercept ($K\lambda/L$) gives the crystallite size and the slope (ϵ) gives the strain.

Williamson Hall plot is plotted between $\beta_R \cos \theta$ and $\sin \theta$. (β_R is the peak width after the correction of instrumental broadening). The intercept $\frac{K\lambda}{L}$ of the Williamson Hall plot gives the crystallite size and the slope ϵ gives the strain in the sample[119].

In addition to the Williamson Hall method, Wilson plot is also widely used to calculate the macrostrain and lattice strain present in the ion irradiated sample. Wilson method[120] can be used, when the grain fragmentation is negligible and the peak broadening is due to the strain. In ion irradiated samples, the lattice strain and macrostrain are calculated using Wilson method. According to Wilson formula the lattice strain is given as

$$\text{Lattice strain} = \frac{\sqrt{(FWHM_{\text{irradiated}}^2 - FWHM_{\text{as_sintered}}^2)}}{4 \tan \theta} \quad \text{Eqn.2.6}$$

where $FWHM_{\text{irradiated}}$ and $FWHM_{\text{as_sintered}}$ are the full width at half maximum of the irradiated sample and as-sintered sample respectively and θ is the Bragg angle.

The macrostrain in the samples is calculated using the formula

$$\text{Macrostrain} = \frac{(d_{hkl})_{\text{irradiated}} - (d_{hkl})_{\text{as_sintered}}}{(d_{hkl})_{\text{as_sintered}}} \quad \text{Eqn.2.7}$$

where $(d_{hkl})_{\text{irradiated}}$ and $(d_{hkl})_{\text{as_sintered}}$ are the inter-planar spacing of the plane (hkl) corresponding to the irradiated and the as-sintered zirconia samples respectively.

In the present thesis work, STOE X-ray diffractometer was used to carry out the X-ray diffraction measurements. The instrument uses Cu K_α of wavelength 1.54 Å as the source.

2.4. Raman scattering

Raman scattering is inelastic scattering of light with momentum and energy transfer between photons and scattering materials (like molecular and lattice vibrations in solids). It is caused by modulations of the susceptibility or polarisability of the scattering material by vibrations or other excitations. In solids, Raman scattering experiment probes the phonons in the solids and it is a nondestructive technique. In the present thesis, the changes in the phonon modes of the ion irradiated zirconia samples are extensively studied using Raman scattering.

2.4.1. Confocal Raman Microscopy

Figure 2.5(a) shows the photograph of WITec RA 300 confocal Raman imaging system which is used to obtain Raman spectra of the zirconia samples. In WITec RA 300, the source is an argon ion laser with two wavelengths 532 nm and 355 nm. Figure 2.5(b) shows the schematic diagram of the components of the confocal Raman imaging system. The instrument consists of a laser source, filter, objective lens, dichroic beam splitter, notch filter, spectrometer and charge coupled device (CCD) camera. The excitation is produced by the laser source and all the unwanted wavelength is removed by the laser line filter. In order to filter out the elastically scattered (Rayleigh) signals, the backscattered light is filtered by the dichroic mirror and then by a notch filter. Then the blocking pinhole spatially filters the remaining signals and these signals are passed on to a spectrometer consisting of a CCD camera to analyze the Raman signal. The instrument has high sensitivity, best performance in spectral resolution, ultrafast Raman imaging with one millisecond integration time per spectrum etc.

In addition to Raman scattering, WITec RA 300 can be used for photoluminescence experiments. Photoluminescence is a nondestructive technique used to probe the electronic structure of the materials. When light falls on the specimen it is

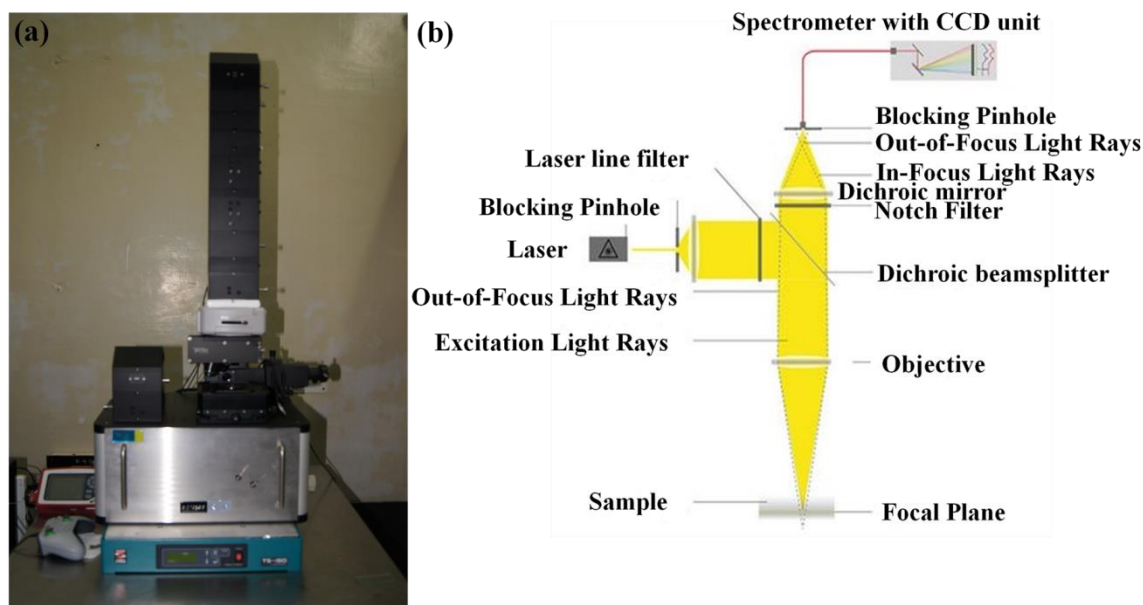


Figure 2.5 (a) Photograph of the WITec RA 300 confocal Raman imaging system (b) Schematic diagram of confocal Raman imaging system with optical components.

absorbed and imparts the excess energy to the specimen and this process is called the photo-excitation. This excess energy is dissipated through the emission of light and this called as luminescence. In case of photo-excitation, the luminescence is termed as the photoluminescence. This technique is used to probe discreet energy levels. There are two types of emission (i) radiative and (ii) non-radiative emission. The electron excited to above the conduction band will try to combine with the hole and the electron excited below the valence band loses its energy through the phonon. The photo-excitation causes the electrons to move in permissible states. These electrons in the permissible states then return to the equilibrium states by releasing the excess energy in the form of light (radiative emission) or without the emission of light (non radiative emission). The energy difference between the levels of transition determines the energy of the emitted light. The intensity of the emitted light is determined by the relative contribution of the radiative process.

2.5. Time resolved photoluminescence spectroscopy

Time resolved photoluminescence (TRPL) spectroscopy is a technique that provides spectral and temporal evolution of the emission from the sample. Electron hole pairs are produced when the sample is illuminated with a short pulse of light. These electron-hole pairs decay to lower energy levels, recombine and emit light. The emitted light consists of a set of wavelength corresponding to the transition energies of the sample.

The measurement of the optical spectrum as a function of time gives information about the transition energies and their lifetime.



Figure 2.6 Photograph of FLS 980 UV-Vis absorption spectrometer.

Figure 2.6 shows the photograph of UV-Vis absorption spectrometer (FLS 980 Edinburg) that can be used to maintain the life time decay measurements and also the spectral measurements of the decay process. Xenon flash lamp is used as the source of light which emits continuous radiation from 230 nm and 2600 nm. The instrument employs transverse sample excitation geometry. Time correlated single photon counting

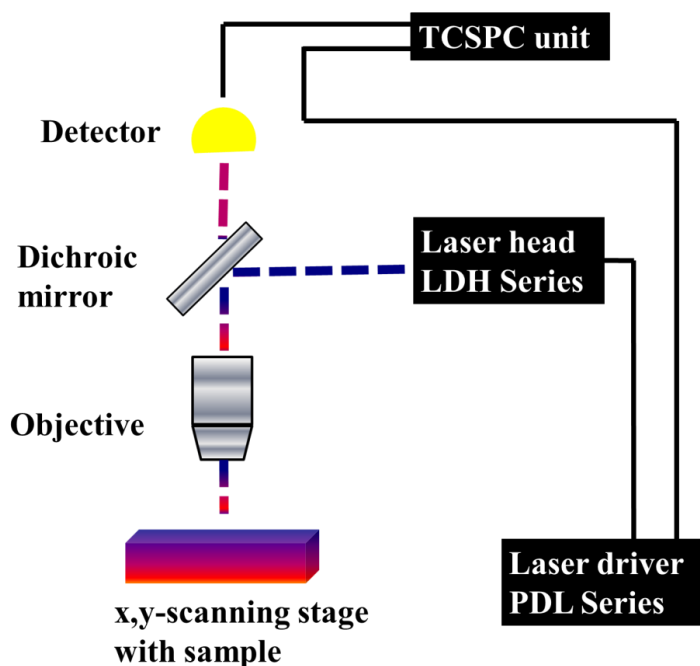


Figure 2.7 Schematic diagram of TRPL measurement system.

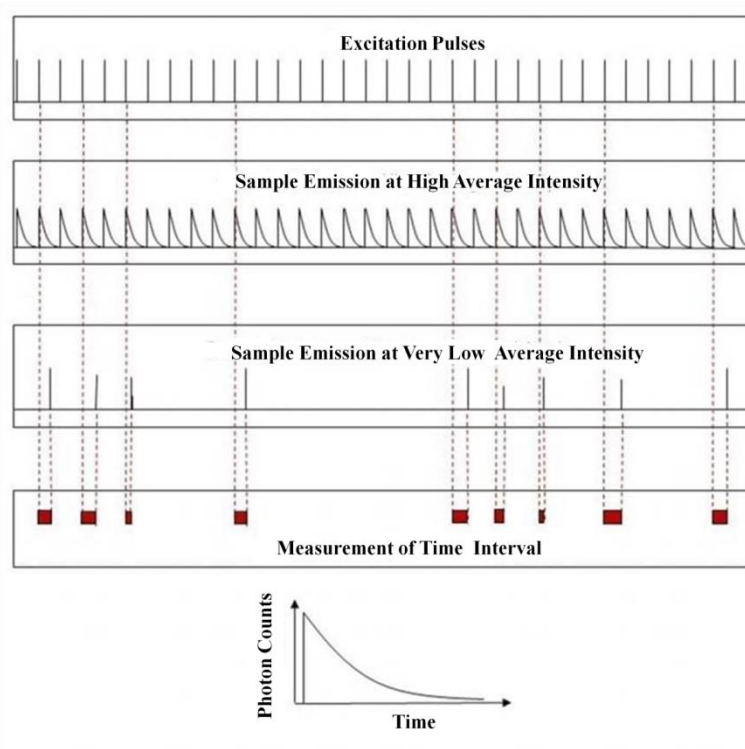


Figure 2.8 Schematic diagram of TCSPC technique used for TRPL measurement.

(TCSPC) technique is used to measure fluorescence decays in the time domain. In principle, single photon events are detected and their time of arrival is correlated to the laser pulse which was used for the excitation of the sample. In TCSPC, the time between the sample excitation and the arrival of the emitted photon at the detector is measured. TCSPC requires a start signal steering the laser pulse and a defined stop signal realized by the detection with single-photon sensitive detectors. The time delay measurements are repeated many times and the delay times are sorted into a histogram that plots the occurrence of emission over time after the excitation pulse. A typical lifetime measurement consists of scanning stage, dichroic mirror, detector, TCSPC unit. Figure 2.7 shows the schematic diagram of the TRPL measurement system.

Figure 2.8 shows schematic diagram of TCSPC measurement technique. A histogram of single photon count as a function of time is built from a series of START and STOP pulses, which are input to the TCSPC electronics. The START pulse is an electrical trigger that is synchronous to the optical excitation pulse and STOP pulse is caused by a single photon reaching the detector. A source produces optical excitation pulses, at a fixed repetition rate and at the same time triggers the START of the TCSPC detector. Fine tuning of the excitation intensity is needed so that very low rate of detected photon (STOP rate) could be obtained. The time between the START and STOP pulses is then recorded

accurately with the help of electronics, and the photoluminescence decay is built after acquiring millions of START-STOP sequences in order (see Figure 2.8).

2.6. Electron microscopy

2.6.1. Scanning electron microscopy

When a specimen is exposed to energetic electrons, the electrons interact with the specimen. Figure 2.9 shows a schematic representation of the process involved during the electron matter interaction and the interaction volume inside the specimen for various experimental conditions.

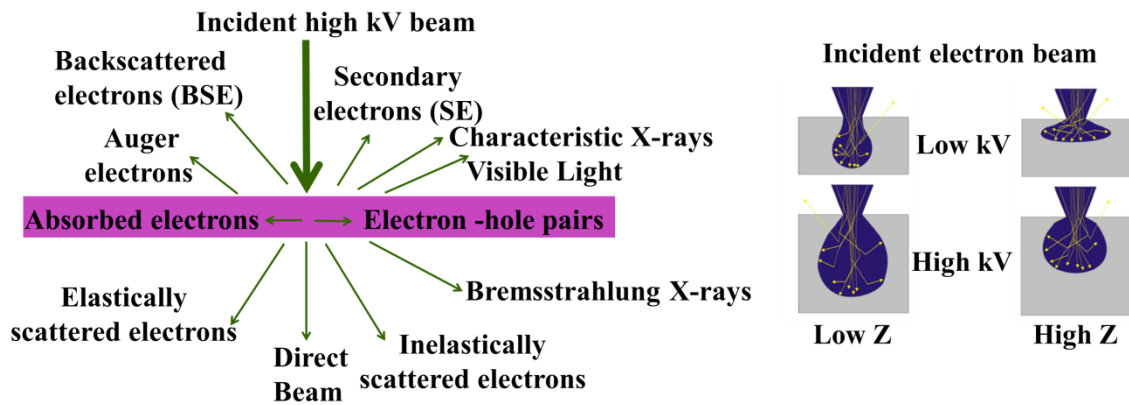


Figure 2.9 (Left) Schematic representation of electron interaction with specimen and (Right) Interaction volume (blue) of the electron beam inside the specimen.

Backscattered electrons (BSE) are the electrons that are elastically scattered by more than 90° . Inelastically scattered electrons are due to the result of continuous interactions between the incident electron and the atoms in the specimen with loss of energy in the primary beam. The ionization of the sample causes the excitation of electron resulting in the production of secondary electrons (SE) with energies less than 50 eV. These backscattered and secondary electrons are used to image and analyze the specimen. These electrons are used to carry out the image formation for the Z contrast and topography of the sample.

The dependence of the shape of the interaction volume inside the specimen and voltage is shown in Figure 2.9. At certain accelerating voltage, the shape of the interaction volume is a tear drop for specimen with low atomic number (Z) and a hemisphere for the specimen with high atomic number. It is seen that the size of the interaction volume and the penetration depth of the electron increases with the increase in electron energy and decreases with the atomic number of the material.

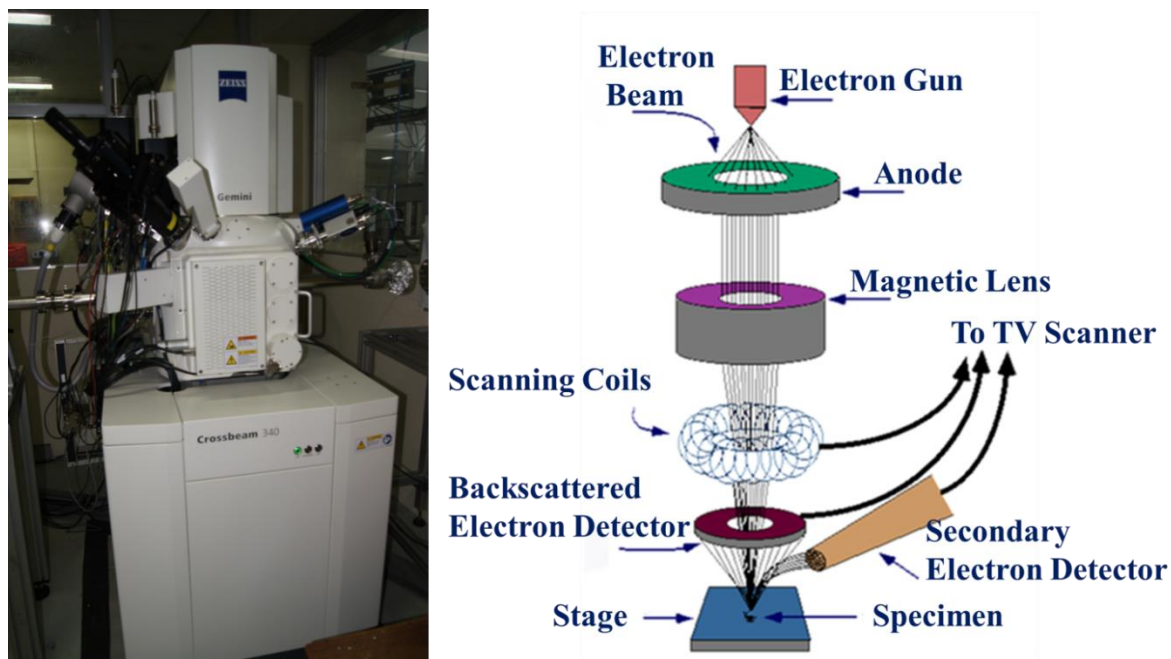


Figure 2.10 (Left) Photograph of Zeiss Crossbeam 360 SEM equipment (Right) Schematic diagram of the components of scanning electron microscopy.

Figure 2.10(a) shows the photograph of Crossbeam 360 from Carl Zeiss used for acquiring the SEM images of the as-sintered and the ion irradiated zirconia samples. It comprises a field emission gun (FEG), secondary electron and secondary ion (SESI) detector, In-lens Duo detector, 5 axis stage manipulator along with various types of detector.

Figure 2.10(b) shows the schematic representation of the components of SEM. The major components of a scanning electron microscope are (i) electron gun (tungsten or field emission gun (FEG)), (ii) anode, (iii) electromagnetic lenses (condenser lens (CL) and objective lens (OL)), (iv) electron detectors (BSE and SE detectors) and (v) specimen stage. This microscopy technique is used to produce the magnified image of an object in real space. The magnified image shows the texture of the surface, the shape and size of the particles. The SEM uses a focused electron beam to scan across the surface of the specimen systematically, producing large numbers of signals (SE and BSE signals). These electron signals are eventually converted to a visual signal displayed on a cathode ray tube (CRT). The SEM uses electron of energy 0.5 keV to 30 keV that are focused using the electromagnetic lenses. The focused electron beam is scanned on the sample surface and SE signal is used for imaging of the sample. The electron beam interacts with the atoms of the sample and produces secondary electron emission by the process of elastic scattering. The secondary electrons (usually of energy < 50 eV) can be detected by special detectors

(SESI, In-lens Duo detectors) and the intensity is proportional to the number of secondary electrons.

2.6.2. Transmission electron microscopy

Transmission electron microscopy (TEM) is powerful tool to provide the information about atomic resolution images, crystal structure, defects, and electronic structure of the specimens. In TEM, the electrons are used as particle as well as waves. A typical 200 keV TEM have the wavelength five orders of magnitude than the visible light and is 2.51 pm.

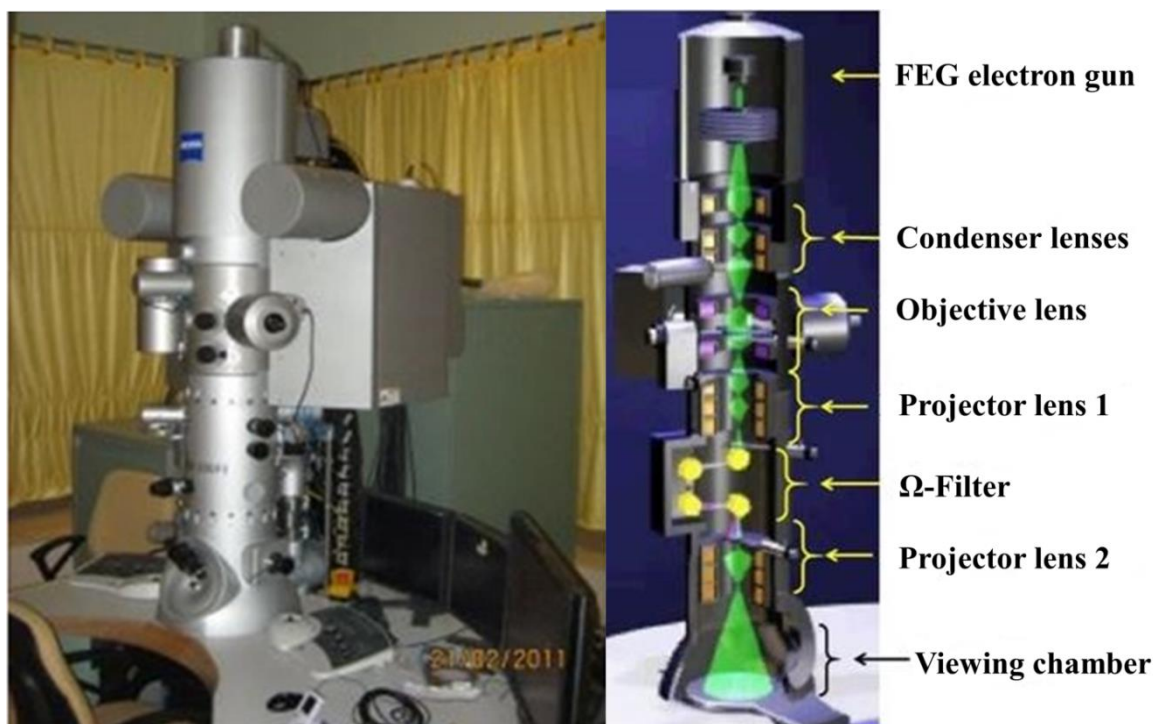


Figure 2.11 (Left) Photograph of LIBRA 200FE high resolution electron microscope (Right) the illustration of the electron path in the TEM

TEM has three main parts (i) the illumination system, (ii) the objective lens and (iii) the imaging system. The gun and the condenser lens form the illumination system and their main function is to take the electrons from the source and transfer to the specimen. It can be made to work in two modes namely the parallel mode (as in TEM, selected area electron diffraction (SAED)) and in the convergent mode (as in STEM, combined beam electron diffraction (CBED)). The objective lens is the main part where the interaction of the electron beam with the sample takes place. Several lenses are used in the imaging system to magnify the produced image, diffraction pattern (DP) produced by the objective lens, focusing the images on the viewing screen with the help of detector TV camera or charge coupled device (CCD)[121].

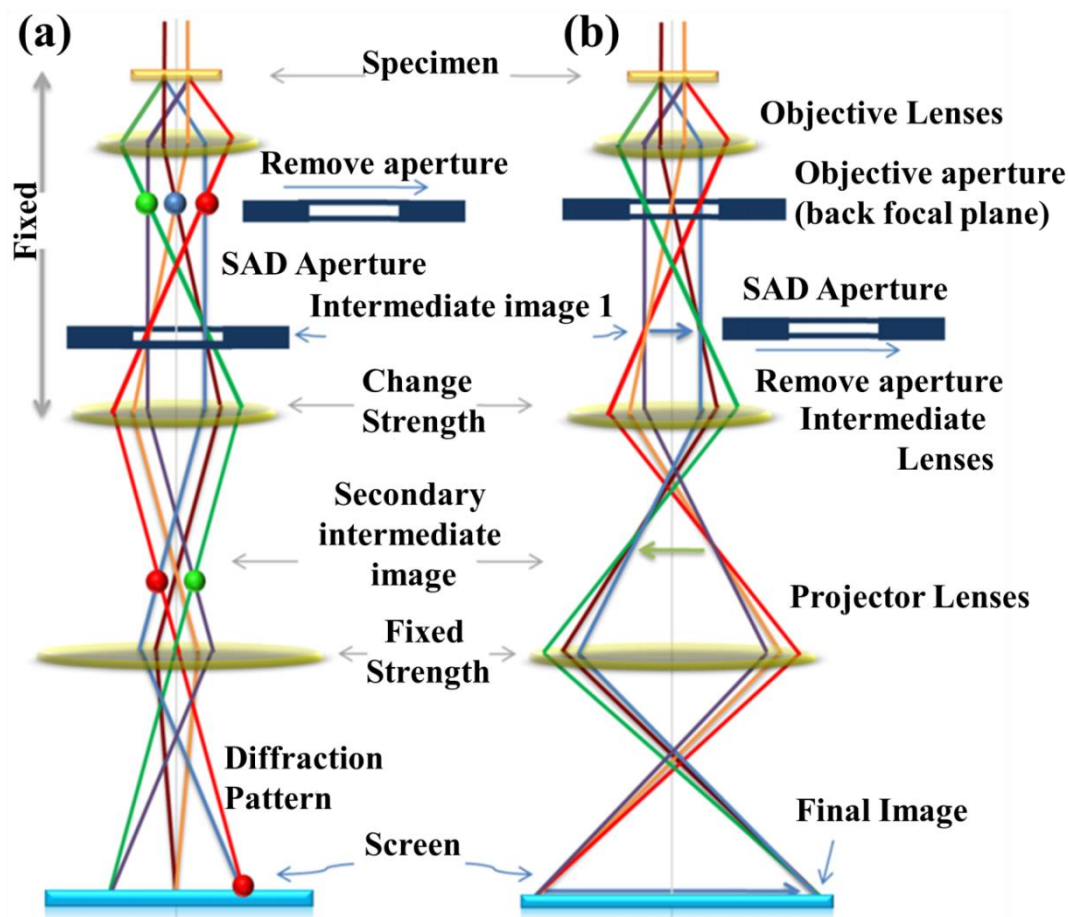


Figure 2.12 Schematic diagram showing the two basic types of operating modes of TEM (a) diffraction mode and (b) imaging mode[121].

Figure 2.11(a) shows the photograph of HRTEM (LIBRA 200FE Carl Zeiss) which is used in the present thesis work extensively. Figure 2.11(b) shows the electron path in the HRTEM. HRTEM is operated at 200 kV. This HRTEM can be used for obtaining high resolution TEM (HRTEM) images, electron diffraction, bright field and dark field images, STEM images and composition analysis using EELS and EDS. The TEM instrument is equipped with a field emission gun (FEG) source and an in column omega filter. The TEM has the information limit of 1.3 Å. Two basic operating modes of the TEM imaging system involve the diffraction mode (DP) and imaging mode. Figure 2.12(a) and Figure 2.12(b) shows the schematic diagram of the TEM operating under diffraction mode and imaging mode respectively. In order to view the diffraction pattern, the TEM is operated in the diffraction mode (projecting the diffraction pattern on the screen). In the diffraction mode, the back focal plane of the objective lens acts as the object plane for the intermediate lens. In the imaging mode, the intermediate lens is adjusted so that its object plane is the image plane of the objective lens.

2.6.2.1. TEM observation of gas bubbles

In TEM image, the contrast will be minimum in the image, when the object is in focus. However, out of focus conditions (defocusing the objective lens) in TEM enable to gather some useful information. There are two different types of focus conditions in TEM namely the underfocus and overfocus.

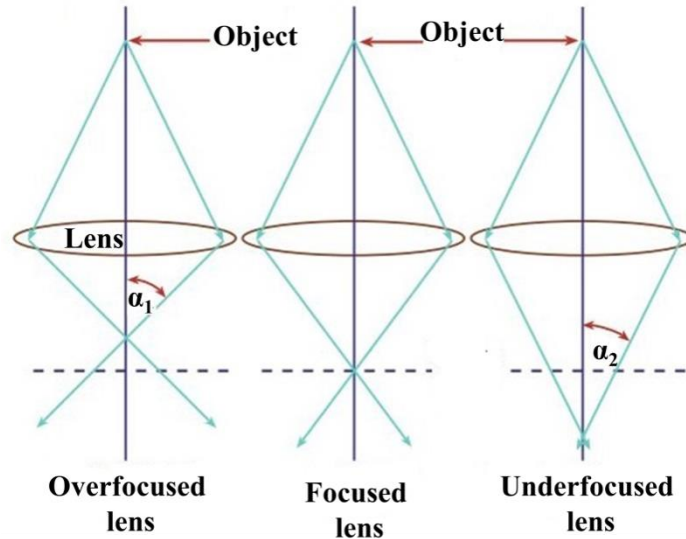


Figure 2.13 Schematic representation of various types of beam focusing conditions in TEM[121].

Figure 2.13 shows the schematic representation of various types of beam focusing conditions in TEM. When it is in proper focus (or ‘in-focus’), the image is formed on the image plane. Over focus is the condition in which the strength of the lens is increased such that the image is formed above the image plane. Underfocus condition refers when the image is formed below the image plane by decreasing the strength of the lens.

Underfocus condition is employed to image bubbles in the samples[121]. Even though it is difficult to image voids, gas filled cavities, holes that are enclosed in the specimen, they can be viewed by defocusing the image and observing a special contrast known as the Fresnel contrast. When the TEM is operated in out of focus conditions (defocus the objective lens), alternative dark and white fringes are seen and it is known as the Fresnel fringes. Figure 2.14 shows the TEM images of 120 keV He^+ ion irradiated zirconia samples taken in different focusing conditions. It is seen that when the TEM is operated in the over focus conditions, the Fresnel fringe is dark. In case of in focus condition, there is no Fresnel fringes and when the beam is under-focus condition, the bright Fresnel fringe is noticed[121].

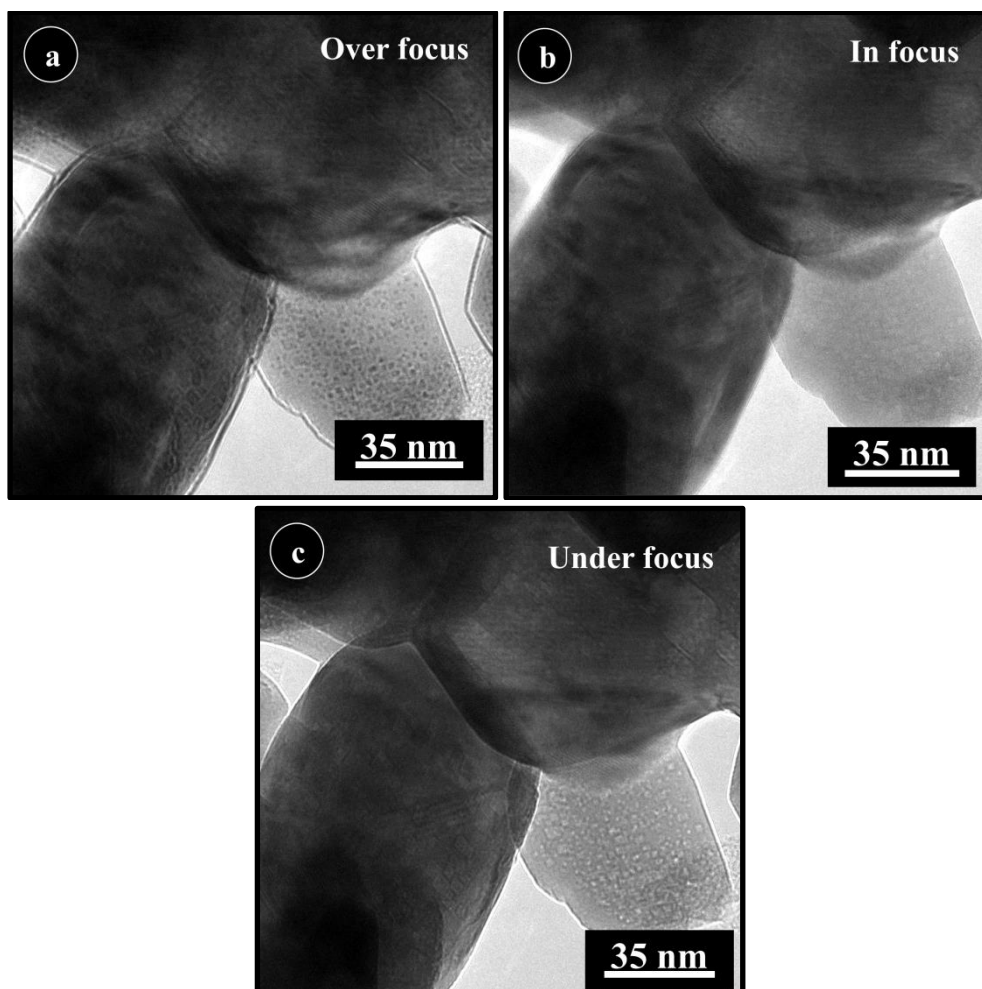


Figure 2.14 TEM images of 120 keV He^+ ion irradiated ZrO_2 (ion fluence $2 \times 10^{17} \text{ ions/cm}^2$, 300 K) taken in different focusing conditions.

2.6.2.2. TEM sample preparation

In order to make the sample suitable for analyzing under TEM, the sample should be made as thin as possible so that they are electron transparent. The typical electron transparent thickness is less than 100 nm [121]. Such thinning of the samples is really challenging. There are various TEM sample preparation methods for different material depending on the sample form (thin film, powder, bulk). Generally the thinning of the sample produces artifacts. In the present thesis, in order to avoid artifacts by the sample preparation methods and to study clearly and accurately the defects produced by the ion irradiation experiment, simpler method has been opted. In this method the ion irradiated samples, in the form of pellet, are scratched by a scalpel blade. The particles are dispersed in propanol and are ultra sonicated for few minutes. Above liquid mixture drawn by a micro pipette is dispersed carefully on a carbon coated copper TEM grid and dried.

2.7. Summary

Detailed experimental procedures followed for the zirconia sample synthesis and the ion irradiation experiments have been discussed. The ion irradiation facility (150 kV accelerator) used in the work is explained. The details of characterization techniques used in the present work such as grazing incidence X-ray diffraction, transmission electron microscopy, scanning electron microscopy, Raman scattering, photoluminescence spectroscopy and time resolved photoluminescence spectroscopy are discussed briefly.

Chapter 3

Ion irradiation induced phase transformation in monoclinic zirconia

3.1. Motivation

Zirconium dioxide (ZrO_2) known as zirconia, is one of the well-researched ceramics known for its high strength, high thermal conductivity, low thermal expansion, low brittleness and high melting point[5–7]. Zirconia exists in three phases with respect to temperature namely monoclinic, tetragonal and cubic (face centered cubic) structure. Monoclinic phase belonging to the phase group ($P_{21}/c, C_{2h}^5$), is the most stable phase at ambient temperature and pressure[122]. At 1170 °C monoclinic zirconia transforms to tetragonal phase with a phase group ($P4_2/nmc, D_{4h}^{15}$). The cubic zirconia is the most stable phase at temperature above 2370 °C and finally melts at 2750 °C. Zirconia is widely known for its high resistance to radiation. It is used as a containment material for nuclear waste[8, 123], and inert matrix fuels[124]. Hence it is important to study the behavior of zirconia under ion irradiation.

There are several groups who have carried out ion irradiation in bulk and nanocrystalline zirconia and reported phase transformation[21, 40–45, 47, 120, 125, 126]. In the case of ion irradiation with swift heavy ions (SHI) (200 MeV Ag^+ ion irradiation in zirconia), monoclinic to tetragonal phase transformation was observed[40]. The evolution of tetragonal phase was attributed to the electronic energy loss, overlapping of latent tracks, and rise in the local temperature[40]. Schuster *et al.*[42] reported the SHI (200MeV/u, U^+) ion irradiation effects in zirconia at various pressures and observed that the phase transformation rate was faster when the ion irradiation was carried out at high pressure (*i.e.*, the ion fluence necessary for the phase transformation was an order of magnitude less). The authors had attributed the faster phase transformation to double ion impact process, where sufficient oxygen vacancies are produced during the first ion impact and the stress produced by these oxygen vacancies are responsible for the phase transformation during the second impact[42].

In the case of high energy heavy ion irradiation in zirconia, Lian *et al.*[41] showed that amorphous to tetragonal phase transformation in bilayer (amorphous/cubic) thin film of nano-zirconia upon 1 MeV Kr^{2+} ion irradiation. These authors attributed that the tetragonal phase is energetically favoured. Zirconia nanoparticles (in tetragonal structure)

in SiO₂ matrix was found to undergo amorphisation, when irradiated with 1 MeV Xe²⁺ ion upto 0.8 dpa itself[47].

In the case of low energy heavy ion irradiation in zirconia, Müller *et al.*, [125] reported 350 keV Ar⁺ ion irradiation effects in thin films (as-prepared and 90 keV Ar⁺ ion implanted) of zirconia and found that the argon bubbles could not be observed in the zirconia thin films. Further, the authors concluded that the implanted argon is not necessary for the phase transformation of monoclinic to tetragonal structure[125]. Even when the ion irradiation was carried out at low temperature (340 keV Xe⁺ ion[127] or 150 keV Ne⁺ ion[44]), monoclinic to tetragonal phase transformation was observed. Still the phase transformation in monoclinic zirconia is not well understood in the context of role of damage or inert gas and/or both.

In the present chapter, to understand the role of damage and inert gas in the context of ion beam induced phase transformation, low energy inert gas ions were irradiated in monoclinic zirconia and the effects are studied using X-ray diffraction (XRD), electron diffraction and Raman scattering analysis systematically.

3.2. Synthesis of monoclinic zirconia

Zirconium acetyl acetonate (ZrAcAc, Sigma Aldrich (98 %)) was used as the precursor material for thermal decomposition method[117]. The precursor powder (\cong 4 gram) was placed in an alumina boat and was kept in a tubular furnace. The heat treatment temperature and time was optimized to obtain single phase monoclinic zirconia powder. The monoclinic zirconia powder was pelletized using a mechanical pelletizer with a pressure of 10 MPa and the pellets were sintered at 930 °C for four hours. Hereafter these sintered single phase monoclinic zirconia is called as as-sintered zirconia.

3.3. Ion Irradiation and characterization methods

These as-sintered monoclinic zirconia pellets were ion irradiated using the 150 kV ion accelerator with helium (He⁺), argon (Ar⁺) and krypton (Kr⁺) ions with energy of 120keV, 120keV and 60 keV respectively. The vacuum maintained in the irradiation chamber was better than 1×10^{-6} mbar. The ion irradiation was carried out at room temperature (300 K) and at low temperature (143 K). The projected range and the straggling of He⁺, Ar⁺ and Kr⁺ ions in ZrO₂ were calculated using SRIM[37] and the values are tabulated in Table 3.1. The as-sintered and the ion irradiated zirconia samples were characterized using grazing incidence X-ray Diffraction (GIXRD) using the STOE diffractometer using Cu-K α ($\lambda=1.541$ Å) radiation. The angle of incidence was kept at 0.2°

for all the measurements. Raman measurements were carried out using micro Raman spectrometer (WITec Alpha RA 300) using Nd-YAG laser having an excitation wavelength of 532 nm and laser power of 0.5 mW.

Table 3.1 Details of ion irradiation parameters.

Ions	Energy	Fluence (ions/cm ²)	Projected Range(R _p) (nm)	Straggling (nm)	ENSP (S _e /S _n)	Temp	Dpa
He ⁺	120 keV	1×10 ¹⁵ – 2×10 ¹⁷	445	128	84.21	300 K 143 K	0.048 – 9.6
Ar ⁺	120 keV	1×10 ¹⁵ – 2×10 ¹⁷	75	31	0.5890	300 K 143 K	2 - 408
Kr ⁺	60 keV	1×10 ¹⁶ – 5×10 ¹⁷	23	10	0.1176	300 K 143 K	34.8 - 1740

Transmission electron microscopy measurements were carried out using LIBRA 200FE HRTEM (Carl Zeiss make) with the information limit of 0.13 nm. For electron beam transparent samples, the zirconia pellet surface was scratched using a scalpel blade and dissolved in propanol. The solution is then dispersed on a carbon coated Cu grid. This sample preparation method is adapted in order to avoid any artifacts during the convectional sample preparation methods like ion milling and FIB method.

3.4. Results

3.4.1. Grazing incidence X-ray diffraction analysis

Figure 3.1(a) shows the X-ray diffraction pattern of the precursor zirconium acetyl acetate. The diffraction pattern matches with the monoclinic structure (ICDD No 00-018-1515) (as shown in Figure 3.1(b)). Figure 3.1(c) shows the X-ray diffraction pattern of the sample obtained upon heat treatment of zirconium acetyl acetate at 600 °C for 5 hrs. The diffraction peaks are found to match with tetragonal (ICDD card no 00-050-1089) and monoclinic (ICDD card no 01-070-2491) structures (refer Figure 3.1(e) and Figure 3.1(f)). The predominant peak in the diffraction pattern corresponds to (101) plane of tetragonal zirconia. The predominant peaks of the monoclinic phase corresponding to the planes (-111) and (111) are low in intensity compared to the predominant peak (101) of the tetragonal phase. Thus it is confirmed that, the heat treatment at 600 °C for 5 hours has led to the formation of zirconia containing both monoclinic and tetragonal phases.

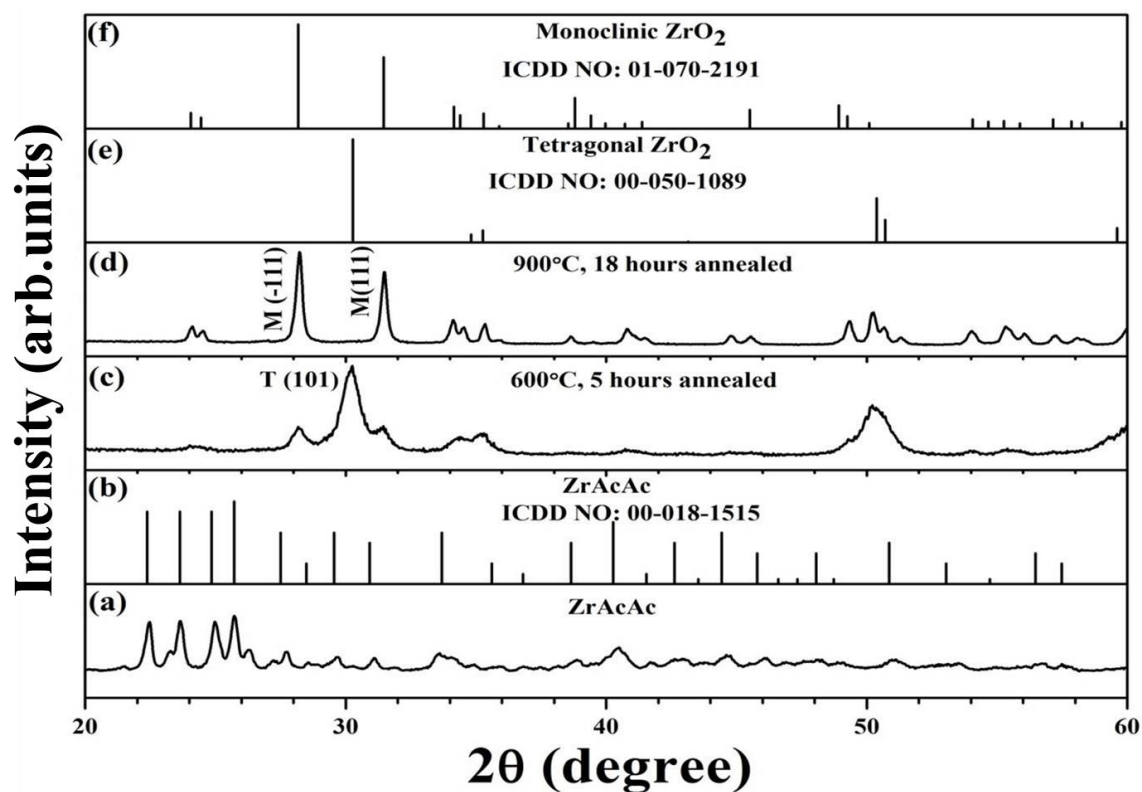


Figure 3.1 (a) GIXRD pattern of the precursor zirconium acetyl acetonate. (b) Stick pattern of the ICDD Card No 00-018-1515 corresponding to monoclinic phase of zirconium acetyl acetonate. GIXRD pattern of the samples obtained as a result of thermal decomposition (c) 600 °C for 5 hour and (d) 900 °C for 18hrs. (e) Stick pattern tetragonal phase (ICDD Card No 00-050-1089) and (f) monoclinic phase (ICDD Card No 01-070-2491) of zirconia.

In order to synthesis single phase monoclinic zirconia, the temperature of the heat treatment and time were optimized. Finally, zirconium acetylacetonate that was heat treated at 900 °C for 18 hours shows the single phase of monoclinic structure (shown in Figure 3.1 (d)). The diffraction peaks were found to match well with the monoclinic phase of zirconia (ICDD card no 01-070-2491). It is observed that the diffraction peak (101) corresponding to the tetragonal phase of zirconia present in the mixed phase (*refer* Figure 3.1(c)) has vanished after heat treatment at 900 °C (*refer* Figure 3.1(d)). In the present experiment, the tetragonal phase was observed at heat treatment at 600 °C itself instead of 1170 °C[128], and this could be due to the smaller size of the zirconia particles. The obtained monoclinic zirconia (after heat treatment at 900 °C) was pelletized and then sintered at 930 °C for four hours. Hereafter these sintered monoclinic zirconia pellet is called as as-sintered zirconia.

To obtain the X-ray diffraction from the ion irradiated samples, the grazing incidence X-ray diffraction is used due to the small projected range of ions in zirconia (*refer* Table 3.1). Figure 3.2(a) shows the GIXRD pattern of the as-sintered zirconia

samples. The diffraction peaks were indexed to the monoclinic structure (ICDD card no 01-070-2491). Figure 3.2(f) shows the expanded view of diffraction peaks obtained from the as-sintered peaks in the 2θ ranges from 27° to 32° . Figure 3.2(b-e) show the GIXRD pattern of He^+ ion irradiated (at 300 K) zirconia for the ion fluences of 1×10^{16} , 5×10^{16} , 1×10^{17} and 2×10^{17} ions/ cm^2 respectively. Figure 3.2(g-j) show their corresponding expanded view of the diffraction pattern for better clarity.

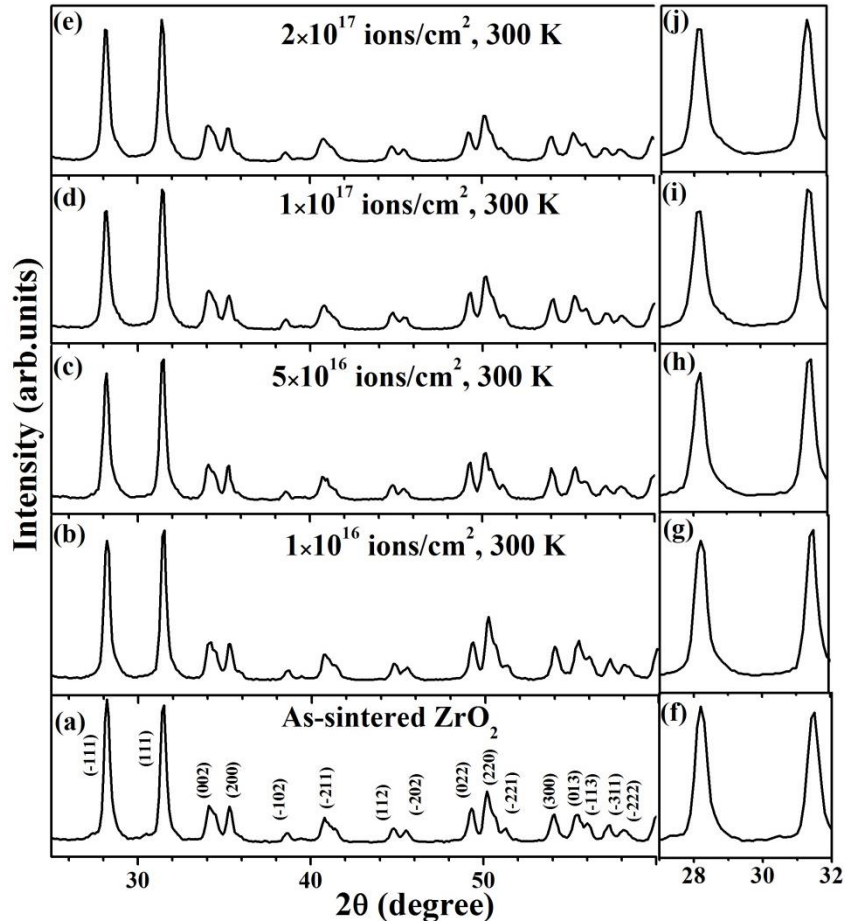


Figure 3.2 GIXRD pattern of the as-sintered and 120 keV He^+ ion irradiated (at 300 K) zirconia samples.

It is observed from Figure 3.2(b-e) that all the diffraction peaks corresponding to the as-sintered zirconia samples (monoclinic peak) remains the same. However the diffraction peaks have been broadened and shifted towards lower 2θ values with respect to the as-sintered zirconia sample. This indicates that upon He^+ ion irradiation at 300 K, strain is introduced in the zirconia samples.

Figure 3.3(b) – Figure 3.3(e) shows the GIXRD pattern of He^+ ion irradiated (at 143 K) zirconia samples for the ion fluences of 1×10^{16} , 5×10^{16} , 1×10^{17} and 5×10^{17} ions/ cm^2 respectively. Figure 3.3(g-j) shows their corresponding expanded view of

the diffraction pattern for better clarity. From Figure 3.3(b) and Figure 3.3(c), it is seen that all the planes corresponding to the as-sintered zirconia remains intact. From Figure 3.3(d) and Figure 3.3(e) it is observed that the all the diffraction peaks corresponding to the as-sintered zirconia samples remains the same except for the emergence of a small peak around 30.2° . This peak is due to (101) plane of tetragonal phase of zirconia (ICDD card No. 01-079-1764).

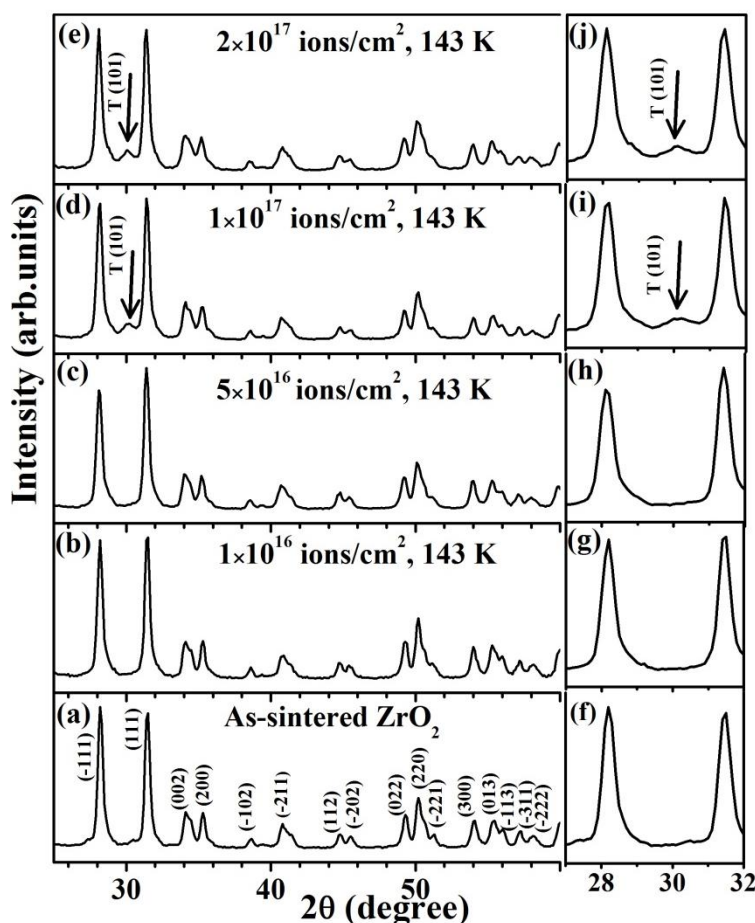


Figure 3.3 GIXRD pattern of the as-sintered and 120keV He^+ ion irradiated (at 143 K) zirconia samples.

Apart from that, it is also observed (from Figure 3.3(b-e)) that, upon He^+ ion irradiation at 143 K, the diffraction peaks have broadened and shifted towards lower 2θ values with respect to the as-sintered zirconia samples. This indicates that strain is induced in the zirconia samples as a result of ion irradiation at 143 K.

From the GIXRD patterns, irrespective of the ion irradiation temperature, it is noticed that there is a shift and broadening of the diffraction peaks upon He^+ ion irradiation. However, Rietveld refinement analysis[129, 130] was not carried out because of small crystallite size (59 nm), very thin implanted layer, small angle of incidence and

roughness of the pellet. Further, in the ion irradiated sample, the evolution of tetragonal phase is seen. In GIXRD pattern, some of the tetragonal planes overlap with existing monoclinic planes, hence it is not possible to apply Williamson-Hall method to estimate the strain.

In GIXRD patterns, the broadening of the peaks can be associated with the strain and grain fragmentation induced by ion irradiation. In the present case, the ion beam induced strain plays a major role and hence Wilson method was employed to estimate the strain induced in the zirconia samples upon ion irradiation. Here the plane (111) corresponding to the monoclinic structure was taken for estimating macrostrain using Wilson method. The macrostrain was calculated using the Eqn.3.1

$$\text{Macrostrain} = \frac{(d_{111})_{\text{irradiated}} - (d_{111})_{\text{as_sintered}}}{(d_{111})_{\text{as_sintered}}} \quad \text{Eqn.3.1}$$

where $(d_{111})_{\text{irradiated}}$ and $(d_{111})_{\text{as_sintered}}$ are the inter-planar spacing of the plane (111) corresponding to the ion irradiated and as-sintered ZrO_2 samples respectively (and shown in Figure 3.4(b)). Figure 3.4(a) shows the variation of peak position of the He^+ ion irradiated zirconia samples as a function of ion fluence.

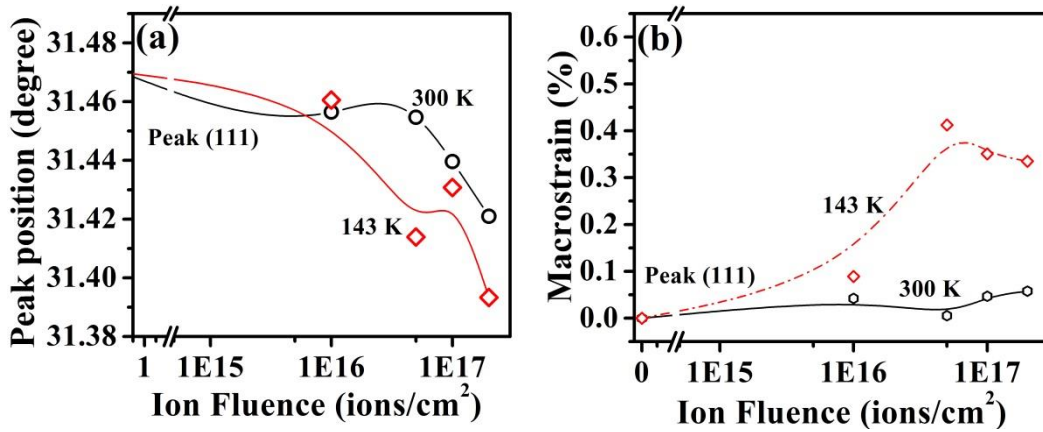


Figure 3.4 (a) Variation of peak position (plane 111) as a function of He^+ ion fluence for ion irradiation temperatures 300 K and 143 K (b) Variation of macrostrain as a function of the He^+ ion fluence for He^+ ion irradiated zirconia samples (300 K and 143 K).

It is observed that the peak positions are shifted towards lower 2θ values irrespective of the irradiation temperature, indicating the presence of tensile strain and increase in the lattice parameter upon He^+ ion irradiation. Figure 3.4(b) shows the variation of macrostrain as a function of He^+ ion fluence. It is observed that the macrostrain increases with the ion fluence for both the ion irradiation temperatures (300 K and 143 K). It is observed from Figure 3.4(b) that for a given He^+ ion fluence, strain

induced in zirconia samples irradiated at 143 K is higher than the samples irradiated at 300 K.

Figure 3.5 shows the GIXRD patterns of the as-sintered zirconia and 120keV Ar⁺ ion irradiated zirconia samples. Figure 3.5(b-d) show the GIXRD patterns of zirconia samples irradiated at room temperature for the ion fluences of 1×10^{15} , 5×10^{16} , and 1×10^{17} ions/cm² respectively.

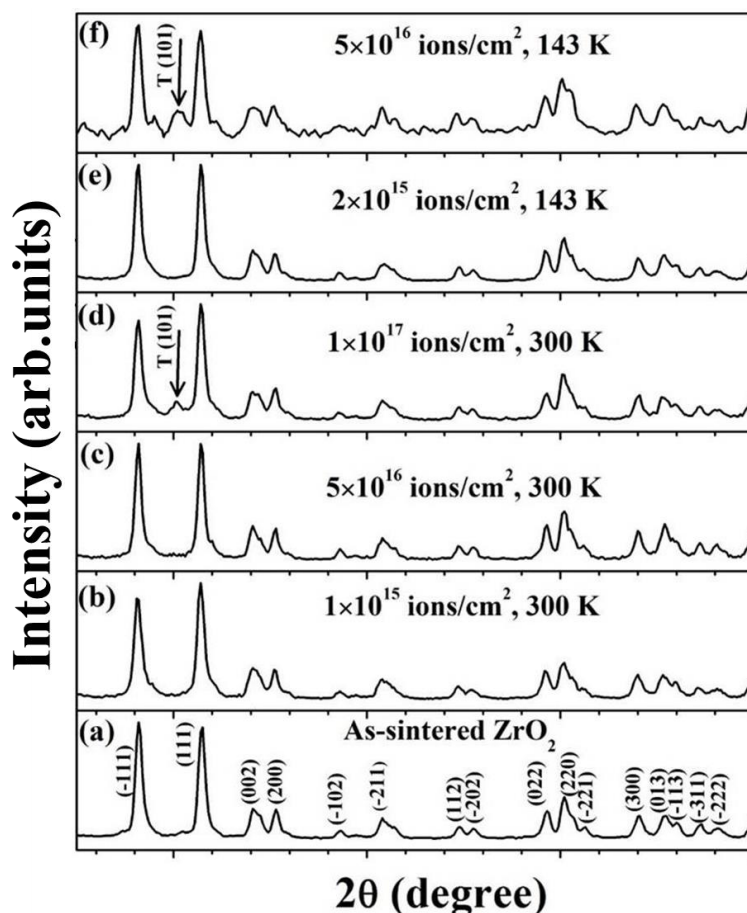


Figure 3.5 GIXRD pattern of the as-sintered and 120 keV Ar⁺ ion irradiated zirconia samples for the ion irradiation temperatures 300 K and 143 K. The tetragonal peak corresponding to the plane (101) is marked.

From Figure 3.5(b) and Figure 3.5(c), it is observed that all the diffraction peaks corresponding to monoclinic zirconia remain the same. It is observed from Figure 3.5(d), that in addition to all the monoclinic peaks, additional peak around the 2θ value 30.2° has appeared. This peak corresponds to the tetragonal plane (101) (ICDD card No. 01-079-1764) of zirconia. Figure 3.5(e) and Figure 3.5(f) show GIXRD patterns of the zirconia samples ion irradiated with Ar⁺ ions at 143 K for the ion fluences 2×10^{15} and 5×10^{16} ions/cm² respectively. From Figure 3.5(e), it is observed that the all the diffraction peaks corresponding to the as-sintered zirconia samples (monoclinic structure) remains the same.

From Figure 3.5(f), it is observed that all the diffraction peaks corresponding to the as-sintered zirconia samples remains the same, except for the emergence of a small peak around the 2θ value 30.2° . This peak is indexed to the plane (101) corresponding to the tetragonal phase of zirconia. The new tetragonal peak is marked with an arrow for visibility. It is also noticed that the tetragonal phase is present in the zirconia samples irradiated for the low ion fluence of 5×10^{16} ions/cm² itself, when the ion irradiation was carried out at 143 K. Apart from the observation of tetragonal structure, upon ion irradiation (at 300 K and 143 K), the diffraction peaks have broadened and shifted towards lower 2θ values irrespective of the irradiation temperature indicating the presence of tensile strain and increase in the lattice parameter upon Ar⁺ ion irradiation. This indicates that strain is induced in the zirconia samples as a result of Ar⁺ ion irradiation.

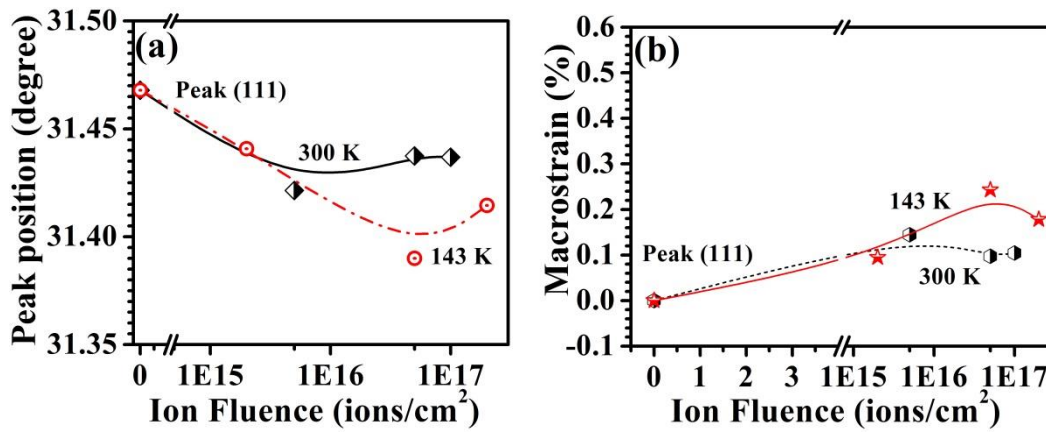


Figure 3.6 (a) Variation of peak position (plane 111) as a function of Ar⁺ ion fluence for ion irradiation temperatures of 300 K and 143 K (b) Variation of macrostrain induced in the zirconia samples upon ion irradiation (300 K and 143 K) as a function of Ar⁺ ion fluence.

Figure 3.6(a) shows the variation of peak position of the plane (111) as a function of ion fluence for both the irradiation temperatures (300 K and 143 K). It is observed that the peak positions were found to decrease with ion fluence upto the ion fluence of 5×10^{16} ions/cm² and for the highest ion fluence (1×10^{17} ions/cm²), the macrostrain increases. Figure 3.6(b) shows the variation of macrostrain as a function of ion fluence (300 K and 143 K).

By comparing the strain (Figure 3.6(b)) in the samples irradiated at 300 K and 143 K, one can easily notice that in the case of ion irradiation at 143 K, the magnitude of the strain is higher than the zirconia samples irradiated at 300 K, for the same ion fluence (5×10^{16} ions/cm²). At the highest ion fluence (1×10^{17} ions/cm²) for both the ion irradiation temperatures (300 K and 143 K), the strain decreases to a lesser extent compared to the ion

fluence 5×10^{16} ions/cm². The reduction of strain is more pronounced for the zirconia samples irradiated at 143 K. This reduction in the strain shows that the accumulated strain relieves itself at the highest ion fluence.

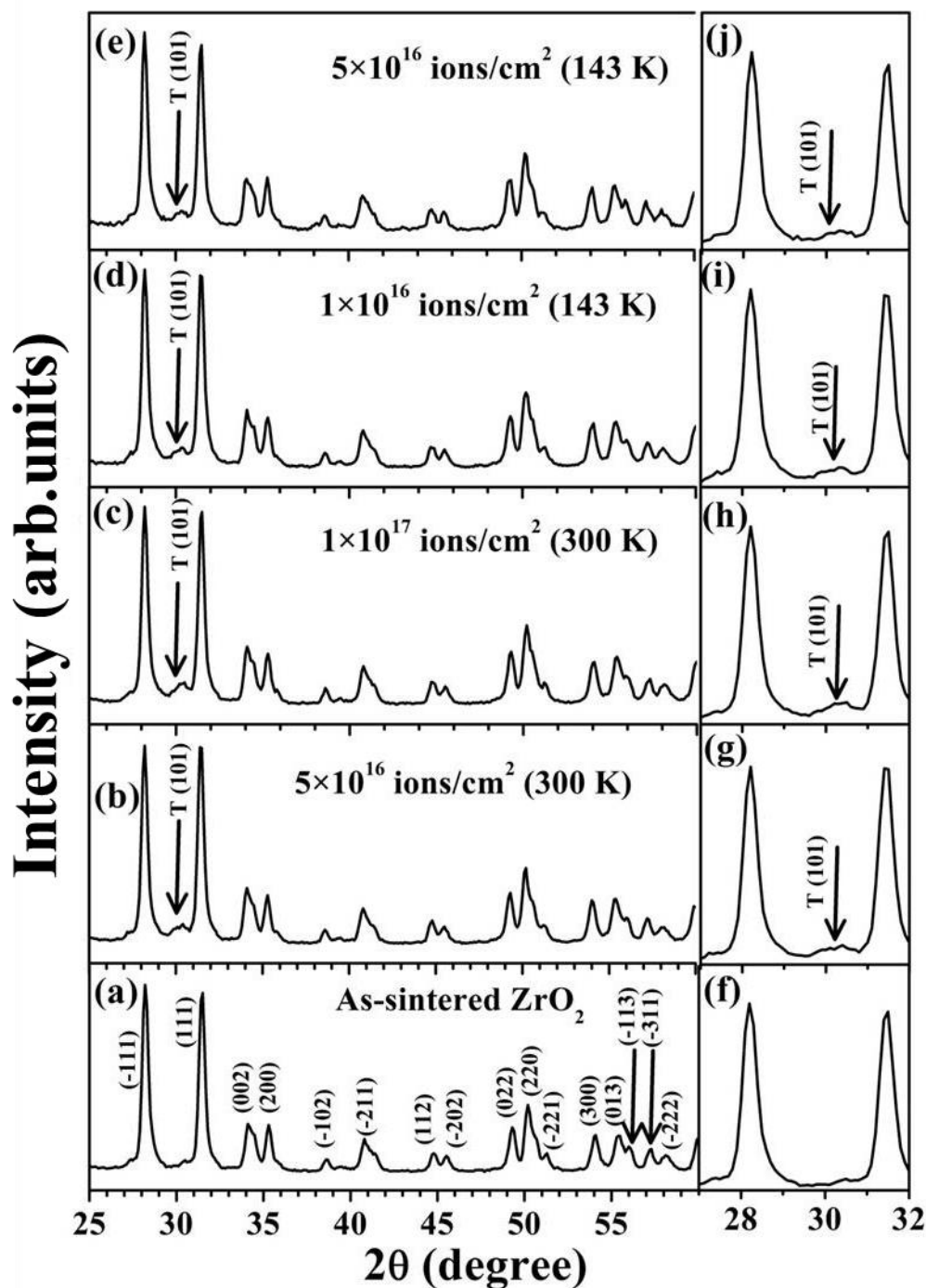


Figure 3.7 (a-e) GIXRD pattern of the as-sintered and 60 keV Kr⁺ ion irradiated (at 300 K and 143 K) zirconia samples. The tetragonal peak corresponding to the plane (101) is marked with an arrow

Figure 3.7 shows the GIXRD pattern of the as-sintered and 60 keV Kr⁺ ion irradiated zirconia samples. Figure 3.7(b) and Figure 3.7(c) shows the GIXRD pattern of

the Kr^+ ion irradiated zirconia samples at 300 K for the ion fluences of 5×10^{16} ions/cm² and 1×10^{17} ions/cm² respectively. Figure 3.7(d) and Figure 3.7(e) show the GIXRD patterns of the Kr^+ ion irradiated zirconia samples at 143 K for the ion fluences of 1×10^{16} ions/cm² and 5×10^{16} ions/cm² respectively. Figure 3.7(f-j) shows the expanded view of their corresponding GIXRD pattern in the 2θ range 27° to 32° . It is observed from Figure 3.7(b-e) that, in addition to all the monoclinic peaks, additional peak around the 2θ value of 30.2° has emerged upon Kr^+ ion irradiation. This peak corresponds to the plane (101) of the tetragonal phase (ICDD No. 01-079-1764) of zirconia. It is also observed that the tetragonal phase is present in the zirconia samples irradiated for the lowest ion fluence itself irrespective of the ion irradiation temperatures. It is also observed that, after ion irradiation (at 300 K and 143 K), the diffraction peaks have broadened and shifted with respect to the as-sintered zirconia samples. This indicates that strain is induced in the zirconia samples as a result of Kr^+ ion irradiation.

Figure 3.8(a) shows the variation of peak position of the plane (111) as a function of ion fluence for both the irradiation temperatures (300 K and 143 K). It is observed that the peak position is shifted towards lower 2θ values (till the ion fluence of 5×10^{16} ions/cm²) irrespective of the irradiation temperature indicating the presence of tensile strain and increase in lattice parameter upon Kr^+ ion irradiation.

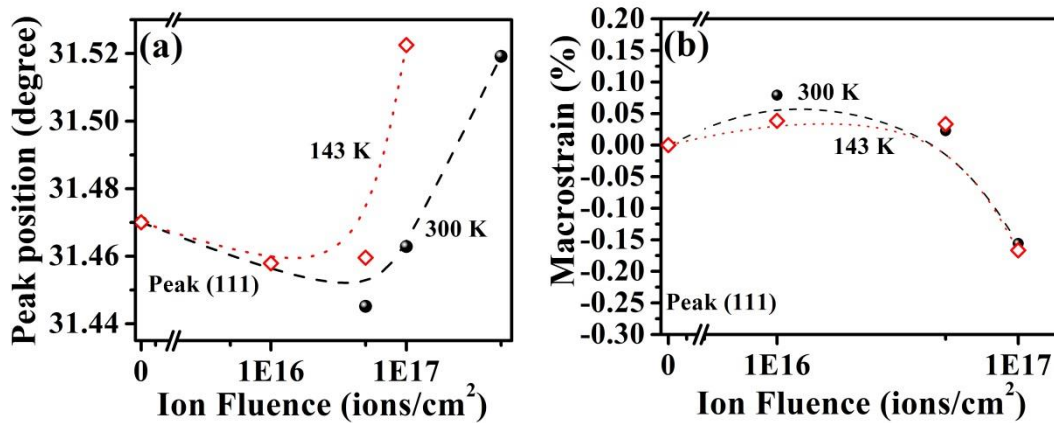


Figure 3.8 (a) Variation of peak position (plane 111) as a function of Kr^+ ion fluence for both the ion irradiation temperatures 300 K and 143 K (b) Variation of macrostrain induced in the zirconia samples as a function of the Kr^+ ion fluence.

However, beyond the ion fluence of 5×10^{16} ions/cm², the peak position increases with respect to the as-sintered and the ion irradiated samples. This indicates that at higher ion fluences, compressive strain is introduced in the zirconia samples. Figure 3.8(b) shows the variation of macrostrain as a function of ion fluence. By comparing the strain (Figure

3.8(b) induced in the zirconia samples irradiated at 300 K and 143 K, it is observed that the strain increases till the ion fluence of 5×10^{16} ions/cm² and then decreases after the Kr⁺ ion fluence 5×10^{16} ions/cm² irrespective of the ion irradiation temperatures.

3.4.2. Electron diffraction analysis

In order to obtain further insight into the phase transformation in monoclinic zirconia under ion irradiation, electron diffraction measurements were carried out. Figure 3.9(a) shows the low magnification bright field TEM image of the as-sintered zirconia sample.

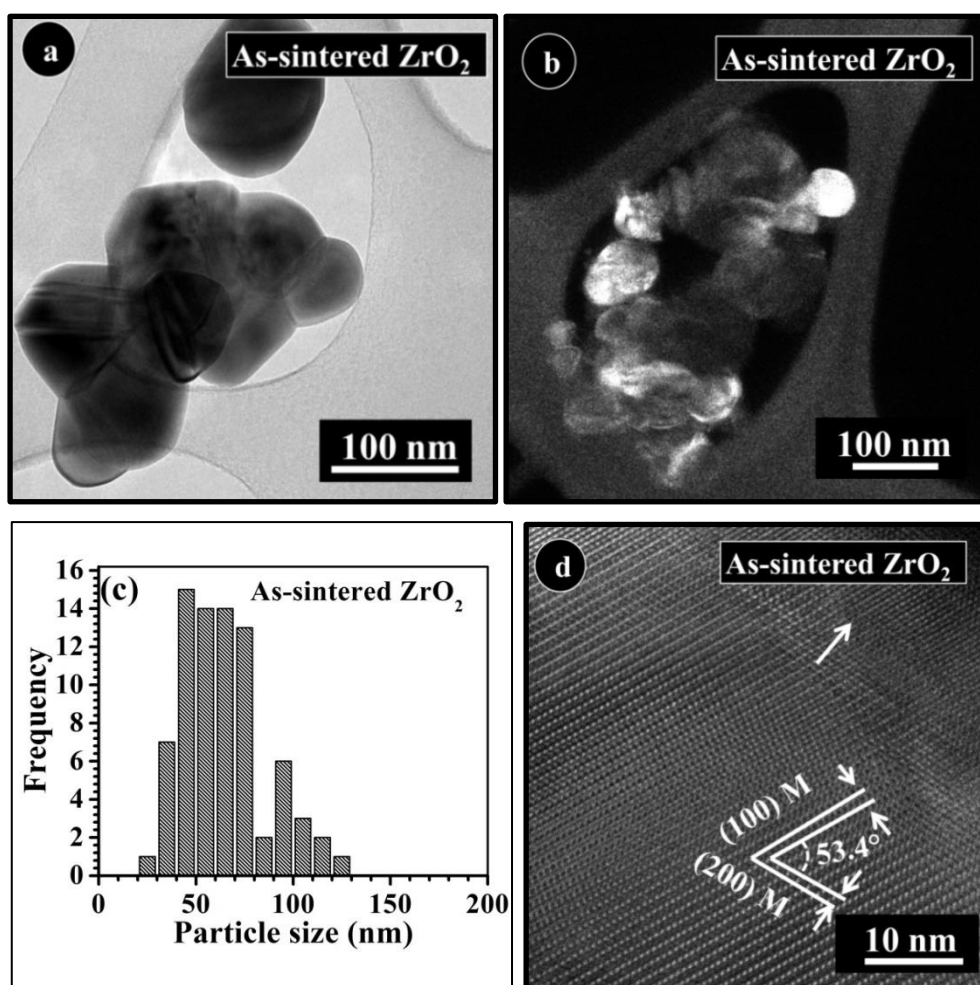


Figure 3.9 (a) Low magnification bright field TEM image, (b) dark field TEM image, (c) particle size distribution of the as-sintered zirconia sample and (d) HRTEM image of the as-sintered zirconia. In the HRTEM image, the planes (200) and (100) corresponds to the monoclinic structure of zirconia and the angle between them 53.4° are clearly marked.

Figure 3.9(b) shows the dark field TEM image of the as-sintered zirconia sample. The size of the particles was measured from many dark field TEM images using ImageJ (image analysis software)[131] and the particle size distribution is plotted (Figure 3.9 (c)). The average size of zirconia particles (as-sintered) is $\cong 59$ nm.

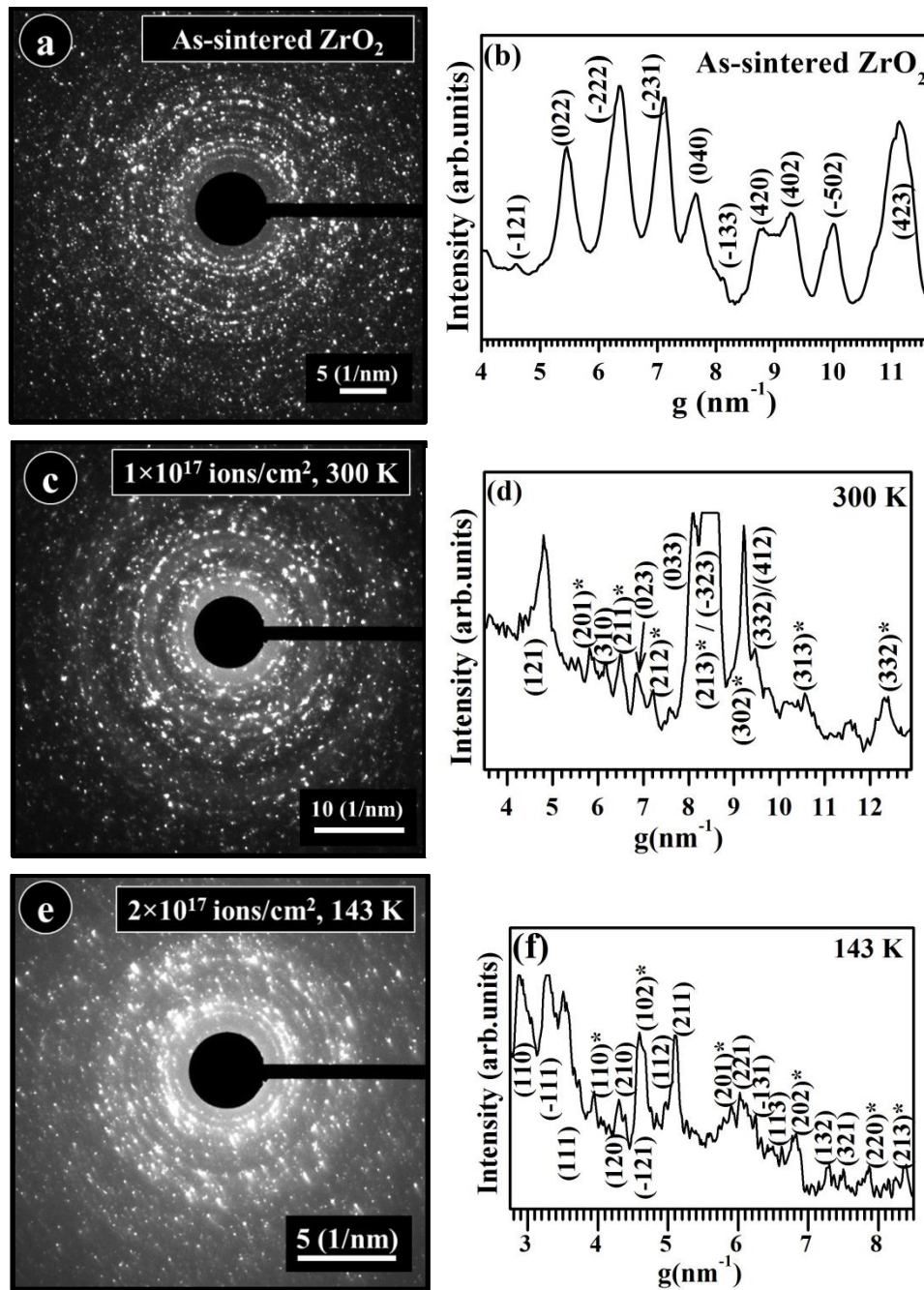


Figure 3.10 Selected area electron diffraction pattern and corresponding radial intensity profile of the (a),(b) as-sintered, (c),(d) 120 keV He^+ ion irradiated (ion fluence $1 \times 10^{17} \text{ ion/cm}^2$, 300 K) and (e),(f) 120 keV He^+ ion irradiated (ion fluence $2 \times 10^{17} \text{ ion/cm}^2$, 143 K) zirconia samples respectively. The new peaks (marked with “*”) are corresponding to the tetragonal phase and other peaks are from the monoclinic phase.

Figure 3.9(d) shows the HRTEM image of the as-sintered zirconia and the planes (100) and (200) are indexed to monoclinic structure (ICDD card no 01-070-2491) of zirconia. Angle between the monoclinic planes (100) and (200) was measured and the value is 53.4° (shown in Figure 3.9(d)), which is consistent with monoclinic structure.

Figure 3.10(a) shows the selected area electron diffraction pattern (SAED) of the as-sintered zirconia sample. Figure 3.10(b) shows the corresponding radial intensity profile obtained from the SAED pattern of as-sintered zirconia. The planes (-121), (022), (-222), (-231), (040), (-133), (420), (402), (-502) and (423) corresponds to monoclinic phase (ICDD card no 01-070-2491) of zirconia. Figure 3.10(c) shows the SAED pattern of the zirconia sample irradiated with He^+ ions (ion fluence $1 \times 10^{17} \text{ ion/cm}^2$) at 300 K. Figure 3.10(d) shows the corresponding radial intensity profile of the zirconia sample ion irradiated at 300 K. It is observed that new peaks (marked with “*”) are present along with the monoclinic peaks. The planes corresponding to the new peaks are (201), (211), (212), (213), (302), (313) and (333) of tetragonal structure (ICDD card no 00-050-1089) of zirconia.

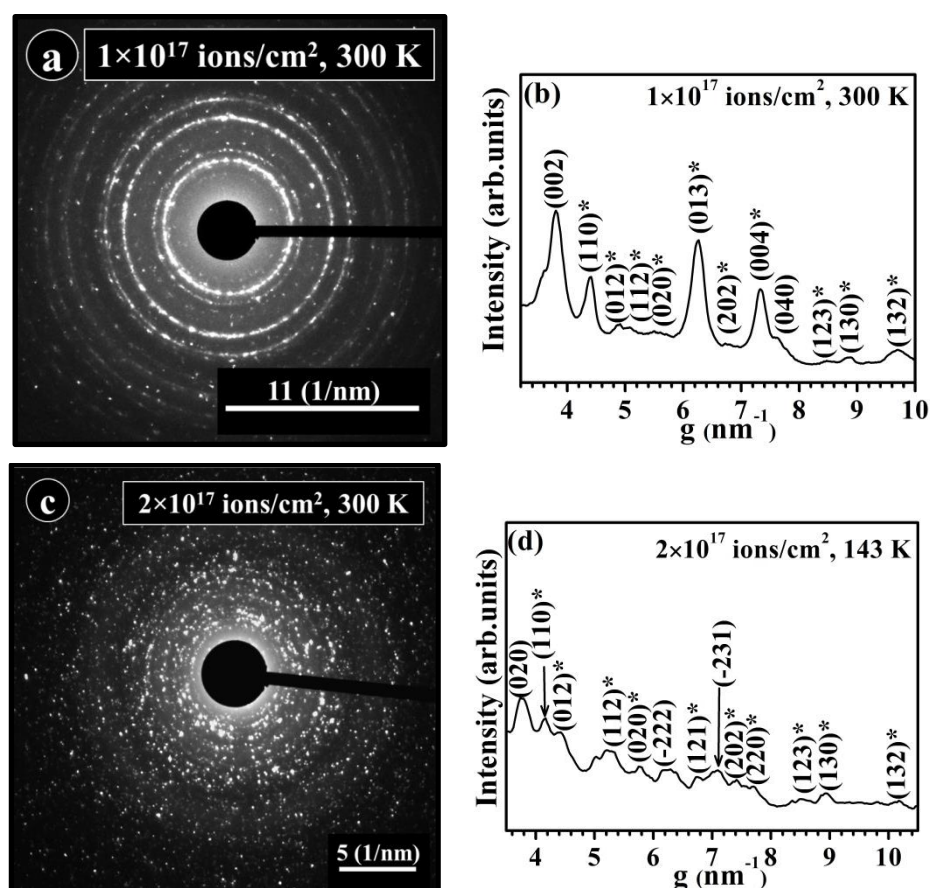


Figure 3.11 Selected area electron diffraction pattern and corresponding radial intensity profile of the (a),(b) 120 keV Ar^+ ion irradiated (ion fluence $1 \times 10^{17} \text{ ion/cm}^2$, 300 K) and (c),(d) 120 keV Ar^+ ion irradiated (ion fluence $2 \times 10^{17} \text{ ion/cm}^2$, 143 K) zirconia samples respectively. The new peaks (marked with “*”) are corresponding to the tetragonal phase and other peaks are from the monoclinic phase.

Figure 3.10(e) shows the SAED pattern of the zirconia samples irradiated with He^+ ions (ion fluence $2 \times 10^{17} \text{ ion/cm}^2$) at 143 K. Figure 3.10(f) shows the corresponding radial

intensity profile of the zirconia sample ion irradiated at 143 K. It is observed that new peaks (marked with “*”) are present in addition to the monoclinic peaks upon He^+ ion irradiation. These new peaks correspond to the planes (110), (102), (201), (202), (220) and (213) of tetragonal structure (ICDD card no 00-050-1089) of zirconia.

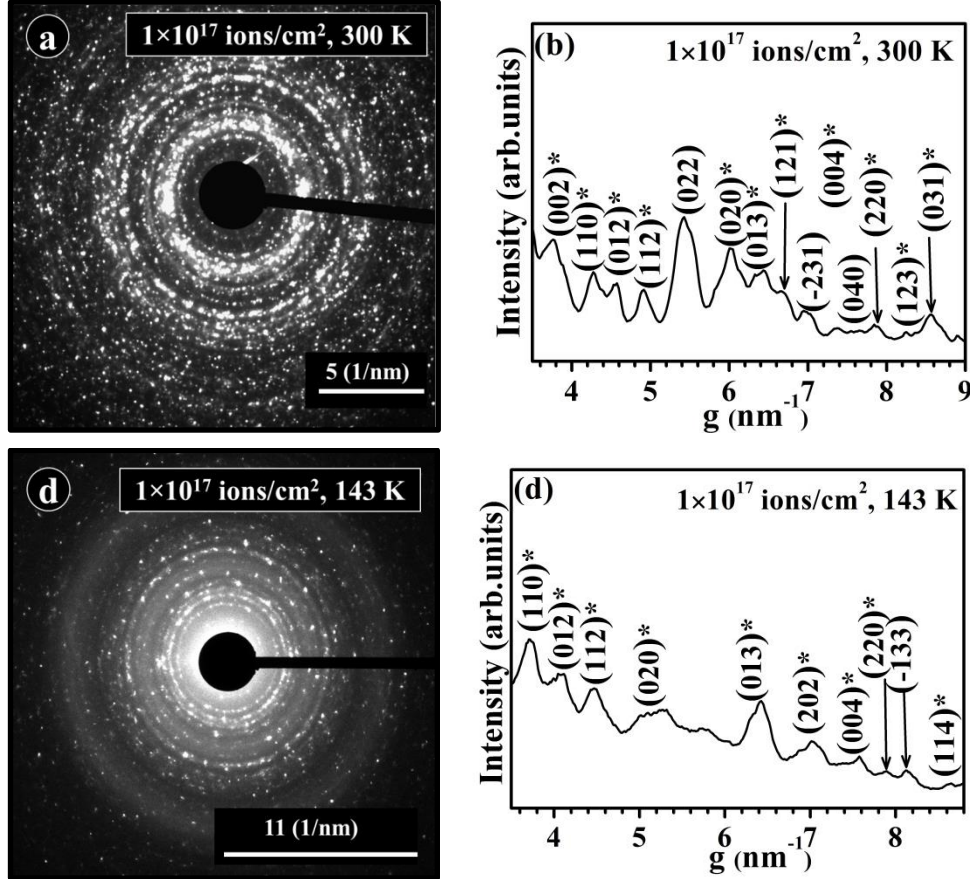


Figure 3.12 Selected area electron diffraction pattern and corresponding radial intensity profile of the (a),(b) 60 keV Kr^+ ion irradiated (ion fluence $1 \times 10^{17} \text{ ion/cm}^2$, 300 K) and (c),(d) 60 keV Kr^+ ion irradiated (ion fluence $1 \times 10^{17} \text{ ion/cm}^2$, 143 K) zirconia samples respectively. The new peaks (marked with “*”) are corresponding to the tetragonal phase and other peaks are from the monoclinic phase.

Figure 3.11(a) shows the SAED pattern of the zirconia samples irradiated with Ar^+ (ion fluence $1 \times 10^{17} \text{ ion/cm}^2$) ions at 300 K. Figure 3.11(b) shows the corresponding radial intensity profile of the Ar^+ ion irradiated (300 K) zirconia sample. It is observed that new peaks (marked with “*”) are present along with the monoclinic peaks. The planes corresponding to the new peaks are (110), (012), (112), (020), (013), (202), (004), (123), (130) and (132) and the planes are corresponding to the tetragonal structure (ICDD card no 00-050-1089) of zirconia. Figure 3.11(c) shows the SAED pattern of the zirconia samples irradiated with Ar^+ (ion fluence $2 \times 10^{17} \text{ ion/cm}^2$) ions at 143 K. Figure 3.11(d) shows the corresponding radial intensity profile of the Ar^+ ion irradiated (143 K) zirconia

sample. It is observed that new peaks (marked with “*”) are present along with the monoclinic peaks. The planes corresponding to the new peaks are (110), (012), (112), (020), (121), (202), (220), (123), (130) and (132) of the tetragonal structure (ICDD card no 00-050-1089) of zirconia.

Figure 3.12(a) shows the SAED pattern of the zirconia samples irradiated with 60 keV Kr^+ (ion fluence 1×10^{17} ion/cm²) ions at 300 K. Figure 3.12(b) shows the corresponding radial intensity profile of the Kr^+ ion irradiated (300 K) zirconia sample. It is observed that new peaks (marked with “*”) are present along with the monoclinic peaks. The planes corresponding to the new peaks are (002), (110), (012), (112), (020), (013), (121), (004), (220), (123) and (031) of the tetragonal structure (ICDD card no 00-050-1089) of zirconia. Figure 3.12(c) shows the SAED pattern of the zirconia samples ion irradiated with Kr^+ (ion fluence 1×10^{17} ion/cm²) ions at 143 K. Figure 3.12(d) shows the corresponding radial intensity profile of the Kr^+ (143 K) ion irradiated zirconia sample. It is observed that new peaks (marked with “*”) are present along with the monoclinic peaks. The planes corresponding to the new peaks are (110), (012), (112), (020), (013) and (202), (004), (220) and (114) of tetragonal structure (ICDD card no 00-050-1089) of zirconia.

3.4.3. Raman scattering analysis

Raman scattering was employed to probe the local structural changes in the zirconia samples upon ion irradiation. Space group symmetry of the monoclinic and tetragonal zirconia are ($P_{21}/C, C_{2h}^5$) and ($P4_2/nmc, D_{4h}^{15}$) respectively. Group theory investigations [132] have predicted that there are 36 lattice vibrational modes ($9A_g + 9A_u + 9B_g + 9B_u$) for monoclinic zirconia, in which 18 modes ($9A_g$ and $9B_g$) are Raman active modes [133–138]. Earlier Raman scattering observations and calculations suggested that there are 9 phonon modes for tetragonal zirconia [135–137] out of which, six modes ($A_{1g} + 2B_{1g} + 3E_g$) are Raman active modes and three modes ($A_{2u} + 2E_u$) are IR active [135].

Figure 3.13(a) shows the Raman spectra of the as-sintered zirconia and He^+ ion irradiated zirconia (300 K). From Figure 3.13(a), it is observed that as-sintered zirconia sample shows fourteen Raman active modes corresponding to the monoclinic zirconia. The Raman modes are identified at 104 cm⁻¹ (A_g), 185 cm⁻¹ ($A_g + B_g$), 196 cm⁻¹ (A_g), 229 cm⁻¹ (B_g), 310 cm⁻¹ (A_g), 339 cm⁻¹ (B_g), 353 cm⁻¹ (A_g), 387 cm⁻¹ (B_g), 481 cm⁻¹ (A_g), 510 cm⁻¹ (B_g), 542 cm⁻¹ (A_g), 566 cm⁻¹ (B_g), 621 cm⁻¹ (B_g) and 644 cm⁻¹ (A_g). The modes corresponding to Zr-O bonds are 310 cm⁻¹ (A_g) and 353 cm⁻¹ (A_g). The modes corresponding to lattice vibration of O-O bonds are 104 cm⁻¹ (A_g), 387 cm⁻¹ (B_g), 481 cm⁻¹

$^1(A_g)$, $510\text{ cm}^{-1}(B_g)$, $542\text{ cm}^{-1}(A_g)$, $566\text{ cm}^{-1}(B_g)$, $621\text{ cm}^{-1}(B_g)$, $644\text{ cm}^{-1}(A_g)$ and for Zr-Zr bonds are $185\text{ cm}^{-1}(A_g+B_g)$, $196\text{ cm}^{-1}(A_g)$, $229\text{ cm}^{-1}(B_g)$ and $339\text{ cm}^{-1}(B_g)$. It is observed that all the Raman modes of the as-sintered zirconia (corresponding to monoclinic structure) are also present in the ion irradiated zirconia samples (300 K). The electron diffraction (Figure 3.10) observation on He^+ ion irradiated zirconia sample shows the

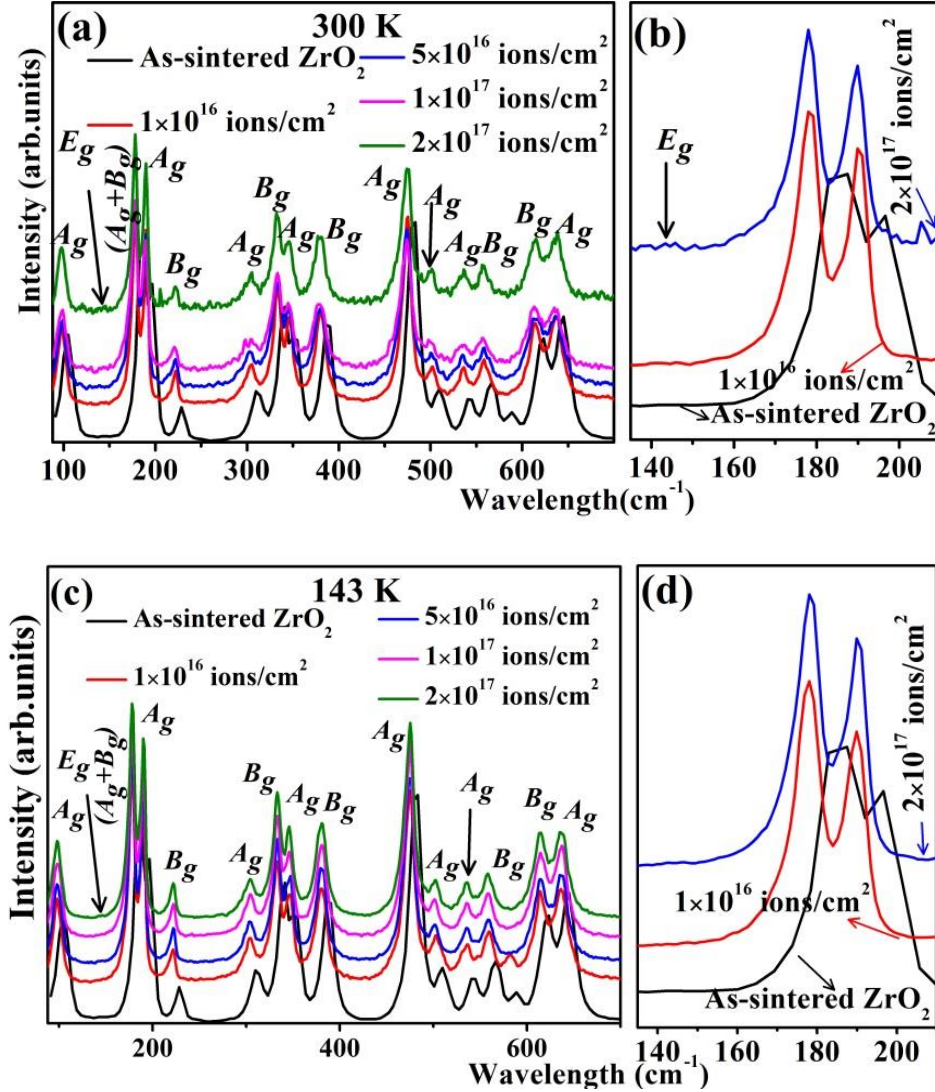


Figure 3.13 Raman spectra of the as-sintered and the 120 keV He^+ ion irradiated zirconia at (a) 300 K and (c) 143 K. (b), (d) shows the expanded view of (a) and (c) respectively.

presence of tetragonal phase. In Raman scattering, the Raman mode around 144 cm^{-1} is expected for the tetragonal phase (E_g mode)[135–137] as marked in Figure 3.13. Even though, the change in the background as a function of ion fluence was seen around 144 cm^{-1} , but clear signature for tetragonal phase is not seen. Figure 3.13(c) shows the Raman spectra of the as-sintered and the zirconia samples ion irradiated at 143 K with He^+ ions. Even in the case of ion irradiation at 143 K, all the Raman modes of the as-sintered

zirconia (corresponding to monoclinic structure) are present. GIXRD (Figure 3.3) and electron diffraction observations (Figure 3.11) on He^+ ion irradiated zirconia sample show the presence of tetragonal phase. Even though, the change in the background as a function of ion fluence was seen around 144 cm^{-1} , clear signature for tetragonal phase is not seen. Figure 3.13(b) and Figure 3.13(d) show the Raman spectra in the region $130\text{--}210\text{ cm}^{-1}$, for the He^+ ion irradiated samples. Even though the Raman modes corresponding to the tetragonal phase is not seen clearly, the shift in the Raman modes corresponding to monoclinic peaks towards lower wavenumber is seen.

Figure 3.14(a) and Figure 3.14(b) show the variation of the peak positions of the Raman modes in the zirconia samples upon He^+ ion irradiation at 300 K and 143 K respectively. It is seen that the Raman peaks shift towards the lower wavenumber with increase in ion fluence. This shift is attributed to various types of strain leading to the decrease in Zr-O bond length caused by the oxygen vacancies[126]. This observed red shift in the Raman modes indicates that the zirconia lattice become strained lattice. This lattice strain could be the reason for monoclinic to tetragonal phase transformation.

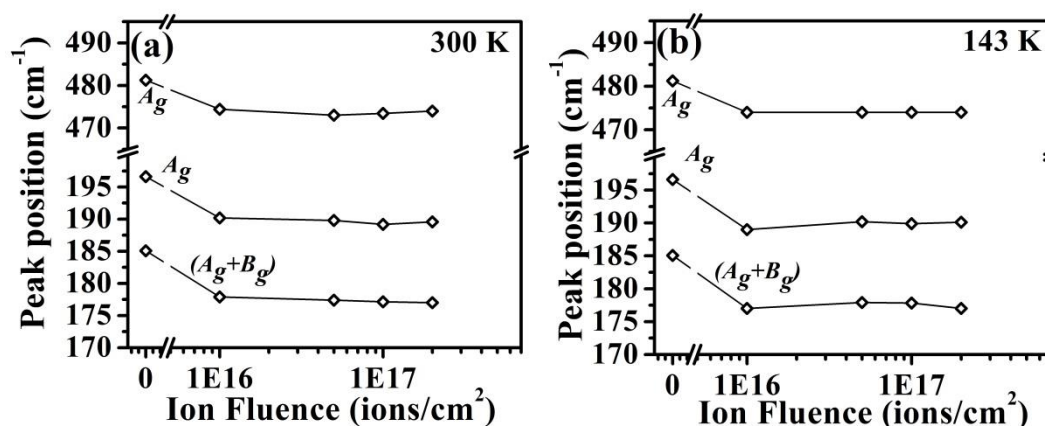


Figure 3.14 Variation of the peak positions of the Raman modes as a function of He^+ ion fluences for the ion irradiation temperature at (a) 300 K and (b) 143 K.

Figure 3.15(a) shows the Raman spectra of the as-sintered zirconia and Ar^+ ion irradiated zirconia (300 K). It is observed that upon Ar^+ ion irradiation, in addition to the Raman modes corresponding to the monoclinic structure, there is a presence of new peak at 144 cm^{-1} . This Raman mode around 144 cm^{-1} corresponds to the E_g mode of tetragonal zirconia[135–137].

The new peak evolves from the lowest ion fluence ($1 \times 10^{16}\text{ ions/cm}^2$) onwards. Figure 3.15(c) shows the Raman spectra of the as-sintered zirconia and the zirconia samples irradiated with Ar^+ ions at 143 K. Upon ion irradiation, in addition to the

monoclinic Raman peaks, the new peak at 144 cm^{-1} emerges even at the lowest ion fluence of $2 \times 10^{15}\text{ ions/cm}^2$ itself. This mode 144 cm^{-1} corresponds to the E_g mode of tetragonal zirconia. In order to have a better understanding of the Raman modes in the range around the new peak 144 cm^{-1} , the expanded view of the Raman spectra is plotted and shown in Figure 3.15(b) and Figure 3.15(d).

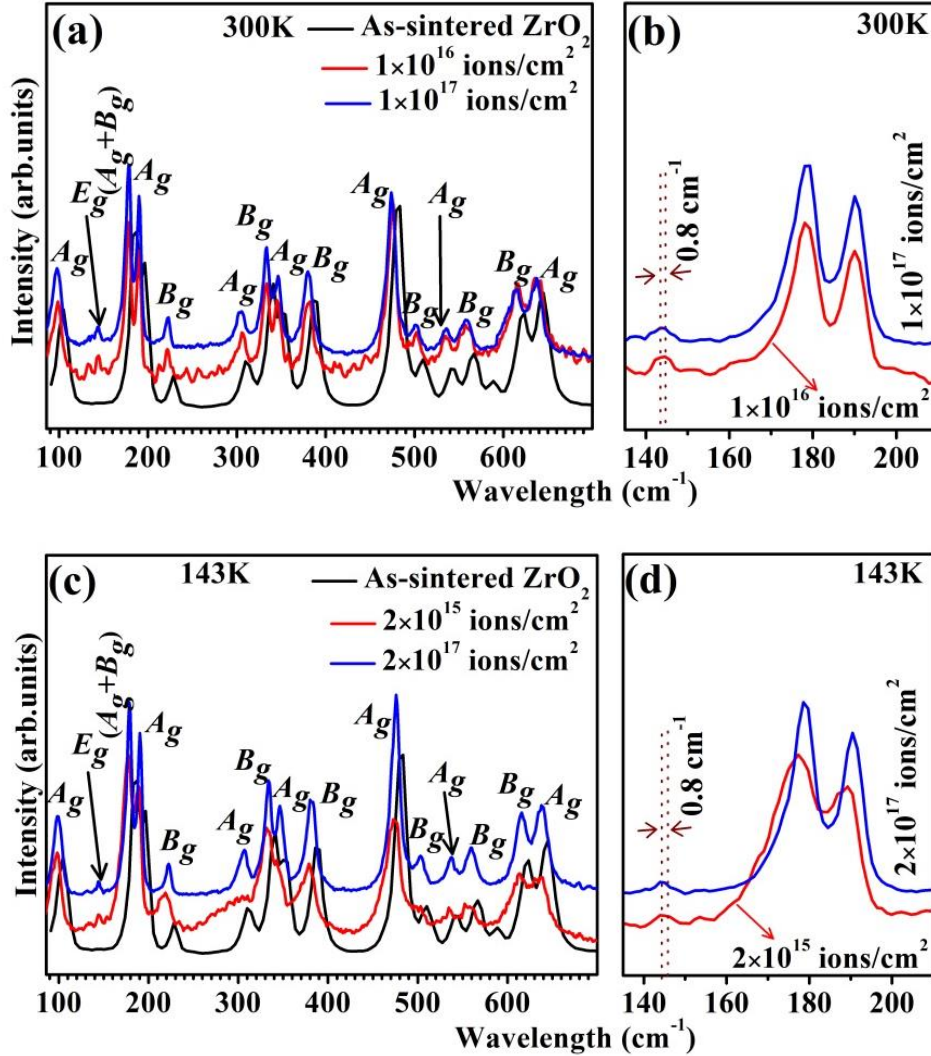


Figure 3.15 Raman spectra of the as-sintered and the 120 keV Ar^+ ion irradiated zirconia at (a) 300 K and (c) 143 K. The appearance of the mode (E_g) at 144 cm^{-1} confirms the formation of tetragonal phase upon ion irradiation. (b), (d) shows the expanded view of (a) and (c) respectively and it clearly shows the shift in the E_g mode (144 cm^{-1})

Figure 3.15(b) shows the expanded view of the Raman spectra (range 135 to 210 cm^{-1}) plotted for the zirconia samples irradiated with Ar^+ ions at 300 K. It is observed that the E_g mode has stiffened by 0.8 cm^{-1} . Figure 3.15(d) shows the expanded view of the Raman spectra (in the range 135 to 210 cm^{-1}) obtained from the zirconia samples

irradiated with Ar^+ ions at 143 K. It is observed that the E_g mode shifted towards lower wave number about 0.8 cm^{-1} .

Figure 3.16(a) and Figure 3.16(b) shows the variation of peak position of the Raman modes with ion fluence for the ion irradiation temperature at 300 K and 143 K respectively. It is observed that in the Ar^+ ion irradiated zirconia samples (300 K and 143 K), the Raman modes shifts towards lower wavenumber with increase in ion fluence. This indicates that upon ion irradiation (300 K and 143 K), the strain is introduced in the lattice of zirconia.

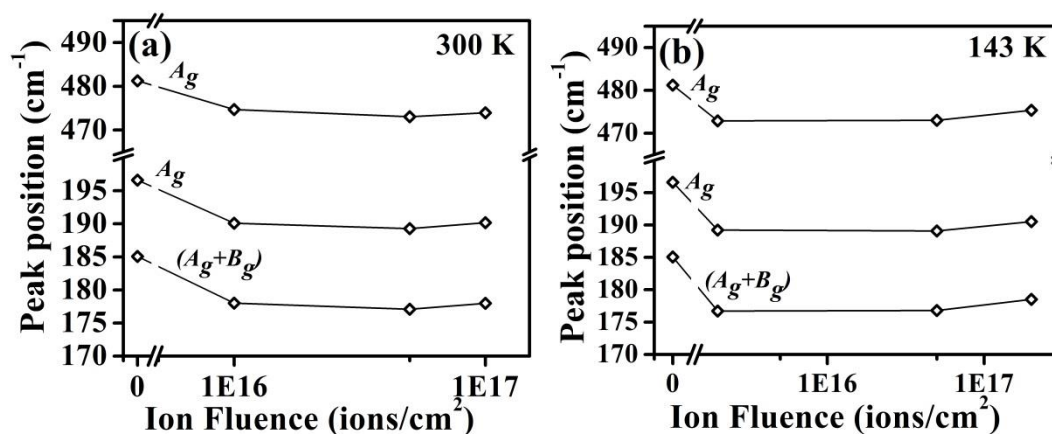


Figure 3.16 Variation of peak position of the Raman modes as a function of Ar^+ ion fluence for the irradiation temperature at (a) 300 K and (b) 143 K.

Figure 3.17(a) shows the Raman spectra of the as-sintered zirconia and Kr^+ ion irradiated zirconia (300 K). Fourteen Raman modes corresponding to monoclinic zirconia are present in the as-sintered zirconia sample. Upon Kr^+ ion irradiation a new peak at 144 cm^{-1} is observed, in addition to the fourteen monoclinic Raman modes. This Raman mode around 144 cm^{-1} corresponds to the E_g mode of tetragonal zirconia[135–137]. Figure 3.17(c) shows the Raman spectra of the as-sintered zirconia and the zirconia samples ion irradiated with Kr^+ ions at 143 K. In this also the additional peak corresponding to the E_g mode (144 cm^{-1}) tetragonal zirconia is observed at the lowest ion fluence of $1 \times 10^{16} \text{ ions/cm}^2$.

Figure 3.17(b) shows the expanded view of Raman modes of the Kr^+ ion irradiated zirconia at 300 K in the range $135\text{--}210 \text{ cm}^{-1}$ for better clarity. The Raman mode at 144 cm^{-1} (corresponding to tetragonal structure) for the highest ion fluence $5 \times 10^{17} \text{ ions/cm}^2$ exhibits a stiffening of about 0.8 cm^{-1} with respect to the lowest ion fluence $1 \times 10^{16} \text{ ions/cm}^2$. Figure 3.17(d) shows the expanded view of the Raman spectra in the range 135 to 210 cm^{-1} obtained from the zirconia samples irradiated with Kr^+ ions at 143 K. In the

ion irradiated zirconia samples (at 143 K), the E_g mode corresponding to tetragonal zirconia exhibits a stiffening of about 3.5 cm^{-1} for the highest ion fluence $5 \times 10^{17} \text{ ions/cm}^2$ with respect to the lowest ion fluence $1 \times 10^{16} \text{ ions/cm}^2$, indicating that large strain is induced in the zirconia samples. This shift is attributed to various types of strain leading to the decrease in Zr-O bond length caused by the oxygen vacancies[126]. From Figure 3.17(a) and Figure 3.17(c) it is also observed that the Raman modes are shifted with respect to the as-sintered zirconia.

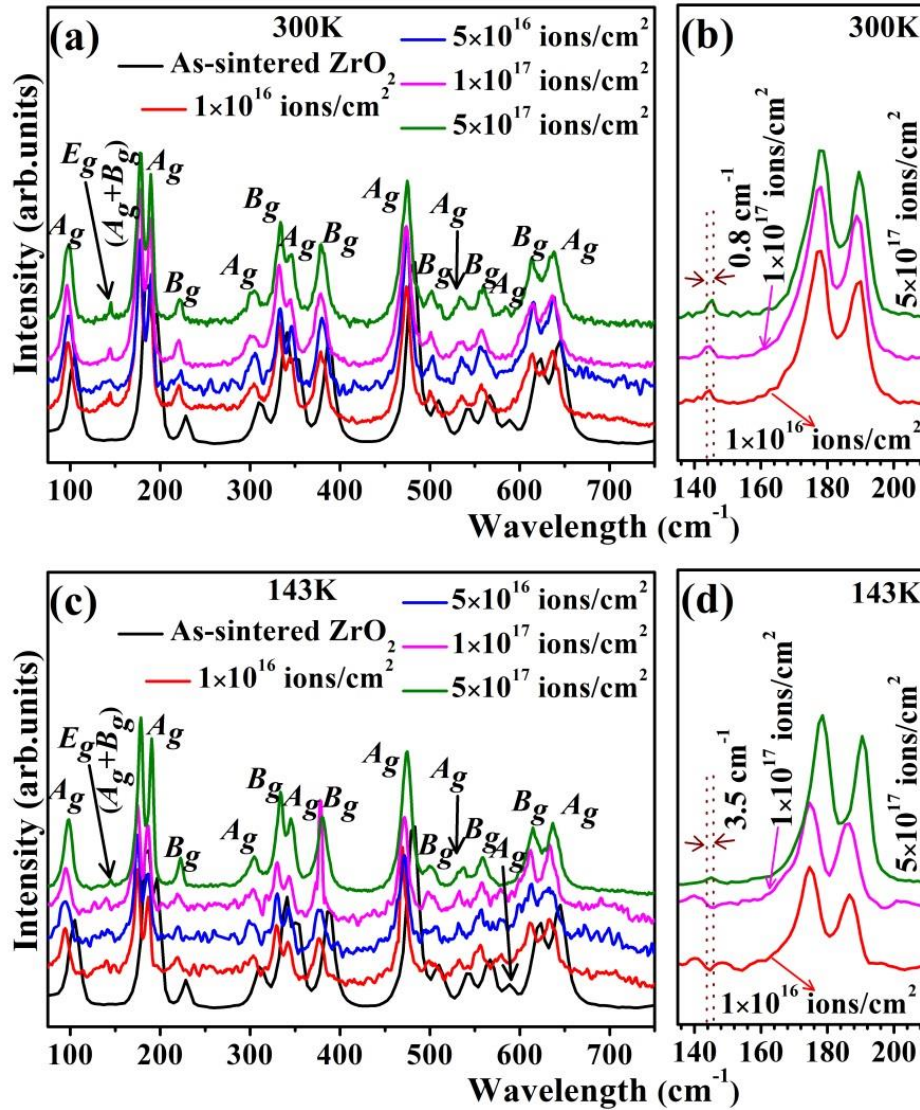


Figure 3.17 Raman spectra of the as-sintered and the 60 keV Kr^+ ion irradiated zirconia at (a) 300 K and (c) 143 K. The appearance of the mode (E_g) at 144 cm^{-1} confirms the formation of tetragonal phase upon ion irradiation. (b), (d) shows the expanded view of (a) and (c) respectively and it clearly shows the shift in the E_g mode (144 cm^{-1}).

Figure 3.18(a) and Figure 3.18 (b) shows the variation of peak position of the Raman modes with ion fluence for the ion irradiation temperatures of 300 K and 143 K

respectively. It is observed that in the ion irradiated zirconia samples (300 K and 143 K), the peak position shifts towards lower wavenumber with the increase in ion fluence. This shift in the Raman peak position indicates that upon ion irradiation (300 K and 143 K) strain has been introduced in the lattice of zirconia.

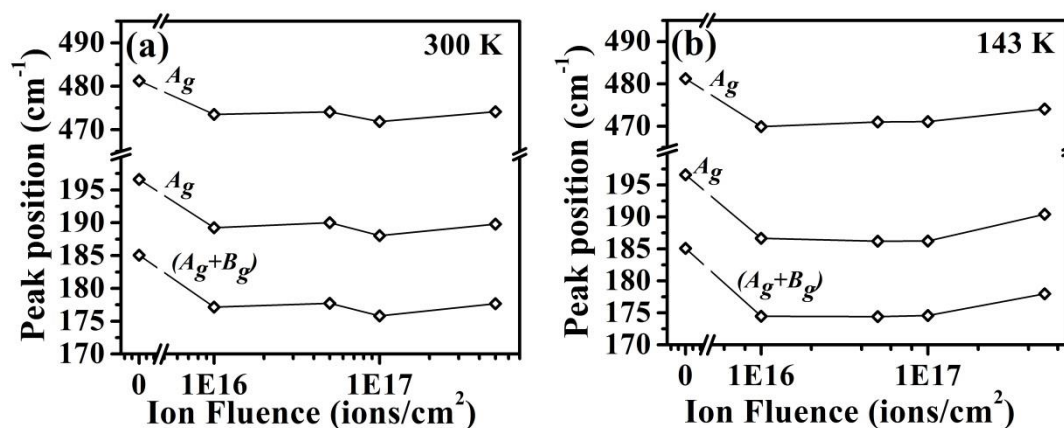


Figure 3.18 Variation of peak position of the Raman modes as a function of Kr^+ ion fluence for the irradiation temperature at (a) 300 K and (b) 143 K.

The fraction of the tetragonal phase ($1 - X_m$) present in the ion irradiated zirconia samples was calculated using the formula[42]

$$X_m = \frac{I_m(185cm^{-1}) + I_m(196cm^{-1})}{I_m(185cm^{-1}) + I_m(196cm^{-1}) + I_t(144cm^{-1})} \quad \text{Eqn.3.2}$$

where X_m is the amount of monoclinic zirconia present in the two phase mixture, I_m is the intensity of the monoclinic peaks, I_t is the intensity of the tetragonal peak. The fraction of tetragonal zirconia present in the two phase mixture is then calculated by the equation $X_t = 1 - X_m$, where X_t and X_m are the amount of tetragonal and monoclinic zirconia present in the two phase mixture. The analysis was carried out using Eqn.3.2 for finding the fraction of tetragonal phase present in the zirconia samples after ion irradiation with He^+ , Ar^+ and Kr^+ ions for various ion fluences. In the case of He^+ ion irradiated zirconia samples, the tetragonal peak at 144 cm^{-1} is not observed even for the highest ion fluence $2 \times 10^{17}\text{ ions/cm}^2$ for both ion irradiation temperatures (as seen from Figure 3.13(b) and Figure 3.13(d)). Hence the fraction of the tetragonal phase in the He^+ ion irradiated zirconia samples was not calculated. The fraction of the tetragonal phase calculated for various ion fluences and ion irradiation temperatures are tabulated in Table 3.2

It is observed that the amount of tetragonal zirconia increases with the increase in the ion fluence. It is also noticed that the phase transformation rate is faster when the ion irradiation was carried out at low temperature. This is indicated by the difference in the

amount of tetragonal zirconia formed at the irradiation temperatures of 300 K (~4.5%) and 143 K (~8.5%), for the ion fluence of 1×10^{17} ions /cm², in the case of Kr⁺ ion irradiation. In case of Ar⁺ ion irradiation, the fraction of the converted phase was 9% (300 K) for the ion fluence 1×10^{17} ions /cm² and 20% (143 K) for the ion fluence 2×10^{17} ions /cm². In case of He⁺ ion irradiated zirconia samples, the Raman modes are not clearly visible, hence the amount of tetragonal phases was not quantified, however, the presence of tetragonal phase is observed from GIXRD and electron diffraction pattern. It is observed that the rate of phase transformation is faster, when the dpa is high and when irradiation was carried out at low temperature.

Table 3.2 Details of ions, ion energy, ion irradiation temperature, ion fluence, damage (in dpa) and the fraction of tetragonal phase formed as a result of ion irradiation (in %)

Temperature	Ions	Energy	Ion Fluence (ions/cm ²)	Fraction of tetragonal phase (%)	Damage (dpa)
300 K	He ⁺	120 keV	1×10^{16}	--	4.8
			2×10^{17}	--	192.0
143 K			1×10^{16}	--	4.8
			2×10^{17}	--	192.0
300 K	Ar ⁺	120 keV	1×10^{16}	9	20.0
			1×10^{17}	9	200.0
143 K			1×10^{16}	10	20.0
			2×10^{17}	20	400.0
300 K	Kr ⁺	60 keV	1×10^{16}	2.5	34.8
			5×10^{16}	3	174.0
			1×10^{17}	4.5	348.0
			1×10^{16}	4.5	34.8
143 K			5×10^{16}	5.5	174.0
			1×10^{17}	8.5	348.0

3.5. Discussion

Monoclinic zirconia was irradiated with 120 keV He⁺, 120 keV Ar⁺ and 60 keV Kr⁺ ions for different irradiation temperatures (300 K and 143 K). Upon ion (He⁺, Ar⁺ and Kr⁺) irradiation, irrespective of the ion irradiation temperature, it is observed that there is a partial transformation from monoclinic to tetragonal phase. The phase transformation is confirmed by GIXRD, Raman scattering and electron diffraction. But the transformation of monoclinic to cubic phase or amorphisation of zirconia upon ion (He⁺, Ar⁺ and Kr⁺) irradiation is not observed. Irrespective of the ion irradiation temperatures, GIXRD and Raman scattering measurements indicates that strain is induced in the zirconia samples upon ion (He⁺, Ar⁺ and Kr⁺) irradiation

With respect to ambient temperature and pressure, zirconia exists in monoclinic phase where surface area and critical size plays the role[19]. Garvie *et al.*, [14] have derived an equation to find the critical size of zirconia to exist in tetragonal phase. Accordingly, the critical size for zirconia to exist in tetragonal phase was calculated to be ≈ 6.1 nm. Reports had also showed the tetragonal phase below 30 nm[14] and monoclinic phase below 10 nm[18]. The energy crossover relations have established the thermodynamically metastable state which becomes stable below a critical size. It is also observed that at larger size, the monoclinic phase has the lowest energy, making it the stable phase[19]. With the reduction of size less than 6 nm, the tetragonal phase tends to have the lowest energy compared to the monoclinic and amorphous phase, making it the most stable phase below 6 nm[47]. It is also established that the amorphous zirconia is the stable form, when the size becomes less than 3 nm[19]. However in the present experiments, the particle size of the as-sintered and the ion (He^+ , Ar^+ and Kr^+) irradiated zirconia samples (measured from the dark field TEM images) are greater than 30 nm and hence the role of size in the phase transformation has been ruled out.

When ions are incident on zirconia, Frenkel pairs are produced. These incident ions lose its energy by the elastic collisions with the material (ZrO_2). The collision leads to the ejection of Zr and O atoms from their original lattice sites. Primary knock on atoms causes atomic displacement of Zr and O creating interstitials and vacancies. It is also known that formation energy is 24.2 eV, 8.88 eV and 8.9 eV for the zirconium neutral vacancy[139], 4 fold and 3 fold oxygen neutral vacancies[140] respectively. By maximum energy transfer, in the case of Kr^+ ion irradiation, the energy of the primary knock on atoms of Zr and O is 59.9 keV and 32.3 keV respectively, and in the case of Ar^+ ion irradiation, the energy of the primary knock on atoms of Zr and O is 101 keV and 98 keV respectively. Hence upon Kr^+ and Ar^+ ion irradiation, more number of oxygen vacancies are expected to be produced. In the case of He^+ ion irradiation, the electronic energy loss dominates over nuclear loss because the S_e/S_n value is 84.21 which is much higher than that of Ar^+ (0.5890) and Kr^+ (0.1176) ion cases.

Simeone *et al.*, [139] have reported ion induced monoclinic to tetragonal phase transition in zirconia using 400 keV Xe^+ ions. The authors have explained the phase transition in two step process; (i) radiation damage produced non-equilibrium concentration of defects in the solid and (ii) propagation of displacive phase transition associated with strain field in the presence of defects. The rate theory[141] describes the

evolution of defects by considering the rate of production and recombination of defects and it is given by

$$\frac{d\xi}{dt} = (\eta\sigma_d - 4\pi r_c N b^2 r \sigma_r \xi^2) \phi - 4\pi r_c D_0 e^{-\frac{E}{k_B T}} \xi^2 \quad \text{Eqn.3.3}$$

where ϕ is the ion flux, σ_d is the displacement cross-section, η is the collision efficiency, r_c is the capture radius, N is the number of atoms per unit volume in the samples, b is the mean free length associated with the recombination collision sequences, σ_r is the recombination collision sequence cross-section[142] and D_0 is the diffusion coefficient of these defects in the target and k_B is the Boltzmann constant. In the present experiments, the ion irradiation was carried out at room temperature (300 K) and at low temperature (143 K), and hence the second term in the rate equation which drives the thermal migration of defects can be neglected. The first term is associated with defect production and recombination and it is proportional to ion flux. In the present experiments, the volume fraction of tetragonal phase increases with the ion fluence. The volume fraction of tetragonal phase is higher when the irradiation was carried out at 143 K than at 300 K, and it is due to less migration of defects at 143 K.

Oxygen vacancies were found to play a role in determining the phase of zirconia. Several works have attributed oxygen vacancies as a prime factor in determining the phase[21, 41, 78] of zirconia. Phase of zirconia could be altered by doping it with yttrium (III) oxide (Y_2O_3). These dopants stabilize the tetragonal phase at room temperature, suppresses the transformation by creating vacancies of oxygen per unit of ZrO_2 [26].

Migration barrier energy for direct exchange mechanism used to be high (>5eV). The migration barrier energy for the oxygen interstitials is 0.365 eV -0.672 eV[143]. Hence the oxygen interstitials having greater migration energy, migrates faster than the oxygen vacancies towards the grain boundaries and get annihilated. Thus as a result, the grains get filled with the oxygen vacancies.

Earlier works on SHI irradiation has also proved that first impact is used to produce the required amount of oxygen vacancies and the second impact is used for the phase transformation. In some earlier works, phase transformation is found to occur at 4.2 dpa itself[43]. However, in the present case, the phase transformation has occurred at higher dpa (Ar^+ and Kr^+ ions).

In addition, the difference in the formation energies between monoclinic and tetragonal zirconia calculated by the first principle method is 0.07 eV/ ZrO_2 [144]. Hence such a small amount of energy could be easily overcome by ion irradiation. Once the

number of oxygen vacancies reaches a threshold value, the temperature required for the phase transformation reduces drastically.

Muller *et al.*, [125] have attributed the phase transformation process completely to the pure radiation damage process rather than the gas bubbles. In the present case, the phase transformation is attributed to pure radiation damage process like defects (interstitials and vacancies) production, annihilation etc.

GIXRD and Raman scattering has shown the presence of strain in the zirconia samples. *Ab initio* calculations has shown that the oxygen vacancies are capable of producing strain fields in the monoclinic phase of zirconia in their neighbourhood [140]. The oxygen vacancies associated with the randomly oriented electric dipoles helps to prevent the coalescence and growth of tetragonal phase [145]. Also it is known that the tetragonal to cubic phase transformation is not sensitive to strain [146]. Hence, in the present case, cubic phase of zirconia is not observed.

The fraction of tetragonal phase in ion irradiated zirconia samples increases with dpa. The amount of the transformed phase is expected to increase with the atomic number of the inert gas ions used. However, in the present experiment the amount of transformation in the Kr^+ ion irradiated zirconia samples is less compared to the amount transformed in the Ar^+ ion irradiated zirconia samples. This is because Kr^+ ion has a shallow projected range (23 nm) and high sputtering yield (8.8 atoms/ion) compared to the Ar^+ ions (sputtering yield: 4.6 atoms/ion). The shallow range of the Kr^+ ions gets easily sputtered out, leading to the less amount of tetragonal phase. In case of low temperature ion irradiation (Ar^+ and Kr^+), the phase transformation is found to occur faster. This is attributed to the immobility of defects and continuous production of oxygen vacancies. The increase in the oxygen vacancies, their reduction of annihilation with the interstitials due to their immobility and the high amount of strain is produced and it leads to the faster rate of phase transformation at low temperatures. The fate of the implanted ions will be discussed in the next chapter.

3.6. Conclusions

As-sintered monoclinic zirconia samples prepared by thermal decomposition method were irradiated with He^+ (120 keV), Ar^+ (120 keV) and Kr^+ (60 keV) ions using the 150 kV ion accelerator. Upon ion irradiation (irrespective of the ions and irradiation temperatures) phase transformation from monoclinic to tetragonal zirconia is observed. The rate of phase transformation is found to be faster when the ion irradiation was carried

at low temperatures. The phase transformation is attributed to the oxygen vacancies and the strain induced by these oxygen vacancies. The faster phase transformation at low temperature ion irradiation is attributed to the immobility of defects and continuous production of oxygen vacancies by ion irradiation. Even though monoclinic to tetragonal phase transformation is observed, there is no trace of cubic phase, as tetragonal to cubic phase transformation is not sensitive to strain.

Chapter 4

Bubble induced swelling in monoclinic zirconia

4.1. Introduction

Inert gases like krypton, argon, xenon and helium are produced inevitably in the nuclear fuel materials during operation of the reactor. These inert gases play an important role in determining the thermal and the mechanical properties of the nuclear fuel. Xenon and krypton either will be released from the fuel matrix, if the kinetics allows the process, or precipitate as small packets of gas inside the fuel matrix, due to their insolubility in the fuel matrix. When they are released, they exert significant pressure on the fuel pin thereby leading to failure of cladding. On the other hand, if they precipitate inside the matrix, it leads to swelling of the fuel material. In either case, inert gases are detrimental to the performance of the fuel. Hence it is important to study the behaviour of the inert gas atoms to know the performance of the fuel materials[10]. In this chapter, the morphological and the microstructural changes in zirconia, under low energy inert gas (He^+ , Ar^+ and Kr^+) ion irradiation are examined using electron microscopy techniques.

4.2. Experiments

The monoclinic zirconia samples were irradiated with low energy inert gas ions (120 keV He^+ , 120 keV Ar^+ and 60 keV Kr^+) at 300 K and 143 K upto ion fluences ranging from 1×10^{15} ions/cm² to 5×10^{17} ions/cm². Scanning electron microscopy (SEM) and transmission electron microscopy (TEM) were employed extensively, to study the morphological and the microstructural changes in the ion irradiated zirconia samples, and the results are discussed in the present chapter.

Scanning electron microscopy experiments were carried out using cross beam 340 model FIB-FESEM (Carl Zeiss make). In-lens detector was used for imaging in the SEM and the working distance was kept around 4 mm. TEM studies were carried out using LIBRA 200FE HRTEM (Carl Zeiss make). The information limit of the HRTEM is 0.13 nm. TEM samples were prepared by scratching the surface of the pellets samples using a scalpel blade and by dissolving it in propanol. The solution was then sonicated and dispersed on a carbon coated copper grid. This method was chosen to avoid the artifacts that would be introduced by alternate/standard methods like FIB or ion milling.

4.3. Morphological analysis using scanning electron microscopy

4.3.1. SEM analysis of the as-sintered zirconia

Figure 4.1(a) shows the SEM image of the as-sintered zirconia sample. The image clearly shows that the as-sintered sample contains spherical grains. It is also observed that the grains are not densely packed and contains many pores. The size of the grains were measured using ImageJ software[131] and the size distribution is plotted (Figure 4.1(b)). The average size of the grains is found to be 55 nm.

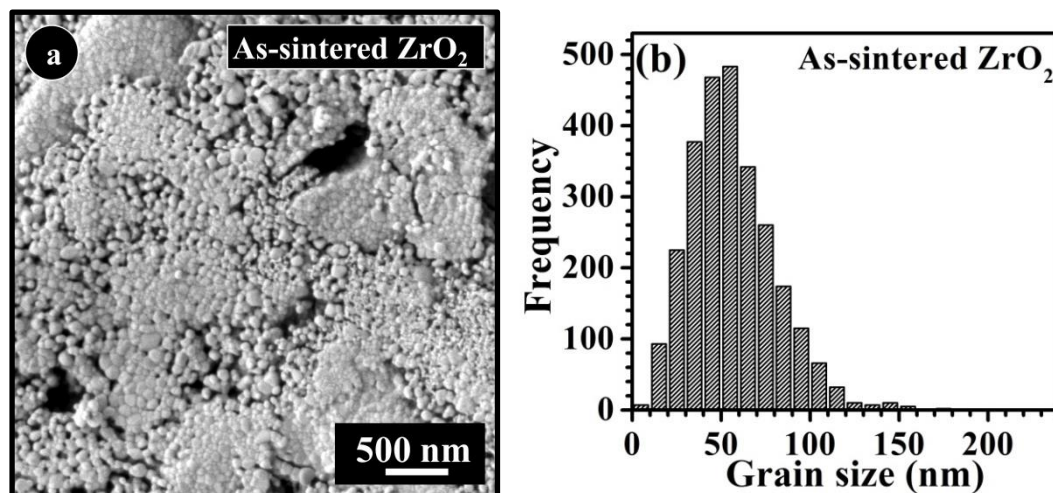


Figure 4.1 (a) SEM image and (b) the grain size distribution of the as-sintered zirconia sample. The shape of the grains is spherical in nature.

4.3.2. SEM analysis of the He⁺ ion irradiated zirconia samples

4.3.2.1. He⁺ ion irradiated (at 300 K) samples

The changes in the morphology of the zirconia samples upon irradiation with 120 keV He⁺ ions, at 300 K, were analyzed using SEM images. The SEM images in Figure 4.2(a), (b), (c) and (d) show the morphology of the zirconia samples irradiated for the ion fluences 5×10^{15} ions/cm², 1×10^{16} ions/cm², 5×10^{16} ions/cm² and 1×10^{17} ions/cm², respectively. There is no change in the spherical shape of the grains due to irradiation in all the four samples, while there is a small reduction in the grain size, when the ion fluence is as high as 1×10^{17} ions/cm². The changes in the morphology and the size of the pores in between the grains show some irregular behaviour upon ion irradiation. The grains are densely packed in the sample irradiated for the ion fluence of 5×10^{15} ions/cm², leading to the reduction in the number and size of the pores (Figure 4.2(a)). The packing is not so dense and pores are seen in the sample irradiated upto the ion fluence of 1×10^{16} ions/cm² (Figure 4.2(b)). Once again the grains are densely packed when the ion fluence is 5×10^{16} ions/cm², and interestingly, now there is 'joining of the grains'. This phenomenon 'joining

of the grains' was more prominent when the ion fluence is 1×10^{17} ions/cm², and there is a reduction in the grain size as mentioned earlier.

The phenomenon of 'joining of the grains', observed in the present case is very much similar to the nano-welding and junction formation phenomena seen in hydrogen titanate nanowires, due to low-energy nitrogen ion irradiation, as reported by Dhal *et al.*, [147]. Dhal *et al.*, [147] have suggested that ion irradiation induced defect formation and dangling bonds may lead to the chemical bonding between the hydrogen titanate nanowires resulting in the nano-welding and junction formation. They have further explained that large scale nano-welding and junction network formation can be ascribed to the localized surface melting due to heat spike, during ion irradiation.

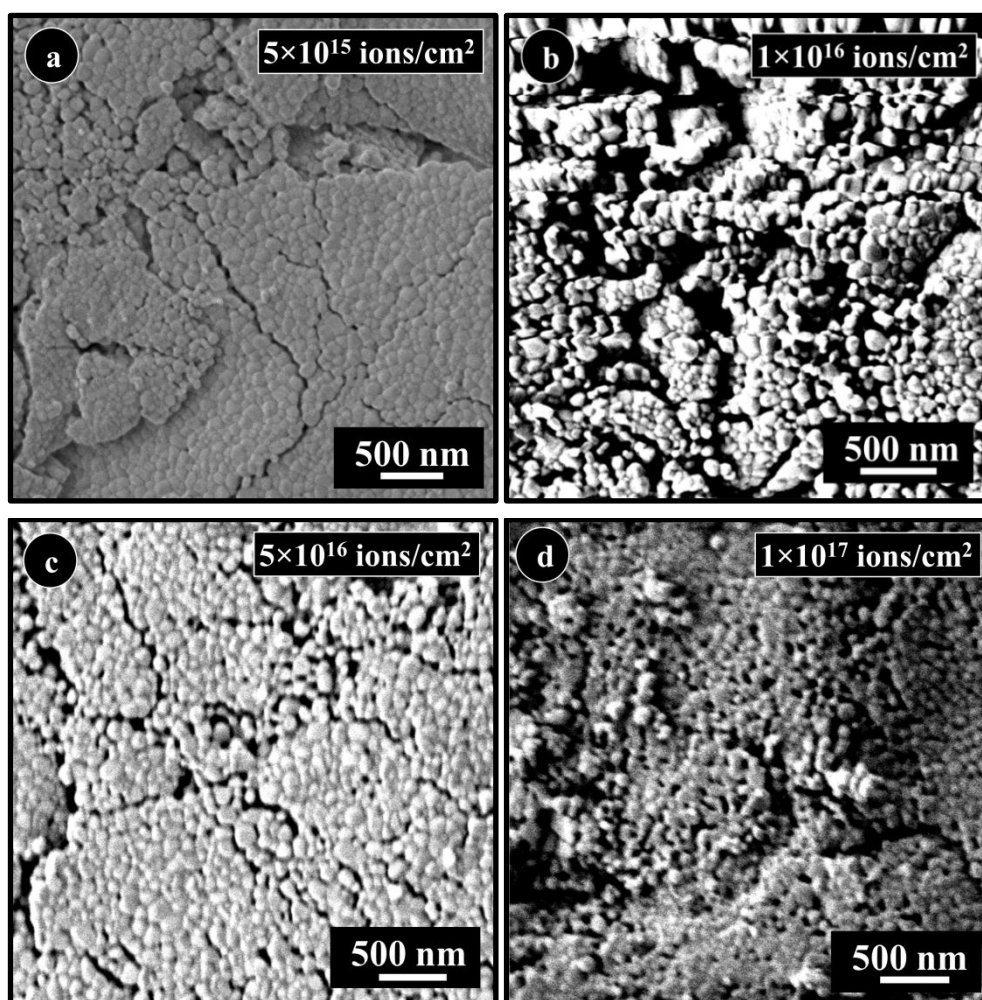


Figure 4.2 SEM images of the 120 keV He^+ ion irradiated zirconia samples for the ion fluences of (a) 5×10^{15} ions/cm², (b) 1×10^{16} ions/cm², (c) 5×10^{16} ions/cm² and (d) 1×10^{17} ions/cm² at 300 K.

In helium ion irradiated zirconia samples, the grain size distribution were analyzed using ImageJ software and the grain size distribution is shown in Figure 4.3. The grain

size distribution in the zirconia samples irradiated for the ion fluences 5×10^{15} ions/cm², 1×10^{16} ions/cm², 5×10^{16} ions/cm² and 1×10^{17} ions/cm² are shown in Figure 4.3 (a), (b), (c) and (d) respectively.

It is seen that there are some changes in the average grain size in zirconia, upon irradiation. But the changes do not show any regular trend in the case of helium ion irradiation at room temperature. The average grain size increases from 55 nm in the as-sintered sample, to 84 nm, when irradiated with helium ions upto the ion fluence of 5×10^{15} ions/cm². The size then reduces to 75 nm when the fluence is 1×10^{16} ions/cm² and again increases to 87 nm for a fluence of 5×10^{16} ions/cm². This is found to be the highest value. Finally, when the ion fluence is 1×10^{17} ions/cm², the average grain size reduces to 72 nm.

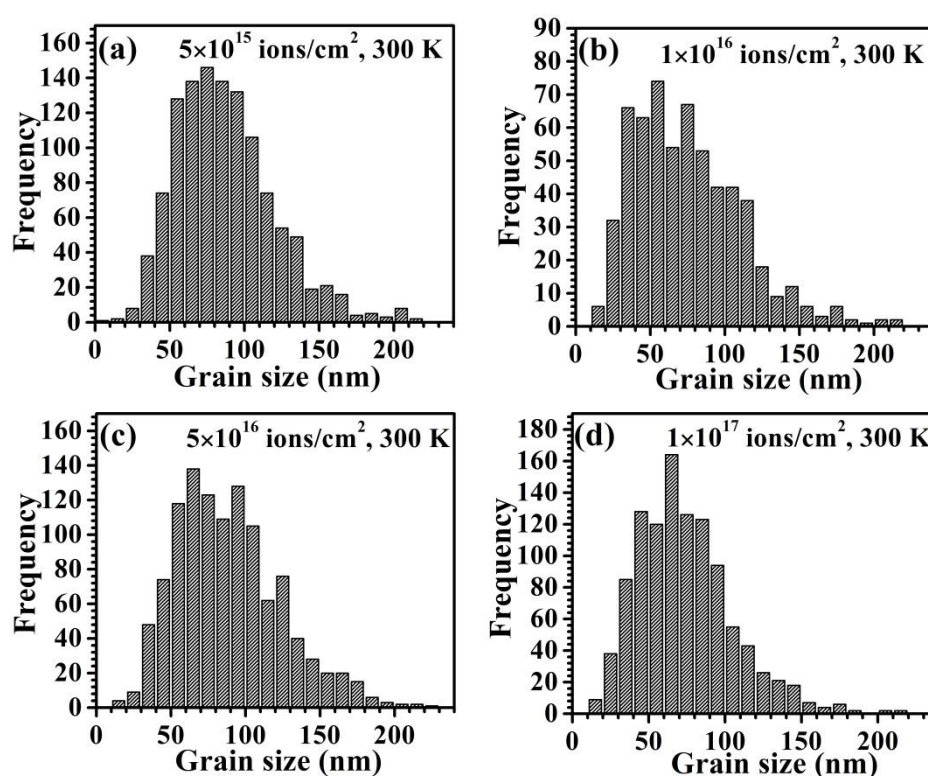


Figure 4.3 Plots showing the grain size distribution in 120 keV He⁺ ion irradiated zirconia samples for the ion fluences of (a) 5×10^{15} ions/cm², (b) 1×10^{16} ions/cm², (c) 5×10^{16} ions/cm² and (d) 1×10^{17} ions/cm² at 300 K.

4.3.2.2. He⁺ ion irradiated (at 143 K) samples

Figure 4.4 shows the SEM images of the zirconia samples irradiated with 120 keV He⁺ ions at 143 K. Figure 4.4(a), (b), (c) and (d) show the SEM images of the zirconia sample for the ion fluences of 1×10^{16} ions/cm², 5×10^{16} ions/cm², 1×10^{17} ions/cm² and 2×10^{17} ions/cm² respectively. It is observed that the zirconia grains retain their spherical

shape during ion irradiation at low temperature also and the grains are apparently densely packed as compared to the as-sintered sample.

The changes in the grain size and the packing of the grains are analyzed from these SEM images. It is observed that the grains are densely packed in the samples irradiated upto the ion fluences of 1×10^{16} ions/cm² (Figure 4.4(a)) and 5×10^{16} ions/cm² (Figure 4.4(b)). The grains are loosely packed when the ion fluence is 1×10^{17} ions/cm² (Figure 4.4(c)). For the highest ion fluence of 2×10^{17} ions/cm², the grains are packed densely as it is in other cases (Figure 4.4 (d)).

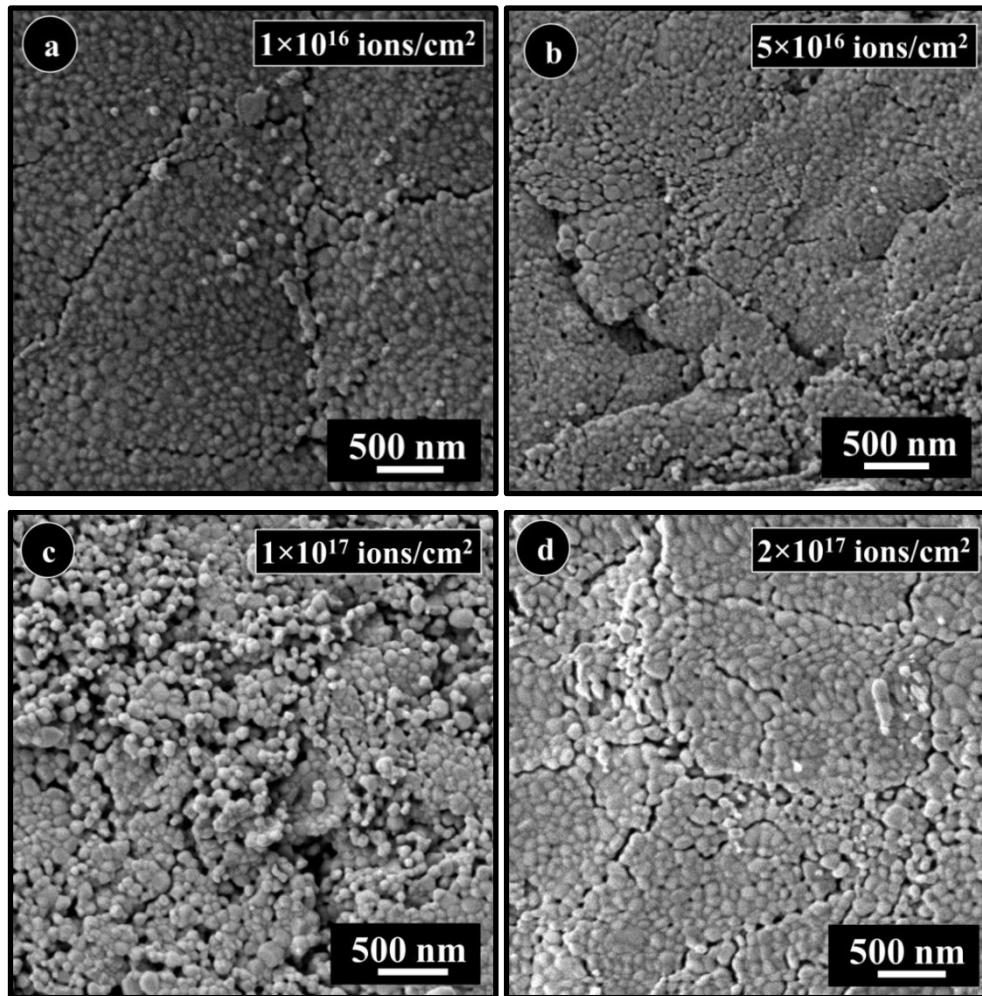


Figure 4.4 SEM images of the He⁺ ion irradiated zirconia samples for the ion fluences of (a) 1×10^{16} ions/cm², (b) 5×10^{16} ions/cm², (c) 1×10^{17} ions/cm² and (d) 2×10^{17} ions/cm² at 143 K.

As far as the grain size is concerned, initially it increases when the ion fluence is 1×10^{16} ions/cm² (Figure 4.4(a)). Then the size decreases for the ion fluence of 5×10^{16} ions/cm² (Figure 4.4(b)). Later on, the grain size increases with the ion fluences as seen from Figure 4.4(c) (1×10^{17} ions/cm²) and Figure 4.4(d) (2×10^{17} ions/cm²). Importantly,

there is no appreciable joining of grains, whereas ion irradiation at 300 K shows the joining of grains even at highest ion fluences.

The size distribution of the grains in all the monoclinic zirconia samples, irradiated with 120 keV He^+ ion at 143 K were analyzed using ImageJ software and the plots are given in Figure 4.5. The plots in Figure 4.5(a), (b), (c) and (d) shows the grain size distributions for the ion fluences of 1×10^{16} ions/cm², 5×10^{16} ions/cm², 1×10^{17} ions/cm² and 2×10^{17} ions/cm² respectively. Unlike the case of room temperature irradiation, the average size of the grains show almost monotonous trend when the sample is irradiated at low temperature. The average grain size increases to 66 nm when the ion fluence is 1×10^{16} ions/cm², whereas in the as-sintered it is 55 nm. Eventhough the grain size reduces to 63 nm when the ion fluence is 5×10^{16} ions/cm², it is not significant change in the grain size. However, the grain size grows to 75 nm and reaches 82 nm when the ion fluence increases to 1×10^{17} ions/cm² and 2×10^{17} ions/cm², respectively. Also, the average size of the grains in He^+ ion irradiated zirconia (143 K) sample is larger than the as-sintered zirconia.

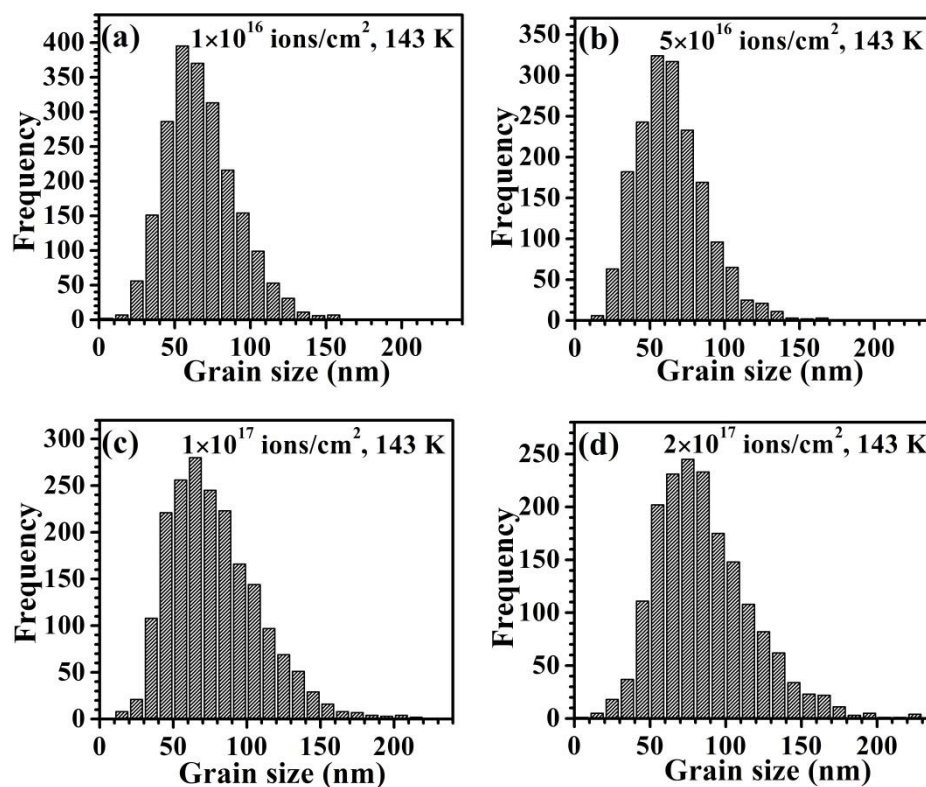


Figure 4.5 Grain size distribution of the He^+ ion irradiated zirconia samples for the ion fluences of (a) 1×10^{16} ions/cm², (b) 5×10^{16} ions/cm², (c) 1×10^{17} ions/cm² and (d) 2×10^{17} ions/cm² at 143 K.

In order to quantify the porosity in the ion irradiated zirconia samples (both at room temperature and at low temperature), the open area (denoted by ‘a’) and the area occupied by the grains (denoted by ‘A’) were measured from the images using ImageJ software. For better statistics, the area was calculated from 10 images from each sample. With the assumption that, buried surface also has the similar morphology of the surface, the ratio of the open area to area occupied by the grains (a/A) provides an estimation of the porosity in the ion irradiated zirconia samples. This ratio ‘ a/A ’ may be called as the fractional area of free space. Figure 4.6(a) shows the fractional area of free space (a/A) as a function of ion fluence for the zirconia samples irradiated with 120 keV He^+ ions at 300 K. Even though the fractional area of free space increases with ion fluence (upto 1×10^{16} ions/cm²) for higher ion fluences, the fractional area of free space decreases with the increase in the ion fluence.

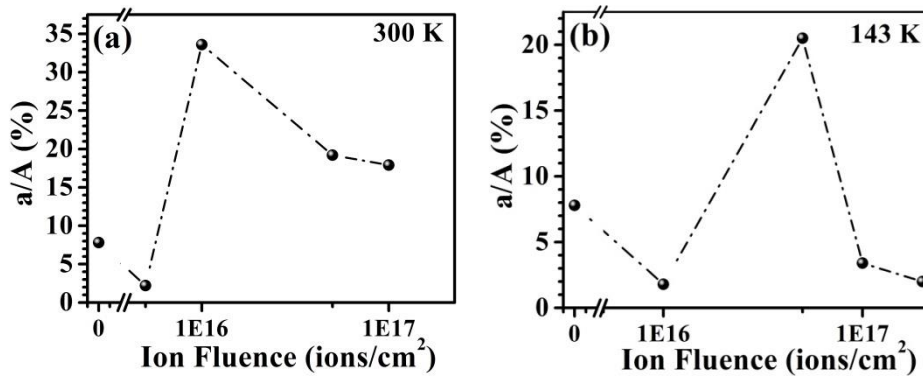


Figure 4.6 Fractional area of free space “ a/A ” as a function of ion fluence, for the He^+ ion irradiated zirconia samples at (a) 300 K and (b) 143 K

Figure 4.6(b) shows the fractional area of free space “ a/A ” as a function of ion fluence for the zirconia samples irradiated with 120 keV He^+ ions at 143 K. It increases upto the ion fluence of 5×10^{16} ions/cm² and then decreases with further increase in the ion fluence. For the highest ion fluence, the fractional area of free space is lower than the as-sintered zirconia sample (Figure 4.6(b)). Both the plots in Figure 4.6 suggest that zirconia grains have become dense, upon helium ion irradiation at 300 K and at 143 K. From the analysis of SEM images and fractional area of free space in He^+ ion irradiated samples, the average grain size of the sample did not change significantly, however the morphology of the sample changes with ion fluence in an irregular fashion. The as-sintered zirconia sample has intrinsic porosity and it changes with ion fluences. This morphological changes in the samples could be due to the convolution of many factors like sputtering[148, 149], phase transformation[150], cavity swelling[151] and ion induced diffusion[152, 153]. In the

present experiments, the sputtering yield is 0.01 atoms per incident ion and it will be very small to induce roughening in the sample as observed in our earlier works[154, 155]. Hence, the role of sputtering is ruled out in the present observation on morphology. However, in present experiments, the convolution of other factors like phase transformation (monoclinic to tetragonal transformation, as evident from diffraction techniques and Raman scattering), bubble induced swelling (TEM observation) and ion beam induced localized surface melting due to heat spike could have played role. It is difficult to delineate the role of individual effects.

4.3.3. SEM analysis of the Ar^+ ion irradiated zirconia samples

The effects of 120 keV Ar^+ ion irradiation in zirconia, both at room temperature (300 K) and at low temperature (143 K) also were studied under SEM.

4.3.3.1. Ar^+ ion irradiated (at 300 K) samples

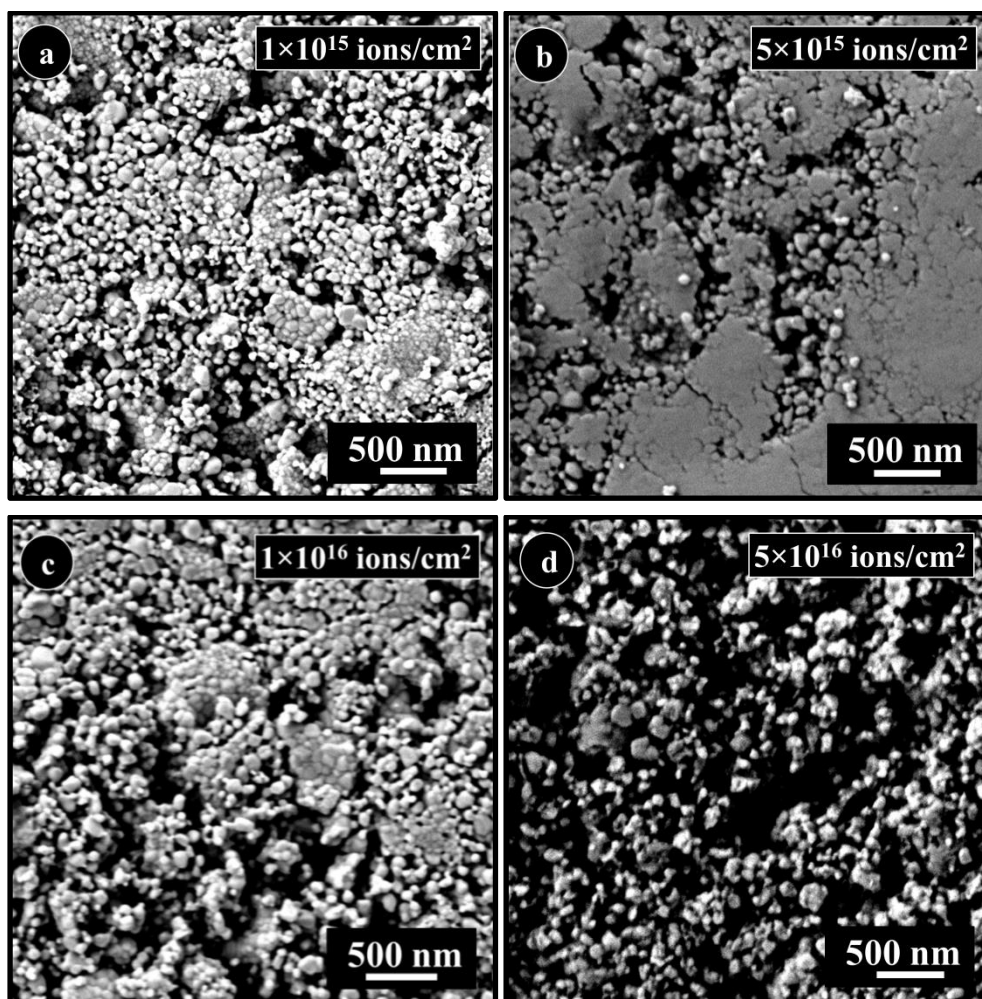


Figure 4.7 SEM images of the 120 keV Ar^+ ion irradiated zirconia samples for the ion fluences of (a) 1×10^{15} ions/cm², (b) 5×10^{15} ions/cm², (c) 1×10^{16} ions/cm² and (d) 5×10^{16} ions/cm² at 300 K.

Figure 4.7 shows the SEM images of the zirconia samples irradiated with 120 keV Ar^+ ions (300 K) for various ion fluences. The grain size for the ion fluences 1×10^{15} ions/cm², 5×10^{15} ions/cm², 1×10^{16} ions/cm² and 5×10^{16} ions/cm² are given in Figure 4.8(a), (b), (c) and (d) respectively. In all the Ar^+ irradiated samples, the grains remain spherical in shape and the grains are less densely packed. The grains are very much loosely packed in the sample where the ion fluence is 5×10^{16} ions/cm², the highest fluence under discussion. None of the samples show dense packing of the grains as seen in the case of helium ion irradiated samples. Even though grains are loosely packed, joining of the grains is noticed in all the samples, except for the lowest fluence. Joining phenomenon is less prominent for the highest ion fluence 5×10^{16} ions/cm². Even though the Ar^+ ion irradiation has not significantly modified the shape of the grains, and has not improved the close packing of the grains, it has significantly changed the average size of the grains in the sample.

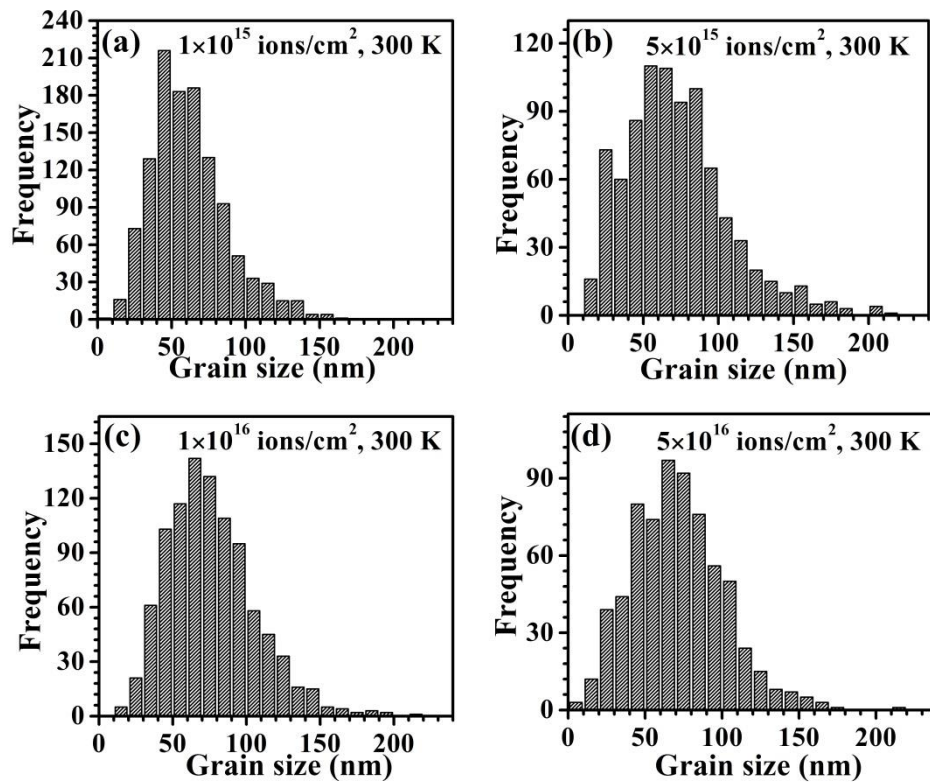


Figure 4.8 Grain size distribution of the zirconia sample upon Ar^+ ion irradiation at 300 K for the ion fluences of (a) 1×10^{15} ions/cm², (b) 5×10^{15} ions/cm², (c) 1×10^{16} ions/cm², (d) 5×10^{16} ions/cm².

In the as-sintered sample, the average grain size is 55 nm. This value increases systematically with the ion fluence when irradiated with Ar^+ ions. The grain size is 59 nm for the fluence of 1×10^{15} ions/cm², and it is 73 nm for the fluence 5×10^{15} ions/cm². It

reaches 74 nm and 72 nm when the fluence increases to 1×10^{16} ions/cm² and 5×10^{16} ions/cm², respectively.

4.3.3.2. Ar⁺ ion irradiated (at 143 K) samples

Figure 4.9 shows the SEM images of the zirconia samples irradiated with 120 keV Ar⁺ ions for various ion fluences at 143 K. Figure 4.9(a) and (b) show the SEM image of the ion irradiated samples for the ion fluences 5×10^{16} ions/cm² and 2×10^{17} ions/cm² respectively. The shape of the grains is spherical in both the cases. In the case of the low ion fluence (*refer* Figure 4.9(a)), the packing of the grains has become loose as compared to the as-sintered zirconia sample. There is joining of grains in some regions of the sample. As the ion fluence increases to 2×10^{17} ions/cm² (*refer* Figure 4.9(b)), the grains are very densely packed compared to the previous ion fluence 5×10^{16} ions/cm² and the as-sintered sample. There is significant increase in the amount of grains that has joined (*i.e.* joining of grains).

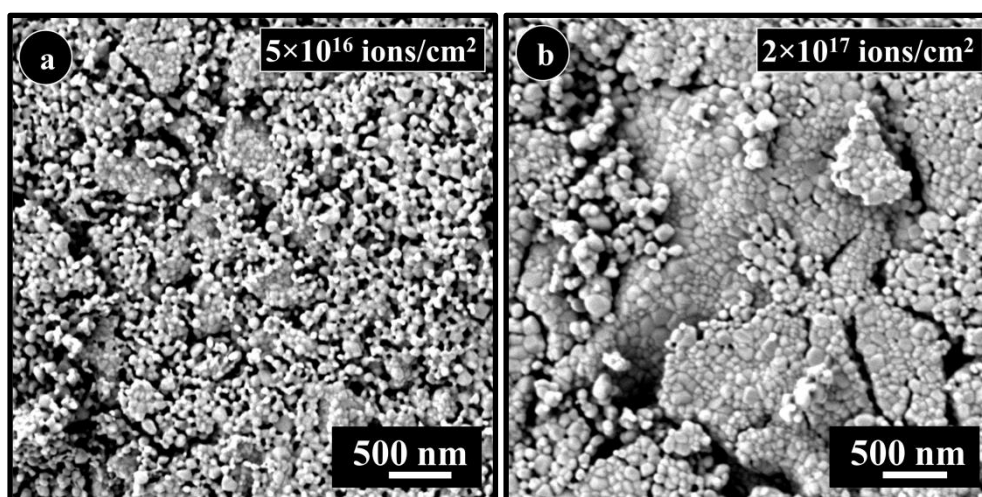


Figure 4.9 SEM images of the 120 keV Ar⁺ ion irradiated zirconia samples for the ion fluences of (a) 5×10^{16} ions/cm² and (b) 2×10^{17} ions/cm² at 143 K.

The grain size distribution for 120 keV Ar⁺ ion irradiated monoclinic zirconia samples for the ion fluences 5×10^{16} ions/cm² and 2×10^{17} ions/cm² are given in Figure 4.10(a) and (b) respectively. The average size of the zirconia grains for the ion fluences 5×10^{16} ions/cm² is 64 nm and it is slightly larger than the average size of the as-sintered zirconia sample. The average size of the zirconia grains for the ion fluences 2×10^{17} ions/cm² is 74 nm. It is observed that the average grain size increases with increase in the ion fluence. When the zirconia samples were irradiated with Ar⁺ ions, joining of the nanograins are seen for both the irradiation temperatures (300 K and 143 K). The joining

of the grains could be due to inhomogeneous distribution of defects, localized melting etc[147].

Figure 4.11(a) shows the fractional area of free space ' a/A ' as a function of ion fluence for the zirconia samples irradiated with 120 keV Ar^+ ions at 300 K. The value (a/A) monotonically increases with ion fluence upto the ion fluence of 5×10^{16} ions/cm². However for the highest ion fluence of 1×10^{17} ions/cm², the fractional area of free space decreases, but it is still higher than that of the as-sintered sample. It suggests that upon Ar^+ ion irradiation at room temperature, the zirconia grains become less dense.

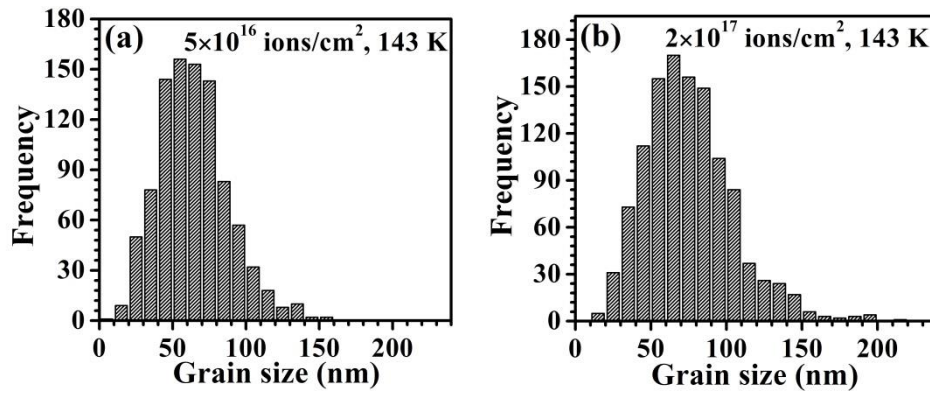


Figure 4.10 Grain size distribution of the Ar^+ ion irradiated zirconia samples for the ion fluences of (a) 5×10^{16} ions/cm² and (b) 2×10^{17} ions/cm² at 143 K.

Figure 4.11(b) shows the fractional area of free space ' a/A ' as a function of ion fluence for the zirconia samples irradiated with 120 keV Ar^+ ions at 143 K. Here the fractional area of free space increases with ion fluence upto the ion fluence of 1×10^{15} ions/cm², however for the highest ion fluence, the fractional area of free space decreases with increase in ion fluence. For the highest ion fluence, the fractional area of free space is almost same as the as-sintered zirconia sample. It suggests that upon Ar^+ ion irradiation at low temperatures (143 K), the zirconia grains become dense.

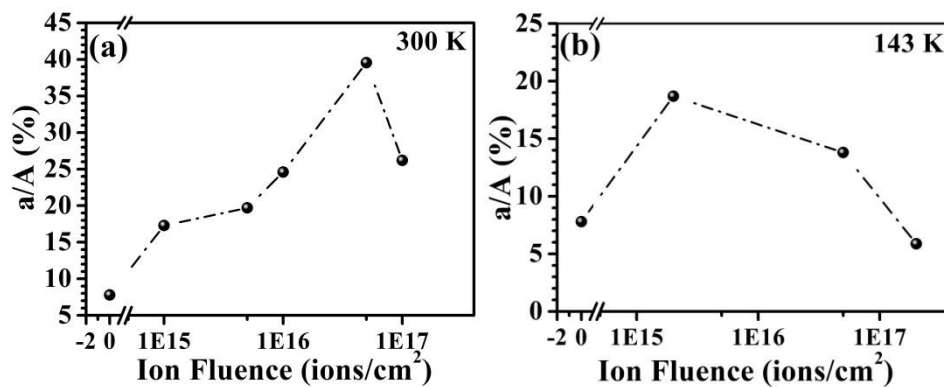


Figure 4.11 Fractional area of free space " a/A " as a function of ion fluence, for the Ar^+ ion irradiated zirconia samples at (a) 300 K and (b) 143 K.

4.3.4. SEM analysis of the Kr^+ ion irradiated zirconia samples

In addition to the effects of He^+ ions and Ar^+ ions in zirconia, the effects of 60 keV Kr^+ ion irradiation were also studied in the present work. The irradiations were carried out both at room temperature (300 K) and at low temperature (143 K), as done in the previous cases, and the changes in the morphology were analyzed under SEM. In case of Kr^+ ion irradiation, the irradiations were carried out for the ion fluences 1×10^{16} ions/cm², 1×10^{17} ions/cm² and 5×10^{17} ions/cm².

4.3.4.1. Kr^+ ion irradiated (at 300 K) samples

Figure 4.12 shows the SEM images of the zirconia samples irradiated with 60 keV Kr^+ ions at 300 K. Figure 4.12(a) shows the SEM image of the Kr^+ ion irradiated zirconia samples for the ion fluence 1×10^{16} ions/cm².

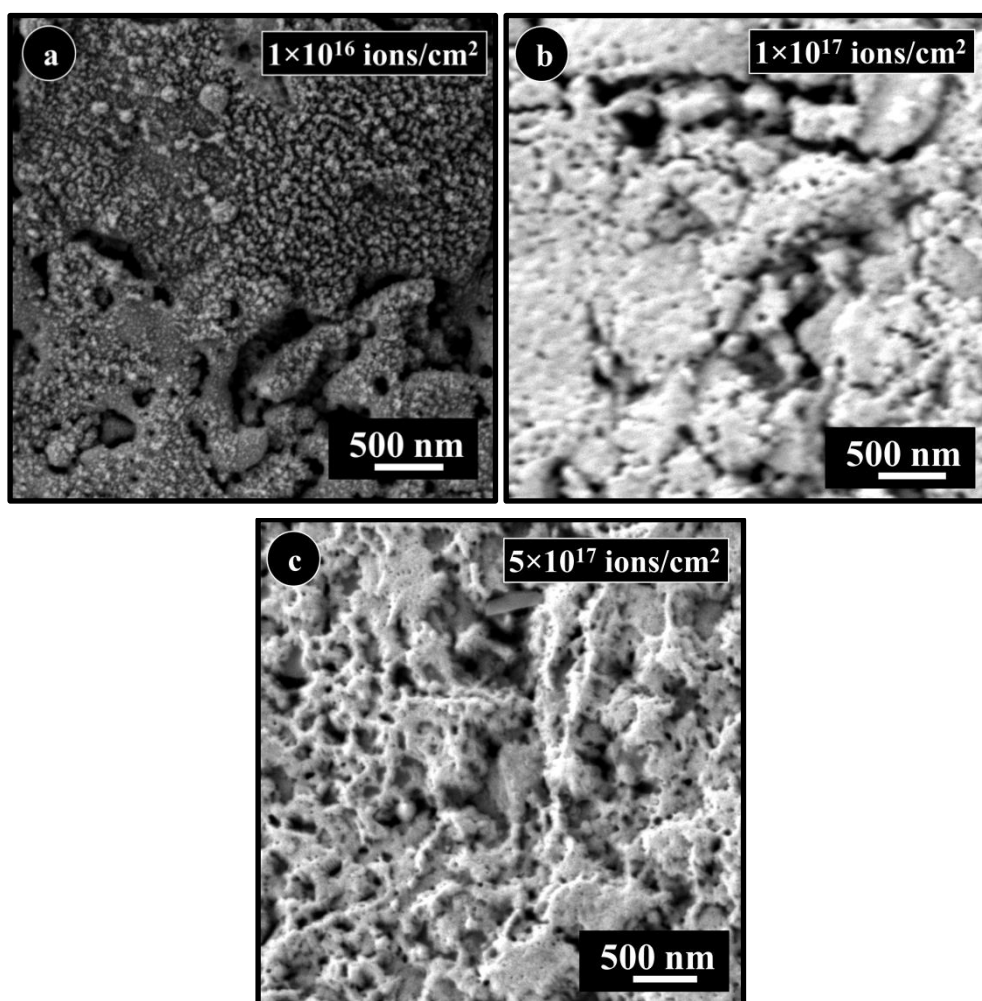


Figure 4.12 SEM images of the 60 keV Kr^+ ion irradiated zirconia samples for the ion fluences of (a) 1×10^{16} ions/cm², (b) 1×10^{17} ions/cm² and (c) 5×10^{17} ions/cm² at 300 K.

It is observed that the morphology is very different from the as-sintered zirconia sample (Figure 4.1(a)). Few grains are seen that are spherical in shape and the grains

appears to be sputtered. As the ion fluence increases to 1×10^{17} ions/cm², the morphology of the sample (Figure 4.12(b)) differs completely from the as-sintered sample. Individual grains are not observed and the grains appear to be joined. For the highest ion fluence 5×10^{17} ions/cm², the SEM image (Figure 4.12 (c)) shows that the individual grains are no longer present, they have completely joined together appearing like a porous material with interconnected ligaments. As the grains are joined and individual grains are not observed, grain size analysis could not be carried out. Localised melting, inhomogeneous distribution of defects like vacancies, interstitials could be attributed to the joining of the grains [147].

4.3.4.2. Kr⁺ ion irradiated (at 143 K) samples

Figure 4.13 shows the SEM images of the zirconia samples irradiated with 60 keV Kr⁺ ions at 143 K. Figure 4.13(a) shows the SEM image of the Kr⁺ ion irradiated zirconia samples for the ion fluence 1×10^{16} ions/cm².

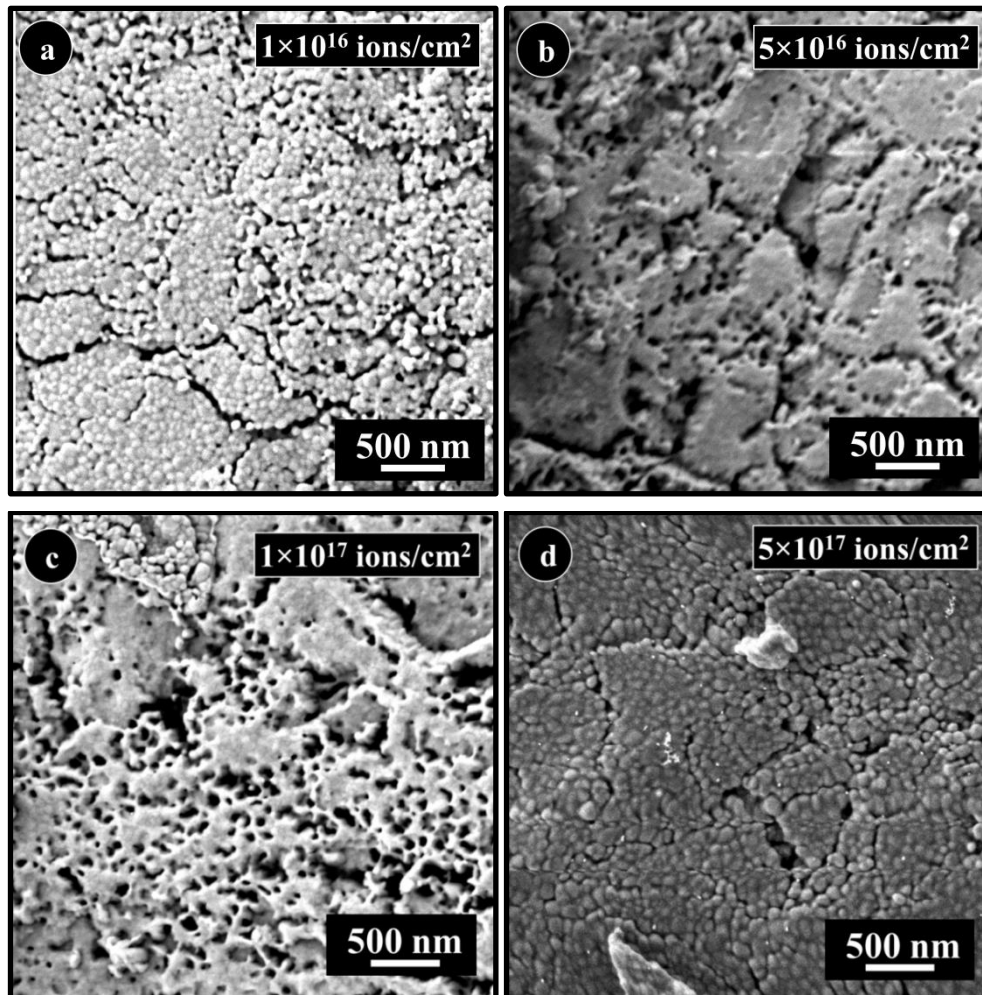


Figure 4.13 SEM images of the 60 keV Kr⁺ ion irradiated zirconia samples for the ion fluences of: (a) 1×10^{16} ions/cm², (b) 5×10^{16} ions/cm², (c) 1×10^{17} ions/cm² and (d) 5×10^{17} ions/cm² at 143 K.

It is observed that the zirconia grains are spherical in shape and the grains are not densely packed as compared to the as-sintered zirconia (Figure 4.1(a)). There is also joining of the grains. As the ion fluence increases to 5×10^{16} ions/cm², it is observed that the individual grains are not present (Figure 4.13(b)) and the grains are joined. Figure 4.13(c) shows the SEM image for the ion fluence 1×10^{17} ions/cm² and it shows joining of the grains. For the highest ion fluence of 5×10^{17} ions/cm², the SEM image (Figure 4.13(d)) surprisingly shows that the grains are densely packed compared to the lower ion fluences. This could be only due to the sputtering of the ion irradiated layer where the grains might have joined. This is also evident from the fact that the grains are spherical in shape and there is no joining of grains unlike in the cases of lower ion fluences.

The grain size distribution for 60 keV Kr⁺ ion irradiated (at 143 K), monoclinic zirconia samples for the ion fluences 1×10^{16} ions/cm² and 5×10^{17} ions/cm², are given in Figure 4.14(a) and (b) respectively. The average size of the grains for the ion fluence 1×10^{16} ions/cm² is 70 nm. The average size of the grains for the ion fluence 5×10^{17} ions/cm² is 85 nm and it is slightly larger than the average size of the as-sintered zirconia. It is observed that the average size measured for the highest ion fluence 5×10^{17} ions/cm² is larger than that of the lower ion fluence 1×10^{16} ions/cm².

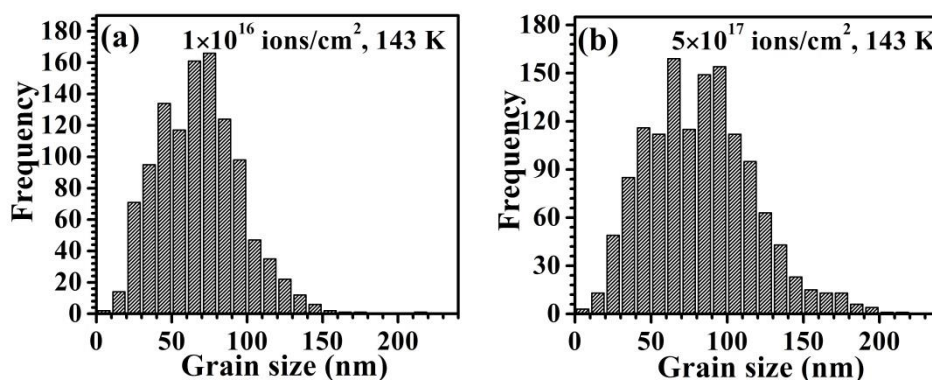


Figure 4.14 Grain size distribution of the 60 keV Kr⁺ ion irradiated zirconia samples for the ion fluences of (a) 1×10^{16} ions/cm² and (b) 5×10^{16} ions/cm² at 143 K

Figure 4.15(a) shows the fractional area of free space ' a/A ' as a function of ion fluence for the zirconia samples irradiated with 60 keV Kr⁺ ions at 300 K. The fractional area of free space, a/A increases with ion fluence upto 1×10^{17} ions/cm², and then decreases. This suggests that upon ion irradiation, the zirconia grains have become dense. For the highest ion fluence, the fractional area of free space is almost the same as the as-sintered zirconia sample, which corroborates with the suggestion that the ion irradiated layer could have been sputtered out.

Figure 4.15(b) shows the fractional area of free space ' a/A ' as a function of ion fluence for the zirconia samples irradiated with 60 keV Kr^+ ions at 143 K. The fractional area of free space ' a/A ' increases with ion fluence upto the ion fluence of 5×10^{16} ions/cm², however for the higher ion fluences, the fractional area of free space decreases with increase in ion fluence. For the highest ion fluence, the fractional area of free space is almost the same as that of the as-sintered zirconia sample. Even though the porous nature of zirconia increases with ion fluence, with continuous ion irradiation, zirconia tends to become dense for the highest ion fluences.

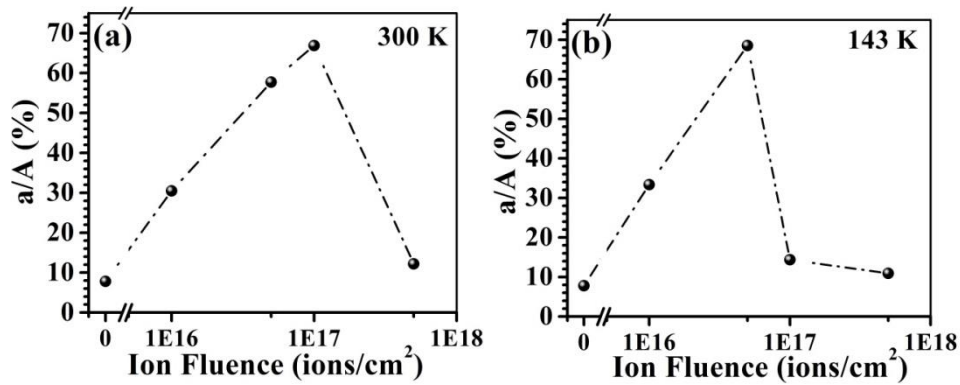


Figure 4.15 Fractional area of free space " a/A " as a function of ion fluence, for the Kr^+ ion irradiated zirconia samples at (a) 300 K and (b) 143 K.

4.4. Microstructural analysis using transmission electron microscopy

In addition to the morphological changes, zirconia also undergoes the microstructural changes upon inert gas ion irradiation. In order to understand the microstructural changes, the irradiated samples were investigated under high resolution transmission electron microscope (HRTEM).

4.4.1. TEM analysis of the He^+ ion irradiated zirconia samples

4.4.1.1. Effects of ion irradiation at room temperature

Zirconia samples irradiated with 120 keV He^+ ions at room temperature (300 K) were investigated under high resolution TEM. It may be recalled that the irradiations were carried out for the ion fluences of 1×10^{16} ions/cm², 1×10^{17} ions/cm² and 2×10^{17} ions/cm². TEM images of all the samples are given in Figure 4.16. All the TEM images are taken in the underfocus condition, in which the embedded inert gas bubbles are identified clearly by their Fresnel fringes.

The microstructure of the sample irradiated for the ion fluence 1×10^{16} ions/cm², is shown in Figure 4.16(a) and (b), former one is low magnification bright field TEM image and the latter one is HRTEM image. Both the images reveal the presence of helium

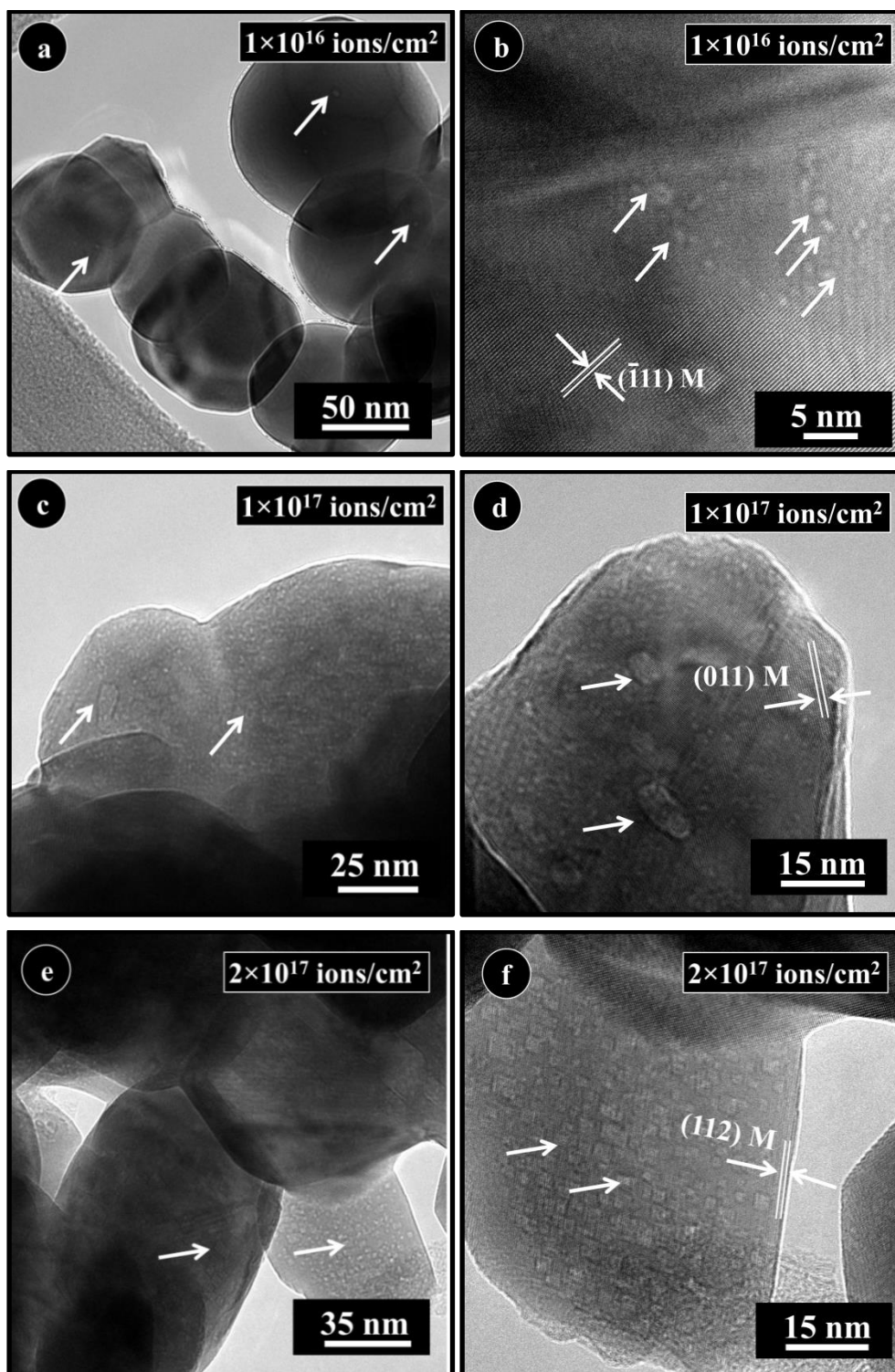


Figure 4.16 TEM image of zirconia samples irradiated with 120 keV He^+ ions at 300 K. (a), (c) and (e) show the low magnification bright filed TEM images of the samples irradiated for the ion fluences 1×10^{16} ions/cm², 1×10^{17} ions/cm² and 2×10^{17} ions/cm², respectively. (b), (d) and (f) show the corresponding HRTEM images of the samples. All the images are recorded at under-focus condition in TEM, where the bubbles are identified with their Fresnel fringes.

bubbles (marked by the arrows in the micrograph). All the helium bubbles are found to be spherical in shape. The $(\bar{1}11)$ planes of the monoclinic zirconia are identified in the

HRTEM image (Figure 4.16(b)). Figure 4.16(c) and (d) shows the low magnification bright field TEM image and HRTEM image of the sample irradiated for the ion fluence of 1×10^{17} ions/cm² respectively. The (011) planes of the monoclinic zirconia are observed in the HRTEM image (Figure 4.16(d)). It is seen that the number density of the bubbles increases apparently. Figure 4.16(e) and (f) show the low magnification bright field TEM image and HRTEM image of the sample irradiated for the ion fluence 2×10^{17} ions/cm².

It is observed that for the highest ion fluence, there is an increase in the bubble number density and the helium bubbles are faceted. The (112) planes of the monoclinic zirconia are identified clearly in the HRTEM image (*refer* Figure 4.16(f)).

The bubble size and size distribution were calculated by analyzing the TEM images with the help of ImageJ software[131]. Bubble size distribution for the He⁺ ion irradiated zirconia sample is shown in the plots (*refer* Figure 4.17). The average bubble size and the areal density of the bubbles are summarized in Table 4.1(*refer* Section 4.5) along with the observations from other inert gas irradiations in zirconia. From the Table 4.1, it is seen that there is no significant change in the average bubble size (1.63 nm and 1.64 nm for the ion fluence 1×10^{16} ions/cm² and 2×10^{17} ions/cm² respectively). However, the plots in Figure 4.17 and the areal number density tabulated in Table 4.1, reveal that the helium bubble number density increases with increase in ion fluences. The swelling due to these bubbles will be discussed in Section 4.5.

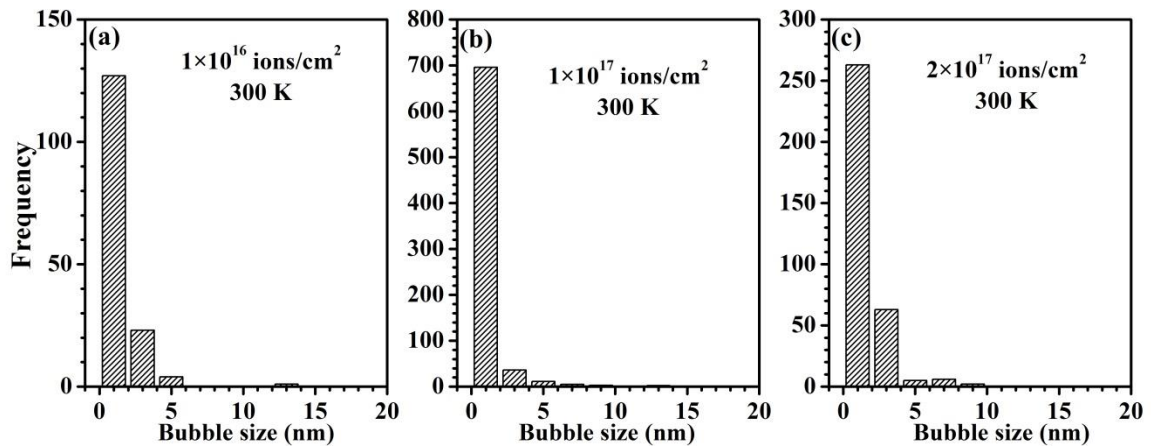


Figure 4.17 The bubble size distribution in the He⁺ ion irradiated (at 300 K) zirconia samples for the ion fluence of (a) 1×10^{16} ions/cm², (b) 1×10^{17} ions/cm² and (c) 2×10^{17} ions/cm².

4.4.1.2. Effects of ion irradiation at low temperature

The zirconia samples were also irradiated with 120 keV He⁺ ions at low temperature (143 K). The irradiations were carried out for two different ion fluences 1×10^{17} ions/cm² and 2×10^{17} ions/cm². Figure 4.18 shows the low magnification bright field

TEM image and HRTEM images of the samples irradiated with 120 keV He^+ ions at low temperature. Figure 4.18(a) and (b) show the low magnification bright field TEM image and HRTEM image of sample irradiated for the ion fluence 1×10^{17} ions/cm² respectively. Similarly, Figure 4.18(c) and (d) show the low magnification bright field TEM image and

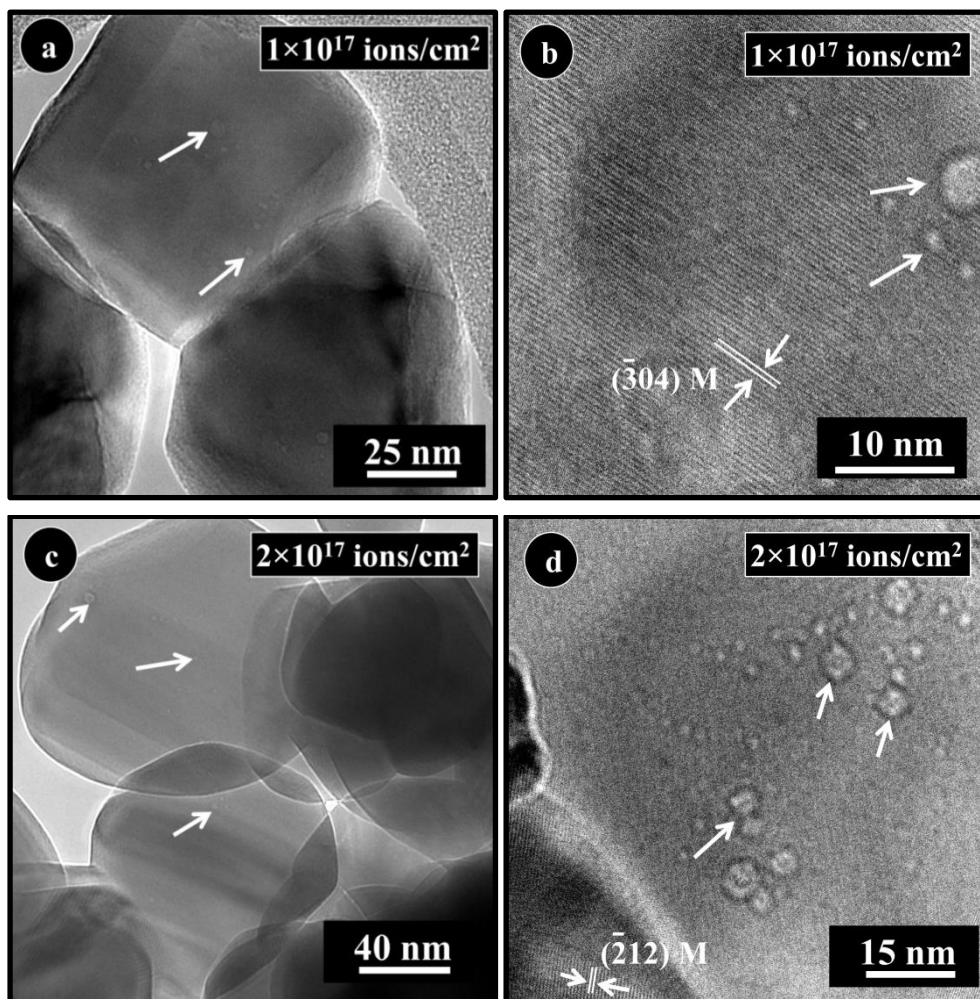


Figure 4.18 (a) Low magnification bright field TEM image of zirconia samples irradiated with 120 keV He^+ ions at 143 K for the ion fluences of (a) 1×10^{17} ions/cm² and (c) 2×10^{17} ions/cm². (b) and (d) show the corresponding HRTEM images of the samples. All the TEM micrographs are recorded in underfocus condition.

HRTEM image of the sample irradiated for the ion fluence 2×10^{17} ions/cm². Helium bubbles are seen in all the images (indicated by arrows) and the bubbles are mostly spherical in shape. In order to characterize the bubbles, the bubble size and size distribution were calculated by analyzing the TEM images with the help of ImageJ software[131]. Bubble size distributions are plotted in Figure 4.19 and the average bubble size and the areal density of the bubbles are summarized in Table 4.1 (refer Section 4.5). From the TEM images and from Table 4.1, it is observed that the helium bubbles are less in number when the irradiation was carried out at low temperature (143 K). This also

means that the areal density of the bubbles is smaller ($3 \times 10^{15}/\text{m}^2$) during ion irradiation at 143 K compared to the areal density of the bubbles ($24 \times 10^{15}/\text{m}^2$) during ion irradiation at 300 K. Further, Table 4.1 shows that the average size of the helium bubbles is larger in the samples irradiated at low temperature (2.89 nm) than the samples irradiated at room temperature (1.64 nm), for the same ion fluence of 2×10^{17} ions/ cm^2 .

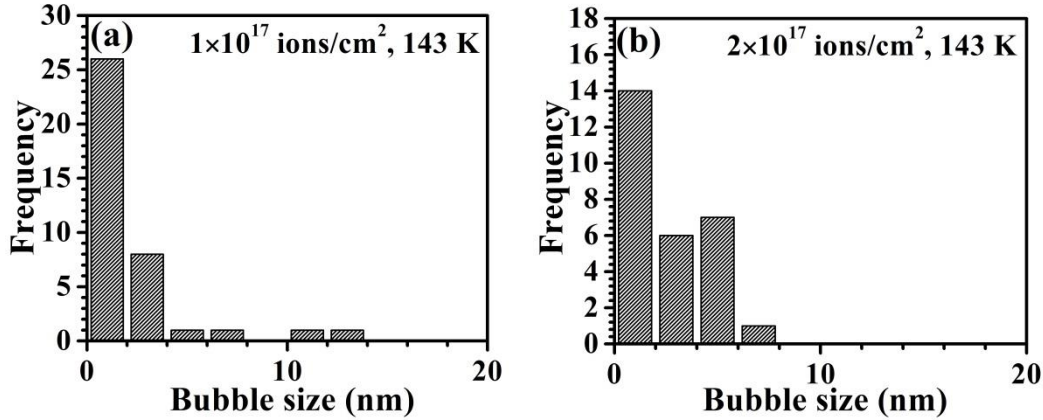


Figure 4.19 The size distribution of the helium bubbles in the zirconia samples irradiated with 120 keV He^+ ions at 143 K, upto the ion fluence of (a) 1×10^{16} ions/ cm^2 and (b) 2×10^{17} ions/ cm^2 .

4.4.2. TEM analysis of the Ar^+ ion irradiated zirconia samples

4.4.2.1. Effects ion irradiation at room temperature

Zirconia samples irradiated with 120 keV Ar^+ ions at room temperature (300 K) were investigated under high resolution TEM. The low magnification bright field TEM image of the sample irradiated for the ion fluence 1×10^{16} ions/ cm^2 is shown in Figure 4.20(a) and the corresponding HRTEM image is shown in Figure 4.20(b). The micrographs reveal the presence of argon bubbles and the argon bubbles are spherical in shape. The (002) planes of the monoclinic zirconia are identified in the HRTEM image. Similarly Figure 4.20(c) and (d) shows the low magnification bright field TEM image and HRTEM image of the sample irradiated for the ion fluence of 1×10^{17} ions/ cm^2 respectively. The TEM images reveal the presence of spherical argon bubbles. The $(\bar{2}11)$ planes of the monoclinic zirconia are identified and marked in the HRTEM image.

The bubbles present in the Ar^+ ion irradiated samples (at 300 K and at 143 K) are characterized in the same way as explained in previous section. The bubble size distribution is given in Figure 4.21. The average size of the bubbles and the areal density of the bubbles are listed in Table 4.1. It is observed from Table 4.1 that the average size of the bubbles increases with the ion fluence when the irradiation was carried at 300 K.

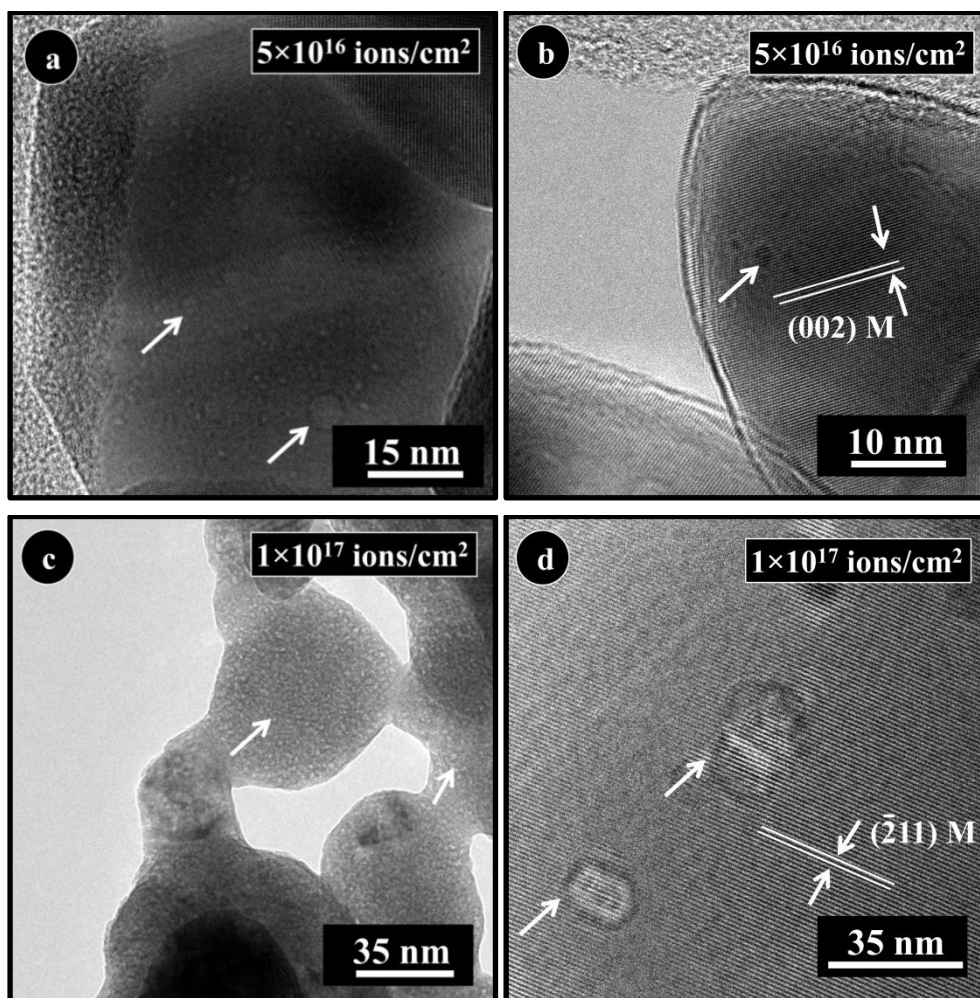


Figure 4.20 (a) Low magnification bright filed TEM image of zirconia samples irradiated with 120 keV Ar^+ ions at 300 K for the ion fluence of (a) $5 \times 10^{16} \text{ ions/cm}^2$ and (c) $1 \times 10^{17} \text{ ions/cm}^2$. (b) and (d) show the corresponding the HRTEM images of the samples. All the TEM micrographs are recorded in underfocus condition.

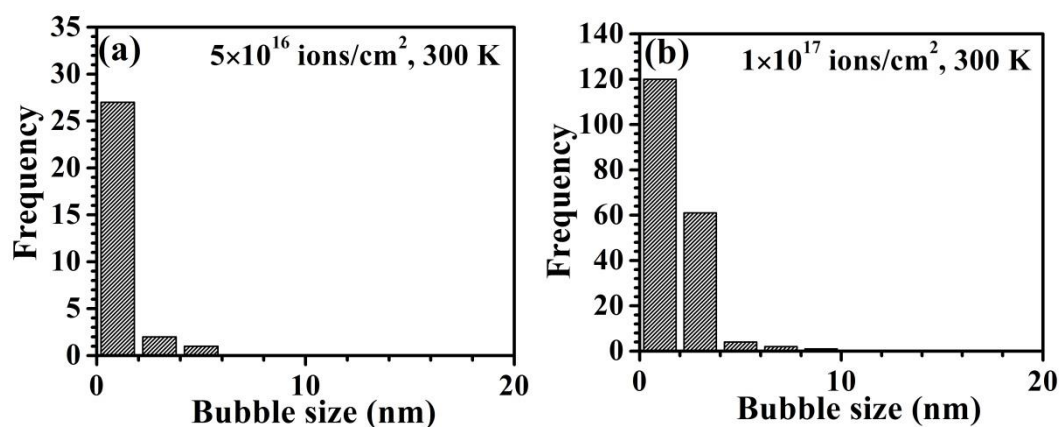


Figure 4.21 The bubble size distribution of the Ar^+ ion irradiated (at 300 K) ZrO_2 samples for the ion fluence of (a) $5 \times 10^{16} \text{ ions/cm}^2$ and (b) $1 \times 10^{17} \text{ ions/cm}^2$

4.4.2.2. Effects of ion irradiation at low temperature

Figure 4.22 shows the TEM images of the zirconia samples irradiated with 120 keV Ar^+ ions at 143 K for the ion fluence of 2×10^{17} ions/cm². Figure 4.22(a) and Figure 4.22(b) shows low magnification bright field TEM image and HRTEM image of the sample respectively. As required for the analysis of bubbles, the images are recorded at underfocus condition. It is observed that the argon bubbles are spherical in shape. Particularly it is observed that bubbles are lesser in number when the irradiation was carried out at low temperature (143 K) compared to irradiation at 300 K.

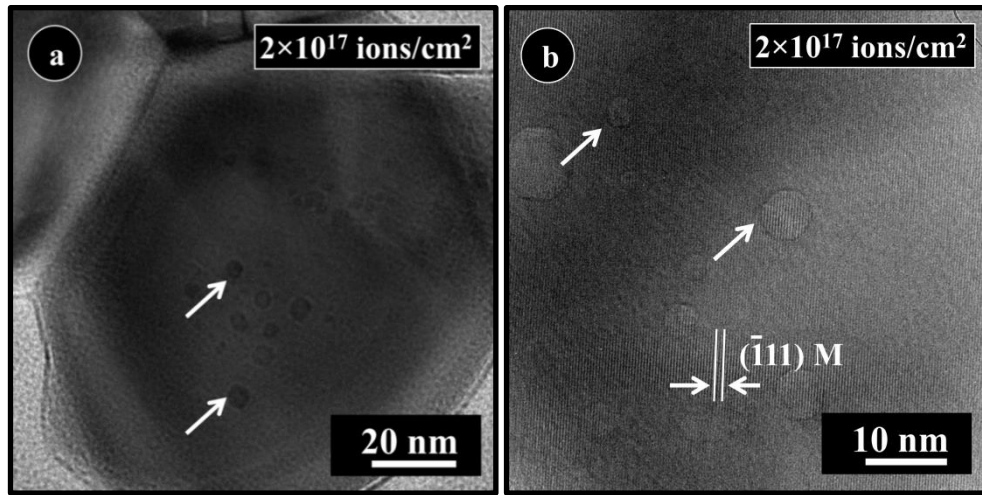


Figure 4.22 (a) Bright field TEM image of 120 keV Ar^+ ion irradiated ZrO_2 (2×10^{17} ions/cm², 143 K) recorded in underfocus condition, and (b) the corresponding HRTEM image. The plane $(\bar{1}11)$ corresponding to the monoclinic phase is clearly seen. Some of the argon bubbles are marked with arrows.

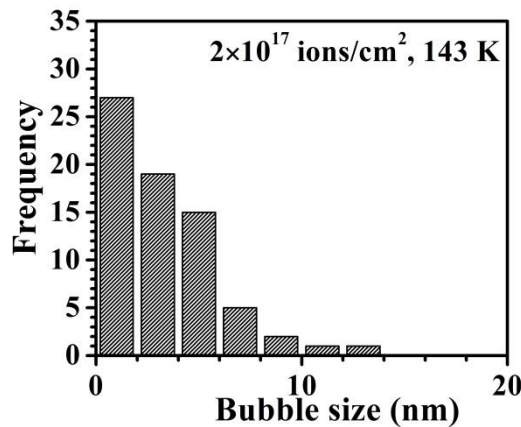


Figure 4.23 The size distribution of the bubbles in zirconia sample irradiated with Ar^+ ion irradiated at 143 K for the ion fluence of 2×10^{17} ions/cm².

The size distribution of the bubbles present in the Ar^+ ion irradiated sample (ion fluence 2×10^{17} ions/cm²) at 143 K also is analyzed in the same way as explained earlier. The bubble size distribution is plotted and shown in Figure 4.23. The bubble areal density

was also calculated. Table 4.1 shows the values of the average bubble size and the areal density of the bubbles.

It is observed from Table 4.1 that the average size of the bubbles increases with the ion fluence when the irradiation was carried out at 300 K. It is also observed that the average size of the bubble is larger in case of the ion irradiation carried at 143 K compared to ion irradiation carried out at 300 K. The bubble areal density increases with ion fluence when the Ar^+ ion irradiation as carried at 300 K. The bubble areal density is found to be less in case of ion irradiation at 143 K compared to the bubble areal density of the zirconia samples irradiated at 300 K.

4.4.3. TEM analysis of the Kr^+ ion irradiated zirconia samples

In continuation of the previous studies, the zirconia samples, irradiated with 60 keV Kr^+ ions were also studied under high resolution TEM.

4.4.3.1. Effects of ion irradiation at room temperature

Figure 4.24 shows the TEM micrographs of zirconia samples, irradiated with 60 keV Kr^+ ions at room temperature (300 K). The irradiations were carried out for the ion fluences of 1×10^{16} ions/cm², 1×10^{17} ions/cm² and 5×10^{17} ions/cm² and the TEM micrographs of all the samples are shown in Figure 4.24. Figure 4.24(a) shows the low magnification bright field TEM image of the zirconia sample irradiated for the ion fluence of 1×10^{16} ions/cm². The image is recorded in underfocus condition which clearly shows the presence of krypton bubbles. The krypton bubbles are almost spherical in shape. It is observed here that the krypton bubbles are formed inside the grains. Figure 4.24(b) shows the HRTEM image of the same sample, where the lattice fringes of the monoclinic zirconia are seen clearly. The $(\bar{1}11)$ planes corresponding to the monoclinic phase of zirconia has been identified and is marked in the micrograph. Figure 4.24(c) shows the low magnification bright field TEM image of the sample (ion fluence of 1×10^{17} ions/cm²) and Figure 4.24(d) shows the HRTEM image of the same sample. In HRTEM image (Figure 4.24(d)), the $(\bar{1}02)$ planes corresponding to monoclinic zirconia has been marked. Importantly, it is observed that the krypton bubbles are formed both inside the grains and on the grain boundaries. But this observation is not true, when the ion fluence reaches 5×10^{17} ions/cm². Figure 4.24(e) shows the low magnification bright field TEM image of the zirconia sample ion irradiated with Kr^+ ions for the ion fluence 5×10^{17} ions/cm². It is seen that the krypton bubbles are formed only inside the grains. Figure 4.24(f) shows the

HRTEM image of the same sample (5×10^{17} ions/cm²) and the ($\bar{1}02$) planes corresponding to the monoclinic phase of zirconia has been identified and is marked in the micrograph.

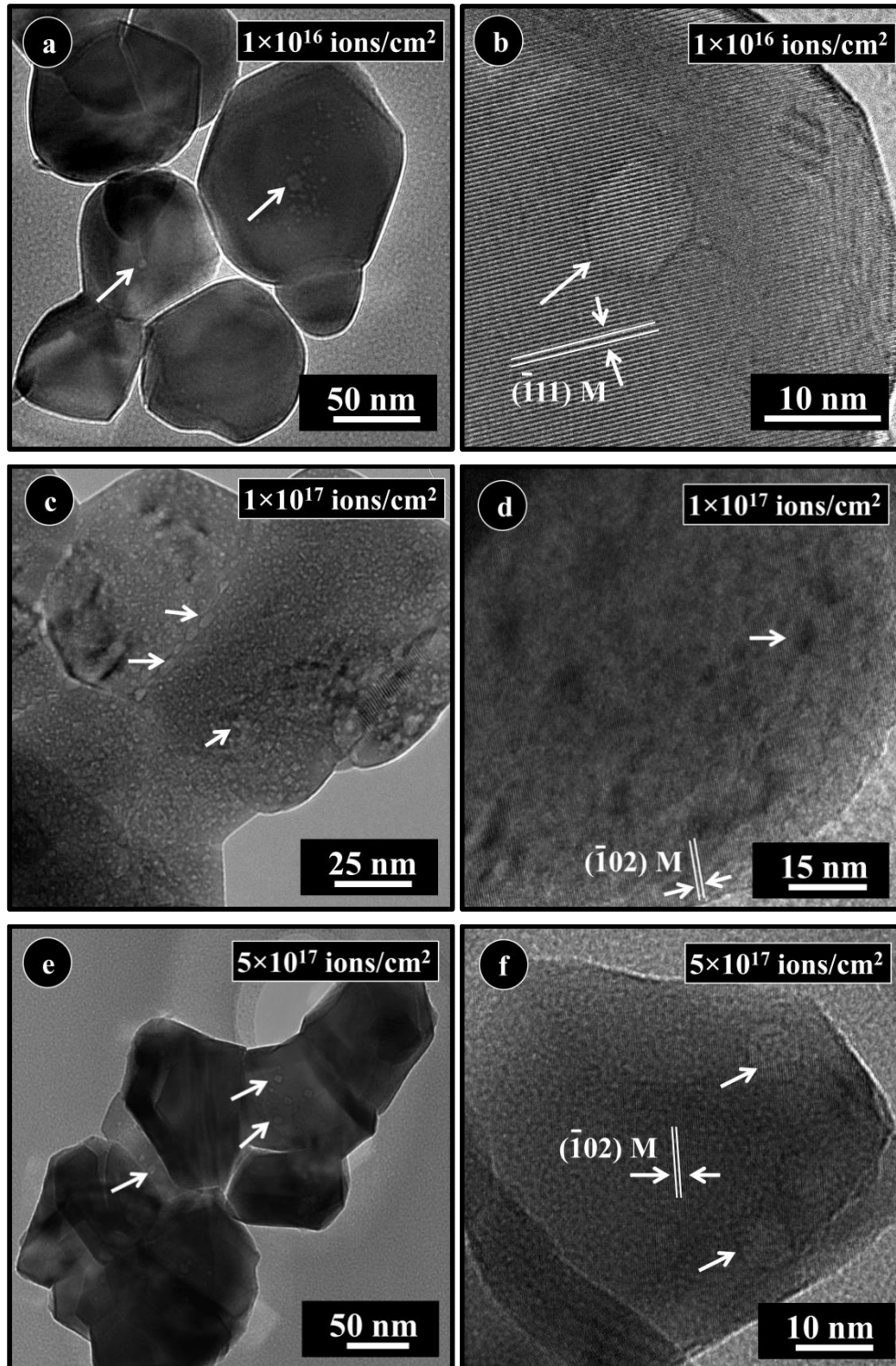


Figure 4.24 (a) Low magnification bright field TEM image of the zirconia samples irradiated with 60 keV Kr⁺ ions at 300 K for the ion fluence of (a) 1×10^{16} ions/cm², (c) 5×10^{16} ions/cm² and (e) 1×10^{17} ions/cm². (b), (d) and (e) show the corresponding HRTEM images of the samples. All the TEM micrographs are recorded in underfocus condition.

In summary, the TEM observations reveal that Kr^+ ion irradiation at room temperature, results in the formation of krypton bubbles. The bubbles are seen only inside the grains for the lower ion fluence (1×10^{16} ions/cm²) and the highest ion fluence (5×10^{17} ions/cm²). Interestingly, for the ion fluence of 1×10^{17} ions/cm², the bubbles are seen both inside the grains and on the grain boundaries.

4.4.3.2. Effects of ion irradiation at low temperature

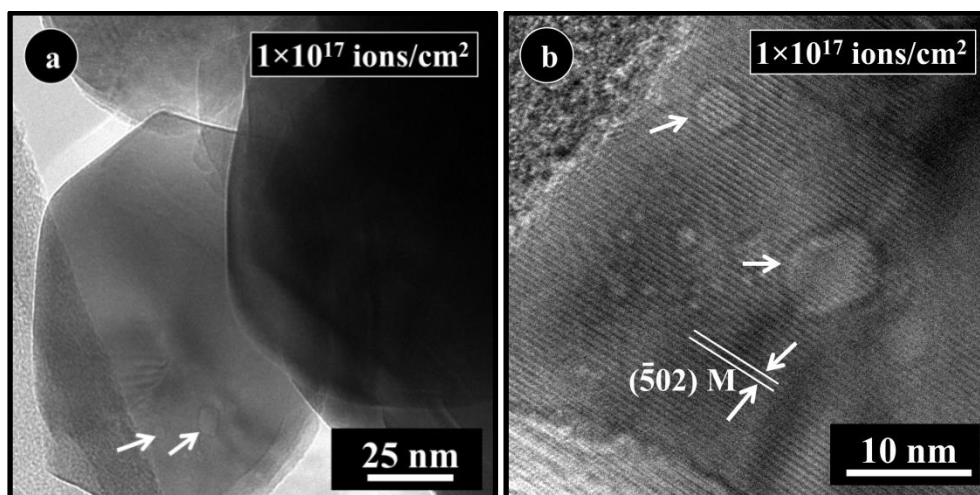


Figure 4.25 (a) Low magnification bright field TEM image and (b) HRTEM image of zirconia sample irradiated with 60 keV Kr^+ ions at 143 K for the ion fluence 1×10^{17} ions/cm². Both the images are recorded in underfocus condition. The $(\bar{5}02)$ plane of the monoclinic phase is marked in (b).

Figure 4.25 shows the TEM images of the zirconia samples irradiated with 60 keV Kr^+ ions at 143 K, for the ion fluence of 1×10^{17} ions/cm². Figure 4.25(a) shows the low magnification bright field TEM image and Figure 4.25(b) shows the HRTEM image of the Kr^+ ion irradiated sample (1×10^{17} ions/cm²). The TEM images clearly show the presence of spherical krypton bubbles. The bubbles are seen only inside the grains. The $(\bar{5}02)$ plane of zirconia is clearly marked and corresponding to monoclinic structure of the zirconia. It is observed that for the same ion fluence, the number of krypton bubbles present in the sample irradiated at low temperature is less than the number of krypton bubbles present in the samples irradiated at room temperature.

The bubble size distribution is plotted and shown in Figure 4.26. The bubble areal density was also calculated. Table 4.1 shows the values of the average bubble size and the areal density of the bubbles. It is observed from Table 4.1, that the average size of the bubbles increases with the ion fluence when the ion irradiation was carried at 300 K. It is also observed that for the same ion fluence (1×10^{17} ions/cm²), the average bubble size is

larger (5.4 nm) when the irradiation is carried out at 300 K compared to the average bubble size (1.1 nm) when the irradiation is carried out at 143 K.

The bubble areal density is less in case of ion irradiation carried out at 143 K compared to the bubble areal density present in the zirconia samples ion irradiated at 300 K. It is also observed that, in the case of room temperature irradiation, the areal number density of the bubble increases with ion fluence upto 1×10^{17} ions/cm² and then decreases for the ion fluence 5×10^{17} ions/cm².

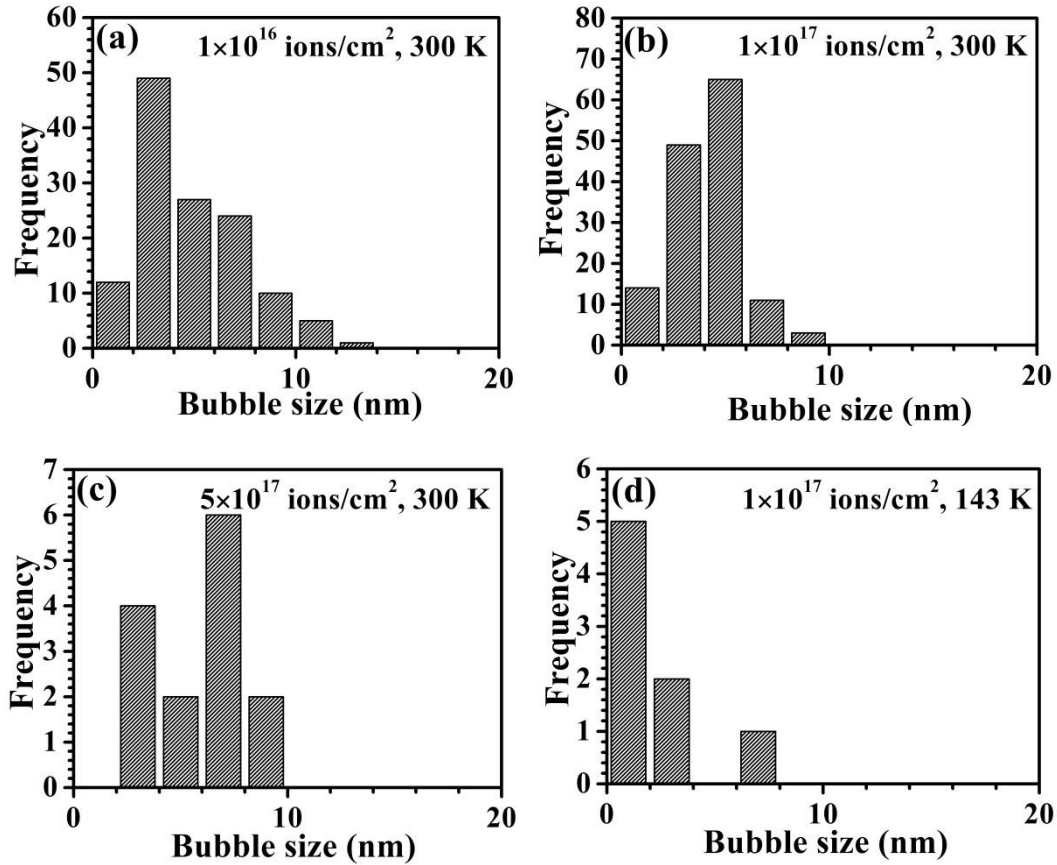


Figure 4.26 The bubble size distribution of the Kr^+ ion irradiated ZrO_2 samples for the ion fluence of (a) 1×10^{16} ions/cm² (300 K), (b) 1×10^{17} ions/cm² (300 K) (c) 2×10^{17} ions/cm² (300 K) and (d) 1×10^{17} ions/cm² (143 K)

4.5. Bubble induced swelling in ion irradiated zirconia

In the case of nuclear fuel materials, the effects of inert gases are one of the major concerns. As described in Chapter 1, inert gases either get released from the fuel, or precipitates inside the fuel leading to the swelling of the material. When TEM micrographs are used to calculate bubble induced swelling, the following equation is generally used

$$S = \frac{\left(\frac{\pi}{6} \sum d^3\right)}{st} \times 100\% \quad \text{Eqn.4.1}$$

where S is the swelling in percentage, d is the average diameter of the bubbles, s is the area of measurement (*i.e.*, the area of the TEM micrograph), t is the thickness of the specimen. In the present experiments, t is taken as 50 nm (measured using EELS which is not given).

Table 4.1 The table lists the average bubble size and the areal density of bubbles for all the ion irradiated zirconia sample.

Ion (Energy)	Sample temperature	Ion Fluence (ions/cm ²)	Average Bubble size (nm)	Bubble areal density (×10 ¹⁵ /m ²)	Swelling (%)
He ⁺ (120 keV)	300 K	1×10 ¹⁶	1.6	8	1.4
		2×10 ¹⁷	1.6	24	2.7
	143 K	2×10 ¹⁷	2.9	3	0.009
Ar ⁺ (120 keV)	300 K	5×10 ¹⁶	1.7	18	0.09
		1×10 ¹⁷	1.9	120	1.6
	143 K	2×10 ¹⁷	2.9	3	0.009
Kr ⁺ (60 keV)	300 K	1×10 ¹⁶	2.8	10	0.03
		1×10 ¹⁷	5.4	32	0.04
		5×10 ¹⁷	7.5	6	0.1
	143 K	1×10 ¹⁷	1.1	3	0.03

Table 4.1 shows the swelling observed in zirconia samples upon He⁺, Ar⁺ and Kr⁺ ion irradiation (at 300 K and at 143 K). It is observed from Table 4.1 that, in all the cases, the bubble induced swelling increases with the ion fluence. It is also observed that the swelling is more when the irradiations are carried out at room temperature compared to the irradiation at low temperature. This is because at low temperatures the defects are immobile and hence cannot assist in the bubble formation. It is further observed that the swelling caused by Kr⁺ ions is relatively less when compared to the swelling caused by He⁺ and Ar⁺ ions. This is due to the sputtering of the ion irradiated layers by the Kr⁺ ions due to its high sputtering yield (8.8 atoms/ion).

4.6. Discussion

Low energy inert gas ion irradiation on monoclinic zirconia led to partial phase transformation from monoclinic to tetragonal structure irrespective of the ions and the

irradiation temperatures. The phase transformation rate is found to be faster when the ion irradiation was carried out at 143 K. It is also observed that, strain is produced in the zirconia samples, irrespective of the ion irradiation temperatures and the ions (He^+ , Ar^+ and Kr^+) used. Further, SEM and TEM observations show the changes in morphology and bubble induced swelling.

The SEM studies reveal that (i) the porosity of the sample increases with the ion fluence, with a reversal in case of the highest ion fluences and (ii) there is joining and junction formation between the zirconia grains. It is known that when the ions are irradiated in a target, vacancies and interstitials are produced. Since the interstitials are capable of moving depending on their recoil energy, there is an inhomogeneous distribution of interstitials and vacancies in the zirconia. The inhomogeneous distribution of defects leads to inhomogeneous stress distribution, leading to local structural deformation in zirconia. These zirconia grains are damaged by the primary ions (He^+ , Ar^+ and Kr^+) and by the cascade collisions. In addition to this, the ion irradiation induced damage, is likely to form dangling bonds on the grain surface leading to the joining of the grains.

Formation of junction was earlier reported in inorganic nanowires[147]. Vacancies and lattice defects at the junction of two zirconia grains created as a result of incident ions and recoiled atoms, leads to the formation of dangling bonds on their surfaces. This leads to the covalent bonding between the zirconia grains at their junction. However, the ion irradiation effects should have a deeper impact than the chemical bonding between the two zirconia grains. The surface of the zirconia grains could undergo a local melting due to the heat produced by ion irradiation. This further helps in the large scale joining and network formation. In the present work, the ion irradiation induced joining is observed in moderate ion fluences involving reasonably low energy ions (120 keV and 60 keV). Most of the works reported for ion beam induced melting, were involved with very low energy ion beams and high power pulsed electron beam.

In addition to the ion irradiation, high degree of curvature of the nano grains could also encourage melting of the surface at temperatures, that is at a fraction of the melting points[156]. The surface melting and its subsequent rapid solidification would lead to the joining and formation of junctions. As the junction and network formation depends on the surface disorder and the local melting, optimal ion fluences and incident energy of the ions are required for the formation of these junctions. The typical threshold energy for the displacement of the target atoms due to incident ion is about 10-25 eV and the typical

binding energy of the surface atom is about 1-5 eV. From the present work, it is observed that the ion fluence plays a crucial role in determining the joining of the grains. It is known that minimum ion fluence is required to create the surface disorder[147].

In case of He^+ (120 keV) and Ar^+ (120 keV) ion irradiation, as the energy is high, the range of the incident ion exceeds the size of the zirconia grains (*see* Table 3.1). In this case the energy transferred from the ions to the sample is not optimal and hence they could not produce enough surface defects and melting required for the joining and formation of junctions. As a result the joining of the grains is not more pronounced. In case of the Kr^+ (60 keV) ion irradiation, range of the incident ions is within the grain size of zirconia (*see* Table 3.1), they could produce surface defects and melting required for the joining and formation of junctions. As minimum ion fluence is necessary to create sufficient disorder, when the ion fluences are lower, there could not be enough joining of the grains as seen in the SEM images of the He^+ , Ar^+ , Kr^+ ion irradiated samples. For higher ion fluences, sputtering and local melting could be high, leading to pronounced joining of the grains (*refer* Figure 4.12).

In case of Kr^+ (60 keV) ion irradiation, shallow range of the incident ions (23 nm) and the high sputtering yield (8.8 atoms/ion) leads to sputtering. Sputtering can lead to the higher rate of re-deposition and the local melting due to the heat produced by ion irradiation could further help in the large scale joining and network formation. However, in case of the zirconia samples ion irradiated at 143 K, the sputtering was significant enough to remove the irradiated layer for the highest ion fluence 5×10^{17} ions/cm² (*refer* Figure 4.13)

In addition to the joining of the grains, TEM investigations show that the bubbles are formed upon ion irradiation (He^+ , Ar^+ and Kr^+) irrespective of the ion irradiation temperatures (300 K and 143 K). In case of the helium and argon ion irradiation, the bubbles are formed inside the grains. However, in case of Kr^+ ion irradiated samples, some bubbles are formed both inside the grains and along the grain boundaries. Irrespective of the ions used for the irradiation purpose, the bubble density is larger when the ion irradiation was carried out at 300 K, compared to the ion irradiation carried out at 143 K. Bubbles formed are spherical in shape for all the ions used for the experimental purpose (He^+ , Ar^+ and Kr^+). However in case of He^+ ion irradiation (300 K), spherical as well as faceted bubbles are seen.

Bubbles and bubble induced swelling are a commonly occurring phenomenon in the nuclear fuels. Bubbles get nucleated either in a homogeneous fashion or in a

heterogeneous fashion. Homogeneous process is the one when the bubble grows when a gas atom by atomic migration gets attracted to the existing bubble. Heterogeneous process is attributed when the formed bubbles grows by trapping vacancies, which (vacancies) in turn leads to trapping of gaseous atoms and there by contributing to the bubble growth. Heterogeneous nucleation is quite a common phenomenon occurring when the bubbles comes in contact with the dislocation lines. Formation of the bubbles depends on minimum number of gas atoms (that are able to form a stable nucleus), the rate at which the lattice vacancies are produced to maintain the stability of the nucleated core and the mobility of the gas atoms.

In case of the He^+ and Ar^+ ion irradiation the bubbles are formed as result of heterogeneous nucleation process. When the vacancies and interstitials are farther away from the grain boundaries the vacancies inside the grains traps the gas atoms leading to the formation of bubbles. The cavity is generally considered to be a bubble when the pressure of gas atoms tends to make the cavity in a spherical shape. The cavity tends to be spherical when the surface energy is altered by the gas atom or when the gas pressure is high enough. The faceted bubbles are the result of the periodicity of the lattice. The cavity tends to be faceted and the facet lie along the closed packed planes[157].

In the case of krypton ion irradiation at room temperature, the bubbles are found only inside the grains for the ion fluences of 1×10^{16} ions/cm², 5×10^{17} ions/cm² and both inside and on the grain boundaries in the case of ion fluence of 1×10^{17} ions/cm². The bubble density is also found to decrease for the ion fluence 5×10^{17} ions/cm². In the case of ion fluence 1×10^{16} ions/cm², the vacancies and interstitials present inside the grains if they are farther apart compared to the grain size and does not recombine. The vacancies present inside the grains, traps the gas atoms leading to the formation of bubbles and its growth. In case of ion fluence 1×10^{17} ions/cm², due to their higher mobility than the vacancies, the interstitials gets attracted to the grain boundaries larger in number, leading to the vacancies inside the grains to trap the gas atoms forming bubbles and bubble growth. However theoretical modeling has also shown that in addition to the vacancy hopping process to anneal the vacancies present inside the grains some interstitials could also be emitted back to the grains and combine with the vacancies[158]. Hence the vacancies that are present in the grain boundaries tend to trap the gas atoms forming bubble. For the ion fluence 5×10^{17} ions/cm² the bubbles formed on the grain boundaries in the previous lower ion fluence (1×10^{17} ions/cm²) as a result of continuous ion irradiation leads to more bubbles and these bubbles links together and finally gets released out of the grain

boundaries. This results in the low areal density of the bubbles for the ion fluence 5×10^{17} ions/cm² than the ion fluence 1×10^{17} ions/cm².

Also, it is observed that the bubble density is considerably less when the ion irradiation was carried out at 143 K. In case of ion irradiation at low temperature using He⁺, Ar⁺ and Kr⁺ ions, the defects are generally rendered immobile at such low temperature and hence prohibits the bubble movement and its growth. Only such vacancies which had directly encountered the gas atoms lead to the formation of bubbles[10].

Swelling is found to be dependent on the ion mass, ion fluence and ion irradiation temperature. It is observed that the bubble density and swelling increases with ion fluence irrespective of the ions used for the irradiation. This is expected, as bubble density is proportional to bubble induced swelling. Swelling is low when the ion irradiation was carried out at 143 K. This is because the defects produced during ion irradiation at low temperatures are immobile and there are not enough mobile defects to assist in the bubble formation. The less bubble density subsequently leads to less bubble induced swelling. Compared to the Ar⁺ ion irradiation, Kr⁺ ions are expected to produce more swelling in the zirconia samples, as the displacement per atom is high for the Kr⁺ ions (see Table 3.1)[37]. However, in the present experiments, the swelling in the Kr⁺ ion irradiated zirconia sample is less than Ar⁺ ion irradiated zirconia sample. This is because of the shallow range (23 nm) of the Kr⁺ ions and its high sputtering yield (8.8 atoms/ion) compared to the Ar⁺ ion (4.6 atoms/ion), the irradiated layer might have removed due to sputtering.

4.7. Conclusions

As-sintered monoclinic zirconia samples prepared by the thermal decomposition method were irradiated with Kr⁺ (60 keV), Ar⁺ (120 keV) and He⁺ (120 keV) ions using the 150 kV accelerator. Upon ion irradiation, (irrespective of the ions used and ion irradiation temperatures), the zirconia sample undergoes a partial phase transformation. There is also ion beam induced strain in the zirconia samples upon ion irradiation. SEM images reveal that there is joining of grains and junction formation. Along with the phase transformation, helium, argon and krypton bubbles are also formed in the zirconia samples irrespective of the ion irradiation temperatures (300 K and 143 K). Even though the bubbles formed during the ion irradiation are spherical in shape, few faceted bubbles are also observed in case of He⁺ ion irradiation. The bubble density and swelling is less when the ion irradiation was carried out at 143 K. Lower bubble density in the zirconia samples

ion irradiated at 143 K is attributed to the immobility of the defects. Less swelling in the Kr^+ ion irradiated zirconia samples (compared to Ar^+ ion irradiated zirconia samples) is attributed to the high sputtering yield of the Kr^+ ions where irradiated layer might have removed during irradiation.

Optical properties of ion irradiated monoclinic zirconia

5.1. Introduction

As mentioned in the previous chapters, the inert gas ion irradiation (He^+ , Ar^+ and Kr^+ ion irradiation at 300 K and 143 K) on monoclinic zirconia shows monoclinic to tetragonal phase transformation along with the formation of inert gas bubbles. Recently, ultrafast laser has produced similar kind of defects in oxides which are equivalent to swift heavy ion (SHI) irradiation where electronic energy loss is the dominant process. Rittman *et al.*, [108] had employed ultrafast laser irradiation on ZrO_2 and had observed monoclinic to tetragonal phase transformation and the results are identical to those produced by SHI irradiation [42]. The ability of ultrafast lasers and SHI irradiation to rearrange and disorder the structures through identical damage processes, provides the link between the two processes (ultrafast and SHI irradiation) of depositing large amounts of ionizing energy into the material.

In order to produce the effects of fission fragment damage (typically $\sim 1\text{MeV}/\text{amu}$) which is equivalent to SHI irradiation, laser irradiation was employed. Further, to understand the evolution of defects, zirconia (laser irradiated, ion irradiated and laser plus ion irradiated) samples were analyzed using photoluminescence spectroscopy and time resolved photoluminescence (TRPL) measurements.

5.2. Experiment

ZrO_2 pellets (as-sintered and He^+ , Ar^+ , Kr^+ ion irradiated) were irradiated using a KrF excimer laser (M/s. COMPexPro. 205) of wavelength 248 nm with a pulse duration of about 25 ns. The power, energy and repetition rate of the laser beam was 680 mW, 133 mJ and 5 Hz respectively. The laser was focused on the pellet surface at normal incidence. The number of laser shots used for the laser irradiation was 200 and 2000 shots and the laser irradiation was carried out in air. The zirconia samples with different ion and laser irradiation conditions are coded and given in Table 5.1. To investigate the morphology of the laser irradiated surface, SEM experiments were carried out with cross beam 340 (Carl Zeiss make) FIB-FESEM. Integrated AFM, Raman, PL spectrometer (model: WITec alpha 300 RA) was used for PL measurements with an excitation energy at 3.49 eV (wavelength 355 nm). The photoluminescence spectra were recorded with the laser power of 0.5 mW. Time resolved photoluminescence measurements were carried out using FLS 980

Edinburg. FLS 980 has a nanosecond flash lamp and picosecond pulsed diode laser for TCSPC measurements. Wavelength used for the measurements was 355 nm and the resolution of the TCSPC detector was 10 ps.

Table 5.1 The table explains the convention followed while giving codes for different zirconia samples which were initially irradiated with an inert gas ion for different ion fluences, at 300 K or 143 K, followed by laser irradiation upto 200 shots or 2000 shots. The sample code does not include information about the inert gas ion used for irradiation.

Sample codes				Number of shots during laser irradiation		
				NIL	200 shots	2000 shots
Details of inert gas ion irradiation	As-prepared			Z-Asp	Z-200LI	Z-2000LI
	Temperature and ion fluence of inert gas ion irradiation	300 K	1×10^{16}	Z-RT-1E16	Z-RT-1E16-200LI	Z-RT-1E16-2000LI
			5×10^{16}	Z-RT-5E16	Z-RT-5E16-200LI	Z-RT-5E16-2000LI
			1×10^{17}	Z-RT-1E17	Z-RT-1E17-200LI	Z-RT-1E17-2000LI
			5×10^{17}	Z-RT-5E17	Z-RT-5E17-200LI	Z-RT-5E17-2000LI
		143 K	1×10^{16}	Z-LT-1E16	Z-LT-1E16-200LI	Z-LT-1E16-2000LI
			5×10^{16}	Z-LT-5E16	Z-LT-5E16-200LI	Z-LT-5E16-2000LI
			1×10^{17}	Z-LT-1E17	Z-LT-1E17-200LI	Z-LT-1E17-2000LI
			5×10^{17}	Z-LT-5E17	Z-LT-5E17-200LI	Z-LT-5E17-2000LI

5.3. SEM analysis of laser irradiation effects on ion irradiated surfaces

5.3.1. SEM analysis of laser irradiated zirconia

Figure 5.1 shows the SEM images of laser irradiated zirconia samples. Figure 5.1(a) shows the morphology of the laser (200 shots) irradiated surface where the inset of Figure 5.1(a) shows the laser spot. When comparing the images of Figure 4.1(a) (before laser irradiation) and Figure 5.1(a) (after laser irradiation), the porosity of the sample has reduced drastically upon laser irradiation. The grain size was measured and the size distribution is shown as inset of Figure 5.1(a). The average size of the grain is found to be ~413 nm. This value is much larger than the average grain size (~ 55 nm) of the as-sintered zirconia sample.

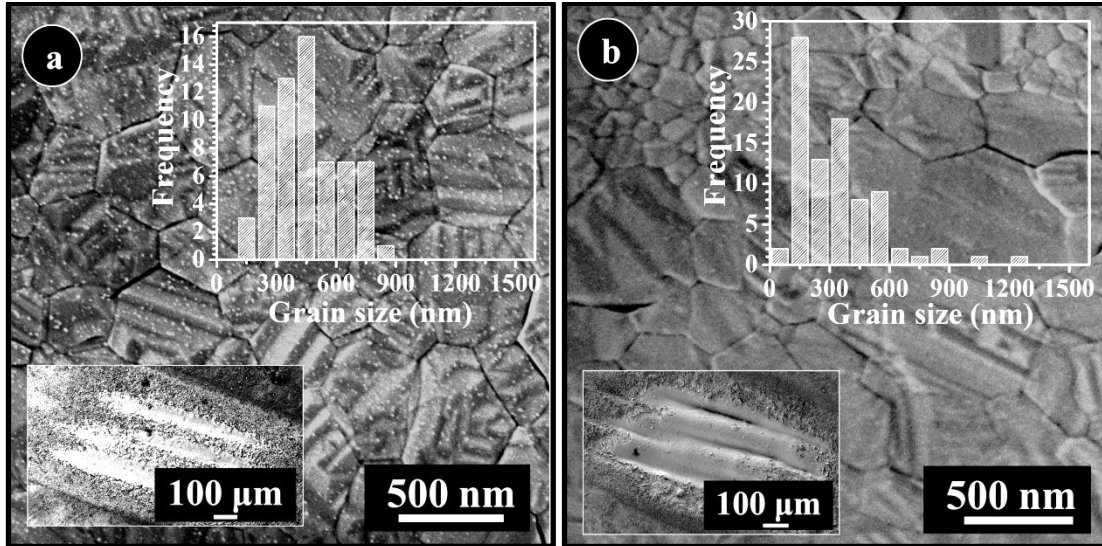


Figure 5.1 SEM images of the laser irradiated zirconia samples for the laser shots of (a) 200 shots and (b) 2000 shots.

Figure 5.1(b) shows the SEM image of the laser (2000 shots) irradiated surface of the zirconia sample (inset Figure 5.1(b) shows the laser spot). The average grain size is found to be ~ 271 nm (size distribution given in the inset of Figure 5.1(b)). It is also observed that the grains have very sharp, distinct, clear boundaries upon laser irradiation.

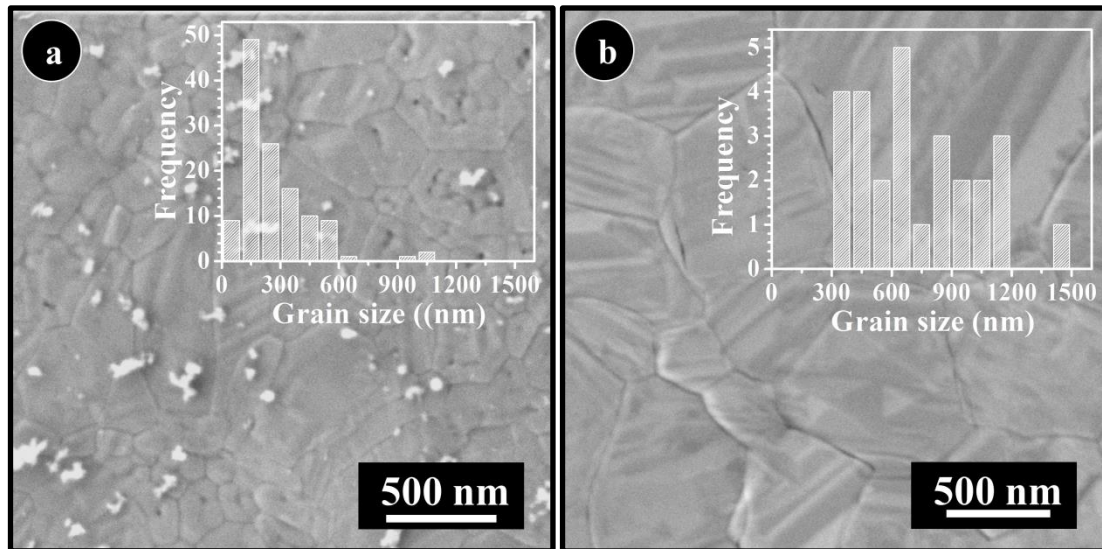


Figure 5.2 SEM images of the laser (200 shots) irradiated on He^+ ion (at 300 K) irradiated zirconia samples for the ion fluences of (a) 1×10^{16} ions/cm² and (b) 2×10^{17} ions/cm².

5.3.2. SEM analysis on laser irradiated on He^+ ion irradiated zirconia samples

The average grain size of the He^+ ion (300 K and 143 K) irradiated and laser (200 shots and 2000 shots) irradiated on He^+ ion irradiated zirconia samples were measured and the values are shown in Table 5.2. The SEM images of the laser (200 and 2000 shots)

irradiation on He^+ ion (300 K and 143 K) irradiated zirconia samples are presented in proceeding sections.

Table 5.2 Average grain size values of the He^+ ion irradiated at 300 K and 143 K, and laser (200 and 2000 shots) irradiation on He^+ ion irradiated zirconia samples

He^+ ion irradiation		Average grain size (nm)		
Temperature	Ion fluence (ions/cm ²)	Before laser irradiation	After laser irradiation	
			200 shots	2000 shots
Room Temperature (300 K)	1×10^{16}	75	150	248
	5×10^{16}	87	146	143
	1×10^{17}	72	155	148
	2×10^{17}	72	650	452
Low Temperature (143 K)	1×10^{16}	66	344	152
	5×10^{16}	63	146	149
	1×10^{17}	75	146	146
	2×10^{17}	82	140	152

5.3.2.1. Laser (200 shots) irradiation on He^+ ion irradiated (at 300 K) samples

Figure 5.2(a) and Figure 5.2(b) shows the SEM images of laser irradiation (200 shots) on the He^+ ion irradiated (at 300 K) zirconia samples for the ion fluences of 1×10^{16} ions/cm² and 2×10^{17} ions/cm² respectively. When comparing the SEM images of the laser irradiated sample (*see* Figure 5.2(a)) with Figure 4.2(b) (before laser irradiation), it is observed that the sample has lost its porosity. Upon laser irradiation, the average grain size (~ 150 nm and ~ 650 nm for the ion fluences of 1×10^{16} ions/cm² and 2×10^{17} ions/cm² respectively) is also found to be larger than the average grain size of the samples before laser irradiation (~ 75 nm and ~ 72 nm for the ion fluences of 1×10^{16} ions/cm² and $\sim 2 \times 10^{17}$ ions/cm² respectively).

5.3.2.2. Laser (2000 shots) irradiation on He^+ ion irradiated (at 300 K) samples

SEM images of the laser irradiated (2000 shots) on He^+ ion irradiated (at 300 K) zirconia samples for the ion fluences 1×10^{16} ions/cm² and 2×10^{17} ions/cm² are shown in Figure 5.3(a) and Figure 5.3(b) respectively. It is observed that there is a reduction in the porosity of the samples upon laser irradiation (*refer* Figure 4.2 (b)). After laser irradiation, the average grain size for the ion fluences 1×10^{16} ions/cm² and 2×10^{17} ions/cm² are ~ 248 nm and ~ 452 nm respectively. However, before laser irradiation, the average grain size is ~ 75 nm and ~ 72 nm for the ion fluences 1×10^{16} ions/cm² and 2×10^{17} ions/cm²

respectively. Hence, in addition to the reduction in the porosity, the average grain size has also increased upon laser irradiation.

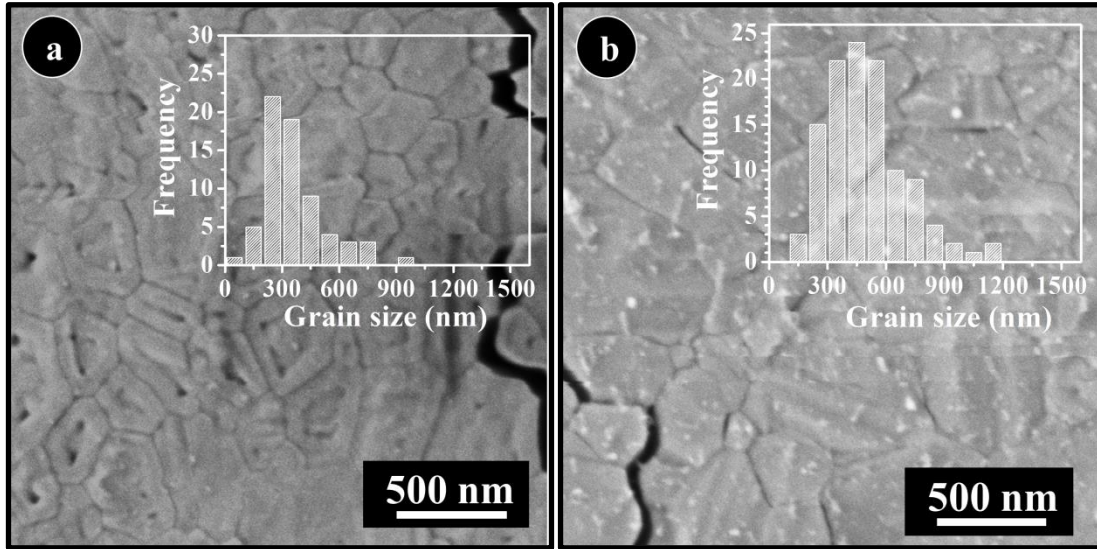


Figure 5.3 SEM images of the laser (2000 shots) irradiated on He⁺ ion (at 300 K) irradiated zirconia samples for the ion fluences of (a) 1×10^{16} ions/cm² and (b) 2×10^{17} ions/cm².

5.3.2.3. Laser (200 shots) irradiation on He⁺ ion irradiated (at 143 K) samples

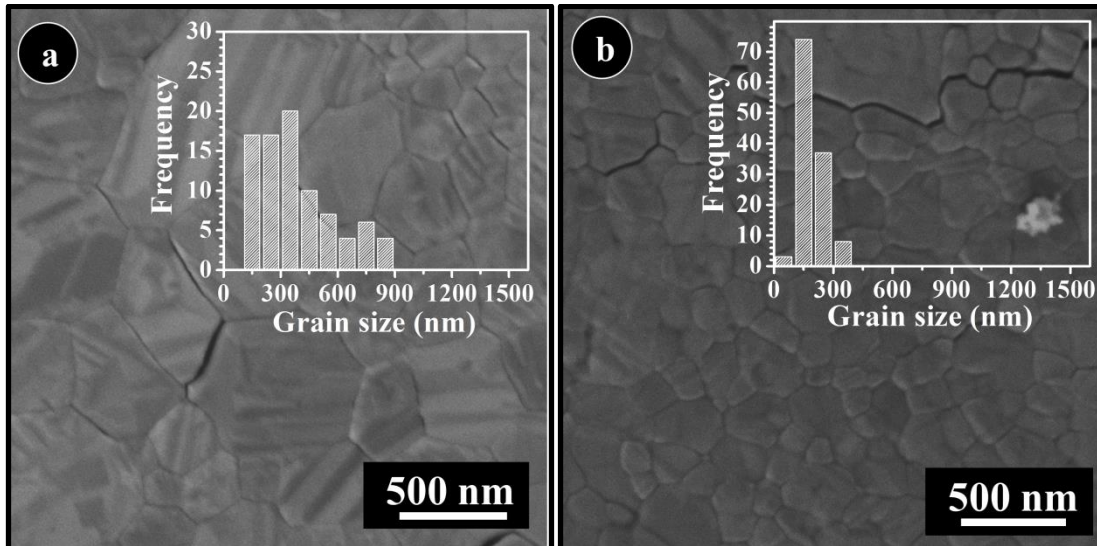


Figure 5.4 SEM images of the laser (200 shots) irradiated on He⁺ ion (at 143 K) irradiated zirconia samples for the ion fluences of (a) 1×10^{16} ions/cm² and (b) 2×10^{17} ions/cm².

Figure 5.4(a) and Figure 5.4(b) show the SEM images of the laser irradiated (200 shots) on He⁺ ion irradiated (at 143 K) zirconia samples for the ion fluences 1×10^{16} ions/cm² and 2×10^{17} ions/cm² respectively. Upon looking at the SEM images, it is noticed that the laser irradiation has resulted in the reduction of porosity (refer Figure 4.4(a) and Figure 4.4(d)). Upon laser irradiation, the grain size is found to be ~ 344 nm and ~ 140 nm for ion fluences 1×10^{16} ions/cm² and 2×10^{17} ions/cm² respectively. The values are much

larger than the average grain size (~ 66 nm for 1×10^{16} ions/cm² and ~ 82 nm for 2×10^{17} ions/cm²) before laser irradiation. Thus laser irradiation has resulted in the increase in average size of the grains.

5.3.2.4. Laser (2000 shots) irradiation on He⁺ ion irradiated (at 143 K) samples

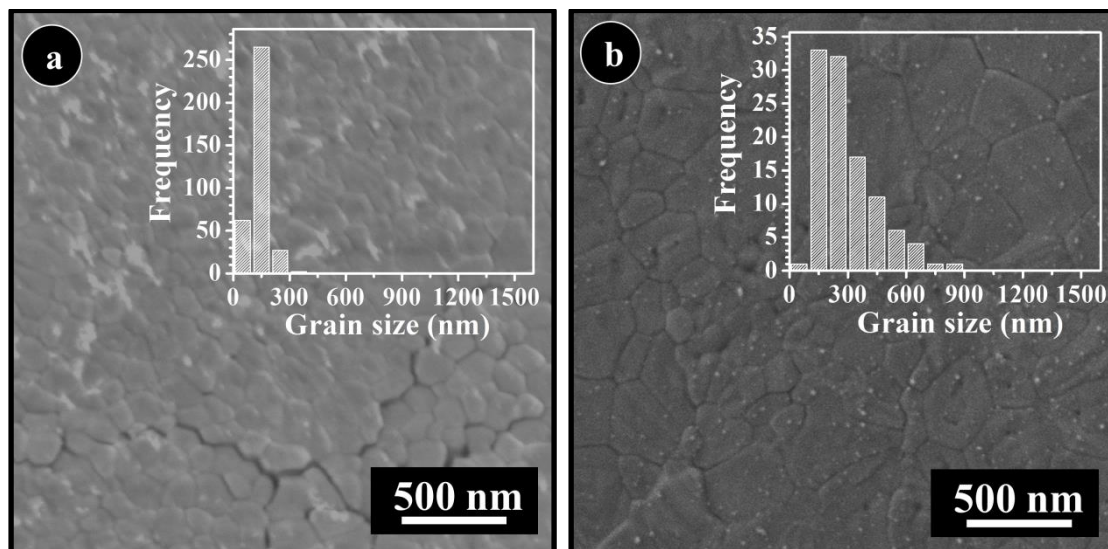


Figure 5.5 SEM images of the laser (2000 shots) irradiated on He⁺ ion (at 143 K) irradiated zirconia samples for the ion fluences of (a) 1×10^{16} ions/cm² and (b) 2×10^{17} ions/cm².

Figure 5.5(a) and Figure 5.5(b) shows the SEM images of the laser irradiated (2000 shots) on He⁺ ion irradiated (at 143 K) zirconia samples for the ion fluences 1×10^{16} ions/cm² and 2×10^{17} ions/cm² respectively. The observations are similar to the samples ion irradiated at 300 K. The samples has lost its porosity (*see* Figure 4.4 (a) and Figure 4.4 (d)) and the average grain size has increased, compared to the samples before laser irradiation. Upon laser irradiation, the average grain size is ~ 152 nm and ~ 152 nm for the ion fluences 1×10^{16} ions/cm² and 2×10^{17} ions/cm² respectively and these values are larger than the average grain size before laser irradiation (~ 66 nm for 1×10^{16} ions/cm² and ~ 82 nm for 2×10^{17} ions/cm²).

5.3.3. SEM analysis on laser irradiated on Ar⁺ ion irradiated zirconia samples

The average grain size of the Ar⁺ ion irradiated (at 300 K and 143 K) and laser irradiation (200 and 2000 shots) on Ar⁺ ion irradiated samples were measured and the values are shown in Table 5.3. The SEM images of the laser irradiation (200 and 2000 shots) on Ar⁺ ion irradiated (at 300 K and 143 K) samples are discussed in proceeding sections.

Table 5.3 Average grain size values of the Ar^+ ion irradiated (at 300 K and 143 K) and laser (200 and 2000 shots) irradiation on Ar^+ ion irradiated zirconia samples

Ar^+ ion irradiation		Average grain size (nm)		
		Before laser irradiation	After laser irradiation	
Temperature	Ion fluence (ions/cm ²)		200 shots	2000 shots
Room Temperature (300 K)	1×10^{15}	59	155	150
	5×10^{15}	73	246	249
	1×10^{16}	74	150	251
	5×10^{16}	72	148	149
	1×10^{17}	85	-	152
Low Temperature (143 K)	2×10^{15}	94	246	247
	1×10^{16}	-	-	300
	5×10^{16}	64	349	345
	2×10^{17}	74	250	150

5.3.3.1. Laser (200 shots) irradiation on Ar^+ ion irradiated (at 300 K) samples

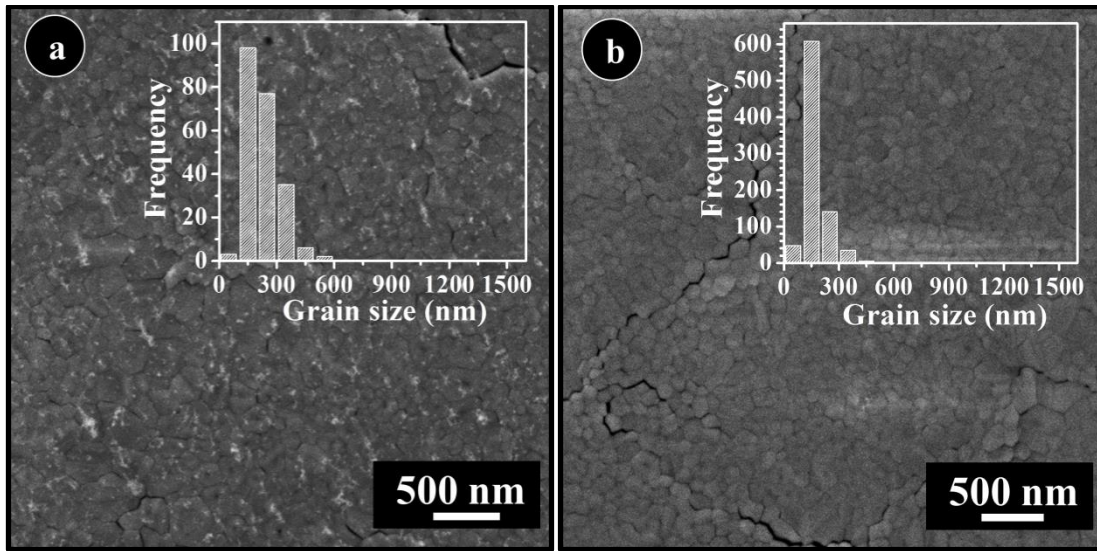


Figure 5.6 SEM images of the laser (200 shots) irradiated on Ar^+ ion irradiated (at 300 K) zirconia samples for the ion fluences of (a) 1×10^{16} ions/cm² and (b) 5×10^{16} ions/cm²

The SEM images of the laser (200 shots) irradiated on Ar^+ ion irradiated (at 300 K) zirconia samples for the ion fluences of 1×10^{16} ions/cm² and 5×10^{16} ions/cm² are shown in Figure 5.6(a) and Figure 5.6(b) respectively. Upon laser irradiation, the Ar^+ ion irradiated surfaces has also lost its porosity (refer Figure 4.7(c) and Figure 4.7(d)) and the average grain size was measured and found to be ~ 150 nm and ~ 148 nm for the ion fluences 1×10^{16} ions/cm² and for 5×10^{16} ions/cm² respectively. These values are larger than that of

the samples before laser irradiation (~ 74 nm for 1×10^{16} ions/cm² and ~ 72 nm for 5×10^{16} ions/cm²).

5.3.3.2. Laser (2000 shots) irradiation on Ar⁺ ion irradiated (at 300 K) samples

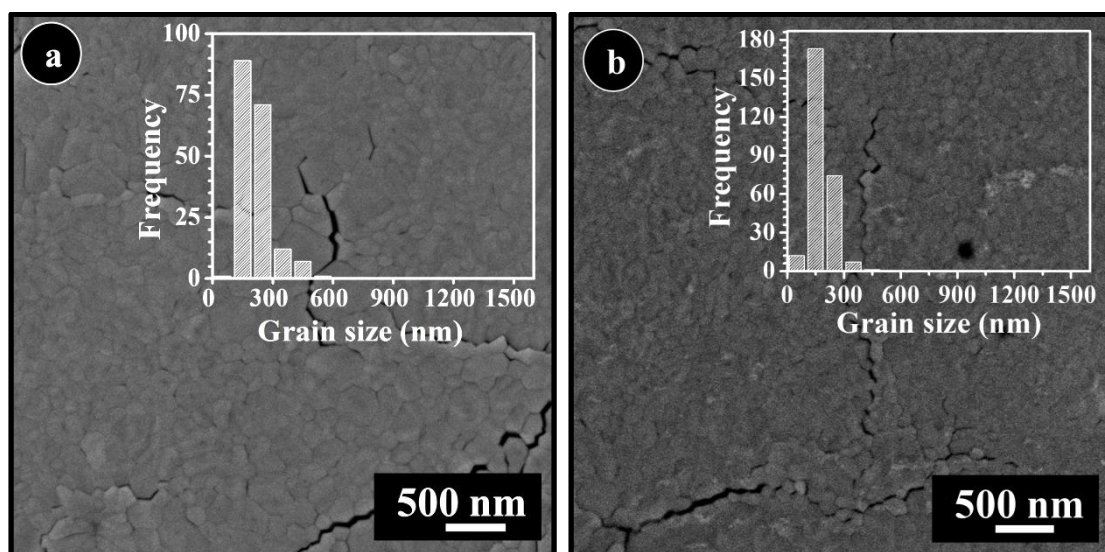


Figure 5.7 SEM images of the laser (2000 shots) irradiated on Ar⁺ ion irradiated (at 300 K) zirconia samples for the ion fluences of (a) 1×10^{15} ions/cm² and (b) 5×10^{16} ions/cm².

Figure 5.7(a) and Figure 5.7(b) shows the SEM images of the laser (2000 shots) irradiated on Ar⁺ ion irradiated (300 K) zirconia samples for the ion fluences of 1×10^{15} ions/cm² and 5×10^{16} ions/cm² respectively. The SEM images from the laser irradiated surface reveal that the samples have lost its porosity (*refer* Figure 4.7(a) and Figure 4.7(d)) and the average grain size (~ 150 nm and ~ 149 nm for the ion fluences 1×10^{15} ions/cm² and 5×10^{16} ions/cm² respectively) has increased, when the SEM images are compared to the ion irradiated samples (~ 74 nm for 1×10^{16} ions/cm² and ~ 72 nm for 5×10^{16} ions/cm²).

5.3.3.3. Laser (200 shots) irradiation on Ar⁺ ion irradiated (at 143 K) samples

SEM images of laser (200 shots) irradiated on the Ar⁺ ion (at 143 K) irradiated zirconia samples for the ion fluences 5×10^{16} ions/cm² and 2×10^{17} ions/cm² are shown in Figure 5.8(a) and Figure 5.8(b) respectively. The samples have lost its porous nature (*see* Figure 4.9) upon laser irradiation. The average grain size is ~ 349 nm and ~ 250 nm for the ion fluences 5×10^{16} ions/cm² and 2×10^{17} ions/cm² respectively after laser irradiation. The values are larger than the average grain size before laser irradiation (~ 64 nm for 5×10^{16} ions/cm² and ~ 74 nm for 2×10^{17} ions/cm²).

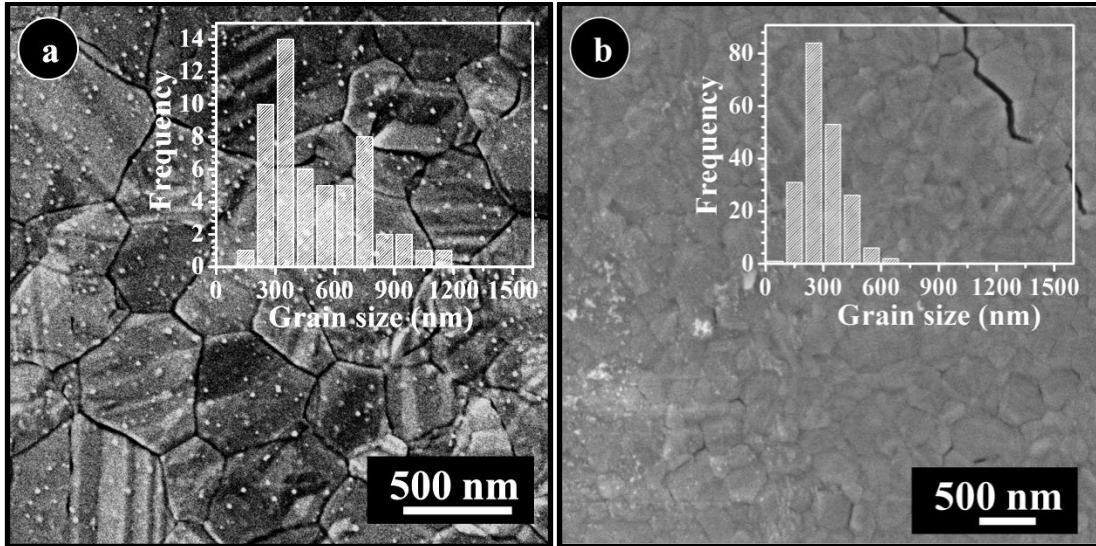


Figure 5.8 SEM images of the laser (200 shots) irradiated on Ar^+ ion irradiated (at 143 K) zirconia samples for the ion fluences of (a) 5×10^{16} ions/cm² and (b) 2×10^{17} ions/cm².

5.3.3.4. Laser (2000 shots) irradiation on Ar^+ ion irradiated (at 143 K) samples

Figure 5.9 (a) and Figure 5.9 (b) shows the SEM images of laser (2000 shots) irradiated on Ar^+ ion irradiated (at 143 K) zirconia samples for the ion fluences of 5×10^{16} ions/cm² and 2×10^{17} ions/cm² respectively. Looking at the SEM images of the laser irradiated surfaces, and comparing it with Figure 4.9 (before laser irradiation), it is noticed that there is a reduction in the porosity. The average grain size (~ 345 nm and 150 nm for the ion fluence 5×10^{16} ions/cm² and 2×10^{17} ions/cm²) is larger than the average grain size before laser irradiation (~ 64 nm for 5×10^{16} ions/cm² and 74 nm for 2×10^{17} ions/cm²).

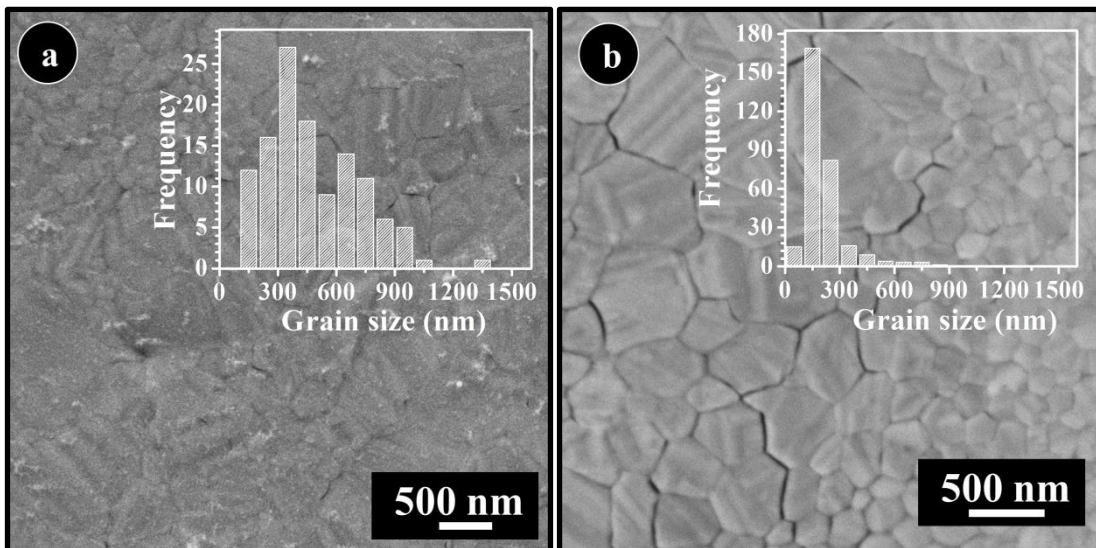


Figure 5.9 SEM images of the laser (2000 shots) irradiated on Ar^+ ion irradiated (at 143 K) zirconia samples for the ion fluences of (a) 5×10^{16} ions/cm² and (b) 2×10^{17} ions/cm².

5.3.4. SEM analysis on laser irradiated on Kr^+ ion irradiated zirconia samples

Table 5.4 Average grain size values of the Kr^+ ion irradiated (at 300 K and 143 K) and laser (200 and 2000 shots) irradiation on Kr^+ ion irradiated zirconia samples

Kr^+ ion irradiation		Average grain size (nm)		
		Before laser irradiation	After laser irradiation	
Temperature	Ion fluence (ions/cm ²)		200 shots	2000 shots
Room Temperature (300 K)	1×10^{16}	-	347	499
	5×10^{16}	-	250	345
	1×10^{17}	-	251	248
	5×10^{17}	-	152	353
Low Temperature (143 K)	1×10^{16}	70	254	658
	5×10^{16}	-	446	254
	1×10^{17}	-	251	536
	5×10^{17}	85	257	449

The average grain size of the Kr^+ ion irradiated (at 300 K and 143 K) and laser (200 and 2000 shots) irradiation on Kr^+ ion irradiated samples were measured and the values are shown Table 5.4. In the following sections, The SEM images of the laser (200 and 2000 shots) irradiated on Kr^+ ion irradiated zirconia samples are discussed.

5.3.4.1. Laser (200 shots) irradiation on Kr^+ ion irradiated (at 300 K) samples

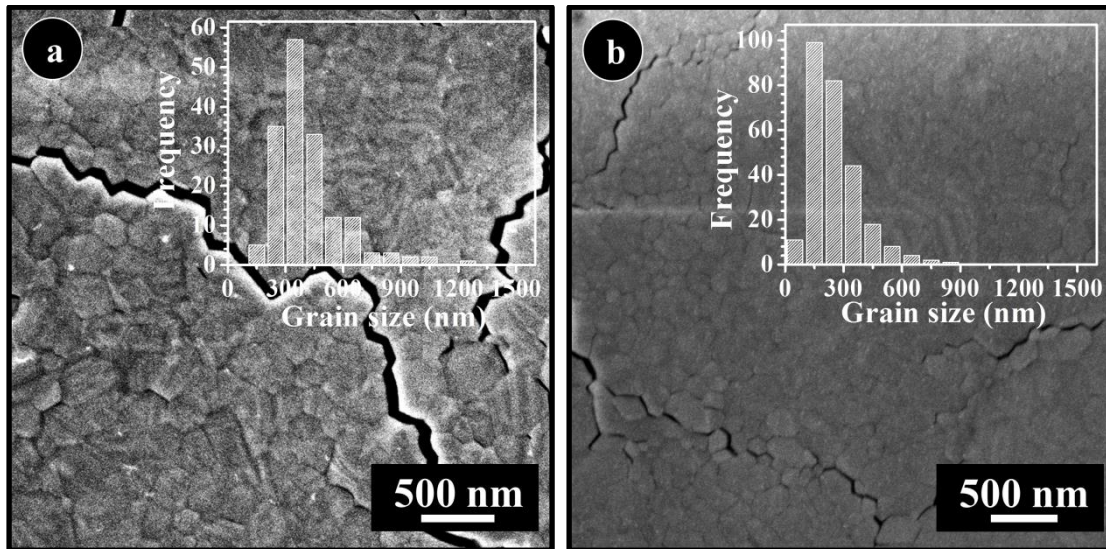


Figure 5.10 SEM images of the laser (200 shots) irradiated on Kr^+ ion irradiated (at 300 K) zirconia samples for the ion fluences of (a) 1×10^{16} ions/cm² and (b) 5×10^{17} ions/cm².

SEM images of the laser (200 shots) irradiated on Kr^+ ion irradiated (at 300 K) zirconia samples for the ion fluences 1×10^{16} ions/cm² and 5×10^{17} ions/cm² are shown in Figure 5.10(a) and Figure 5.10(b) respectively. When Figure 5.10(a) and Figure 5.10(b)

(after laser irradiation) are compared with the SEM images of the samples before laser irradiation (Figure 4.12(a) and Figure 4.12(c)), it is observed that, the sample has lost its porosity and grains with sharp, distinct boundaries are also clearly observed. The average size of the grain is found to be ~ 347 nm and ~ 152 nm for the ion fluences 1×10^{16} ions/cm² and 5×10^{17} ions/cm² respectively. Upon, laser irradiation, the high burn up structure is absent and it could be due to the grain growth and coalescence which might have reduced the porosity.

5.3.4.2. Laser (2000 shots) irradiation on Kr⁺ ion irradiated (at 300 K) samples

Figure 5.11(a) and Figure 5.11(b) shows the SEM images of the laser (2000 shots) irradiated on the Kr⁺ ion irradiated (at 300 K) zirconia samples for the ion fluences 1×10^{16} ions/cm² and 5×10^{17} ions/cm² respectively. When comparing Figure 5.11(a) and Figure 5.11(b) (after laser irradiation) with their corresponding SEM images (before laser irradiation (Figure 4.12(a) and Figure 4.12(c))), it is observed that the sample has lost its porosity and grains with clear grain boundaries are visible. Upon laser irradiation, the average grain size is found to increase significantly (~ 499 nm and ~ 353 nm for the ion fluences 1×10^{16} ions/cm² and 5×10^{17} ions/cm² respectively).

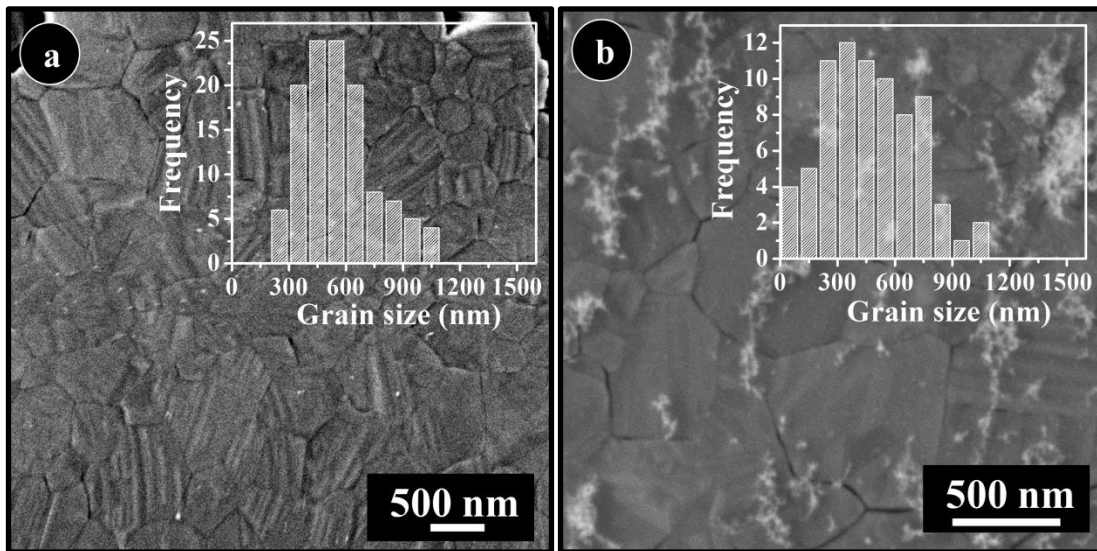


Figure 5.11 SEM images of the laser (2000 shots) irradiated on Kr⁺ ion irradiated (at 300 K) zirconia samples for the ion fluences of (a) 1×10^{16} ions/cm² and (b) 5×10^{17} ions/cm².

5.3.4.3. Laser (200 shots) irradiation on Kr⁺ ion irradiated (at 143 K) samples

SEM images of the laser (200 shots) irradiated on Kr⁺ ion irradiated (at 143 K) zirconia samples for the ion fluences 1×10^{16} ions/cm² and 5×10^{17} ions/cm² are shown in Figure 5.12(a) and Figure 5.12(b) respectively. When comparing Figure 5.12(a) and Figure 5.12(b) to the corresponding SEM images of the samples before laser irradiation

(refer Figure 4.13(a) and Figure 4.13(d)), it is observed that laser irradiation has resulted in the reduction of porosity of the samples. The grains in the laser irradiated samples are clearly seen and they have distinct grain boundaries. The average grain size is larger than the ion irradiated samples (~ 70 nm for 1×10^{16} ions/cm² and ~ 85 nm for 5×10^{17} ions/cm²) and found to be ~ 254 nm and ~ 257 nm for the ion fluences of 1×10^{16} ions/cm² and 5×10^{17} ions/cm² respectively.

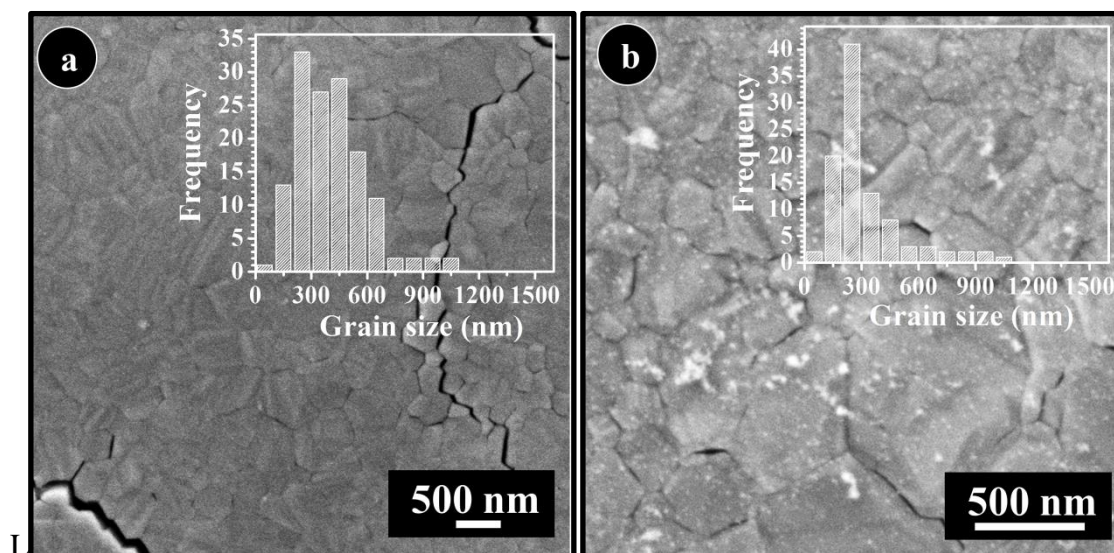


Figure 5.12 (a) SEM images of the laser (200 shots) irradiated on Kr⁺ ion irradiated (at 143 K) zirconia samples for the ion fluences of (a) 1×10^{16} ions/cm² and (b) 5×10^{17} ions/cm².

5.3.4.4. Laser (2000 shots) irradiation on Kr⁺ ion irradiated (at 143 K) samples

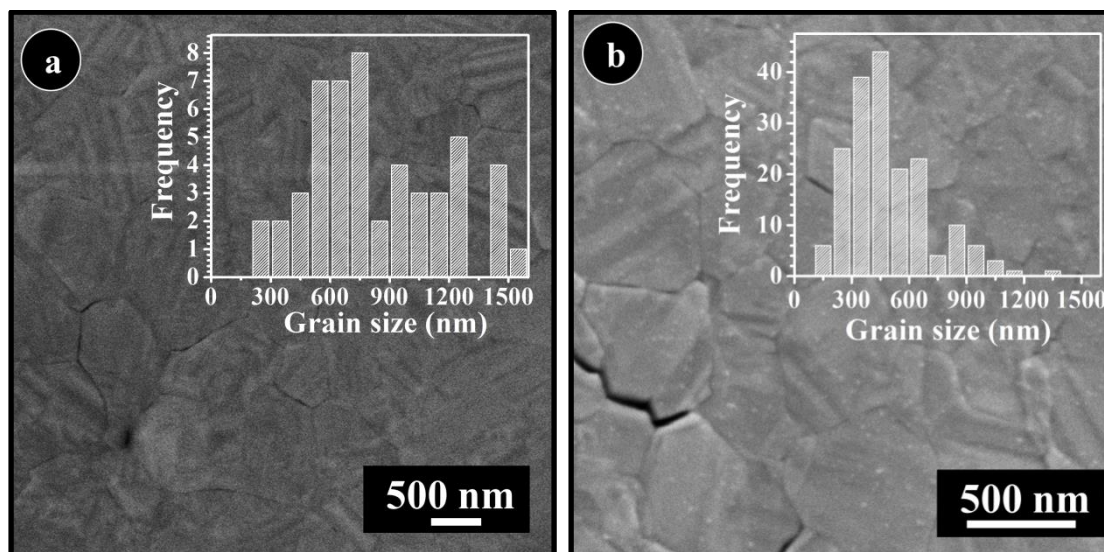


Figure 5.13 SEM images of the laser (2000 shots) irradiated on Kr⁺ ion irradiated (at 143 K) zirconia samples for the ion fluences of (a) 1×10^{16} ions/cm² and (b) 5×10^{17} ions/cm².

Figure 5.13(a) and Figure 5.13(b) shows the SEM images of the laser (2000 shots) irradiated on the Kr⁺ ion (143 K) irradiated zirconia samples for the ion fluences of

1×10^{16} ions/cm² and 5×10^{17} ions/cm² respectively. When the SEM images of the laser irradiated spots were compared to the SEM images of the sample before laser irradiation (*refer* Figure 4.13(a) and Figure 4.13(d)), it is found that the samples have lost its porous nature and the grains have distinct grain boundaries. The average grain size of the samples after laser irradiation is found to increase (~ 658 nm and ~ 449 nm for the ion fluences 1×10^{16} ions/cm² and 5×10^{17} ions/cm² respectively) compared to the average grain size of the samples before laser irradiation (~ 70 nm and ~ 85 nm for ion fluences 1×10^{16} ions/cm² and 5×10^{17} ions/cm² respectively).

5.4. Photoluminescence analysis of laser and ion irradiated ZrO₂

5.4.1. PL analysis of as-sintered and laser irradiated zirconia samples

Figure 5.14(a) shows the photoluminescence (PL) spectra obtained from the as-sintered and laser irradiated zirconia samples. A broad PL peak is observed around 2.5 eV in both the as-sintered and laser irradiated zirconia samples. It is reported that the F centers are responsible for the PL peak at 2.5 eV[159]. Since the peak at ~ 2.53 eV is related to anionic defects (oxygen vacancies with electrons (F, F⁺ centers)) and distortion in the symmetry of oxygen ions, the change in the PL intensity is related to the concentration of these anionic defects. Experiments also show that the intrinsic defects responsible for the photoluminescence are related to oxygen vacancies[93, 157]. Thus change in the shape and intensity of the PL spectra is attributed to the defects present in the zirconia samples. It is observed that upon laser irradiation, the PL intensity has decreased. Moreover, the PL intensity decreases with the increase in laser shots. The intensity of luminescence is estimated by the following equation[160]

$$F = \Phi I_0 (1 - e^{-\varepsilon bc}) \quad \text{Eqn.5.1}$$

where I_0 is the intensity of incident light, Φ is the ratio of radiative recombination, ε is the absorption coefficient of defects and b is the thickness of the material and c is the concentration of defects. The concentration of defects and the ratio of radiative recombination play important role in determining the PL intensity. Upon laser irradiation, the grain growth has occurred and hence the grain boundaries have significantly decreased (*refer* Figure 5.1) compared to the as sintered zirconia (*refer* Figure 4.1(a)). Hence, the decrease in the number of grain boundaries leads to the decrease in the number of defects which give rise to reduction in PL intensity. From this, it can be inferred that, upon laser irradiation, the number of defects present in the as-sintered zirconia sample has decreased.

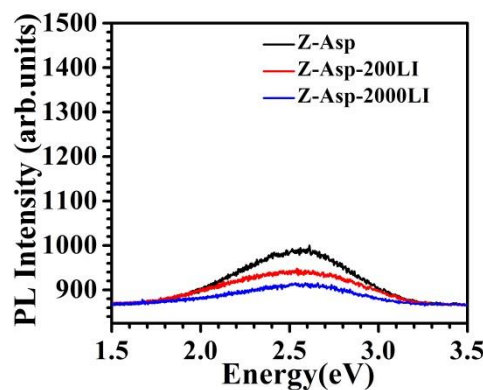
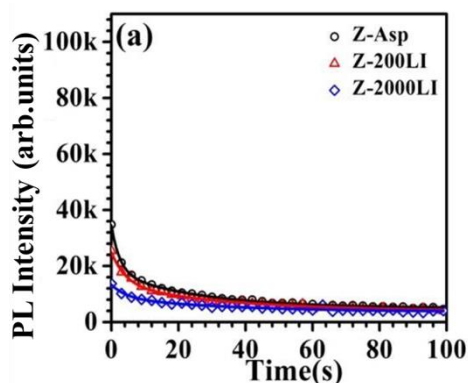


Figure 5.14 Photoluminescence spectra of the as-sintered and laser (200 shots and 2000 shots) irradiated zirconia samples

The PL intensity obtained from the zirconia samples decreases as a function of time when the experiments were carried out using the laser with the power of 0.5 mW (Figure 5.15(a)). The decay of PL intensity obtained from the as-sintered and laser irradiated zirconia samples reaches the maximum at the instant, then gradually decreases and becomes stable, when $t > 40$ seconds. The decay of the PL intensity with respect to the time of exposure is well fitted by the bi-exponential decay governed by the following equation.

$$I(t) = I_1 \exp\left(-\frac{t}{\tau_1}\right) + I_2 \exp\left(-\frac{t}{\tau_2}\right) \quad \text{Eqn.5.2}$$

where τ_1 and τ_2 are the decay time and I_1 and I_2 are the weight factor of the decay channel. The fast component (τ_1) represents intrinsic recombination while the slow component (τ_2) is most likely associated with localized states induced by defects, impurities etc. Such longer characteristic times (τ_1, τ_2) on the order of seconds suggest the deep level of these trap states.



(b)

Sample	Laser power - 0.5 mW	
	τ_1 (seconds)	τ_2 (seconds)
Z-Asp	2.5	26
Z-200LI	4.3	34.6
Z-2000LI	3.8	38.5

Figure 5.15 (a) Decay of the photoluminescence intensity with respect to time of exposure obtained from the as-sintered and laser (200 and 2000 shots) irradiated zirconia samples and (b) Time constants of the PL intensity decay extracted by bi exponential curve fitting.

Figure 5.15(b) shows the values of τ_1 and τ_2 values obtained from the PL measurements (room temperature) on as-sintered and laser (200 and 2000 shots) irradiated zirconia samples. It is observed that upon laser irradiation, the values of τ_2 increases with the number of laser shots. As the number of defects and time constants varies inversely with each other, it can be concluded that upon laser irradiation, the number of defects decreases.

5.4.2. PL analysis of He⁺ ion irradiated and laser irradiated zirconia samples

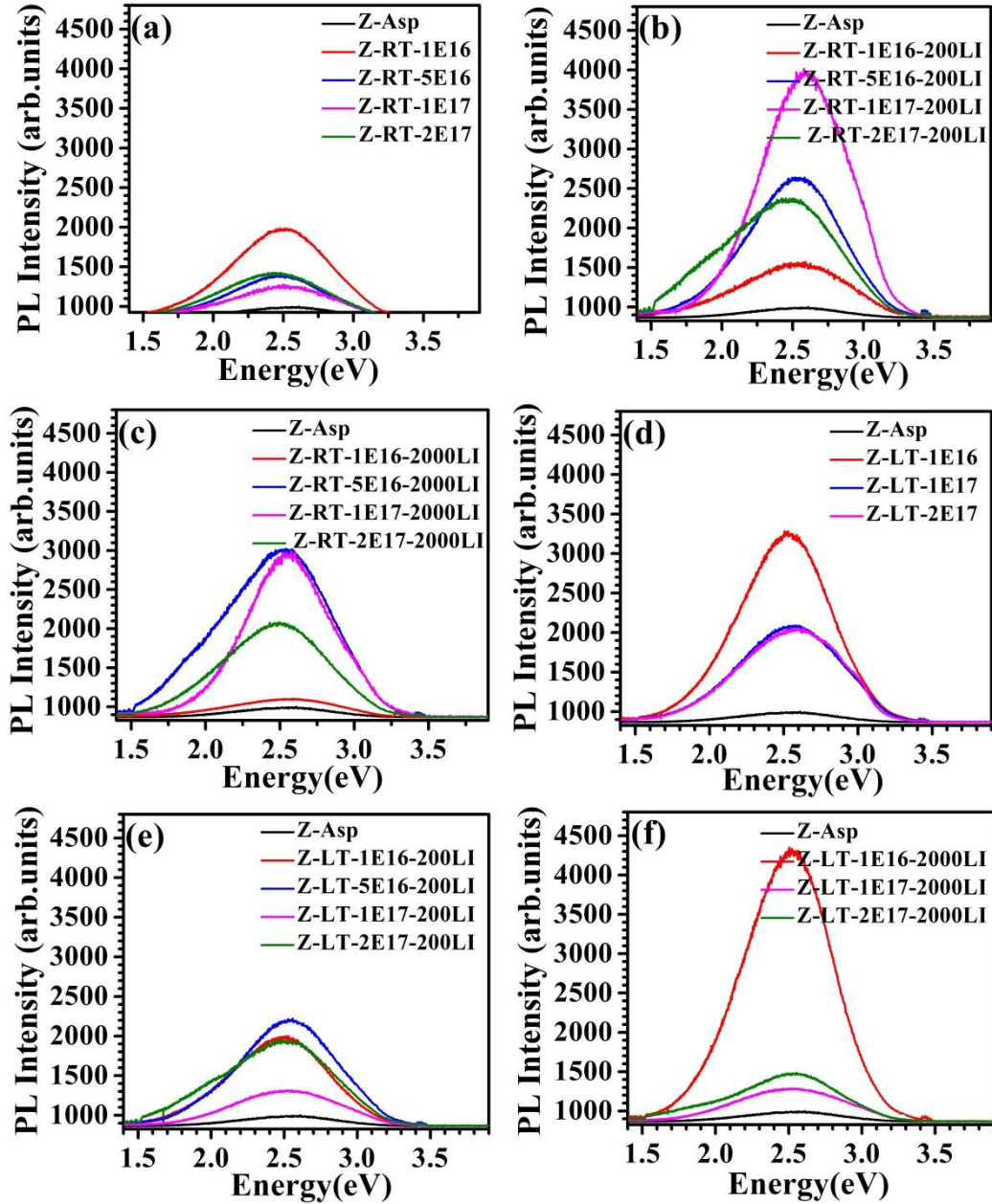


Figure 5.16 PL spectra of zirconia samples with different conditions. (a) He⁺ ion irradiated (at 300 K), and further irradiated with laser for (b) 200 shots, and (c) 2000 shots, (d) He⁺ ion irradiated (at 143 K) and further irradiated with laser for (e) 200 shots, and (f) 2000 shots.

Figure 5.16 shows the photoluminescence (PL) spectra of the laser (200 shots and 2000 shots) irradiation on He⁺ ion irradiated zirconia samples. Figure 5.16(a) shows the PL spectra of He⁺ ion irradiated (300 K) zirconia samples. It is observed that the PL intensity has increased upon ion irradiation. However, the PL intensity of the sample for the ion fluence of 2×10^{17} ions/cm² has decreased, compared to the PL intensity of the sample for the ion fluence of 1×10^{16} ions/cm².

Figure 5.16(b) shows the PL spectra of the laser (200 shots) irradiated on the He⁺ ion irradiated (at 300 K) zirconia samples. It is observed that the PL intensity increases upon laser irradiation. The PL intensity for the ion fluence 2×10^{17} ions/cm² has decreased compared to the PL intensity for the ion fluence of 5×10^{16} ions/cm² and 1×10^{17} ions/cm². SEM observations (*refer* Table 5.2) show the average grain size for the ion fluence 2×10^{17} ions/cm² (~ 650 nm) is much larger than average grain size for the ion fluence 1×10^{17} ions/cm² (~ 155 nm). The number of grain boundaries is less for the highest ion fluence, and it give rise to less number of defects compared to the ion fluence 1×10^{17} ions/cm², hence the reduction of PL intensity is observed for the highest ion fluence (2×10^{17} ions/cm²).

Figure 5.16(c) shows the PL spectra obtained from the laser (2000 shots) irradiated on the He⁺ ion irradiated (at 300 K) zirconia samples. Upon laser irradiation, the PL intensity has increased for the zirconia sample which is irradiated upto the ion fluence of 1×10^{17} ions/cm², however the PL intensity has decreased for the highest ion fluence 2×10^{17} ions/cm². From SEM observations (*refer* Table 5.2), the average grain size for the ion fluence 2×10^{17} ions/cm² (~ 452 nm) is much larger than average grain size for the ion fluence 1×10^{17} ions/cm² (~ 148 nm). The number of grain boundaries is less for the highest ion fluence, and hence the reduction of PL intensity is observed for the highest ion fluence (2×10^{17} ions/cm²).

Figure 5.16(d) shows the PL spectra obtained from the He⁺ ion irradiated (at 143 K) zirconia samples. It is observed that the PL intensity increases upon ion irradiation. However, the PL intensity of the ion fluence 2×10^{17} ions/cm² decreases compared to the PL intensity of the ion fluence 1×10^{16} ions/cm². SEM observations (*refer* Table 5.2) show the average grain size for the ion fluence 2×10^{17} ions/cm² (~ 82 nm) is larger than average grain size for the ion fluence 1×10^{16} ions/cm² (~ 66 nm). Since the average grain size increases for the highest ion fluence, the reduction in PL intensity is observed.

Figure 5.16(e) shows the PL spectra of the laser (200 shots) irradiated on the He⁺ ion irradiated (at 143 K) zirconia samples. Upon laser irradiation, even though the PL

intensity decreases for the ion fluence 1×10^{17} ions/cm² (compared to the ion fluence 5×10^{16} ions/cm²), the PL intensity for the highest ion fluence 2×10^{17} ions/cm² increases. SEM observations (*refer* Table 5.2) on laser irradiated samples show that the average grain size for the ion fluence 1×10^{17} ions/cm² and 2×10^{17} ions/cm² are ~ 146 nm and ~ 140 nm respectively. The change in PL intensity could be attributed to annealing and/or production of defects during laser irradiation.

Figure 5.16(f) shows the PL spectra obtained from the laser (2000 shots) irradiation on the He⁺ ion irradiated (at 143 K) zirconia samples. It is observed that the PL intensity has increased upon laser (2000 shots) irradiation. Even though the PL intensity decreases for the ion fluence 1×10^{17} ions/cm², the PL intensity for the ion fluence 2×10^{17} ions/cm² has slightly increased compared to the PL intensity of the ion fluence 1×10^{17} ions/cm².

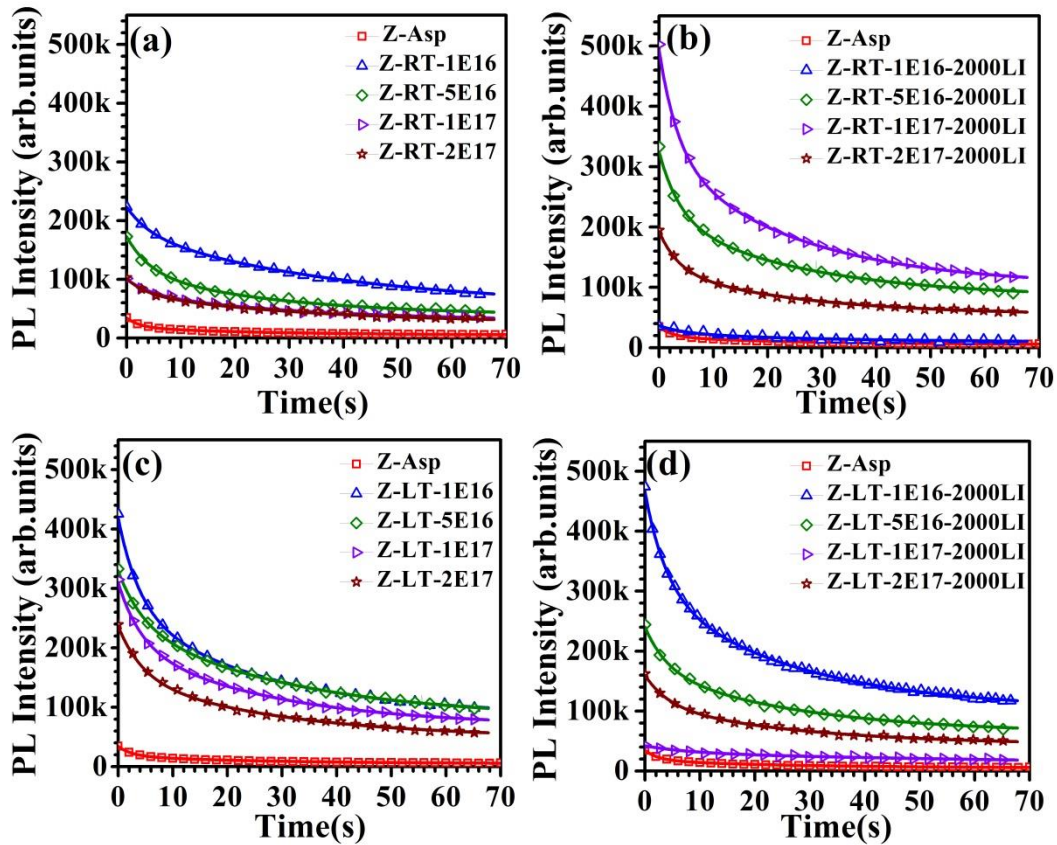


Figure 5.17 Decay of the photoluminescence intensity with respect to time of exposure obtained from the zirconia samples (a) He⁺ ion irradiated (at 300 K), (b) He⁺ ion irradiated (at 300 K) and further irradiated with laser for 2000 shots, (c) He⁺ ion irradiated (143 K) and (d) He⁺ ion irradiated (143 K) further irradiated with laser for 2000 shots.

SEM observations (*refer* Table 5.2) show the average grain size for the ion fluence 1×10^{17} ions/cm² (~ 146 nm) and the average grain size for the ion fluence 2×10^{17} ions/cm²

(~ 152 nm). By comparing the results of laser irradiation for 200 and 2000 shots on He⁺ ion (143 K) irradiated samples, it is noticed that, for the laser shots on low ion fluence samples, production of the defects occurs, whereas for the highest ion fluence, laser irradiation has annealed the defects[108].

Figure 5.17 shows the decay of the PL intensity with respect to time of exposure obtained from the He⁺ ion irradiated (at 300 K and 143 K) and further laser (2000 shots) irradiated zirconia samples. For all the zirconia samples (He⁺ ion irradiated and further laser irradiated), the decay of the PL intensity is well fitted by the bi-exponential decay and the values of τ_1 and τ_2 are tabulated in Table 5.5.

From the Table 5.5, it is observed that the slow component τ_2 value increases for the ion fluence 1×10^{16} ions/cm² (40 s) compared to the as-sintered zirconia (26 s) sample. Further, for the highest ion fluence 2×10^{17} ions/cm², the τ_2 (33 s) value has decreased. This indicates that the large number of defects is produced in the sample for the ion fluence 2×10^{17} ions/cm² compared to the ion fluence 1×10^{16} ions/cm². In the presence of large number of defects, the recombination becomes faster and hence the τ_2 value decreases for the highest ion fluence 2×10^{17} ions/cm². The observation is consistent with the PL intensity obtained for the He⁺ ion irradiated zirconia samples.

Table 5.5 Decay time constants (τ_1 and τ_2) of the PL intensity with respect to time of exposure obtained from the He⁺ ion irradiated (at 300 K and 143 K) and further laser (200 and 2000 shots) irradiated zirconia samples.

He ⁺ ion irradiation		Decay time constants (τ_1 and τ_2)					
		Before laser irradiation		After laser irradiation			
				200 shots		2000 shots	
Temperature	Ion fluence (ions/cm ²)	τ_1	τ_2	τ_1	τ_2	τ_1	τ_2
Room Temperature (300 K)	1×10^{16}	4.3	40.0	3.9	24.5	4.8	33.5
	5×10^{16}	4.3	27.3	3.9	25.2	3.8	26.0
	1×10^{17}	4.5	32.7	3.2	22.9	3.5	25
	2×10^{17}	3.6	33	3.8	24.9	3.6	25.3
Low Temperature (143 K)	1×10^{16}	3.8	25.5	4.3	28.7	3.9	26.4
	5×10^{16}	3.7	25	3.7	25	4.0	27.8
	1×10^{17}	4.0	26.7	4.4	31.6	8.2	102.6
	2×10^{17}	4.4	28.8	3.9	24.2	4.2	27.8

In the case of laser (200 shots and 2000 shots) irradiation on He⁺ ion irradiated (at 300 K) zirconia samples (refer Table 5.5), the slow component τ_2 value decreases upon laser irradiation. This observation is consistent with the PL intensity of the laser irradiation

on the He⁺ ion irradiated (at 300 K) zirconia samples. In the case of laser (200 shots and 2000 shots) irradiation on He⁺ ion irradiated (at 143 K) zirconia samples (*refer* Table 5.5), only for two samples (Z-LT-1E17-2000LI and Z-LT-1E17-200LI) alone, the τ_2 value increases and the PL intensity of these samples also decreases significantly. This observation is due to annealing of defects (produced during the ion irradiation) during laser irradiation.

5.4.3. PL analysis of Ar⁺ ion irradiated and laser irradiated zirconia samples

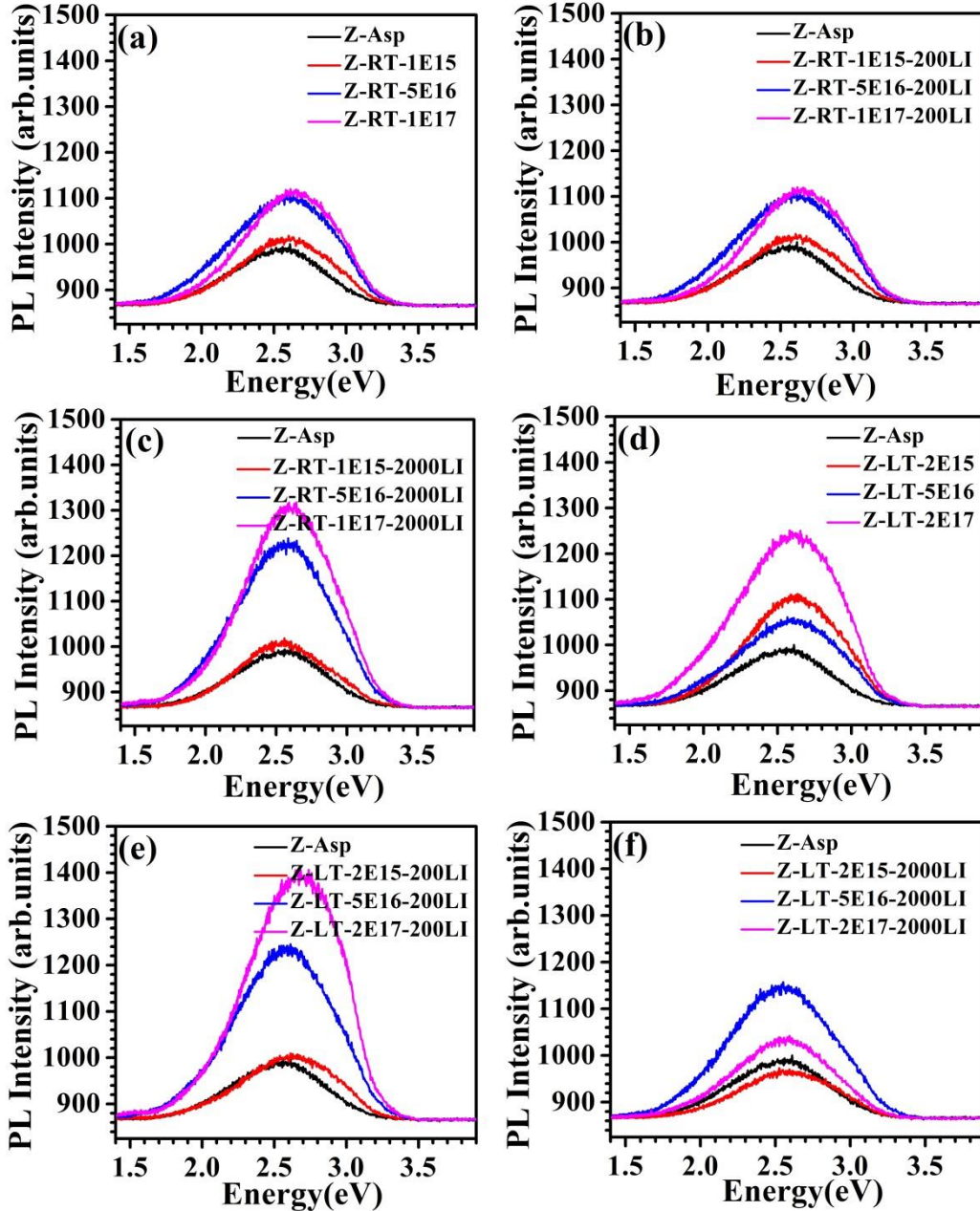


Figure 5.18 PL spectra of zirconia samples with different conditions. (a) Ar⁺ ion irradiated (at 300 K), and further irradiated with laser for (b) 200 shots, and (c) 2000 shots, (d) Ar⁺ ion irradiated (at 143 K), further irradiated with laser for (e) 200 shots, and (f) 2000 shots.

Figure 5.18 shows the PL spectra of the Ar⁺ ion irradiated (at 300 K and 143 K) and laser (200 shots and 2000 shots) irradiated on Ar⁺ ion irradiated zirconia samples. It is observed that the PL intensity increases upon ion as well as laser irradiation. Upon ion irradiation, irrespective of irradiation temperatures (300 K and 143 K), the PL intensity systematically increases with the ion fluence and it indicates that defect concentration increases with the ion fluence.

However, in case of the sample Z-LT-2E17-2000LI, the PL intensity (for the highest ion fluence 2×10^{17} ions/cm²) decreases compared to the ion fluence 5×10^{16} ions/cm². This could be either due to annealing of defects by laser (2000 shots) or due to recombination of defects. In the case of laser irradiation on as-sintered zirconia samples (refer Figure 5.1), the native oxygen vacancies are annealed out and the PL intensity reduces. However in the case of Ar⁺ ion irradiated sample, even 2000 shots of laser irradiation was not able to anneal out the oxygen vacancies and hence the PL intensity has not reduced.

Similar to the He⁺ ion irradiated zirconia samples (refer Figure 5.17), the decay of the PL intensity as a function of exposure time for all the Ar⁺ ion irradiated and laser (200 shots and 2000 shots) irradiation on Ar⁺ ion irradiated zirconia samples were fitted by the bi-exponential decay model (refer Eqn.5.2) and the values of τ_1 and τ_2 are tabulated in Table 5.6.

Table 5.6 Decay time constants (τ_1 and τ_2) of the PL intensity with respect to time of exposure obtained from the Ar⁺ ion irradiated (at 300 K and 143 K) and further laser (200 and 2000 shots) irradiated zirconia samples

Ar ⁺ ion irradiation		Decay time constants (τ_1 and τ_2) (seconds)					
		Before laser irradiation		After laser irradiation			
				200 shots		2000 shots	
Temperature	Ion fluence (ions/cm ²)	τ_1	τ_2	τ_1	τ_2	τ_1	τ_2
Room Temperature (300 K)	1×10^{15}	1.9	20.6	4.7	34.8	2.4	24
	5×10^{16}	1.9	22.8	4	26	2.2	22.7
	1×10^{17}	1.7	19.2	2	21.2	2.2	23.8
Low Temperature (143 K)	2×10^{15}	2	21.6	2	21.02	2.2	22.35
	5×10^{16}	2.4	24.5	2	21.13	1.8	21.47
	2×10^{17}	2.3	31.9	1.9	20.57	5	36.55

In case of laser (200 shots) irradiation on Ar⁺ ion irradiated (at 300 K) zirconia samples, it is observed from Table 5.6, that the slow component τ_2 value decreases with the ion fluence. From the Table 5.6, it is also observed that the slow component τ_2 value

has increased for the ion fluence 1×10^{15} ions/cm² (34.8 s) compared to the as-sintered zirconia (26 s) sample. Further the size of the grain has increased upon laser irradiation (150 nm) drastically compared to as-sintered ZrO₂ (~ 55 nm) (refer Table 5.3). However, the PL intensity did not change significantly, hence, the changes in τ_2 might be due to grain growth.

Further, for the laser (200 shots) irradiation, in the case of highest ion fluence 1×10^{17} ions/cm², the τ_2 (21.2 s) value decreased. This indicates that the large number of defects produced in the sample for the ion fluence 1×10^{17} ions/cm² compared to the ion fluence 1×10^{15} ions/cm². In the presence of large number of defects, the recombination becomes faster and hence the τ_2 value decreases. The observation is consistent with the PL intensity obtained for the laser (200 shots) irradiated on Ar⁺ ion irradiated (at 300 K) zirconia samples.

In case of Ar⁺ ion irradiated (at 143 K) zirconia samples (refer Table 5.6), it is observed that the slow component τ_2 value increases for the ion fluence 2×10^{17} ions/cm² (31.9 s) compared to the ion fluence 2×10^{15} ions/cm² (21.6 s) sample. The observation is not consistent with the PL intensity of Ar⁺ ion irradiated (at 143 K) zirconia samples. From SEM observations (refer Section 4.3.3.2), it is observed that the porosity decreases upon Ar⁺ ion irradiation without significant change in the grain size (94 nm to 74 nm) and hence τ_2 value increases. In case of laser (2000 shots) irradiation on Ar⁺ ion irradiated (143 K) zirconia samples, the slow component τ_2 value increases significantly for ion fluence of 2×10^{17} ions/cm² and it is consistent with PL intensity observation.

5.4.4. PL analysis of Kr⁺ ion irradiated and laser irradiated zirconia samples

Figure 5.19 shows the PL spectra of the Kr⁺ ion irradiated (at 300 K and 143 K) and laser (200 shots and 2000 shots) irradiated on Kr⁺ ion irradiated zirconia samples. Figure 5.19(a) shows the PL spectra of as-sintered and Kr⁺ ion irradiated (at 300 K) zirconia samples. It is observed that the PL intensity of the ion fluence 5×10^{17} ions/cm² has decreased compared to the PL intensity of the ion fluence 1×10^{17} ions/cm². For the highest ion fluence (5×10^{17} ions/cm²), SEM observation (refer Figure 4.12) shows the porous microstructure and the pores might have act as a sink for the defects and hence the PL intensity has reduced.

Figure 5.19(b) shows the PL spectra of the laser (200 shots) irradiated on the Kr⁺ ion irradiated (at 300 K) zirconia samples. It is also observed that the PL intensity increases for the ion fluence 1×10^{16} ions/cm², then decreases for the next successive ion

fluences till 1×10^{17} ions/cm² and then again increases for the highest ion fluence 5×10^{17} ions/cm². SEM observations (refer Table 5.4) show the average grain size for the ion fluence 1×10^{16} ions/cm², 1×10^{17} ions/cm², and 5×10^{17} ions/cm² are ~ 347 nm, ~ 251 nm, and ~ 152 nm respectively. The number of grain boundaries is more for the highest ion fluence (5×10^{17} ions/cm²) and it gives rise to more number of defects compared to the ion fluence 1×10^{17} ions/cm², hence the increase of PL intensity is observed.

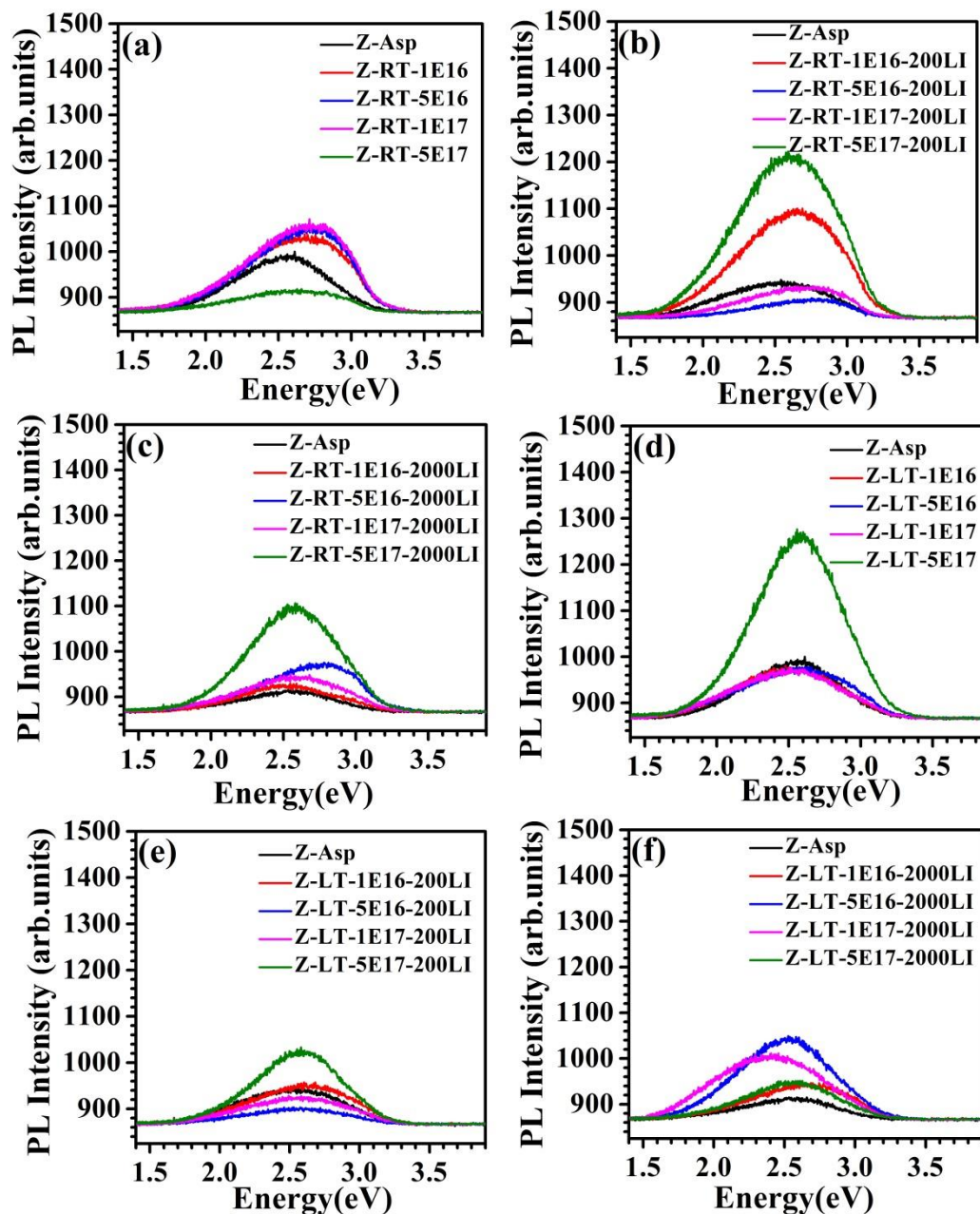


Figure 5.19 PL spectra of zirconia samples with different conditions. (a) Kr⁺ ion irradiated (at 300 K), and further irradiated with laser for (b) 200 shots, and (c) 2000 shots, (d) Kr⁺ ion irradiated (at 143 K), further irradiated with laser for (e) 200 shots, and (f) 2000 shots.

Figure 5.19(c) shows the PL spectra of the laser (2000 shots) irradiated on the Kr⁺ ion irradiated (at 300 K) zirconia samples. The PL intensity has increased significantly for the highest ion fluence (5×10^{17} ions/cm²) compared to other ion fluences. SEM observations (*refer* Table 5.4) show the average grain size for the ion fluence 5×10^{17} ions/cm² (~ 353 nm) is much larger than average grain size for the ion fluence 1×10^{17} ions/cm² (~ 248 nm). During laser irradiation, distinct fluence regimes exist, in which either bond weakening, melting due to electron-phonon coupling, or shock wave propagation is the dominant damage mechanism. The two thresholds that define these regimes are (1) the thermal melting threshold that defines the fluence necessary to thermally melt the material and (2) the shock melting threshold that defines the fluence necessary for the shock wave to generate dislocations[161–163]. For the highest ion fluence, the defects production might be in the saturation region, in the beginning, it might have annealed the defects (where grain growth occurs) and later, laser might have produced defects via bond weakening mechanism[108].

Figure 5.19(d) shows the PL spectra of the Kr⁺ ion irradiated (at 143 K) zirconia samples. The PL intensity for the highest ion fluence 5×10^{17} ions/cm² is higher than the as-sintered and lower ion fluences. From the SEM observations (*refer* Figure 5.13), for the highest ion fluence (5×10^{17} ions/cm²), the porous microstructure has vanished due to sputtering of the layer. The grain size for the ion irradiated sample (ion fluence 5×10^{17} ions/cm²) is comparable with the as-sintered sample and the grains are irradiated with Kr⁺ ions (produces defects without pores or sinks), leading to the increase in PL intensity.

Figure 5.19(e) shows the PL spectra of the laser (200 shots) irradiated Kr⁺ ion irradiated (at 143 K) zirconia samples. The PL intensity for the ion fluence 5×10^{17} ions/cm² is higher than the PL intensity for the ion fluence 1×10^{17} ions/cm². This indicates that large number of defects is present for the highest ion fluence 5×10^{17} ions/cm² compared to 1×10^{17} ions/cm² and hence the laser shots were not able to anneal out such large number of defects.

Figure 5.19(f) shows the PL spectra of the laser (2000 shots) irradiated on the Kr⁺ ion irradiated (at 143 K) zirconia samples. It is observed that the PL intensity increases upon laser irradiation. The PL intensity for the ion fluence 5×10^{17} ions/cm² decreases compared to the ion fluence 1×10^{17} ions/cm². Due to more number of laser shots (*i.e.*, 2000 shots) irradiation, local heating might have annealed out the defects and hence the reduction in PL intensity. Also, the starting morphology of the samples (for the ion fluences 1×10^{17} ions/cm² and 5×10^{17} ions/cm²) were very different one with porous

microstructure (before laser irradiation) and other one is non-porous fully packed, and also upon laser irradiation the grain restructuring has occurred.

Table 5.7 Decay time constants (τ_1 and τ_2) of the PL intensity with respect to time of exposure obtained from the Kr⁺ ion irradiated (at 300 K and 143 K) and further laser (200 and 2000 shots) irradiated zirconia samples.

Kr ⁺ ion irradiation		Decay time constants (τ_1 and τ_2) (seconds)					
		Before laser irradiation		After laser irradiation			
				200 shots		2000 shots	
Temperature	Ion fluence (ions/cm ²)	τ_1	τ_2	τ_1	τ_2	τ_1	τ_2
Room Temperature (300 K)	1×10 ¹⁶	2.40	25.2	2.0	21.1	2.7	24.2
	5×10 ¹⁶	2.54	27.7	2.2	22.5	2.1	23.1
	1×10 ¹⁷	2.37	24.8	3	29.9	2.2	22.9
	5×10 ¹⁷	1.73	21.5	1.9	20.4	1.9	22.4
Low Temperature (143 K)	1×10 ¹⁶	3.1	31	2.5	23.3	1.4	22.8
	5×10 ¹⁶	2.9	24.9	1.5	23.1	5	37.2
	1×10 ¹⁷	4.0	46.3	2.3	25.5	2.5	22.3
	5×10 ¹⁷	1.5	20.5	1.9	22.5	3.6	33.3

Similar to the He⁺ irradiated ion (at 300 K and 143 K) zirconia samples (refer Eqn.5.2), the decay of the PL intensity for all the Kr⁺ ion irradiated and further laser (200 and 2000 shots) irradiated zirconia samples, were well fitted by the bi-exponential decay and the values of τ_1 and τ_2 are tabulated in Table 5.7. For Kr⁺ ion irradiation at 300 K or 143 K, the slow component τ_2 values are consistent with the PL intensity, where the PL intensity significantly changes for the highest ion fluence. It is observed from Table 5.7, that the values of τ_2 for the Kr⁺ ion irradiated (at 300 K) samples decreases for the highest ion fluence 5×10¹⁷ ions/cm² (21.5 s) compared to the ion fluence 1×10¹⁷ ions/cm² (24.8 s). This is consistent with the PL intensity and indicates that pores act as a sink for the defects (refer Figure 4.12) and hence the short decay time.

From Table 5.7, it is observed that the slow component τ_2 value of the laser (200 shots) irradiated on the Kr⁺ ion irradiated (at 300 K) zirconia samples decreases for the highest ion fluence 5×10¹⁷ ions/cm² (20.4 s) compared to the ion fluence 1×10¹⁷ ions/cm² (29.9 s). The observation is consistent with the PL intensity of the laser (200 shots) irradiated on the Kr⁺ ion irradiated (at 300 K) zirconia samples. This indicates that the large number of defects produced in the sample for the ion fluence 5×10¹⁷ ions/cm² compared to the ion fluence 1×10¹⁷ ions/cm² and hence the short decay time.

Also it is noticed that the slow component τ_2 value of the Kr^+ ion irradiated (at 143 K) zirconia sample, decreases for the ion fluence 5×10^{17} ions/cm² (20.5 s) compared to the ion fluence 1×10^{17} ions/cm² (46.3 s). The observation is consistent with the PL intensity obtained for the Kr^+ ion (143 K) irradiated zirconia samples. This indicates the more defects present in the non-porous sample (5×10^{17} ions/cm²) leading to the fast decay.

Similarly upon laser (200 shots) irradiation, the τ_2 value for the sample Z-LT-5E17-200LI decreases (22.5 s) compared to the sample Z-LT-1E17-200LI (25.5 s). This indicates that the fast decay time is due to the large number of defects present in the sample Z-LT-5E17-200LI. In case of the laser (2000 shots) ion irradiation, the τ_2 values increases for the sample Z-LT-5E17-200LI (33.3 s), compared to the sample Z-LT-1E17-200LI (22 s), and is consistent with the PL intensity. This indicates that annealing of defects due to the local heating upon laser shots (2000) has led to the large τ_2 values.

5.5. Time resolved photoluminescence spectroscopy

Excitation and emission spectra of the as-sintered zirconia samples were recorded using excitation energy of 3.2 eV. Figure 5.20(a) shows the excitation and emission spectra of the as-sintered zirconia samples. The as-sintered zirconia sample shows a broad excitation band ranging from 3 eV to 4 eV (250 nm to 450 nm) centered at 3.2 eV (385 nm). The corresponding emission spectra appears as a broad band ranging from 2 eV to 3 eV (400 nm to 650 nm) with its emission peak at 2.57 eV (482 nm).

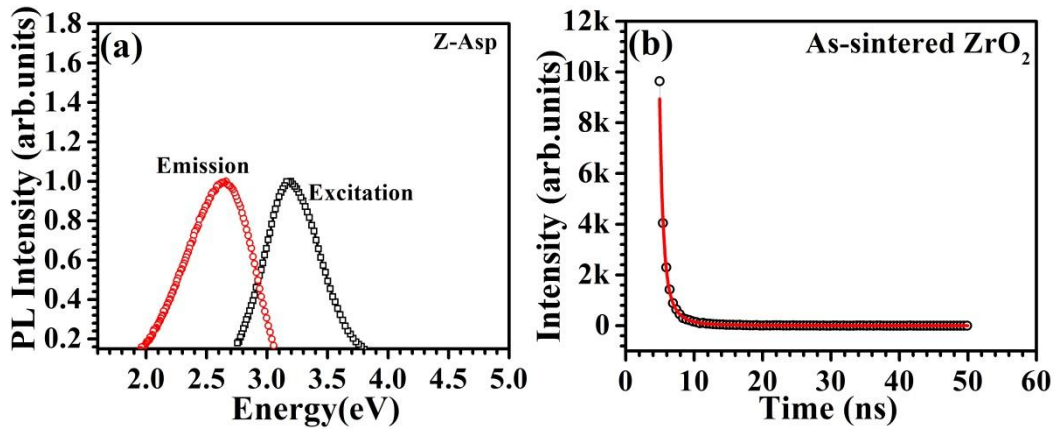


Figure 5.20 (a) Excitation and emission spectra and (b) time resolved photoluminescence (TRPL) spectrum for the as-sintered zirconia sample

In order to know the nature of the defects responsible for the visible emission (2.57 eV, 482 nm) produced upon ion irradiation, time resolved photoluminescence spectroscopy measurements were carried out. Figure 5.20(b) shows the TRPL spectrum for the as-sintered zirconia sample.

The luminescence decay curve of the as-sintered zirconia sample was well fitted with a triple exponential model given as

$$I(t) = A_1 \exp(-t/\tau_1) + A_2 \exp(-t/\tau_2) + A_3 \exp(-t/\tau_3) \quad \text{Eqn.5.3}$$

where τ_1, τ_2 and τ_3 are the decay times and A_1, A_2 and A_3 are relative magnitudes. The best fit for the triple exponential model suggests three emissive states as the overall contribution of multiple pathways for relaxation determines the lifetime of a single state by the equation

$$\tau = \frac{1}{k_{rv} + k_{nr,v} + k_{nr,d}} \quad \text{Eqn.5.4}$$

where τ is the lifetime of the state, k_{rv} is the rate of radiative decay to the valence state, $k_{nr,v}$ is the rate of nonradiative decay to the valence state and $k_{nr,d}$ is the rate of nonradiative decay to the defect. Thus, the three time constants suggest that there are three emissive states responsible for the emission at 2.5 eV (480 nm).

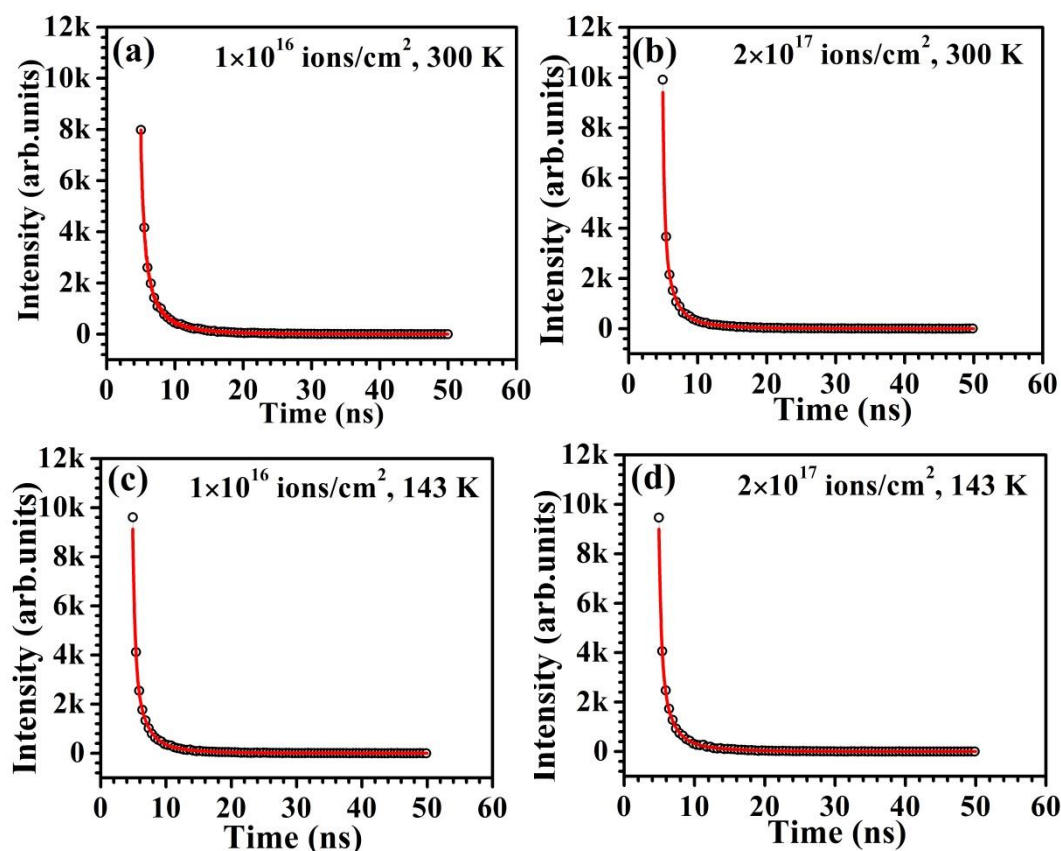


Figure 5.21 Time resolved photoluminescence spectra for the zirconia samples irradiated with He^+ ions for the ion fluences of (a) $1 \times 10^{16} \text{ ions/cm}^2$ (at 300 K) (b) $2 \times 10^{17} \text{ ions/cm}^2$ (at 300 K) (c) $1 \times 10^{16} \text{ ions/cm}^2$ (at 143 K) and (d) $2 \times 10^{16} \text{ ions/cm}^2$ (at 143 K).

In case of the as-sintered zirconia samples, the three time constants are found to be 0.3 ns, 1 ns and 4.3 ns. Very small (fast) time scales (0.3 ns - 1 ns) might include the free

and bound exciton states, because the lifetime of the free exciton is < 0.1 ns and of impurity or defect/bound exciton is ≤ 1 ns[164–167]. In the present experiments, the emissive state with a time constant around 4 ns -5 ns is associated with the native defects and contributes the 19.65% for the as-sintered zirconia sample.

Table 5.8 PL lifetime of the as-sintered and ion (He^+ , Ar^+ and Kr^+) irradiated (at 300 K and 143 K) zirconia samples. It is to be noted that the lifetime is in nano seconds

Ions	Fluence ions/cm ²	PL lifetime (ns)					
		Room Temperature 300 K			Low Temperature 143 K		
		$\tau_1(\text{ns})$ Rel %	$\tau_2(\text{ns})$ Rel %	$\tau_3(\text{ns})$ Rel %	$\tau_1(\text{ns})$ Rel %	$\tau_2(\text{ns})$ Rel %	$\tau_3(\text{ns})$ Rel %
As sintered		0.3 21.02%	1 59.33%	4.3 19.65%			
He^+	1×10^{16}	0.3 21.60%	1.4 49.12%	5.2 29.29%	0.3 19.39%	1.5 47.34%	5.1 33.28%
	5×10^{16}	0.3 16.61%	1.5 47.71%	5.5 35.68%	0.4 19.28%	1.6 45.90%	5.7 34.82%
	1×10^{17}	0.3 21.60%	1.4 49.12%	5.1 29.29%	0.3 19.02%	1.6 47.18%	5.6 33.79%
	2×10^{17}	0.3 17.86%	1.3 46.55%	5.1 35.60%	0.3 20.42%	1.5 46.37%	5.3 33.22%
Ar^+	1×10^{15}	0.3 22.18%	1.2 48.95%	4.3 28.88%			
	2×10^{15}				0.3 21.17%	1 52.07%	4 26.76%
	5×10^{15}	0.3 19.53%	1.2 48.90%	4.6 31.57%			
	1×10^{16}	0.3 16.76%	1.2 48.62%	4.5 34.62%			
	5×10^{16}	0.4 23.01%	1.5 46.77%	5.4 30.22%	0.3 20.77%	1.2 50.26%	4.4 28.96%
	1×10^{17}	0.3 27.04%	1.2 50.83%	4.5 22.14%			
	2×10^{17}				0.3 20.58%	1.3 48.12 %	4.8 48.12%
Kr^+	1×10^{16}	0.3 27.98%	1.1 48.84%	4.1 23.18%	0.2 18.53%	1 48.98%	3.9 32.49%
	5×10^{16}	0.3 20.92%	1.3 49.84%	4.5 29.23%	0.2 19.75%	1 50.18%	4.3 30.07%
	1×10^{17}	0.4 22.28%	1.4 47.93%	4.9 29.80%	0.3 16.61%	1.5 47.71%	5.4 35.68%
	5×10^{17}	0.5 28.96%	1.2 54.73%	4.2 16.31%	0.3 22.07%	1.6 48.69%	5.4 29.24%

Similar to the as-sintered zirconia sample, time resolved photoluminescence spectroscopy measurements were carried out for all the ion (He^+ , Ar^+ and Kr^+ ions) irradiated zirconia samples. The luminescence decay curve of the ion irradiated zirconia samples were fitted with a triple exponential model (*refer* Eqn.5.3) and the corresponding

life time are given in Table 5.8. Figure 5.21 shows the TRPL of zirconia samples that were irradiated with He^+ ions for different ion fluences (1×10^{16} ions/cm² (at 300 K), 5×10^{16} ions/cm² (at 300 K), 1×10^{17} ions/cm² (at 143 K) and 5×10^{17} ions/cm² (at 143 K)).

The lifetime for the defect component as well as the contribution for PL spectrum increases significantly upon He^+ ion irradiation independent of the irradiation temperature. Further, the changes in the lifetime as a function ion fluences show the dynamics of the defects which is consistent SEM and PL observations. It is also noticed from Table 5.8 that, irrespective of the ion irradiation temperatures, the contribution from the defects to the emissive peak increases for the zirconia samples irradiated with Ar^+ and Kr^+ ions as compared to the as-sintered zirconia. This indicates that defects are produced upon Ar^+ and Kr^+ ion irradiation. In the case of Ar^+ and Kr^+ ion irradiation, changes in the lifetime as a function ion fluences show the dynamics of the defects and is consistent with the SEM and PL observations.

The green emission peak at 2.48 eV could be due to the recombination between an electron in single positively charged oxygen vacancy (V_O^+) and a hole in the valence band. The band from 2-3 eV could be due to optical transitions between either of the transition couples F^0 , F^+ (2.72 eV), F^+ , F^{2+} (2.64 eV) and F^0 , F^{2+} (2.08 eV)[168]. It is also reported that the slow constants (3-5 ns) identify the nature of the F^+ emission centers[168].

5.6. Discussion

Zirconia samples were irradiated with He^+ , Ar^+ and Kr^+ ions followed by laser irradiation (200 and 2000 shots). All the samples were characterized with SEM, PL and TRPL measurements. SEM observations on laser irradiated samples shows grain growth as well as decrease in porosity in both as-sintered and ion irradiated zirconia samples. This observation is well supported with PL intensity where the reduction in grain boundaries gives rise to reduction in the PL intensity. The PL peak (around 2.53 eV which is associated with oxygen related defects) intensity corresponds to the number of defects which is in good agreement with the SEM and TRPL observations.

Zirconia is considered to have band gap value of ~ 5 eV[157, 169, 170]. The valence electron configurations of zirconium and oxygen are $4s^2 4p^6 4d^2 5s^2$ and $2s^2 2p^4$ respectively[157]. Experimental observations and theoretical calculations have reported that the upper valence band (VB) of zirconia consists of O 2p states while the lower part of the conduction band (CB) consists of Zr 4d states[157]. In ideal ZrO_2 , only Zr-O bonds exist which does not give rise to any luminescence. The luminescence in oxide material

arises due structural defects that introduces electronic states in the band gap[102]. Luminescence in ZrO_2 can be attributed to (1) impurity/dopants, (2) intrinsic self-trapped excitons and (3) due to intrinsic defects (F , F^+ and Zr^{3+})[95, 102]. Defects and vacancies in insulators can lead to the formation of localized states near conduction band edge. When the defects and vacancies undergo perturbation, these perturbations are characterized by discrete energy levels within the band gap. When defect concentration becomes large, the defect can form cavities or distribute in the atom network. These intrinsic defects (anion) are assigned to the formation of electrons (F and F^+ centers)[171]. The intrinsic delocalized states could be affected by the distortion in the lattice. In the present experiments, bubbles are formed for all the ion irradiated zirconia samples. These bubbles are associated with the transition couple F^0 , F^+ corresponding to the energy 2.72 eV. This is consistent with the PL observation and the bubble areal density (*refer* Table 4.1).

In earlier works, the peak at ~ 2.53 eV (490 nm) is attributed to the effect of impurity namely titanium ions[97–99] (which are present in trace concentrations), and/or attributed to the transitions of F^+ -centers (the oxygen vacancies that trapped one electron) from the excited state into the ground state[94, 100]. When Ti doped ZrO_2 is excited with ultraviolet (UV) irradiation, electron hole pairs are created and excited. These excited electrons are trapped by the shallow level which is due to the oxygen vacancies. The holes are trapped by the Ti^{3+} creating Ti^{4+} centers[97, 98].

The thermal energy in ambient conditions causes the release of electrons from the shallow traps and then the recombination of these electrons with the Ti^{4+} creates the excited state of Ti^{3+} leading to the emission of ~ 2.53 eV (490 nm). However, in the present experiments, the trace level of Ti is absent as evident from X-ray fluorescence experiment (*see* Figure A.1). Hence, the peak at ~ 2.53 eV (490 nm) is due to oxygen vacancies, distortion in the symmetry of oxygen ion and not due to titanium impurities. The band ranging from 2 eV-3 eV could be due to optical transitions between the F centers. Earlier report[159] on yttria stabilized zirconia have attributed the PL band (~ 2.55 eV) to F_a centers.

Also computational study on zirconia has revealed that the optical transition energies of various F centers[168]. When an oxygen atom is removed, it leaves two electrons in the lattice of ZrO_2 . A doubly occupied defect state appears in the energy gap at about 2.8 eV above the valence band. The two electrons that were in the O $2p$ states now occupies the newly created gap state centered on the vacancy (F center) with contributions from Zr $4d$ states. Singly positively charged oxygen vacancies (F^+) are

created when one oxygen atom and one electron are simultaneously removed. In this case, the defects states are split into two spin components: (1) one with a singly occupied spin-up state (2.78 eV from the VB) and (2) other unoccupied spin-down level at the bottom of the CB. The occupied defect state is highly localized on the vacancy site and the neighboring Zr atoms also have small contributions. The F^{2+} center is created when one electron is removed from the F^+ defect and the empty defect states merged with the bottom of the conduction band[168]. Calculations have shown that the F centers involves with a series of optical transitions between 2.08 eV to 4.19 eV. The band from 2-3 eV is attributed to the optical transitions between either of the transition couples F^0 , F^+ (2.72 eV), F^+ , F^{2+} (2.64 eV) and F^0 , F^{2+} (2.08 eV)[168].

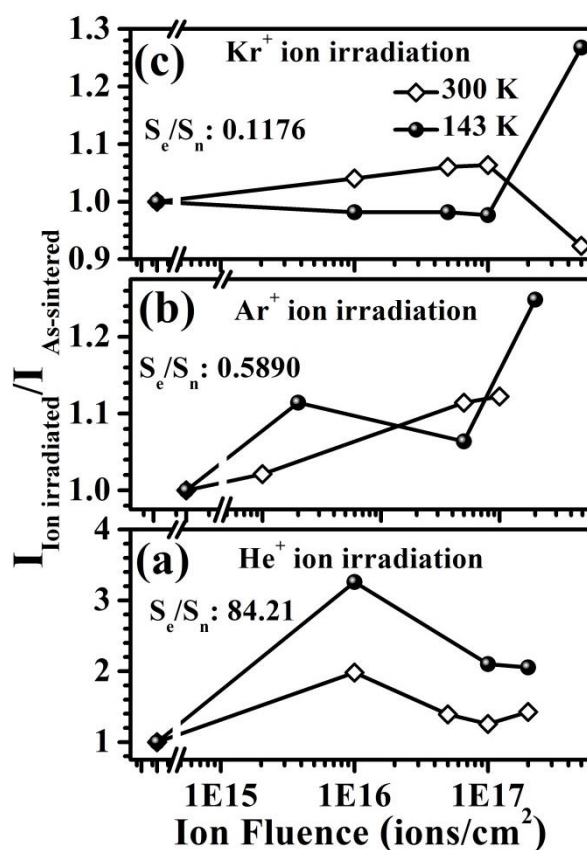


Figure 5.22 Plot of PL intensity ratio ($I_{\text{ion irradiated}} / I_{\text{As-sintered}}$) as a function ion fluence for (a) He^+ (b) Ar^+ and (c) Kr^+ ion irradiated zirconia samples. The samples are irradiated at 300 K and 143 K.

Time scales of the emissive states obtained from TRPL measurements also indicates that, there is production of defects upon ion (He^+ , Ar^+ , and Kr^+) irradiation. In the present thesis, oxygen vacancies are more likely to be formed, as the formation energy for oxygen vacancies is less than the primary knock on atoms (PKA) energy (refer Section

3.5), for all the ion (He^+ , Ar^+ and Kr^+) irradiation cases. Hence, the PL band at 2.53 eV (490 nm) is attributed to the oxygen vacancies.

Figure 5.22 shows the PL intensity ratio between ion irradiated and as-sintered ($I_{\text{ion irradiated}}/I_{\text{As-sintered}}$) samples as a function of ion fluence for ion (He^+ , Ar^+ and Kr^+ ions) irradiated zirconia samples. In case of He^+ ion irradiation, it is observed from Figure 5.22(a), that the intensity ratio increase till the ion fluence of 1×10^{16} ions/cm² and then decreases for higher ion fluences, independent of sample temperatures during ion irradiation. In He^+ ion irradiation, electronic energy loss is dominant (S_e/S_n : 84.21), and the cascades (produced by the He^+ ions) used to be light cascades, hence beyond the ion fluence of 1×10^{16} ions/cm², the annealing of defects occurs. Since the electronic energy loss is the dominant energy loss mechanism, the ionization-induced annealing can effectively remove nearly all the radiation-induced defects. Such ionization induced annealing of pre-existing defects were reported in silicon carbides [172].

In the case of Ar^+ ion irradiation, the PL intensity ratio was found to increase with the ion fluence independent of sample temperature during ion irradiation (*refer* Figure 5.22(c)). The nuclear energy loss is dominant because of low values of S_e/S_n (0.5890). The cascades are dense cascades and the damage production will be large. The defect production is proportional to ion fluence, and hence the PL intensity ratio increases with ion fluence.

From Figure 5.22(c), in case of Kr^+ ion irradiation at 300 K, the PL intensity ratio was found to increase with the ion fluence till the ion fluence of 1×10^{17} ions/cm², and for the highest ion fluence, the PL intensity ratio decreases significantly. In the case of Kr^+ ion irradiation at 143 K, the observation was in opposite trend to the samples irradiated at 300 K. However, the changes in the PL intensity ratio upto the ion fluence of 1×10^{17} ions/cm² is not very significant, but for the highest ion fluence, the PL intensity ratio shows significant changes. Similar to the Ar^+ ion irradiation, nuclear energy loss is dominant (S_e/S_n : 0.1176) mechanism in Kr^+ ion irradiation, and the damage cascades are dense cascades. Hence the PL intensity ratio is expected to increase with ion fluence, but the sputtering yield (8.8 atoms/ion) in Kr^+ ion irradiation is high compared to Ar^+ ion irradiation (sputtering yield: 4.6 atoms/ion).

Apart from that the swelling results on Kr^+ ion irradiated samples (*refer* Section 4.5 and Table 4.1) show that the swelling increases with ion fluence. However, in the case of ion irradiation at 143 K, the swelling is less compared to the samples irradiated at 300 K. The vacancies produced during ion irradiation assists in the bubble formation and

when the sample has less swelling where the vacancies are accommodated in the lattice give rise to increase in PL intensity ratio for the highest ion fluence.

5.7. Conclusions

Photoluminescence and time resolved photoluminescence experiments were carried out on zirconia (as-sintered, ion (He^+ , Ar^+ and Kr^+) irradiated (at 300 K and 143 K) and laser irradiated (200 and 2000 shots)) samples. SEM observation on the laser irradiated samples shows grain growth. From PL measurements, it is observed that ion irradiation leads to the production of defects and laser irradiation leads to the annealing of defects. However, when laser and ion irradiation are combined, the competition between the production and recovery of anionic defects (oxygen related vacancies) in these processes (ion irradiation and laser irradiation) decide the final oxygen vacancy concentration. The oxygen vacancy concentration dictates the phase transformation (induced by stress) and swelling (relieve the stress by bubble formation).

Chapter 6

Summary and scope for future work

6.1. Summary

This thesis deals with the low energy inert gas ion irradiation in monoclinic zirconia. Ion irradiation was carried out for creating damage and the effects were studied using GIXRD, Raman scattering, electron diffraction, photoluminescence and time resolved photoluminescence spectroscopy. Further, laser irradiation was carried on the ion irradiated zirconia sample to study the effects created by 1MeV/nucleon and to understand the nature of the defects produced during ion irradiation.

In the present thesis, low energy inert gas ion irradiation effects in monoclinic zirconia is studied to understand the correlation between phase transformations (monoclinic to tetragonal), bubble induced swelling and luminescence properties. For this purpose, monoclinic zirconia (synthesized by thermal decomposition method) was irradiated using low energy inert gas ions (120 keV He⁺, 120 keV Ar⁺ and 60 keV Kr⁺) at 300 K and 143 K.

6.2. Phase transformation upon ion irradiation

Radiation stability of irradiated monoclinic zirconia was studied using GIXRD, Raman scattering and transmission electron microscopy. GIXRD patterns showed the presence of a tetragonal phase and the diffraction peaks are shifted for all irradiated samples irrespective of the ions and irradiation temperatures. Raman scattering showed the presence of tetragonal peak (144 cm⁻¹, E_g mode) and shift in the Raman modes associated with monoclinic phase in all the ion irradiated zirconia samples. Selected area electron diffraction pattern also revealed the presence of tetragonal phase.

Phase transformation is attributed to pure radiation damage process and the amount of oxygen vacancies produced during the ion irradiation plays an important role in the phase transformation. Oxygen vacancies are known to induce strain and when their concentration reaches a threshold value, the strain lowers the phase transformation temperature. The amount of transformed phase was found to be more for the samples ion irradiated at 143 K compared with the samples irradiated at 300 K for the same ion fluence. In addition, strain was also found be higher when the irradiation was carried out at 143 K. The faster rate of phase transformation is attributed to the immobility of the defects and continuous production of oxygen vacancies. It was observed that the amount of

transformed tetragonal phase was low in the Kr^+ ion irradiated zirconia samples, compared to the Ar^+ ion irradiated zirconia samples (refer Table 6.1). This is attributed to the shallow range (23 nm) of the Kr^+ ions and the high sputtering yield (8.8 atoms/ion) compared to Ar^+ ions (sputtering yield: 4.6 atoms/ion).

Table 6.1 The table lists the fraction of tetragonal phase, swelling and macrostrain in the zirconia samples upon inert gas ion irradiation.

Energy Ions	Temp.	Ion Fluence (ions/cm ²)	Dpa	Macro Strain (%)	Fraction of tetragonal phase (%)	Swelling (%)
120 keV He^+	300 K	1×10^{16}	0.048	0.04	-	1.4
		2×10^{17}	9.6	0.06	-	2.7
	143 K	1×10^{16}	0.048	0.09	-	
		2×10^{17}	9.6	0.33	-	0.009
120 keV Ar^+	300 K	1×10^{16}	20		9	
		1×10^{17}	200	0.10	9	1.6
	143 K	1×10^{16}	20		10	
		2×10^{17}	400	0.18	20	0.009
60 keV Kr^+	300 K	1×10^{16}	34.8	0.08	2.5	0.03
		5×10^{16}	174	0.02	3	
		1×10^{17}	348		4.5	0.04
	143 K	1×10^{16}	34.8	0.04	4.5	0.1
		5×10^{16}	174	0.03	5.5	
		1×10^{17}	348		8.5	0.03

6.3. Bubbles formation and bubble induced swelling

Morphological and microstructural changes in the ion irradiated zirconia samples were characterized by scanning electron microscopy and transmission electron microscopy. SEM images revealed that upon ion irradiation, the porosity of the samples decreases. In addition to the reduction in the porosity, joining of the grains was also observed. In case of Kr^+ ion irradiation, the joining of the grains is so high that they formed a network due to local melting during ion irradiation. These structures resembled more like the high burn up structure. TEM results revealed the formation of inert gas bubbles upon ion irradiation for all the ions irrespective of the irradiation temperatures (300 K and 143 K).

Average bubble size, bubble density and swelling was calculated (refer Table 4.1) and it was found that bubble number density is very low in the samples irradiated at 143 K. The bubble formation was explained in terms of heterogenous nucleation process. Bubble areal density and bubble induced material swelling was found to be low when the irradiation was carried out at 143 K. This is because of the immobility of the defects at

such low temperatures. Bubble areal density was high (for the same ion fluence) in case of the Ar^+ ion irradiation compared to the He^+ and Kr^+ ion irradiation. However, it is expected to be high for the Kr^+ ion irradiation, but the sputtering of the Kr^+ ion irradiated layer (due to its high sputtering yield and shallow projected range) makes the bubble formation less favorable compared to the Ar^+ ion irradiation.

6.4. Luminescence properties of ion and laser irradiated monoclinic zirconia

To study the effects produced by the fission fragment damage which is similar to SHI irradiation, laser irradiation (200 and 2000 shots) were employed. In order to study the evolution of the defects produced during the ion irradiation, photoluminescence and time resolved photoluminescence spectroscopy were employed.

PL measurements show the presence of a broad band around 2.53 eV. This broad band is attributed to the oxygen vacancies. The slow lifetime (4-5 ns) obtained from the TRPL measurements also confirmed the production of defects (oxygen related vacancies) upon ion (He^+ , Ar^+ and Kr^+) irradiation presence of defects. The PL intensity ratio ($I_{\text{ion irradiated}}/I_{\text{as-sintered}}$) as a function of ion fluence was also plotted (*refer* Figure 5.22). From the PL intensity ratio it was observed that, in case of He^+ ion irradiation, the ion irradiation induced annealing was observed. However, in case of Ar^+ ion irradiation, the PL intensity ratio was found to increase with the ion fluence as defect production varies in proportion with the ion fluence. In case of Kr^+ ion irradiation, whether the vacancy assists the bubble formation or gets accommodated in the lattice determines the PL intensity ratio.

When the vacancies are mobile and form bubbles, the stress due vacancies are less in the sample which gives rise to the reduction in monoclinic to tetragonal phase transformation as evident from Raman scattering and electron diffraction experiments. From the observations of GIXRD, SAED, Raman scattering, electron microscopy, PL and TRPL measurements, it is concluded that the oxygen vacancy concentration dictates the phase transformation (stress induced by oxygen related vacancies) and swelling (stress relieved by bubble formation).

6.5. Scope for future work

In addition to the irradiation conditions used in the thesis work, inclusion of other conditions like high temperature and pressure would also lead to more structural phase transformation. This could make possible the transformation that is not possible at ambient conditions. In addition, fission fragment damage in inert gas ion implanted monoclinic

zirconia and its interaction, bubble induced swelling and damage by the swift heavy ions can be studied. As yttria stabilised zirconia is found to be radiation resistant, its radiation response to low energy inert gas ions could be studied to explore the structural transformation and morphological changes.

A.1 X-Ray Fluorescence spectroscopy

X-Ray fluorescence spectroscopy measurements were carried out to check the presence of impurities in the as-sintered zirconia samples in particular Ti impurity. Figure A.1 shows the X-Ray fluorescence spectra obtained from the as-sintered zirconia samples and titanium (for reference).

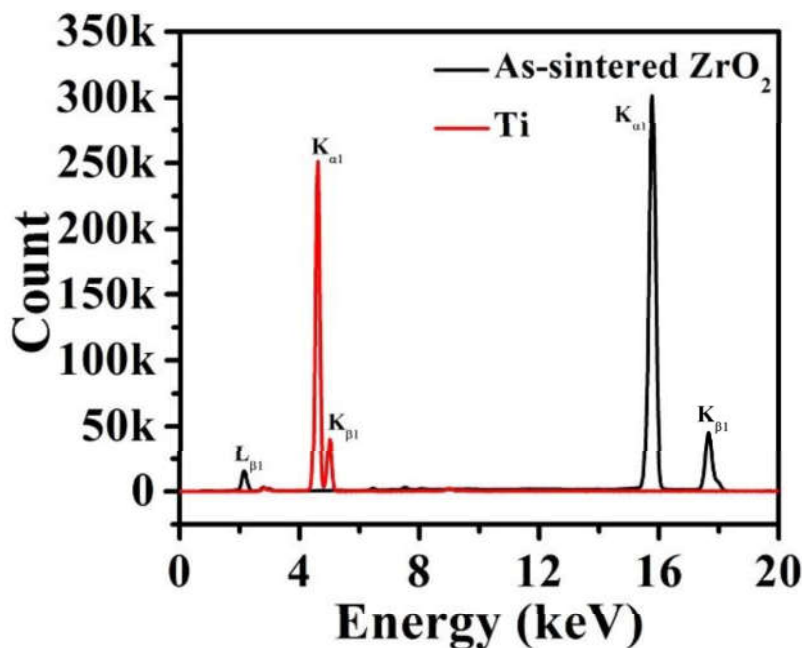


Figure A.1 X-Ray fluorescence spectra obtained from (a) as-sintered ZrO_2 and (b) Titanium (Ti). Count for Ti is multiplied by 10 for clarity. It is observed that Ti impurities are absent in the as-sintered ZrO_2

As observed from X-ray fluorescence spectra, the as-sintered samples shows the presence of $L_{\beta 1}$ (2.126 keV), $K_{\alpha 1}$ (15.775 keV) and $K_{\beta 1}$ (17.668 keV) corresponding to zirconium. Presence of titanium was also checked by taking the X-ray fluorescence measurements using titanium as reference. It is noticed that the spectral peaks corresponding to the element Titanium appears around $K_{\alpha 1}$ (4.512 keV) and $K_{\beta 1}$ (4.933 keV). However, it is observed that the energy peaks corresponding to titanium ($K_{\alpha 1}$ (4.512 keV) and $K_{\beta 1}$ (4.933 keV)) is absent in the as-sintered zirconia samples. Thus the presence of titanium cannot be attributed to the observed PL band at 2.53 eV (refer Section 5.6).

References

- [1] INTERNATIONAL ATOMIC ENERGY AGENCY, Viability of Inert Matrix Fuel in Reducing Plutonium Amounts in Reactors, IAEA-TECDOC-1516, *Vienna*, (2006)
- [2] Gosset D., Provot B., Boron carbide as a potential inert matrix: an evaluation, *Prog. Nucl. Energy*, (2001), **38**, 263–266
- [3] Kloosterman J.L., Damen P.M.G., Reactor physics aspects of plutonium burning in inert matrix fuels, *J. Nucl. Mater.*, (1999), **274**, 112–119
- [4] VERRALL R.A., Development of Inert-Matrix, Carrier Fuels for Burning Plutonium or Actinide-Waste, In: Proc. 5th International Conference on CANDU Fuel, Toronto, Canada., (1997)
- [5] Wuchina E., Opila E., Opeka M., Fahrenholtz W., Talmy I., UHTCs: Ultra-High Temperature Ceramic Materials for extreme Environment Applications, *Electrochem. Soc. Interface*, (2007), **16**, 30–36
- [6] Padture N.P., Gell M., Jordan E.H., Thermal Barrier Coatings for Gas-Turbine Engine Applications, *Science*, (2002), **296**, 280–284
- [7] Vassen R., Cao X., Tietz F., Basu D., Stöver D., Zirconates as New Materials for Thermal Barrier Coatings, *J. Am. Ceram. Soc.*, (2004), **83**, 2023–2028
- [8] Gong W.L., Lutze W., Ewing R.C., Zirconia ceramics for excess weapons plutonium waste, *J. Nucl. Mater.*, (2000), **277**, 239–249
- [9] Gong W.L., Lutze W., Ewing R.C., Reaction sintered glass: a durable matrix for spinel-forming nuclear waste compositions, *J. Nucl. Mater.*, (2000), **278**, 73–84
- [10] Olander D.R., Fundamental aspects of nuclear reactor fuel elements, *Technical Information Center, Office of Public Affairs Energy Research and Development Administration*, (1976)
- [11] Vollath D., Fischer F.D., Hagelstein M., Szabó D. V., Phases and phase transformations in nanocrystalline ZrO₂, *J. Nanopart. Res.*, (2006), **8**, 1003–1016
- [12] Holmes H.F., Fuller E.L., Gammage R.B., Heats of Immersion in the Zirconium Oxide-Water System, *J. Phys. Chem.*, (1972), **76**, 1497–1502
- [13] Mayo M.J., Suresh A., Porter W.D., Thermodynamics For Nanosystems: Grain and Particle-Size Dependent Phase Diagrams, *Rev. Adv. Mater. Sci.*, (2003), **5**, 100–109
- [14] Garvie R.C., The Occurrence of Metastable Tetragonal Zirconia as a Crystallite Size Effect, *J. Phys. Chem.*, (1965), **69**, 1238–1243
- [15] Garvie R.C., Stabilization of the Tetragonal Structure in Zirconia Microcrystals, *J. Phys. Chem.*, (1978), **82**, 218–224
- [16] V. Filipovich and A. Kalinina, The Structure of Glass, edited by N. A. Torapov and E. A. Porai-Koshits, In: *Consultants Bureau, New York*, (1965), Vol. 5, 34
- [17] Meldrum A., Boatner L.A., Ewing R.C., Size effects in the irradiation-induced crystalline-to-amorphous transformation, *Nucl. Instruments Methods B*, (2003), **207**, 28–35
- [18] Bremholm M., Becker-Christensen J., Lversen B.B., High-pressure, High-

- Temperature Formation of Phase-Pure Monoclinic Zirconia Nanocrystals Studied by Time-Resolved in situ Synchrotron X-Ray Diffraction, *Adv. Mater.*, (2009), **21**, 3572–3575
- [19] Pitcher M.W., Ushakov S. V., Navrotsky A., Woodfield B.F., Li G., Boerio-Goates J., Tissue B.M., Energy Crossovers in Nanocrystalline Zirconia, *J. Am. Ceram. Soc.*, (2005), **88**, 160–167
- [20] Namavar F., Wang G., Cheung C.L., Sabirianov R.F., Zeng X.C., Mei W.N., Bai J., Brewer J.R., Haider H., Garvin K.L., Thermal stability of nanostructurally stabilized zirconium oxide, *Nanotechnology*, (2007), **18**, 415702–415707
- [21] Lu F., Zhang J., Huang M., Namavar F., Ewing R.C., Lian J., Phase Transformation of Nanosized ZrO₂ upon Thermal Annealing and Intense Radiation, *J. Phys. Chem. C*, (2011), **115**, 7193–7201
- [22] Ohtaka O., Fukui H., Kunisada T., Fujisawa T., Funakoshi K., Utsumi W., Irifune T., Kuroda K., Kikegawa T., Phase relations and equations of state of ZrO₂ under high temperature and high pressure, *Phys. Rev. B*, (2001), **63**, 174108–174115
- [23] Ohtaka O., Kume S., Ito E., Synthesis and Phase Stability of Cotunnite-Type Zirconia, *J. Am. Ceram. Soc.*, (1988), **71**, C448–C449
- [24] Eichler J., Eisele U., Rödel J., Mechanical Properties of Monoclinic Zirconia, *J. Am. Ceram. Soc.*, (2004), **87**, 1401–1403
- [25] Hannink R.H.J., Kelly P.M., Muddle B.C., Transformation Toughening in Zirconia-Containing Ceramics, *J. Am. Ceram. Soc.*, (2004), **83**, 461–487
- [26] Contreras M.E., Orozco H., Medina-Flores A., Espitia I., Structural analysis of yttria partially stabilized zirconia, *Rev. Mex. Fis. S*, (2009), **55**, 127–129
- [27] Arashi H., Yagi T., Akimoto S., Kudoh Y., New high-pressure phase of ZrO₂ above 35 GPa, *Phys. Rev. B*, (1990), **41**, 4309–4313
- [28] Haines J., Léger J.M., Atouf A., Crystal Structure and Equation of State of Cotunnite-Type Zirconia, *J. Am. Ceram. Soc.*, (1995), **78**, 445–448
- [29] Bouvier P., Djurado E., Lucazeau G., Le Bihan T., High-pressure structural evolution of undoped tetragonal nanocrystalline zirconia, *Phys. Rev. B*, (2000), **62**, 8731–8737
- [30] Leger J.M., Tomaszewski P.E., Atouf A., Pereira A.S., Pressure-induced structural phase transitions in zirconia under high pressure, *Phys. Rev. B*, (1993), **47**, 14075–14083
- [31] Desgreniers S., Lagarec K., High-density ZrO₂ and HfO₂: Crystalline structures and equations of state, *Phys. Rev. B*, (1999), **59**, 8467–8472
- [32] Lowther J.E., Dewhurst J.K., Leger J.M., Haines J., Relative stability of ZrO₂ and HfO₂ structural phases J., *Phys. Rev. B*, (1999), **60**, 14485–14488
- [33] Jaffe J.E., Bachorz R.A., Gutowski M., Low-temperature polymorphs of ZrO₂ and HfO₂: A density-functional theory study, *Phys. Rev. B*, (2005), **72**, 144107–144115
- [34] Mondal A., Ram S., Formation of a new polymorph of ZrO₂ with orthorhombic crystal structure contained in a mesoporous structure, *Chem. Phys. Lett.*, (2003), **382**, 297–306
- [35] Luo X., Zhou W., Ushakov S. V., Navrotsky A., Demkov A.A., Monoclinic to

- tetragonal transformations in hafnia and zirconia: A combined calorimetric and density functional study, *Phys. Rev. B*, (2009), **80**, 134119–134131
- [36] Dewhurst J., Lowther J.E., Relative stability, structure, and elastic properties of several phases of pure zirconia, *Phys. Rev. B*, (1998), **57**, 741–747
- [37] Ziegler J.F., Biersack, J, P, Littmark U., “The Stopping and Range of Ions in Solids,” *New York: Pergamon*, (1985)
- [38] R. Spohr, Ion Tracks and Microtechnology: Principles and Applications, *Vieweg Bertelsmann Publishing Group International*, (1990)
- [39] Gary Was, Windows M., Corporation M., Hori K., Sakajiri A., Fundamentals of Radiation Materials Science, *Springer Berlin Heidelberg, Berlin, Heidelberg*, (2007)
- [40] Sharma A., Varshney M., Shin H.J., Kumar Y., Gautam S., Chae K.H., Monoclinic to tetragonal phase transition in ZrO₂ thin films under swift heavy ion irradiation: Structural and electronic structure study, *Chem. Phys. Lett.*, (2014), **592**, 85–89
- [41] Lian J., Zhang J., Namavar F., Zhang Y., Lu F., Haider H., Garvin K., Weber W.J., Ewing R.C., Ion beam-induced amorphous-to-tetragonal phase transformation and grain growth of nanocrystalline zirconia, *Nanotechnology*, (2009), **20**, 245303–245309
- [42] Schuster B., Fujara F., Merk B., Neumann R., Seidl T., Trautmann C., Response behavior of ZrO₂ under swift heavy ion irradiation with and without external pressure, *Nucl. Instruments Methods B*, (2012), **277**, 45–52
- [43] Lu F., Zhang J., Navrotsky A., Ewing R., Lian J., Temperature and Size Effects on Radiation-Induced Phase Transformation in Monoclinic Nano-Sized Zirconia, *Microsc. Microanal.*, (2010), **16**, 1624–1625
- [44] Valdez J.A., Chi Z., Sickafus K.E., Light ion irradiation-induced phase transformation in the monoclinic polymorph of zirconia, *J. Nucl. Mater.*, (2008), **381**, 259–266
- [45] Schuster B., Lang M., Klein R., Trautmann C., Neumann R., Benyagoub A., Structural phase transition in ZrO₂ induced by swift heavy ion irradiation at high-pressure, *Nucl. Instruments Methods B*, (2009), **267**, 964–968
- [46] Zhang Y., Jiang W., Wang C., Namavar F., Edmondson P.D., Zhu Z., Gao F., Lian J., Weber W.J., Grain growth and phase stability of nanocrystalline cubic zirconia under ion irradiation, *Phys. Rev. B*, (2010), **82**, 1–7
- [47] Meldrum A., Boatner L.A., Ewing R.C., Nanocrystalline Zirconia Can Be Amorphized by Ion Irradiation, *Phys. Rev. Lett.*, (2002), **88**, 255031–255034
- [48] Lu F., Wang J., Lang M., Toulemonde M., Namavar F., Trautmann C., Zhang J., Ewing R.C., Lian J., Amorphization of nanocrystalline monoclinic ZrO₂ by swift heavy ion irradiation, *Phys. Chem. Chem. Phys.*, (2012), **14**, 12295–12300
- [49] Hojo T., Yamamoto H., Aihara J., Furuno S., Sawa K., Sakuma T., Hojou K., Radiation effects on yttria-stabilized zirconia irradiated with He or Xe ions at high temperature, *Nucl. Instruments Methods B*, (2005), **241**, 536–542
- [50] Klaumünzer S., Schumacher G., Dramatic growth of glassy Pd₈₀Si₂₀ during heavy-ion irradiation, *Phys. Rev. Lett.*, (1983), **51**, 1987–1990

-
- [51] Klaumünzer S., Hou M., Schumacher G., Coulomb Explosions in a Metallic Glass Due to the Passage of Fast Heavy Ions?, *Phys. Rev. Lett.*, (1986), **57**, 850–853
- [52] Audouard A., Balanzat E., Fuchs G., Jousset J.C., Lesueur D., Thome L., Radiation Damage Induced by Electronic-Energy Loss in Amorphous Metallic Alloys, *Europhys. Lett.*, (1988), **5**, 241–245
- [53] Iwase A., Sasaki S., Iwata T., Nihira T., Anomalous Reduction of R_{stage-I} Recovery in Nickel Irradiated with Heavy Ions in the Energy Range 100–120 MeV, *Phys. Rev. Lett.*, (1987), **58**, 2450–2453
- [54] Klaumünzer S., Schumacher G., Rentzsch S., Vogl G., Söldner L., Bieger H., Severe Radiation Damage By Heavy Ions in glassy Pd₈₀Si₂₀, *Acta Metall.*, (1982), **30**, 1493–1502
- [55] Audouard A., Balanzat E., Fuchs G., Jousset J.C., Lesueur D., Thome L., High-Energy Heavy-Ion Irradiations of Fe 85 B 15 Amorphous Alloy: Evidence for Electronic Energy Loss Effect, *Europhys. Lett.*, (1987), **3**, 327–331
- [56] Barbu A., Dunlop A., Lesueur D., Averbach R.S., Latent Tracks Do Exist in Metallic Materials, *Europhys. Lett.*, (1991), **15**, 37–42
- [57] Audouard A., Balanzat E., Bouffard S., Jousset J.C., Chamberod A., Dunlop A., Lesueur D., Fuchs G., Spohr R., Vetter J., Thomé L., Evidence for Amorphization of a Metallic Alloy by Ion Electronic Energy Loss, *Phys. Rev. Lett.*, (1990), **65**, 875–878
- [58] Lesueur D., Dunlop A., Damage creation via electronic excitations in metallic targets part II : A theoretical model, *Radiat. Eff. Defects Solids*, (1993), **126**, 163–172
- [59] Fleischer R.L, Price P. B, Walker R.M, Nuclear tracks in solids : Principles and applications, *University of California Press, United States*, (1975)
- [60] Wang Z.G., Dufour C., Paumier E., Toulemonde M., The Se sensitivity of metals under swift-heavy-ion irradiation: a transient thermal process, *J. Phys. Condens. Matter*, (1994), **6**, 6733–6750
- [61] Toulemonde M., Dufour, Ch, Meftah A., Paumier E., Transient thermal processes in heavy ion irradiation of crystalline inorganic insulators, *Nucl. Instruments Methods B*, (2000), **166**, 903–912
- [62] Szenes G., General features of latent track formation in magnetic insulators irradiated with swift heavy ions, *Phys. Rev. B*, (1995), **51**, 8026–8029
- [63] Seitz Fand J. S. Koehler, Displacement of Atoms during Irradiation., *Academic Press, London/New York*, (1956)
- [64] Klaumünzer A.B. and S., Radiat. Eff. Defects Solids, *Radiat. Eff. Defects Solids*, (1993), **105**
- [65] M. Toulemonde, E. Paumier, and Dufour. Ch, Thermal spike model in the electronic stopping power regime. *Rad. Eff. Def. Solids*, In: (1993), 126:1–4,
- [66] Benyagoub A., Mechanism of the monoclinic-to-tetragonal phase transition induced in zirconia and hafnia by swift heavy ions, *Phys. Rev. B*, (2005), **72**, 094114
- [67] Hémon S., Chailley V., Dooryhée E., Dufour C., Gourbilleau F., Levesque F., Paumier E., Phase transformation of polycrystalline Y₂O₃ under irradiation with
-

- swift heavy ions, *Nucl. Instruments Methods B*, (1997), **122**, 563–565
- [68] Benyagoub A., Levesque F., Couvreur F., Gibert-Mougel C., Dufour C., Paumier E., Evidence of a phase transition induced in zirconia by high energy heavy ions, *Appl. Phys. Lett.*, (2000), **77**, 3197–3199
- [69] Benyagoub A., Couvreur F., Bouffard S., Levesque F., Dufour C., Paumier E., Phase transformation induced in pure zirconia by high energy heavy ion irradiation, *Nucl. Instruments Methods B*, (2001), **175–177**, 417–421
- [70] Benyagoub A., Kinetics of the crystalline to crystalline phase transformation induced in pure zirconia by swift heavy ion irradiation, *Nucl. Instruments Methods B*, (2003), **206**, 132–138
- [71] Benyagoub A., Evidence of an ion-beam induced crystalline-to-crystalline phase transformation in hafnia, *Eur. Phys. J. B*, (2003), **34**, 395–398
- [72] Benyagoub A., Swift heavy ion induced crystalline-to-crystalline phase transition in zirconia and hafnia: A comparative study, *Nucl. Instruments Methods B*, (2004), **218**, 451–456
- [73] Gibert-Mougel C., Couvreur F., Costantini J.M., Bouffard S., Levesque F., Hémon S., Paumier E., Dufour C., Phase transformation of polycrystalline zirconia induced by swift heavy ion irradiation, *J. Nucl. Mater.*, (2001), **295**, 121–125
- [74] Benyagoub A., Levesque F., Dramatic change of the kinetics of the phase transition induced in pure zirconia by swift heavy-ion irradiation, *Europhys. Lett.*, (2002), **60**, 580–586
- [75] Baldinozzi G., Simeone D., Gosset D., Monnet I., Le Caër S., Mazerolles L., Evidence of extended defects in pure zirconia irradiated by swift heavy ions, *Phys. Rev. B*, (2006), **74**, 132107–132110
- [76] Balasaritha P., Amirthapandian S., Magudapathy P., Krishnan R., Panigrahi B.K., Krypton ion induced structural phase transition in zirconia thin film, In: AIP Conference Proceedings, (2017), 030015–030017
- [77] Eichler A., Tetragonal Y-doped zirconia: Structure and ion conductivity, *Phys. Rev. B*, (2001), **64**, 174103–174110
- [78] Lu X., Liang K., Gu S., Zheng Y., Fang H., Effect of oxygen vacancies on transformation of zirconia at low temperatures, *J. Mater. Sci.*, (1997), **32**, 6653–6656
- [79] He L., Yablinsky C., Gupta M., Gan J., Kirk M.A., Allen T.R., Transmission Electron Microscopy Investigation of Krypton Bubbles in Polycrystalline CeO₂, *Nucl. Technol.*, (2013), **182**, 164–169
- [80] Rose M., Balogh A.G., Hahn H., Instability of irradiation induced defects in nanostructured materials, *Nucl. Instruments Methods B*, (1997), **127/128**, 119–122
- [81] Misra A., Demkowicz M.J., Zhang X., Hoagland R.G., The radiation damage tolerance of ultra-high strength nanolayered composites, *JOM*, (2007), **59**, 62–65
- [82] Spino J., Santa Cruz H., Jovani-Abril R., Birtcher R., Ferrero C., Bulk-nanocrystalline oxide nuclear fuels - An innovative material option for increasing fission gas retention, plasticity and radiation-tolerance, *J. Nucl. Mater.*, (2012), **422**, 27–44

- [83] Ukai S., Fujiwara M., Perspective of ODS alloys application in nuclear environments, *J. Nucl. Mater.*, (2002), **307–311**, 749–757
- [84] He L.F., Valderrama B., Hassan A.R., Yu J., Gupta M., Pakarinen J., Henderson H.B., Gan J., Kirk M.A., Nelson A.T., Manuel M. V., El-Azab A., Allen T.R., Bubble formation and Kr distribution in Kr-irradiated UO₂, *J. Nucl. Mater.*, (2015), **456**, 125–132
- [85] Evans J.H., van Veen A., Westerduin K.T., A TEM and TDS study of gas release from bubbles in krypton-implanted uranium dioxide, *J. Nucl. Mater.*, (1992), **195**, 250–259
- [86] Nogita K., Une K., High resolution TEM observation and density estimation of Xe bubbles in high burnup UO₂ fuels, *Nucl. Instruments Methods B*, (1998), **141**, 481–486
- [87] Hojou K., Radiation Effects on Ytria-stabilized ZrO₂ Single Crystals with Helium and Xenon Ions at RT and 923 K, In: AIP Conference Proceedings, (2003), 647–652
- [88] Zhang Y., Zhao Z., Guo G., Irradiation effects of displacement damage and gas atoms in Ytria-stabilized zirconia irradiated by Au and helium ions, *Nucl. Instruments Methods B*, (2017), **403**, 33–37
- [89] Pu G., Zou J., Lin L., Zhang K., Liu B., Ma F., Wang Q., Li Q., Effects of He ion irradiation on the microstructures and mechanical properties of t' phase yttria-stabilized zirconia ceramics, *J. Alloys Compd.*, (2019), **771**, 777–783
- [90] Venkataraj S., Kappertz O., Weis H., Drese R., Jayavel R., Wuttig M., Structural and optical properties of thin zirconium oxide films prepared by reactive direct current magnetron sputtering, *J. Appl. Phys.*, (2002), **92**, 3599–3607
- [91] Lai L.J., Lu H.C., Chen H.K., Cheng B.M., Lin M.I., Chu T.C., Photoluminescence of zirconia films with VUV excitation, *J. Electron Spectros. Relat. Phenomena*, (2005), **144–147**, 865–868
- [92] Gottmann J., Husmann A., Klotzbücher T., Kreutz E.W., Optical properties of alumina and zirconia thin films grown by pulsed laser deposition, *Surf. Coat. Technol.*, (1998), **100–101**, 415–419
- [93] Smits K., Grigorjeva L., Millers D., Sarakovskis A., Grabis J., Lojkowski W., Intrinsic defect related luminescence in ZrO₂, *J. Lumin.*, (2011), **131**, 2058–2062
- [94] Petrik N.G., Taylor D.P., Orlando T.M., Laser-stimulated luminescence of yttria-stabilized cubic zirconia crystals, *J. Appl. Phys.*, (1999), **85**, 6770–6776
- [95] Lakshmi J.S., John Berlin I., Daniel G.P., Thomas P. V., Joy K., Effect of calcination atmosphere on photoluminescence properties of nanocrystalline ZrO₂ thin films prepared by solgel dip coating method, *Physica B*, (2011), **406**, 3050–3055
- [96] Joy K., Maneeshya L. V., Thomas J.K., Thomas P. V., Effect of sol concentration on the structural, morphological, optical and photoluminescence properties of zirconia thin films, *Thin Solid Films*, (2012), **520**, 2683–2688
- [97] Cong Y., Li B., Yue S., Fan D., Wang X.J., Effect of Oxygen Vacancy on Phase Transition and Photoluminescence Properties of Nanocrystalline Zirconia Synthesized by the One Pot Reaction, *J. Phys. Chem. C*, (2009), **113**, 13974–13978

-
- [98] Wang Z., Zhang J., Zheng G., Liu Y., Zhao Y., The unusual variations of photoluminescence and afterglow properties in monoclinic ZrO₂ by annealing, *J. Lumin.*, (2012), **132**, 2817–2821
- [99] Chernov V., Belykh A., Meléndrez R., Barboza-Flores M., Beta radiation induced thermoluminescence in pure ZrO₂ prepared by sol-gel, *J. Non. Cryst. Solids*, (2006), **352**, 2543–2547
- [100] Cong Y., Li B., Lei B., Li W., Long lasting phosphorescent properties of Ti doped ZrO₂, *J. Lumin.*, (2007), **126**, 822–826
- [101] Liang J., Jiang X., Liu G., Deng Z., Zhuang J., Li F., Li Y., Characterization and synthesis of pure ZrO₂ nanopowders via sonochemical method, *Mater. Res. Bull.*, (2003), **38**, 161–168
- [102] Lin C., Zhang C., Lin J., Phase Transformation and Photoluminescence Properties of Nanocrystalline ZrO₂ Powders Prepared via the Pechini-type Sol-Gel process, *J. Phys. Chem. C*, (2007), **111**, 3300–3307
- [103] John Berlin I., Lakshmi J.S., Sujatha Lekshmy S., Daniel G.P., Thomas P. V., Joy K., Effect of sol temperature on the structure, morphology, optical and photoluminescence properties of nanocrystalline zirconia thin films, *J. Sol-Gel Sci. Technol.*, (2011), **58**, 669–676
- [104] Joy K., Berlin I.J., Nair P.B., Lakshmi J.S., Daniel G.P., Thomas P. V., Effects of annealing temperature on the structural and photoluminescence properties of nanocrystalline ZrO₂ thin films prepared by solgel route, *J. Phys. Chem. Solids*, (2011), **72**, 673–677
- [105] Smits K., Grigorjeva L., Łojkowski W., Fidelus J.D., Luminescence of oxygen related defects in zirconia nanocrystals, *Phys. Status Solidi*, (2007), **4**, 770–773
- [106] Salah N., Habib S.S., Khan Z.H., Djouider F., Thermoluminescence and photoluminescence of ZrO₂ nanoparticles, *Radiat. Phys. Chem.*, (2011), **80**, 923–928
- [107] Xie Y., Ma Z., Liu L., Su Y., Zhao H., Liu Y., Zhang Z., Duan H., Li J., Xie E., Oxygen defects-modulated green photoluminescence of Tb-doped ZrO₂ nanofibers, *Appl. Phys. Lett.*, (2010), **97**, 141916–141918
- [108] Rittman D.R., Tracy C.L., Cusick A.B., Abere M.J., Torralva B., Ewing R.C., Yalisove S.M., Ultrafast laser and swift heavy ion irradiation: Response of Gd₂O₃ and ZrO₂ to intense electronic excitation, *Appl. Phys. Lett.*, (2015), **106**, 171914–171918
- [109] Stöcker C., Baiker A., Zirconia aerogels: effect of acid-to-alkoxide ratio, alcoholic solvent and supercritical drying method on structural properties, *J. Non. Cryst. Solids*, (1998), **223**, 165–178
- [110] Moravec P., Smolík J., Keskinen H., Mäkelä J.M., Leviansky V. V., Vapor Phase Synthesis of Zirconia Fine Particles from Zirconium Tetra-Tert-Butoxide, *Aerosol Air Qual. Res.*, (2007), **7**, 563–577
- [111] Srdić V. V., Winterer M., Comparison of nanosized zirconia synthesized by gas and liquid phase methods, *J. Eur. Ceram. Soc.*, (2006), **26**, 3145–3151
- [112] Hwangbo Y., Lee Y.I., Facile synthesis of zirconia nanoparticles using a salt-assisted ultrasonic spray pyrolysis combined with a citrate precursor method, *J.*
-

- Alloys Compd.*, (2019), **771**, 821–826
- [113] Tai C.Y., Hsiao B.Y., Chiu H.Y., Preparation of spherical hydrous-zirconia nanoparticles by low temperature hydrolysis in a reverse microemulsion, *Colloids Surf. A Physicochem. Eng. Asp.*, (2004), **237**, 105–111
- [114] Meskin P.E., Ivanov V.K., Barantchikov A.E., Churagulov B.R., Tretyakov Y.D., Ultrasonically assisted hydrothermal synthesis of nanocrystalline ZrO₂, TiO₂, NiFe₂O₄ and Ni_{0.5}Zn_{0.5}Fe₂O₄ powders, *Ultrason. Sonochem.*, (2006), **13**, 47–53
- [115] Vollath D., Sickafus K.E., Synthesis of nanosized ceramic oxide powders by microwave plasma reactions, *Nanostructured Mater.*, (1992), **1**, 427–437
- [116] Cheng L., Li W., Li Y., Yang Y., Li Y., Cheng Y., Song D., Thermal analysis and decomposition kinetics of the dehydration of copper sulfate pentahydrate, *J. Therm. Anal. Calorim.*, (2019), **135**, 2697–2703
- [117] Mahfouz R.M., Ahmed G.A.W., Al-Wassil A.I., Siddiqui M.R.H., Al-Otaibi A.M., Radiation-induced synthesis of ZrO₂ nanoparticles by thermal decomposition of zirconium acetylacetonate, *Radiat. Eff. Defects Solids*, (2013), **168**, 950–958
- [118] P. Scherrer, *Nachr. Ges. Wiss. Göttingen*, (1918), **26**, 98–100
- [119] C. Suryanarayana, M. G. Norton, *X-Ray Diffraction A practical Approach* (1998), *Plenum Press, New York, n.d.*
- [120] Kalita P., Ghosh S., Sattonnay G., Singh U.B., Grover V., Shukla R., Amirthapandian S., Meena R., Tyagi A.K., Avasthi D.K., Role of temperature in the radiation stability of yttria stabilized zirconia under swift heavy ion irradiation: A study from the perspective of nuclear reactor applications, *J. Appl. Phys.*, (2017), **122**, 025902–025909
- [121] Williams David B., Barry Carter C., *Transmission Electron Microscopy: A Textbook for Materials Science*, *Springer US*, (2009)
- [122] Yoshimura M., Phase Stability of Zirconia, *Am. Ceram. Soc. Bull.*, (1988), **67**, 1950–1955
- [123] Lutze W., Gong W.L., Ewing R.C., Ceramic Waste Forms for Excess Weapons Plutonium, In: *The Environmental Challenges of Nuclear Disarmament*, (2000), 65–74
- [124] T MUROMURA Y.H., FLUORITE TYPE PHASE IN NUCLEAR WASTE CERAMICS WITH HIGH ZIRCONIA AND ALUMINA CONTENTS, *J. Nucl. Mater.*, (1987), **151**, 55–62
- [125] Müller, Th, Kästle G., Boyen H.G., Eisenmenger J., Ziemann P., Holgado J.P., Gonzalez-Elipe A.R., Structural phase transitions in ZrO₂ films induced by ion bombardment - Argon irradiation versus implantation, *J. Appl. Phys.*, (2003), **93**, 5251–5254
- [126] Rawat M., Das A., Shukla D.K., Rajput P., Chettah A., Phase D.M., Ramola R.C., Singh F., Micro-Raman and electronic structure study on kinetics of electronic excitations induced monoclinic-to-tetragonal phase transition in zirconium oxide films, *RSC Adv.*, (2016), **6**, 104425–104432
- [127] Sickafus K.E., Matzke H., Hartmann T., Yasuda K., Valdez J.A., Chodak P., Nastasi M., Verrall R.A., Radiation damage effects in zirconia, *J. Nucl. Mater.*, (1999), **274**, 66–77

- [128] Chevalier J., Gremillard L., Virkar A. V., Clarke D.R., The tetragonal-monoclinic transformation in zirconia: Lessons learned and future trends, *J. Am. Ceram. Soc.*, (2009), **92**, 1901–1920
- [129] Simeone D., Baldinozzi G., Gosset D., Zalczer G., Béar J.F., Rietveld refinements performed on mesoporous ceria layers at grazing incidence, *J. Appl. Crystallogr.*, (2011), **44**, 1205–1210
- [130] Simeone D., Baldinozzi G., Gosset D., Le Caer S., Béar J.F., Grazing incidence X-ray diffraction for the study of polycrystalline layers, *Thin Solid Films*, (2013), **530**, 9–13
- [131] Schneider C. A, Rasband W. S., Eliceiri K.W, NIH Image to ImageJ: 25 years of image analysis, *Nat. Methods*, (2012), **9**, 671–675
- [132] Siu G.G., Stokes M.J., Liu Y., Variation of fundamental and higher-order Raman spectra of ZrO₂ nanograins with annealing temperature, *Phys. Rev. B*, (1999), **59**, 3173–3179
- [133] Kim B.K., Hamaguchi H.O., Mode Assignments of the Raman Spectrum of Monoclinic Zirconia by Isotopic Exchange Technique, *Phys. Status Solidi Basic Res.*, (1997), **203**, 557–563
- [134] E. ANASTASSAKIS., B. PAPANICOLAOU. I.M.A., LATTICE DYNAMICS AND LIGHT SCATTERING IN HAFNIA AND ZIRCONIA*, *J. Phys. Chem. Solids*, (1975), **36**, 667–676
- [135] Xinglun TANG;Xiuhua ZHENG, Raman Scattering and t-Phase lattice Vibration of 3% (Mole fraction) Y₂O₃-ZrO₂, *J. Mater. Sci. Technol*, (2004), **20**, 485–489
- [136] Barberis P., Merle-Méjean T., Quintard P., On Raman spectroscopy of zirconium oxide films, *J. Nucl. Mater.*, (1997), **246**, 232–243
- [137] Quintard P.E., Barbéris P., Mirgorodsky A.P., Merle-Méjean T., Comparative Lattice-Dynamical Study of the Raman Spectra of Monoclinic and Tetragonal Phases of Zirconia and Hafnia, *J. Am. Ceram. Soc.*, (2002), **85**, 1745–1749
- [138] ISHIGAME M., SAKURAI T., Temperature Dependence of the Raman Spectra of ZrO₂, *J. Am. Ceram. Soc.*, (1977), **60**, 367–369
- [139] Simeone D., Baldinozzi G., Gosset D., Le Caër S., Phase transition of pure zirconia under irradiation: A textbook example, *Nucl. Instruments Methods B*, (2006), **250**, 95–100
- [140] Foster A.S., Sulimov, V.B, Gejo, F. Lopez, Shluger, A. L, Nieminen, R, M, Structure and electrical levels of point defects in monoclinic zirconia, *Phys. Rev. B*, (2001), **64**, 224108–224117
- [141] BULLOUGH R., NEWMAN, R.C, The kinetics of migration of point defects to dislocations, *Reports Prog. Phys.*, (1970), **33**, 101–148
- [142] Martin G., Bellon P., Driven Alloys, *Solid State Phys.*, (1996), **50**, 189–331
- [143] Yang J., Youssef M., Yildiz B., Oxygen self-diffusion mechanisms in monoclinic Zr O₂ revealed and quantified by density functional theory, random walk analysis, and kinetic Monte Carlo calculations, *Phys. Rev. B*, (2018), **97**, 024114–024120
- [144] Christensen A., Carter E.A., First-principles study of the surfaces of zirconia, *Phys. Rev. B*, (1998), **58**, 8050–8064

- [145] Baldinozzi G., Simeone D., Gosset D., Dutheil M., Neutron Diffraction Study of the Size-Induced Tetragonal to Monoclinic Phase Transition in Zirconia Nanocrystals, *Phys. Rev. Lett.*, (2003), **90**, 216103–216106
- [146] Boulbitch A.A., Tolédano P., Phase Nucleation of Elastic Defects in Crystals Undergoing a Phase Transition, *Phys. Rev. Lett.*, (1998), **81**, 838–841
- [147] Dhal S., Chatterjee S., Sarkar S., Tribedi L.C., Bapat R., Ayyub P., Nano-welding and junction formation in hydrogen titanate nanowires by low-energy nitrogen ion irradiation, *Nanotechnology*, (2015), **26**, 235601–235606
- [148] Stanford M.G., Mahady K., Lewis B.B., Fowlkes J.D., Tan S., Livengood R., Magel G.A., Moore T.M., Rack P.D., Laser-Assisted Focused He⁺ Ion Beam Induced Etching with and without XeF₂ Gas Assist, *ACS Appl. Mater. Interfaces*, (2016), **8**, 29155–29162
- [149] de Winter D.A.M., Mulders J.J.L., Redeposition characteristics of focused ion beam milling for nanofabrication, *J. Vac. Sci. Technol. B Microelectron. Nanom. Struct.*, (2007), **25**, 2215
- [150] Linnros J., Elliman R.G., Brown W.L., Divacancy control of the balance between ion-beam-induced epitaxial crystallization and amorphization in silicon, *J. Mater. Res.*, (1988), **3**, 1208–1211
- [151] Yutani K., Kishimoto H., Kasada R., Kimura A., Evaluation of Helium effects on swelling behavior of oxide dispersion strengthened ferritic steels under ion irradiation, *J. Nucl. Mater.*, (2007), **367-370 A**, 423–427
- [152] Martin G., Maillard S., Brutzel L. Van, Garcia P., Dorado B., Valot C., A molecular dynamics study of radiation induced diffusion in uranium dioxide, *J. Nucl. Mater.*, (2009), **385**, 351–357
- [153] Mayr S.G., Ashkenazy Y., Albe K., Averback R.S., Mechanisms of Radiation-Induced Viscous Flow: Role of Point Defects, *Phys. Rev. Lett.*, (2003), **90**, 4
- [154] Balasaritha P., Amirthapandian S., Magudapathy P., Sarguna R.M., Srivastava S.K., Panigrahi B.K., Ion beam induced phase transformation and krypton bubble formation in monoclinic zirconium oxide, *J. Nucl. Mater.*, (2018), **508**, 385–394
- [155] Balasaritha P., Amirthapandian S., Magudapathy P., Sarguna R.M., Srivastava S.K., Krishnan R., Low energy Ar⁺ ion irradiation effects in monoclinic zirconia, *Nucl. Instruments Methods B*, (2019), **441**, 23–32
- [156] Nanda K.K., Sahu S.N., Behera S.N., Liquid-drop model for the size-dependent melting of low-dimensional systems, *Phys. Rev. A*, (2002), **66**, 013208–013215
- [157] Shi L. Bin, Wang Y.P., Li M.B., Native defect formation and migration in monoclinic zirconium dioxide, *Mater. Sci. Semicond. Process.*, (2014), **27**, 586–592
- [158] Bai X.M., Voter A.F., Hoagland R.G., Nastasi M., Uberuaga B.P., Efficient Annealing of Radiation Damage Near Grain Boundaries via Interstitial Emission, *Science*, (2010), **327**, 1631–1634
- [159] LLopis J., Luminescence of MgO and CaO Stabilized ZrO₂ Crystals, *Phys. Status Solidi*, (1990), **119**, 661–667
- [160] Zhou L.H., Zhang C.H., Yang Y.T., Li B.S., Enhanced photoluminescence of Ar⁺ implanted sapphire before and after annealing, *J. Lumin.*, (2010), **130**, 226–230

- [161] Kumar A., Pollock T.M., Mapping of femtosecond laser-induced collateral damage by electron backscatter diffraction, *J. Appl. Phys.*, (2011), **110**, 083114–083118
- [162] Feng Q., Picard Y.N., McDonald J.P., Van Rompay P.A., Yalisove S.M., Pollock T.M., Femtosecond laser machining of single-crystal superalloys through thermal barrier coatings, *Mater. Sci. Eng. A*, (2006), **430**, 203–207
- [163] Feng Q., Picard Y.N., Liu H., Yalisove S.M., Mourou G., Pollock T.M., Femtosecond laser micromachining of a single-crystal superalloy, *Scr. Mater.*, (2005), **53**, 511–516
- [164] Huang M.H., Room-Temperature Ultraviolet Nanowire Nanolasers, *Science*, (2001), **292**, 1897–1899
- [165] Bertram F., Christen J., Dadgar A., Krost A., Complex excitonic recombination kinetics in ZnO: Capture, relaxation, and recombination from steady state, *Appl. Phys. Lett.*, (2007), **90**, 041917–041919
- [166] Jung S.W., Park W.I., Cheong H.D., Yi G.C., Jang H.M., Hong S., Joo T., Time-resolved and time-integrated photoluminescence in ZnO epilayers grown on Al₂O₃(0001) by metalorganic vapor phase epitaxy, *Appl. Phys. Lett.*, (2002), **80**, 1924–1926
- [167] Wischmeier L., Voss T., Rückmann I., Gutowski J., Correlations between surface-excitonic emission bands in ZnO nanowires, *Nanotechnology*, (2008), **19**, 135705–135709
- [168] Imparato C., Fantauzzi M., Passiu C., Rea I., Ricca C., Aschauer U., Sannino F., D’Errico G., De Stefano L., Rossi A., Aronne A., Unraveling the Charge State of Oxygen Vacancies in ZrO_{2-x} on the Basis of Synergistic Computational and Experimental Evidence, *J. Phys. Chem. C*, (2019), **123**, 11581–11590
- [169] Hendriks M.G.H.M., ten Elshof J.E., Bouwmeester H.J.M., Verweij H., The electrochemical double-layer capacitance of yttria-stabilised zirconia, *Solid State Ionics*, (2002), **146**, 211–217
- [170] Sinhamahapatra A., Jeon J.P., Kang J., Han B., Yu J.S., Oxygen-Deficient Zirconia (ZrO_{2-x}): A New Material for Solar Light Absorption, *Sci. Rep.*, (2016), **6**, 1–8
- [171] Emeline A., Kataeva G. V., Litke A.S., Rudakova A. V., Ryabchuk V.K., Serpone N., Spectroscopic and Photoluminescence Studies of a Wide Band Gap Insulating Material: Powdered and Colloidal ZrO₂ sols, *Langmuir*, (1998), **14**, 5011–5022
- [172] Zhang Y., Sachan R., Pakarinen O.H., Chisholm M.F., Liu P., Xue H., Weber W.J., Ionization-induced annealing of pre-existing defects in silicon carbide, *Nat. Commun.*, (2015), **6**, 1–7

Thesis Highlight

Name of the Student: **P. BALASARITHA**

Name of CI: **Indira Gandhi Centre for Atomic Research**

Enrolment No.: **PHYS 02 2014 04 004**

Thesis Title: **Inert gas ion irradiation effects on microstructural and optical properties of monoclinic zirconia**

Discipline: **Physical Sciences**

In the present thesis, low energy inert gas (120 keV He⁺, 120 keV Ar⁺ and 60 keV Kr⁺) ion irradiation effects in monoclinic zirconia (one of the materials proposed as inert matrix fuels) is studied to understand the correlation between phase transformation (monoclinic to tetragonal), bubble induced swelling and luminescence properties.

The observations (GIXRD, Raman scattering and electron diffraction) showed that there is a transformation of monoclinic to tetragonal (Fig.1) upon ion irradiation in all the three (He⁺, Ar⁺, and Kr⁺ ion irradiation) cases. **The strain was found to be higher in the zirconia samples where the ion irradiation was carried out at 143 K compared to that at 300 K.** The fraction of the transformed phase was estimated from Raman scattering results and found to increase with the ion fluence. **The amount of the transformed phase (tetragonal) was found to be higher in the case of ion irradiation at 143 K.** TEM investigations show bubble induced swelling (Fig. 2). **The bubble induced swelling was found to be low when the ion irradiation was carried out at 143 K** and it is attributed to the immobility of the defects at such low temperatures.

PL studies showed a band around 2.5 eV (480 nm) for all the ion irradiated samples and it is attributed to the oxygen vacancies. The PL intensity is related to the amount of defects present in the samples. From the PL intensity ratio (Fig. 3), it is observed that when electronic energy loss is dominant, the ionization induced annealing led to reduction defect concentration. But in the cases where nuclear energy loss is dominant case, the defect concentration increases. The phase transformation was attributed to the presence of oxygen vacancies and also to the strain induced by these oxygen vacancies in the zirconia lattice.

When the vacancies are mobile and form bubbles, the stress due to vacancies are less in the sample and that explains the reduction in monoclinic to tetragonal phase transformation which is evident from Raman scattering and electron diffraction experiments. **From the observations of GIXRD, SAED, Raman scattering, electron microscopy, PL and TRPL measurements, it is concluded that the oxygen vacancy concentration dictates the phase transformation (stress induced by oxygen related vacancies) and swelling (stress relived by bubble formation).**

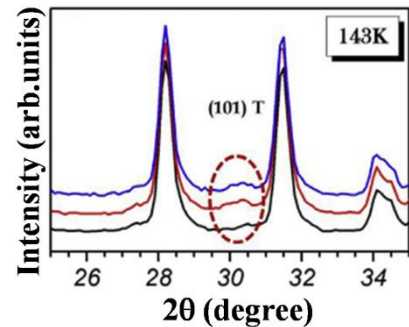


Fig.1 Tetragonal peak in the XRD of Kr⁺ ion irradiated zirconia (1×10^{17} ions/cm²)

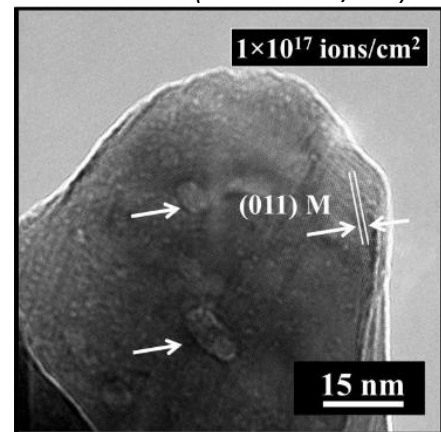


Fig.2 TEM image of the 120 keV He⁺ ion irradiated (at 300 K) zirconia sample

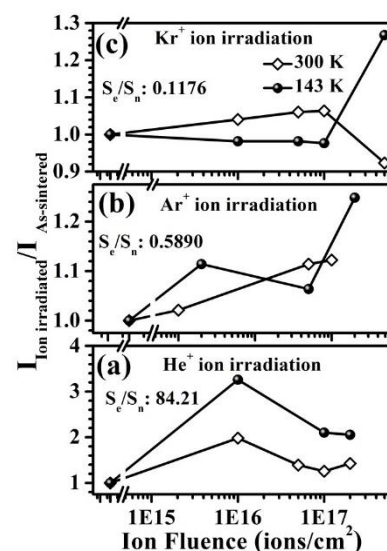


Fig.3 Plot of PL intensity ratio as a function ion fluence for various ion irradiation on zirconia sample